



Cite this: *Chem. Soc. Rev.*, 2018, 47, 2921

Functional and stability orientation synthesis of materials and structures in aprotic Li–O₂ batteries

Peng Zhang,^a Yong Zhao^{id}*^a and Xinbo Zhang^{id}*^b

The lithium–O₂ battery is one of most promising energy storage and conversion devices due to its ultrahigh theoretical energy density and hence has broad application potential in electrical vehicles and stationary power systems. However, the present Li–O₂ battery suffers from a series of challenges for its practical application, such as its low capacity and rate capability, poor round-trip efficiency and short cycle life. These challenges mainly arise from the sluggish and unsustainable discharge and charge reactions at lithium and oxygen electrodes, which determine the performance and durability of a battery. In this review, we first provide insights on the present understanding of the discharge/charge mechanism of such a battery and follow up with establishing a correlation between the specific materials/structures of the battery modules and their functionality/stability within the recent progress in electrodes, electrolytes and redox mediators. Considerable emphasis is paid to the importance of functional orientation design and the synthesis of materials/structures towards accelerating and sustaining the electrode reactions of Li–O₂ batteries. Moreover, the future directions and perspectives of rationally constructed material and surface/interface structures, as well as their optimal combinations are proposed for enhancement of the electrode reaction rate and sustainability, and consequently for a better performance and durability of such batteries.

Received 18th January 2018

DOI: 10.1039/c8cs00009c

rsc.li/chem-soc-*rev*

1. Introduction

With the great demand for advanced energy storage and conversion solutions for electrical vehicles with a long driving range,

the development of next-generation batteries with a high energy density is urgent and necessary.^{1–3} The rechargeable lithium–oxygen (Li–O₂) battery (Fig. 1), sometimes called the Li–air battery, has become one of most promising candidates that can deliver a high electrical energy density higher than possible in the state-of-the-art Li-ion battery.^{4–11} In 2009, IBM Company decided to launch the “Battery 500” project, with the great aim of exploiting a Li–O₂ battery that could operate for a driving range of 500 miles for automobiles.¹² To date, four types of Li–O₂ batteries, including aprotic, aqueous, hybrid and solid-state batteries, have been reported, with the aprotic Li–O₂ battery

^a Key Lab for Special Functional Materials of Ministry of Education, Collaborative Innovation Center of Nano Functional Materials and Applications, Henan University, Kaifeng, Henan, 475004, P. R. China. E-mail: zhaoyong@henu.edu.cn

^b State Key Laboratory of Rare Earth Resource Utilization Changchun Institute of Applied Chemistry, Chinese Academy of Sciences, Changchun, Jiling, 130022, P. R. China. E-mail: xbzhang@ciac.jl.cn



Peng Zhang

Peng Zhang received his PhD from Lanzhou Institute of Chemical Physics, Chinese Academy of Sciences, in 2016. He currently works at the Key Lab for Special Functional Materials of the Ministry of Education, Henan University. His research interests focus on the preparation of functional catalysts and on uncovering the discharging/charging mechanism for lithium oxygen batteries.



Yong Zhao

Yong Zhao received his PhD from Institute of Chemistry, Chinese Academy of Sciences, in 2008 under the supervision of Prof. Lei Jiang. After a period working as a postdoctoral fellow with Prof. Kazuhito Hashimoto at the University of Tokyo (2008–2015), he became a full professor at Henan University in 2016. His research interests focus on the mechanism of electrocatalytic reactions and catalyst innovation in fuel cells and Li–O₂ batteries.

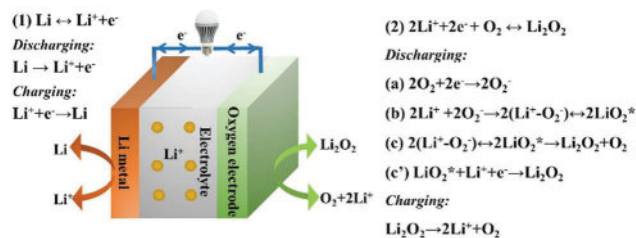


Fig. 1 Schematic illustration of a Li– O_2 battery and the corresponding reactions at the Li-metal (left side) and oxygen electrodes (right side).

the most studied one due to its high energy capacity, good rechargeability and relatively simple construction.^{13–16}

Coupling lithium-metal at the anode and oxygen at the cathode, together with using an organic electrolyte in aprotic Li– O_2 battery, with Li_2O_2 as the discharge product, can provide a theoretical capacity of 3861 mA h g^{-1} (capacity based on the Li-anode).¹³ This is much higher than that of today's Li-ion batteries, which have a maximum capacity of 200–300 mA h g^{-1} (capacity based on the anodic material). In terms of the theoretical energy density, this could be as high as 3458 W h kg^{-1} (energy density based on Li-metal and oxygen), with the level even approaching that of the present gasoline system (energy density, 12–17 MJ kg^{-1} ; thermal efficiency, ~30–40%).² However, the present energy density and stability of Li– O_2 batteries are far away from these theoretical values.^{2,11} The disparity between reality and idealization mainly arises from the sluggish and unsustainable reactions at the electrodes of the battery,^{17–19} which cause a low capacity and rate capability, a poor round-trip efficiency and an unsatisfactory stability of practical devices.²⁰

The total reactions of an aprotic Li– O_2 battery with Li_2O_2 as the products can be described by the equation: $2\text{Li} + \text{O}_2 \leftrightarrow \text{Li}_2\text{O}_2$ ($E_{\text{ocv}} = 2.96$ V),⁹ while the separate discharge/charge reactions at the anode and cathode can be described with the equations: (i) at the lithium electrode, $\text{Li} \leftrightarrow \text{Li}^+ + \text{e}^-$ ($E_a = -3.05$ V vs. standard hydrogen electrode (SHE), Li oxidation and reduction);



Xinbo Zhang

materials for batteries, fuel cells, electrochemical water splitting and carbon dioxide reduction.

Xinbo Zhang obtained his PhD from Changchun Institute of Applied Chemistry (CIAC), Chinese Academy of Sciences (CAS), in 2005. After periods working as a Japan Society for the Promotion of Science (JSPS) postdoctoral fellow (2005–2007) and as a research associate at the National Institute of Advanced Industrial Science and Technology (2007–2009), he became a full professor at CIAC. His research interests mainly focus on functional inorganic

Since the pioneering work of aprotic Li– O_2 batteries by Littauer and Tsai, great efforts have been devoted to solve the existing problems of Li– O_2 batteries.^{4,16,22–35} Previous advances have already identified that the rate and stability of the electrode reactions could be promoted through the rational design of materials and structure for the electrode, electrolyte and additives as well as by a detailed understanding of the electrode reaction mechanism.^{8,36–43} The scope of this review is the recent progress made in illustrating the discharge/charge mechanism of Li– O_2 batteries and the construction of efficient materials and structures for stable and fast electrode reactions by strengthening their functionality for Li– O_2 batteries.^{44–55} Consequently, the directions and perspective will be concentrated on the further optimized design and combination of materials and structures. This should be beneficial for the rapid progress of this next-generation energy storage/conversion system. According to these frameworks, this comprehensive paper overviews the following topics:

(1) The present understanding of the discharge/charge reactions mechanism at the Li-electrode and O_2 -electrode as well as the challenges and resolved strategies for achieving a high-performance and long-term stability of Li– O_2 batteries (Fig. 2).

(2) The recent advances made with lithium electrodes for preventing dendrite formation and side reactions by using a solid–electrolyte-interface film, inorganic/polymer membrane or substitution of the Li-metal by a lithiated composite to increase the Coulombic efficiency and sustainability of the Li-metal (Fig. 2).

(3) The recent advances made with oxygen electrodes by constructing efficient catalysts, utilizing a porous structure or electrode surface engineering to accelerate Li_2O_2 formation and decomposition, promote mass transport and increased Li_2O_2 storage space, and to induce the growth of large quantity and conductive Li_2O_2 (Fig. 2).

(4) The recent advances in screening liquid, quasi-solid and solid-state electrolytes with high Li^+ conductivity, stability and

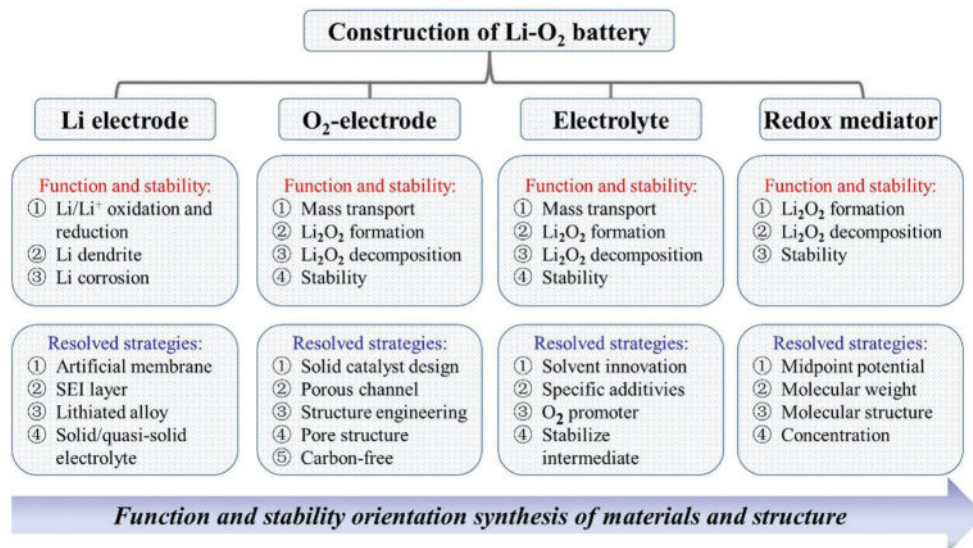


Fig. 2 The function and stability orientation synthesis of materials and structures for the: (a) lithium electrode; (b) oxygen electrode; (c) electrolyte; (d) redox mediator in aprotic Li–O₂ batteries.

good performance, as well as in modulation of the reaction intermediates by solvents and functional additives to increase the mass transport efficiency and electrolyte stability, achieve a fast rate of Li₂O₂ formation and decomposition and to promote the growth of abundant Li₂O₂ (Fig. 2).

(5) The recent advances made in screening soluble redox mediators for accelerating Li₂O₂ formation and decomposition reactions, and for decreasing the side reactions, as well as promoting the growth of a large quantity of Li₂O₂ (Fig. 2).

All these aspects intend to promote the fast and reversible charge/discharge of Li–O₂ cells based on an understanding of the fundamental cell chemistry and functional materials/structure synthesis. In the following, we summarize the current understanding of the mechanism occurring during charge/discharge processes, as well as the critical challenges and the corresponding resolved strategies.

2. Mechanism, challenges, and resolved strategies

In a typical operation of aprotic Li–O₂ batteries, the Li-metal anode is oxidized to Li⁺ and releases electrons during the discharge process, whereby consequently, O₂ accepts the electrons and is reduced to Li₂O₂ with incorporating Li⁺ at the cathode surfaces. In the following charging process, the formed Li₂O₂ is decomposed to O₂ and Li⁺ at the cathode, and Li⁺ in the electrolyte is reduced to metallic Li at the anode. Compared to the single-electron reaction on the anode (Li⁺ + e[−] ↔ Li), the elemental steps for the two-electron-transfer reaction process at the cathode (2Li⁺ + O₂ + 2e[−] ↔ Li₂O₂) are more complicated. The cathodic discharge/charge mechanisms are still controversial, and in this section, we will mainly focus on the proposed mechanisms for Li₂O₂ formation and decomposition, and the challenges for the fast and sustainable

reactions of Li₂O₂ formation and decomposition, as well as their resolved strategies to solve the challenges.

2.1 Mechanism, challenges and resolved strategies at the Li-anode

At the anode, Li-metal is oxidized to Li⁺ and electrons in the discharge process, and *vice versa*, the Li⁺ ion is reduced by a one-electron-transfer pathway in the charge process (Li ↔ Li⁺ + e[−]). Compared to Li-metal oxidation in the discharge process, the reduction of Li⁺ ion to Li is more complicated in the charge process. The easy and undesirable formation of Li dendrite in the charge process is one of the biggest challenges to overcome, and results in safety issues with Li-electrodes (Fig. 2).^{56,57} This is due to the possibility that the Li dendrites could penetrate the separator in the battery, resulting in a short-circuit and safety problems for the battery. This has also been a persistent problem for various kinds of lithium-metal-based batteries over the past 40 years.^{58–60} Moreover, lithium-metal is a highly reactive chemical and can easily react with some organic solvents, electrolyte additives, and the crossover O₂, CO₂, N₂ molecules, and so on.^{61,62} It also induces a low Coulombic efficiency and energy density loss in the battery. More detailed information about Li dendrite formation and the parasitic reactions at the Li-anode will be discussed in the Li-anode section.

One of the attempts to solve the above-mentioned issues involves the construction of a stable solid–electrolyte-interface (SEI) layer on the Li-metal, composed of inorganic lithium components, such as Li₂CO₃, Li₂O and LiF.³⁸ However, dendrite formation and the side reactions on Li-metal cannot be completely prevented. For instance, Li₂O is reactive to some electrolytes (such as DMSO).⁶³ Another strategy to solve these issues is to use a Li⁺-conductive polymer/inorganic membrane between the anode and cathode;⁵⁶ for example, a NASICON-type Li_{1-x}Al_x(TiGe)_{2-x}Si_yP_{3-y}O₁₂ ceramic membrane. This can preclude the negative effect of lithium

dendrites and terminate some of the side reactions. However, some of the metal cations in the membrane, for example Ti^{4+} and Ge^{4+} , can be reduced by lithium-metal, with the ceramic membrane suffering damage through these facile reactions.⁶⁴ The third strategy for Li-anode optimization is substitution of the Li-metal with a lithiated composite or alloy.⁶⁵ These composite materials do not lead to dendrite formation to a large extent. One of the limitations for lithiated-composite-based batteries may be their low energy density in comparison to that of lithium-metal. Furthermore, the lithiated electrode suffers from a risk of collapse due to the volumetric changes during cell cycling.⁶⁵ One of recent reviews regarding the side reactions at the Li-anode in Li-metal-based batteries described this in detail.⁶⁶ In the following Li-anode section, we briefly discuss the recent progress made for the protection and substitution of lithium anodes, typically in Li–O₂ batteries, which are mainly based on utility promotion and the use of substituted candidates of the highly reactive lithium-metal for achieving sustainable reactions at the Li-electrode.

2.2 Mechanism, challenges, and resolved strategies for reactions at the O₂-electrode

At the O₂ electrode, the discharge/charge reactions of an aprotic Li–O₂ battery with Li₂O₂ as the product can be described as $2\text{Li}^+ + 2\text{e}^- + \text{O}_2 \leftrightarrow \text{Li}_2\text{O}_2$. O₂ is reduced to O₂[−] in the primary state, followed by combination with Li⁺ and electrons to form the LiO₂ intermediate and Li₂O₂ products in the discharge process. *Vice versa*, Li₂O₂ is oxidized to Li⁺ and O₂. Compared to the reactions at the Li-electrode, the oxygen reduction reaction (ORR) and oxygen evolution reaction (OER) with two-electron-transfer pathways at the O₂ electrode are more complicated.^{51,64,67–73} This is due to the fact that ORR and OER are evolved at the triple-phase contact interface between the electrolyte (liquid phase), the oxygen electrode (solid phase), and an oxygen molecule (gas phase). The efficiency of electron transfer and mass transport need to be high enough to achieve the fast ORR and OER rates, but the present ORR and OER processes are still sluggish due to several remaining challenges (Fig. 2). First, the mass transport of Li⁺ ions and O₂ gas through the electrolyte and cathode pore is a key factor influencing the rates of the discharge/charge reactions, especially at the region of sufficient overpotentials.⁷⁴ Second, aprotic ORR and OER are step-by-step reactions, and some intermediates can evolve, such as O₂[−], solvated Li⁺–O₂[−] and adsorbed LiO₂* species.⁵ The complicated reaction pathway and intermediates are difficult to modulate, resulting in the slow electrochemical kinetics of overall ORR and OER.⁵ Third, the slow reaction kinetics of ORR for Li₂O₂ formation and OER for Li₂O₂ decomposition induces a deviation in the discharge/charge profiles of Li–O₂ batteries, leading to a low round-trip efficiency.^{21,75} Fourth, the solid by-products (such as Li₂CO₃, LiOH and alkyl Li-salts) produced from the corrosion of the electrode and electrolyte materials are difficult to decompose in the charging process.⁷⁶ The generation of these by-products is one of the reasons for cathode passivation and pore clog blocking of the oxygen electrode, limiting the cell discharge capacity and

compromising rechargeability.⁷⁷ The above-mentioned issues are proposed could be partially solved by rational design of the solid catalysts, which can accelerate the rates of OER and ORR and inhibit the generation of by-products.⁷⁸ Furthermore, the construction of a suitable pore structure of the oxygen electrode is one of the most effective protocols to enhance the rate and stability of Li₂O₂ formation/decomposition reactions, based on the increased mass transport efficiency.⁷⁹

Another critical point to note is that the electrochemically deposited Li₂O₂ product is an insulator with a calculated band gap of 4–5 eV (electrical conductivity, 10^{-12} – 10^{-13} S cm^{−1}), which also has a low solubility in most organic solvents at room temperature.¹³ The insufficient electron transfer and ionic transport properties of solid Li₂O₂ are key bottlenecks for achieving high ORR and OER rates. The tuneable formation of Li₂O₂ crystal with enhanced conductivity by surface engineering and element doping may have an impact on the performance of Li–O₂ batteries.⁸⁰ Except for their low conductivity, the quantity of discharge Li₂O₂ products has a direct correlation with the cell capacity, while the morphology of formed Li₂O₂ is one of the most important factors to control the quantity of Li₂O₂ on the cathode.¹⁶ The designed cathodes with a large surface area and pore volumes for the storage of large Li₂O₂ clusters make a positive contribution to the high capacity of Li–O₂ batteries.⁸¹ In this section, we focus on the discharge/charge reaction mechanism, followed by the proposed functionality of the cathode catalyst/structure for enhanced reaction characteristics,⁸² such as Li₂O₂ formation in a large quantity,⁸³ tuneable Li₂O₂ conductivity⁸⁰ and improved mass transport efficiency.⁸⁴ Additionally, the degradation mechanism of cathode materials and electrolyte component attack initiated by the cathode are illustrated, and discussed with regard to delaying the sudden death of a cell.

2.2.1 Mechanism for the discharge reaction. As discussed previously, the cathodic discharge reaction is complicated due to its elemental steps with a two-electron-transfer-reaction process ($2\text{Li}^+ + \text{O}_2 + 2\text{e}^- \leftrightarrow \text{Li}_2\text{O}_2$). The elemental steps involve several intermediate species and final insulating products, so confirming these species with *in situ* and *ex situ* techniques should be highly important to illustrate the discharge mechanism. Establishing the mechanism will be beneficial for the design and synthesis of functional materials for high-performance Li–O₂ batteries.

2.2.1.1 Initial elemental reaction in Li₂O₂ formation. The first step in the discharge process is generally recognized as O₂ adsorption on the active sites of the electrode, followed by the initial elemental reaction step for O₂ reduction. Many researchers have made great efforts to identify the first discharge intermediate product in the aprotic Li–O₂ system. The ORR was primarily investigated in an aprotic medium by Abraham *et al.*, with tetrabutylammonium (TBA⁺) used as a soft acid to combine with the soft base O₂[−] through forming stable TBA⁺–O₂[−] based on Pearson's hard–soft acid–base (HSAB) theory.⁸⁵ As shown in Fig. 3a, after feeding oxygen, anodic ($E_{\text{pa}} = 2.40$ V) and cathodic ($E_{\text{pc}} = 2.34$ V) peaks appear and the charge area ratio ($Q_{\text{a}}/Q_{\text{c}}$) under the peaks is close to unity, indicating an reversible ORR

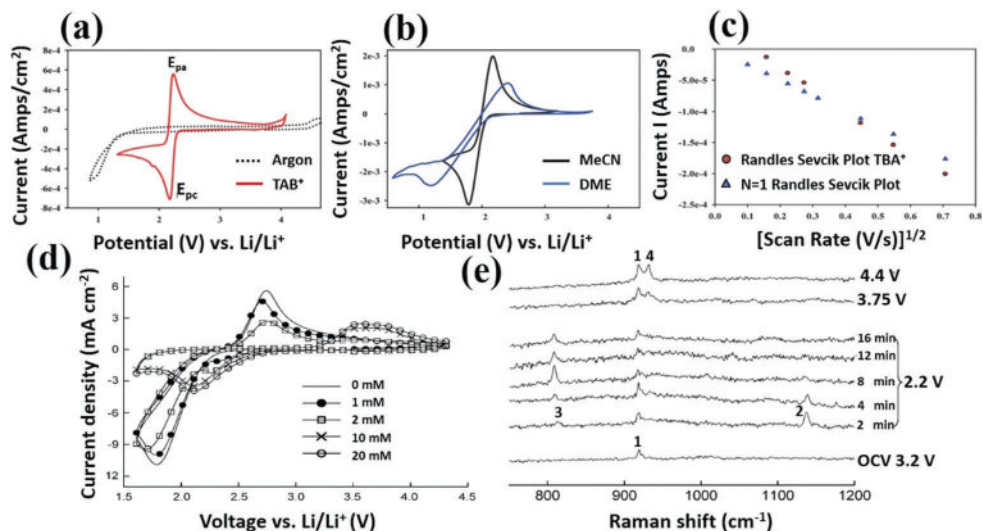


Fig. 3 (a) Cyclic voltammograms (CVs) for the ORR in 0.1 M TBAPF₆ (red, iR corrected) and Ar background (dotted) in DMSO; (b) CVs (iR uncorrected) for ORR in 0.1 M TBAPF₆/CH₃CN (black) and TBAPF₆/DME (blue); (c) Randles–Sevcik plot of peak current vs. square root of the scan rate in 0.1 M TBAPF₆/DMSO;⁸⁶ (d) CVs in O₂-saturated 0.1 M *n*-Bu₄NClO₄/CH₃CN with different LiClO₄ concentrations; (e) *in situ* SERS during O₂ reduction and re-oxidation on Au in O₂-saturated 0.1 M LiClO₄/CH₃CN (spectra collected at a series of times and at the reducing potential of 2.2 V vs. Li/Li⁺, followed by other spectra at the oxidation potentials; the peaks were assigned as follows: (1) C–C stretch of CH₃CN at 918 cm⁻¹, (2) O–O stretch of Li₂O₂ at 1137 cm⁻¹, (3) O–O stretch of Li₂O₂ at 808 cm⁻¹ and (4) Cl–O stretch of ClO₄⁻ at 931 cm⁻¹).⁸⁷ Reprinted with permission from ref. 86 and 87. Copyright 2010 and 2011 American Chemical Society and Wiley-VCH Verlag GmbH & Co. KGaA.

in this system (0.1 M TBAPF₆ in DMSO).⁸⁶ Simultaneously, similar behaviours were also observed in the electrolytes of TBAPF₆/CH₃CN and TBAPF₆/1,2-dimethoxyethane (DME) (Fig. 3b), suggesting the close mechanism of O₂ reduction in organic solutions. To confirm the exact electron transfer number during the ORR, the authors portrayed the data in a Randles–Sevcik curve for the reaction process (Fig. 3c) based on the equation: $I_{pa} = (2.69 \times 10^5) \times n^{3/2} \times A \times D^{1/2} \times V^{1/2} \times C$, in which O₂ concentration C , electrode area A , the number of transferred electrons n and the diffusion coefficient D were constant parameters. The obtained n was in close agreement with the $n = 1$ in a theoretical plot, indicating that the ORR was a one-electron-reduction process.

The aprotic ORR process was further studied in a Li⁺-containing medium to illustrate the effect of Li⁺ on the ORR process, which was demonstrated by Abraham *et al.*⁸⁵ and Peng *et al.*⁸⁷ As shown in Fig. 3d, when the LiClO₄ concentration was increased in *n*-Bu₄NClO₄-CH₃CN solution (organic ammonium ions can also form ion pairs with O₂⁻, like TBA⁺), a new reduction peak appeared at the higher potentials (~2.3 V) in comparison with the original O₂ reduction peak.⁸⁷ The magnitude of the new peak was strengthened with the increased Li⁺ concentration, which was due to a chemical step following the electrochemical reduction. This chemical reaction could severely deplete the O₂⁻ concentration and shift the reduction potential in a positive direction. When the Li⁺ concentration exceeded that of O₂, all the O₂⁻ was consumed by reacting with Li⁺. As a result, the reduction peak at low potential disappeared, and only one reduction peak at high potential then remained. This indicated that O₂⁻ was unstable in the Li⁺-containing electrolyte, as it combined with Li⁺ to form a more stable LiO₂ complex.

The above-mentioned points indicated that the initial ORR step is O₂ adsorption, and a subsequent O₂ reduction occurred on the electrode. For example, with carbon material possessing intrinsic defects,^{94,95} noble metals^{85,96–98} and many metal oxides catalysts,^{99–102} O₂ was preferentially adsorbed on the electrode surface due to the thermodynamics being favourable. In contrast, the first discharge step was also supposed to be initial Li⁺ adsorption on some of specific catalyst electrodes. For example, heteroatom-doped carbon materials showed a preferable Li⁺-adsorption property. Five possible N configurations, namely graphitic N (graphN1), double graphitic N (graphN2), tri-N pyridinic (pyriN3), pyrrolic-like N (pyrroN3) and in-plane tetra-N pyridinic (pyriN4), were presented on a graphene surface in N-doped carbon in one study.⁸⁸ Density functional theory (DFT) calculations indicated that the O₂ adsorption step was endothermic, while the two Li-containing steps had downhill profiles in the free energy profiles. This indicated spontaneous Li⁺ adsorption in the open circuit condition (Fig. 4a). In the equilibrium condition (Fig. 4b), all the intermediary steps of the initial nucleation of Li₂O₂ became endothermic for the graphN1, graphN2 and pyrroN3 sites. In contrast, step 1 was downhill while steps 2 and 3 were uphill for pyriN3 and pyriN4. The results indicated that the nucleated process favoured the reaction paths of 'Li⁺ → Li → LiO₂ → Li₂O₂ → Li₃O₂ → Li₃O₄ → Li₄O₄' on the active sites, which was due to the strong electron-withdrawing capability of pyridinic-N, especially pyriN4. This surface-nucleated mode prohibited the formation of dissolved LiO₂, and probably resulted in Li₂O₂ formation through a surface-growth path with the feature of small Li₂O₂ clusters or Li₂O₂ film. As shown in Fig. 4c–f, Li₂O₂ film was confirmed to have been deposited on the surface of nitrogen-doped

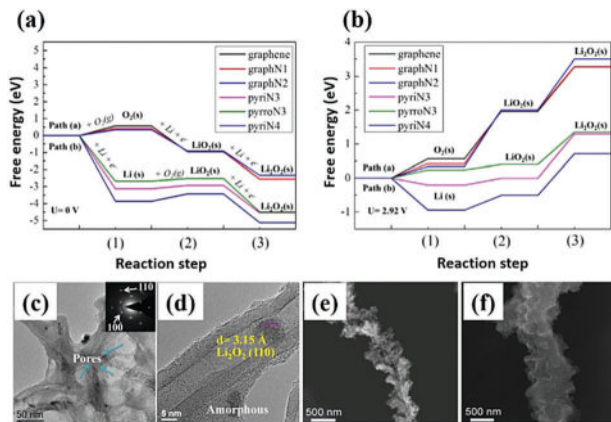


Fig. 4 Calculated energetic profiles of the initial nucleation of Li_2O_2 on the surface of pristine and different N-doped graphenes at (a) $U = 0$ V and (b) $U = 2.92$ V;⁸⁸ (c) TEM and (d) HR-TEM images of an N-doped graphene/carbon nanotube composite cathode after the 10th discharge (inset in (c): corresponding SAED of the NGC cathode after the 10th discharge ($1000 \text{ mA h g}_C^{-1}$); white circles were simulated Li_2O_2 [001] axis patterns, which were superimposed over the experimental diffraction pattern);⁸⁹ SEM images of (e) the pristine vertically aligned N-doped coral-like carbon nanofibre and (f) the discharged fibre ($4000 \text{ mA h g}_C^{-1}$).⁹⁰ Reprinted with permission from ref. 88–90. Copyright 2014 and 2015 Wiley-VCH Verlag GmbH & Co. KGaA and American Chemical Society.

graphene/carbon nanotube composite after discharge to $1000 \text{ mA h g}_C^{-1}$.⁸⁹ Similarly, even after discharge to $4000 \text{ mA h g}_C^{-1}$, small Li_2O_2 particles and Li_2O_2 film were still found to be produced on nitrogen-doped coral-like carbon nanofibres.⁹⁰ It should be noted that Li_2O_2 with a small size is not an inevitable result at the N-doped cathode, as it was also affected by the density of pyridinic-N.

In addition to N-doped carbon, the $\alpha\text{-MnO}_2$ material was also found to prefer Li^+ adsorption instead of O_2 adsorption. As seen in Fig. 5a, during the discharge process, the a/b (tetragonal unit cell, lattice parameter $a = b$) lattice parameter of $\alpha\text{-MnO}_2$ is increased significantly from 9.8280 to 10.4340 \AA with a minimal change to c (2.85), corresponding to about 12.5% expansion of the volume.⁹¹ After cell recharge, the lattice parameter was decreased to 10.0233 \AA , indicating the insertion and extraction of Li^+ or LiO_x during the discharge and charge process. In Fig. 5b, it can be seen that the tendency of the O_2 content was identical with that of Li^+ , while the quantity of decreased or increased atom ratio of Li^+ was two times larger than for O_2 . This indicated the insertion/extraction of Li^+ and Li_2O into $\alpha\text{-MnO}_2$ during the cycle of a Li-O_2 cell. Trahey *et al.* reported the insertion voltage (*vs.* Li^+/Li) for Li^+ and Li_xO_y through DFT calculations (Fig. 5c). During discharge, Li^+ was first inserted in to $2 \times 2 \text{ MnO}_6$ tunnels to obtain an oxygen and subsequently another Li^+ and oxygen.⁹² Furthermore, Jiao *et al.* compared the oxidation state of Mn in pure $\alpha\text{-MnO}_2$ and K^+ -containing $\alpha\text{-MnO}_2$ *via* environmental *in situ* X-ray absorption spectroscopy.¹⁰³ They found that K^+ could suppress the change of Mn oxidation state to Mn^{3+} during discharge, restricting the insertion of Li^+ and Li_2O to some extent. However, during *in situ* XRD tests, Chan *et al.* also did not collect crystalline Li_2O_2

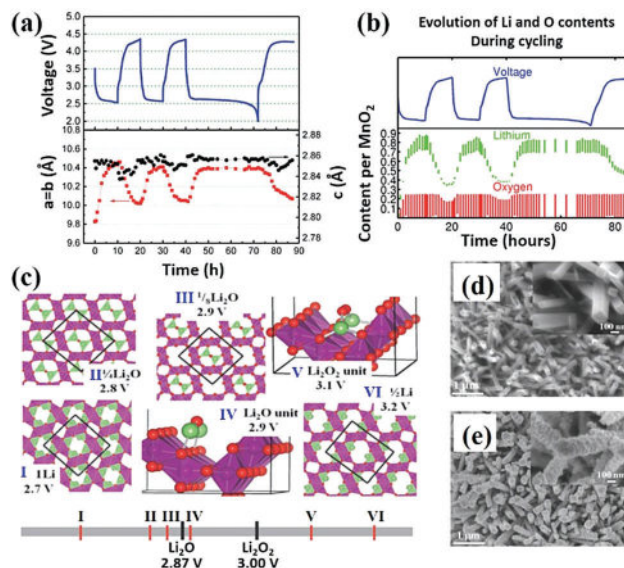


Fig. 5 (a) Three cycles of a $\text{Li}/\alpha\text{-MnO}_2\text{-O}_2$ cell (top) during which the lattice parameters of the $\alpha\text{-MnO}_2$ electrode/electrocatalyst were determined by *in situ* synchrotron XRD (bottom); (b) changes in Li (green) and O (red) contents during cycling as deduced from the XRD tests and DFT-based model;⁹¹ (c) atomic configurations and calculated equilibrium potentials *vs.* Li/Li^+ at a standard $p\text{O}_2$ for various Li-O_2 reaction products with $\alpha\text{-MnO}_2$ (the largest (green) sphere was Li, the smallest (red) sphere was O, and Mn was shown inside (purple) the octahedral; the formation of various Li-O_2 species (I–V), including Li_2O -doped $\alpha\text{-MnO}_2$ (I–III) occurring at potentials bracketed by those of the two stages of Li^+ -insertion (I and VI), and in close proximity to the potentials for Li_2O_2 and Li_2O formation);⁹² (d) SEM image of $\alpha\text{-MnO}_2$ nanorod arrays grown on a carbon paper electrode and (e) discharged to 2 V at 104 mA g^{-1} .⁹³ Reprinted with permission from ref. 91–93. Copyright 2013, 2015 and 2017 Wiley-VCH Verlag GmbH & Co. KGaA and Royal Society of Chemistry.

peaks through the XRD patterns after discharge to 2.0 V , indicating the formation of amorphous Li_2O_2 .⁹¹ Recently, the discharge product on pure $\alpha\text{-MnO}_2$ arrays was investigated. As shown in Fig. 5d and e, even at a low current density of 104 mA g^{-1} , there were only tiny Li_2O_2 particles and Li_2O_2 film formed after discharge to 2 V , just as with the morphology on N-doped carbon materials.

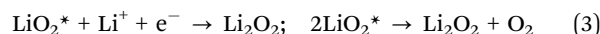
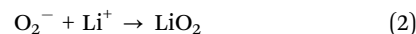
The nucleation process on Li^+ preferential materials is probably faster than that for O_2 preferential ones due to all the steps proceeding on the electrode surface without any solution process. For example, $\alpha\text{-MnO}_2$ -based materials exhibited better ORR activity than the other types of Mn_xO_y (Mn_2O_3 , Mn_3O_4 , $\beta\text{-MnO}_2$, $\gamma\text{-MnO}_2$ and $\lambda\text{-MnO}_2$).¹⁰⁴ Similarly, many N-doped carbon materials have shown good battery performance.^{80,89,105–108} It seems that the Li^+ preferential materials are superior electrode materials for aprotic Li-O_2 cells, although this viewpoint is still controversial. The detailed discussion of specific metal oxides with Li^+ -adsorption capability is presented in the O_2 -electrode section.

2.2.1.2 Second and third elemental reactions in Li_2O_2 formation. After the adsorbed O_2 molecule was reduced to O_2^- , the subsequent elemental reaction proceeds to generate the following species. In Peng's reports, the signals of LiO_2 and O_2^- species

were both detected on a Au electrode surface with an *in situ* SERS technique.⁹⁶ As shown in Fig. 3e, they directly identified the formation of LiO₂ on the electrode surface at a discharge potential of 2.2 V (peak marked '2') *via in situ* SERS.⁸⁷ With the passage of time, the LiO₂ peak diminished after 8 minutes, whereas the Li₂O₂ peak increased from 2 min to 8 min. The unchanged spectrum from 8 min to 16 min indicated that no further electrochemical reaction occurred. Otherwise, the LiO₂ peak would still exist due to a one-electron ORR. *In situ* SERS provided the direct spectroscopic evidence that LiO₂ was an intermediate on the electrode surface during the ORR in an aprotic Li–O₂ battery, where it disproportionated to the stable Li₂O₂ (2LiO₂ → Li₂O₂ + O₂).

The O₂[−]/LiO₂ species probably existed not only in its adsorbed state (O₂^{−*}, LiO₂^{*}, where '*' represents adsorbed species) but also in its dissolved state (O_{2dis}, LiO_{2dis}, where 'dis' represents dissolved species), as suggested by Shao-Horn *et al.*⁹⁷ To get direct evidence for the existence of intermediates in the electrolyte, Herranz *et al.* used rotating ring disc electrode (RRDE) voltammetry to compare the disc current (current for O₂[−] formation) and ring current (current for O₂[−] oxidation) in the O₂-saturated solution of tetrabutylammonium bis(trifluoromethylsulfonyl)imide (TBATFSI) in 1-butyl-1-methylpyrrolidinium bis(trifluoromethylsulfonyl)imide (Pyr₁₄TFSI) and propylene carbonate (PC) solvents.¹⁰⁹ As presented in Fig. 6a, the potential at the ring electrode was set at 2.85 V vs. Li/Li⁺ to the oxide O₂[−]. The increased current density at the Pt-ring electrode confirmed the existence of the O₂[−] intermediate in the electrolyte. The diffusion efficiency of O₂[−] in the ionic liquid was lower than that in PC, resulting in the uncompleted diffusion of O₂[−] from the disc, particularly at the lower rotation speed. This further led to the shift in oxidation peak in the disc voltammograms as well as the delayed ring current. Furthermore, Zhang *et al.* introduced

5,5-dimethyl-pyrroline *N*-oxide (DMPO) as a probe to capture the formed O₂[−] and to generate new, stable electron paramagnetic resonance (EPR) signals.¹¹⁰ As presented in Fig. 6c, six pairs of strong and clear EPR signals could be detected after the discharge time of 90 min. The peak shapes and positions were identical to the standard EPR signal from KO₂ (Fig. 6b). The signals at the initial discharge stage were attributed to the species from O₂[−] reacting with moisture in the electrolyte and with the binder on the electrode. Additionally, Ye *et al.* also directly observed soluble LiO₂ (LiO_{2sol}) in the Li⁺-containing DMSO electrolyte and the formation of Li₂O₂ on a Au electrode surface in a Au/Li/Li system (metallic Li as the reference and counter electrodes) by using *in situ* UV-vis absorption spectroscopy and *in situ* SERS.¹¹¹ Based on these findings, the elemental discharge mechanism was proposed as follows:



2.2.2 Challenge and resolved strategies for Li₂O₂ formation

2.2.2.1 Modulation of mass transport. As mentioned previously, the discharge reaction at the O₂-electrode evolves at the triple-phase contact interface between the electrolyte (liquid phase), the oxygen electrode (solid phase) and the oxygen molecule (gas phase). The rate of mass transport needs to be high enough to achieve the fast ORR rates, especially at the region of high current density.⁷⁵ In general, the mass transport could be divided into two parts: diffusion in the electrolyte and diffusion in the pores of the electrode. The mass transport ability for Li⁺ ions and O₂ in the electrolytes is partly controlled by their phase states, and those are the liquid-state, quasi-solid-state and solid-state media. Many properties, such as the polarity, viscosity, volatility and ionic conductivity of the solvents should be well evaluated to meet the demand for fast Li⁺ ion and O₂ transport rates.^{74,112,113} Except for modulation of the electrolyte composition, the mass transport ability for Li⁺ ions and O₂ is correlated with the pore structure of the O₂-electrode, since Li₂O₂ was finally deposited on the surface and in the pores of the cathode. The mass transport properties of Li–O₂ batteries are discussed in the following O₂-electrode and electrolyte sections in detail.

2.2.2.2 Modulation of LiO₂^{*} formation. As LiO₂^{*} at the O₂-electrode and LiO_{2dis} in the electrolyte play dominant roles in the discharge process of Li–O₂ batteries, their relationship was investigated by Bruce's group.¹¹⁴ They pointed out that a LiO₂ adsorption-desorption equilibrium existed at the electrode/electrolyte, which was denoted by LiO₂^{*} ↔ Li_{dis}⁺ + O_{2dis}[−] + LiO_{2dis}. In this work, they proved that high donor number (DN, Lewis basicity) solvents could promote the strong solvation of Li⁺ and result in the shift to the right direction of this equilibrium. Thus, Li₂O₂ was mainly produced *via* the disproportionation of dissolved LiO_{2dis} in the electrolyte, significantly delaying the passivation of the electrode surface and yielding large Li₂O₂ aggregation.

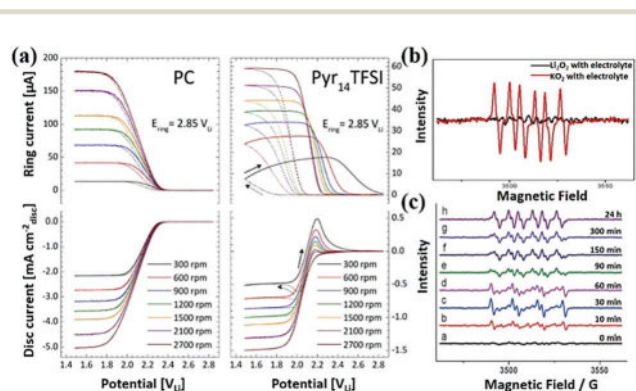


Fig. 6 (a) Capacitively, non-ohmically corrected disc and ring currents recorded at 50 mV s^{−1} in O₂-saturated 0.2 M TBATFSI in PC (left) or O₂-saturated Pyr₁₄TFSI (right), at rotation rates of between 300 and 2700 rpm and continuously holding the Au ring at 2.85 V_{Li} (dotted and solid lines correspond to the currents recorded in negative-going and positive-going scans, respectively, as indicated by the arrows on the right-hand panel);¹⁰⁹ (b) EPR spectra of KO₂ and Li₂O₂ in DMSO; (c) EPR spectra of the discharged electrolytes at the air-permeable side, measured at different discharge times.¹¹⁰ Reprinted with permission from ref. 109 and 110. Copyright 2012 and 2014 American Chemical Society and Wiley-VCH Verlag GmbH & Co. KGaA.

As a result, the large Li_2O_2 aggregation *via* a solution-growth pathway presented a high battery capacity. Oppositely, the low DN solvent induced the equilibrium to the left direction, resulting in the generation of adsorbed LiO_2^* to produce the film-like Li_2O_2 . This discharge route is known as the surface-growth pathway and it usually exhibits a low cell capacity. Except for the high DN electrolyte (including the solvent and Li salt⁵), additives with a high acceptor number (AN, Lewis acidity) could also stabilize the O_2^- in the electrolyte. The above-mentioned equilibrium was also shifted to the right side in this case.^{16,115–121} The discussion about the solvent, Li-salt and additives in the electrolyte on the cell discharge characteristics is presented in the following electrolyte section.

Except for the effect of the solvents and general additives, soluble redox mediators (SRMs) are another type of special electrolyte additives for facilitating enhanced reaction kinetics of Li_2O_2 formation. In this case, the electrochemical reduction of O_2 or Li^+ in the first step can be partly transformed by chemical reduction with SRMs (redox potential $< 2.96 \text{ V vs. Li}^+/\text{Li}$). The reduced form of SRMs could reduce O_2 chemically in bulk electrolyte, which shifted the discharge process from the solid-growth to solution-growth pathway, which delayed the passivation of the cathode and improved the battery capacity. Compared to the limited contact interface between Li_2O_2 and cathode catalysts, SRMs with tuneable midpoint potentials can act as “liquid catalysts” everywhere in the electrolyte, and so the electron transfer between SRMs and cathode/ O_2 becomes flexible.¹²² Moreover, some specific SRMs could reduce O_2 and consequently bind the formed superoxide, greatly enhancing the cyclic stability of Li- O_2 batteries.⁷⁵ The detailed discussion of this is presented in the following SRM section in detail.

In addition to the role of the electrolyte, the discharge current densities (current rates) are also one of the most critical factors to influence the $\text{LiO}_2^* \leftrightarrow \text{LiO}_{2\text{dis}}$ equilibrium.^{123–126} At a high current rate, the high density of electrons transferred from the electrode surface can prompt the depletion of LiO_2^* through secondary electrochemical reduction or surface disproportionation (eqn (3)). In this case, only a small quantity of $\text{LiO}_{2\text{dis}}$ could be formed in solution through the solution-growth pathway. Here, the Li_2O_2 usually presents a film-like morphology with a low cell capacity at the high current density. Oppositely, at a low current density, the one-electron ORR dominates at the electrode surface, providing the chance for O_2 and LiO_2 to exist in the electrolyte. This resulted in the generation of Li_2O_2 through a solution-growth pathway, exhibiting a typical toroid morphology and high discharge capacity of batteries. The current density passage on the electrode surface can be modulated by the electrode structure (specific surface area and pore structure), and this is shown in the following O_2 -electrode section.

2.2.3 Mechanism for the charge reaction at the O_2 -electrode.

The charging process of Li- O_2 batteries usually presents a high overpotential even larger than 1 V. The properties of the discharge product Li_2O_2 , for example, the purity and surface defects of Li_2O_2 , strongly influence the origin of the overpotential.^{127–129} Rational design of the reaction interface, such as the $\text{Li}_2\text{O}_2/\text{cathode}$ and $\text{Li}_2\text{O}_2/\text{electrolyte}$, is highly important to accelerate

the charge reactions, resulting in the high energy efficiency of Li- O_2 batteries.¹²⁸ Moreover, the superoxide is supposed to be an intermediate product during discharge, and the modulation of the superoxide might have an impact on the charge characteristics.

2.2.3.1 Li_2O_2 decomposition with a one-electron-transfer path.

In the OER process, superoxide (LiO_2) is supposed to be a reaction intermediate when Li_2O_2 is decomposed to Li^+ and O_2 . Wang *et al.* used environmental transmission electron microscopy to show the formation of LiO_2 or not during the charging step.⁴³ As shown in Fig. 7, when the cell was charged after 48 s, two diffraction spots assigned to LiO_2 were found to represent an intermediate phase during Li_2O_2 decomposition. This indicated the possible decomposition of Li_2O_2 through a one-electron route ($\text{Li}_2\text{O}_2 \rightarrow \text{Li}^+ + \text{LiO}_2 + \text{e}^-$, $2\text{LiO}_2 \rightarrow \text{Li}_2\text{O}_2 + \text{O}_2$).

In the real operation of Li- O_2 batteries, some experimental evidence also supports the possible single-electron Li_2O_2 decomposition with LiO_2 as an intermediate. Wang *et al.* found that when the content of *N*-butyl-*N*-methylpyrrolidinium bis(trifluoromethylsulfonyl)imide (PYR₁₄TFSI) in DME electrolyte was improved, the cell charge overpotential was remarkably decreased (Fig. 8a–d).¹³¹ After five cycles of cells with 100% PYR₁₄TFSI, the average charge overpotential was as low as $\sim 0.2 \text{ V}$. This was attributed to the transformation of two-electron Li_2O_2 oxidation to a one-electron pathway with the addition of PYR₁₄TFSI (Fig. 8e). To prove this hypothesis, the superoxide was labelled in the electrolyte by nitrotetrazolium blue chloride. As a result, 18.7% of the discharge products were found to be dissolved (or dispersed) in PYR₁₄TFSI. Simultaneously, Sun *et al.* also built a Li- O_2 battery with PYR₁₄TFSI as the solvent and it also exhibited a low OER overpotential of about 0.2 V (Fig. 8f). Except for the role of the electrolyte solvent, the cathode material was also suggested to induce the one-electron pathway for Li_2O_2 oxidation. As shown in Fig. 8g, a $\text{RuO}_2/\text{carbon nanotube}$ (CNT) cathode was found to achieve a low OER overpotential of about 0.2 V, while the reaction pathway was suggested by analysis with

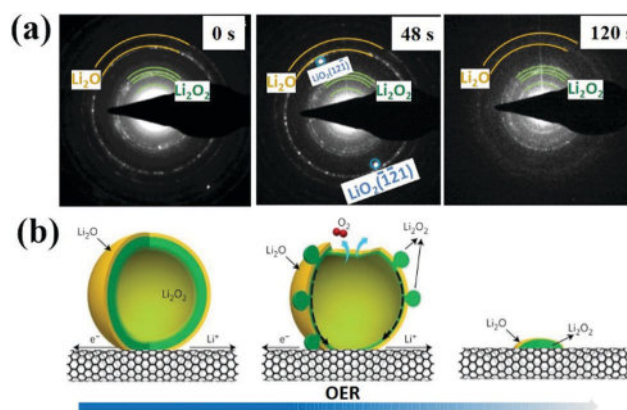


Fig. 7 (a) Time-resolved SAED patterns illustrating the case of charging, in which Li_2O_2 decomposes, leading to the collapse of the hollow spherical particles, as schematically illustrated in (b); the dashed arrows indicate the mass and charge-transfer direction.⁴³ Reprinted with permission from ref. 43. Copyright 2017 Nature Publishing Group.

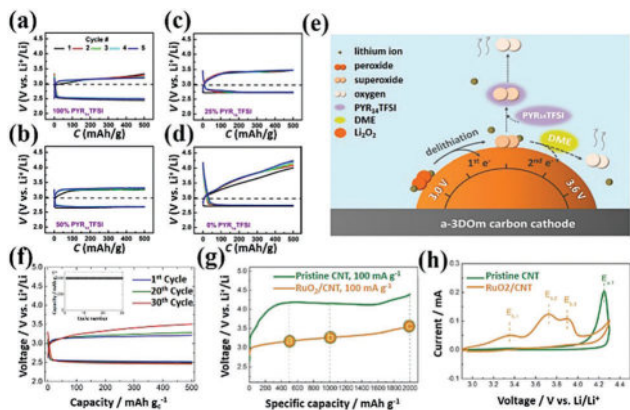


Fig. 8 (a–d) Discharge/recharge behaviours of three-dimensionally ordered mesoporous carbon in PYR₁₄TFSI/DME electrolytes during the first five cycles (the electrolyte compositions were (a) 100% PYR₁₄TFSI; (b) 50% PYR₁₄TFSI, 50% DME; (c) 25% PYR₁₄TFSI, 75% DME and (d) 100% DME).¹³¹ (e) Schematic illustration of the decomposition pathways of Li₂O₂ when PYR₁₄TFSI was present. The key hypothesis was that the solvation effect by PYR₁₄TFSI promoted the single-electron pathway (the upward branch in the illustration) that featured low recharge overpotentials; (f) voltage profiles of the Li/PYR₁₄TFSI–LiTFSI/O₂ battery cycled applying a specific current of 50 mA g^{−1} limiting the capacity to 500 mA h g^{−1} (the inset shows the cycling trend); (g) the recharge curves of Li–O₂ cells with CNT or RuO₂/CNT at a current density of 200 mA g^{−1} and a charge of 2000 mA h g^{−1}.¹³² (h) CV of the discharged CNT cathode and the discharged RuO₂/CNT cathode in Li–O₂ cells at a constant scan rate of 0.1 mV s^{−1}.⁸³ Reprinted with permission from ref. 83, 131 and 132. Copyright 2014, 2015 and 2016 Wiley-VCH Verlag GmbH & Co. KGaA and American Chemical Society.

CV tests for the assembled Li–O₂ cell (Fig. 8h). The peak E_{b1} (3.35 V) and E_{b2} (3.72 V) represented the oxidation of LiO₂-like species and some Li₂O₂ through a one-electron pathway for the RuO₂/CNT cathode. In contrast, only one oxidation peak ranked above 4 V was observed for the pristine-CNT cathode.

2.2.3.2 Li₂O₂ decomposition with a two-electron-transfer path.

In contrast to single-electron Li₂O₂ decomposition, most research has suggested direct Li₂O₂ decomposition with a two-electron-transfer pathway. For example, Peng's, Zhang's and Lu's groups tried to use *in situ* SERS, EPR and RRDE techniques to illustrate the existence of a superoxide or not during the OER process.^{87,133–135} All of these studies approved the direct decomposition of Li₂O₂ through a two-electron pathway (Li₂O₂ → 2Li⁺ + O₂ + 2e[−]) without any superoxide species after the delithiation process. Based on these conclusions, the rate of Li₂O₂ decomposition would be strongly dependent on the properties of the discharged products on the cathode, such as the size, morphologies, defects and crystalline structure of Li₂O₂.

Shao-Horn *et al.* analyzed the relationship between the crystal grain size of Li₂O₂ and the OER overpotentials.¹³⁰ Two characteristic Li₂O₂ morphologies were produced on CNT electrodes at different current densities: discs/toroids (50–200 nm, Fig. 9a) at low rates/overpotentials (10 mA g^{−1} or $E > 2.7$ V vs. Li⁺/Li), or small particles (<20 nm, Fig. 9b) at higher rates/overpotentials ($i > 100$ mA g^{−1} or $E < 2.7$ V vs. Li⁺/Li).

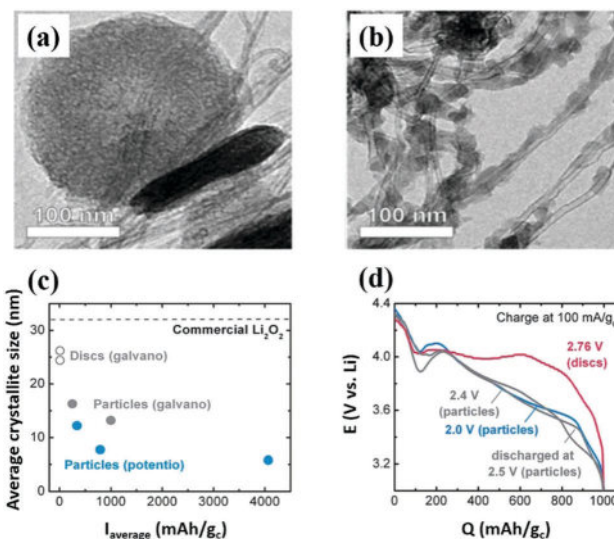


Fig. 9 TEM images of potentiostatically discharged CNT electrodes (a) at $E > 2.74$ V to 2000 mA h g^{−1} (PITT discharge), (b) 2.6 V to 5000 mA h g^{−1}; (c) the crystal size determined from XRD as a function of average discharge current for CNT electrodes discharged to 1000 mA h g^{−1} under galvanostatic or potentiostatic conditions, and comparison with commercial Li₂O₂; (d) charging profile comparison for electrodes discharged to 1000 mA h g^{−1} over a range of potentiostatic conditions and charged at 100 mA g^{−1}.¹³⁰ Reprinted with permission from ref. 130. Copyright 2013 Royal Society of Chemistry.

Correspondingly, the cell charge potential with disc Li₂O₂ was also larger than that with small particles (Fig. 9d).

Ceder *et al.* further found an alternative reaction pathway based on a top tactic of delithiation of Li₂O₂ to form off-stoichiometric Li_{2−x}O₂ with small OER overpotentials of ~0.3–0.4 V through DFT calculation.¹²⁹ With these basics, Nazar *et al.* established an OER mechanism using *in operando* X-ray diffraction.¹³⁶ In this work, the authors found the different charge profiles between the electrochemically generated Li₂O₂ (E-Li₂O₂) and commercial Li₂O₂ (C-Li₂O₂) (Fig. 10). For E-Li₂O₂, the initial low charge voltage (2.8–3.4 V) originated from the oxidation of amorphous Li₂O₂ (Fig. 10a). Then, the second step was the decomposition of the Li_{2−x}O₂ transformed from Li₂O₂ platelets through delithiation. Simultaneously, from the XRD data, they found that the smallest and thinnest platelet crystallites were oxidized preferentially, leaving the largest platelets at the end of charge. Also, the continuous increase in charge voltage may be also influenced by the side products, such as lithium hydrate and lithium formate, which can be decomposed around 3.8 V vs. Li⁺/Li. For C-Li₂O₂, owing to its high chemical purity and large size, its OER voltage was started from ~3.6 V through the oxidation of delithiated Li_{2−x}O₂ (Fig. 10c). Liu also used an *in operando* synchrotron XRD technique to investigate Li₂O₂ decomposition on the CNT cathode. The quantitative tracking of Li₂O₂ during the electrochemical operation of Li–O₂ batteries was provided by using *in situ* synchrotron radiation XRD.¹³⁷ The charging process was divided into two parts. The initial part was the decomposition of small Li₂O₂ particles, followed by the more dominant oxidation through the [100] direction of the

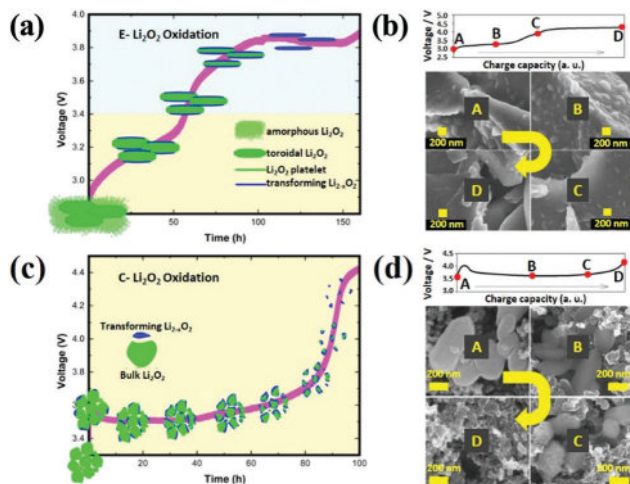


Fig. 10 Illustration showing the mechanism of (a) electrochemically formed Li_2O_2 (E- Li_2O_2) and (c) commercial Li_2O_2 (C- Li_2O_2) oxidation during the charge process as determined from X-ray diffraction; SEMs recorded at different stages of the oxidation of E- Li_2O_2 and C- Li_2O_2 are depicted in panels (b) and (d), respectively.¹³⁶ Reprinted with permission from ref. 136. Copyright 2014 American Chemical Society.

Li_2O_2 nanocrystals. For the second part, Li^+ was stripped from the interlayer to form an off-stoichiometric intermediate with a higher oxidation rate. It was found that some of the current during the initial charge process did not originate from Li_2O_2 , indicating that the impurities on the Li_2O_2 surface were related to parasitic products formed during discharge.

2.2.4 Challenge and resolved strategies for Li_2O_2 decomposition

2.2.4.1 Solid catalyst innovation for Li_2O_2 decomposition. The electrically deposited Li_2O_2 is an insulating material and insoluble in most aprotic solvents under general conditions, resulting in the slow kinetics of charge reactions.¹³⁸ In most cases of Li- O_2 batteries, the initial charge potential of the battery increased quickly in the charge profiles.¹³⁹ The charge reaction, also called Li_2O_2 decomposition, occurred at the interface of the cathode/ Li_2O_2 interface or Li_2O_2 /electrolyte. When Li_2O_2 decomposition takes place at the cathode/ Li_2O_2 interface, it is classed as a catalysis-effective process with a direct electron-transfer pathway. The O_2 release and subsequent electrical contact between the electrode and Li_2O_2 should be well studied. When the reaction occurs at the Li_2O_2 /electrolyte interface, the electron transfer between the electrolyte components, Li_2O_2 , and electrode is the critical factor for the charging process.

To confirm the cathode/ Li_2O_2 interface, Gu *et al.* investigated the real-time decomposition of Li_2O_2 using *in situ* environmental scanning electron microscopy in a CNT/ Li_2O /Li system.¹⁴⁰ As shown in Fig. 11, the decomposition of the Li_2O_2 particle was initiated locally at the Li_2O_2 surface without CNT, followed with proceeding into the Li_2O_2 bulk along a certain direction. The electronic and ionic conductivities of Li_2O_2 were suggested to be important for sustaining Li_2O_2 oxidation. Also, in Zhu's report,¹³⁷ they found that the parasitic products formed on Li_2O_2 surfaces were oxidized primarily at the initial charging state. These results indicated that the initial charge reaction could take place at the Li_2O_2 /electrolyte interface.

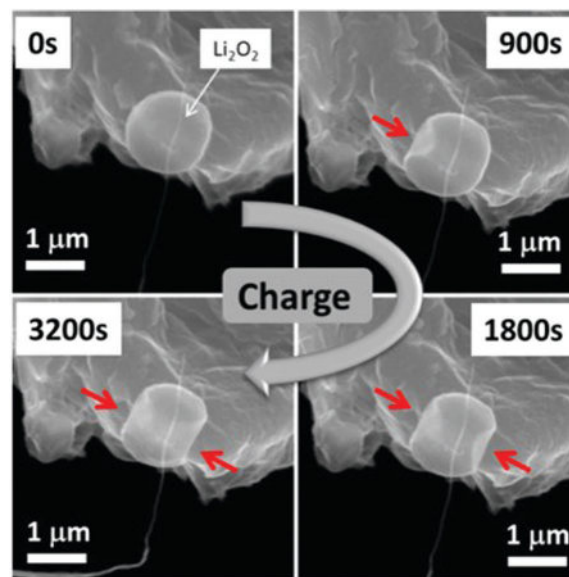


Fig. 11 SEM images captured at 0, 900, 1800 and 3200 s showing the decomposition process of the spherical Li_2O_2 particle (red arrows indicate the position where the particle is decomposed).¹⁴⁰ Reprinted with permission from ref. 140. Copyright 2014 American Chemical Society.

Some other works also reported that the cathode/ Li_2O_2 interface could be the initial reaction sites.^{28,135,141} Shao-Horn *et al.* checked the decomposition process of produced Li_2O_2 in an *ex situ* Li- O_2 cell,¹⁴¹ while it was assembled with the structure of a discharged-multi-walled CNT (MWCNT)/LiAlSiO_x solid-electrolyte/Si nanowire for adapting to vacuum. It was found that the Li_2O_2 located at the cathode/ Li_2O_2 interface was first oxidized during the charge process (Fig. 12a-d). Peng *et al.* further illustrated the initial reaction interface by using the isotope labelling of Li_2O_2 ,²⁸ in which Au/ $\text{Li}_2^{16}\text{O}_2/\text{Li}_2^{18}\text{O}_2$ double interface layers were used as a model system. During the charging process, the vanishing of the $\text{Li}_2^{16}\text{O}_2$ peak before the $\text{Li}_2^{18}\text{O}_2$ peak indicated the oxidation of Li_2O_2 film initially at the electrode/ Li_2O_2 interface (Fig. 12e and f). Lu *et al.* built a Li/solid-state lithium-ion conductive glass-ceramics membrane (LICGC)/carbon + Ru battery, primarily filled with Li_2O_2 . It was proved that the Ru catalyst could decompose Li_2O_2 effectively, resulting in a decrease in the OER overpotential and an increase in the cell cycling stability.¹³⁵ Based on the evidence of the solid-solid contact of the catalyst and Li_2O_2 , it was hypothesized that Li extraction started at the Li_2O_2 /catalyst interface and generated Li vacancies in the initial OER step. The key role of the catalyst was emphasized in stabilizing the interface between the catalyst and Li_2O_2 . With regard to this matter, we discuss the functional design of cathodic catalysts towards improving their catalytic activity and stability for Li_2O_2 decomposition in the O_2 -cathode section.

2.2.4.2 Electrolyte innovation for Li_2O_2 decomposition. Compared to the electrode/ Li_2O_2 interface, the contact area of the electrolyte/ Li_2O_2 interface is substantially increased because the Li_2O_2 surface is surrounded by an electrolyte composed of solvent and additives.^{142,143} This could potentially accelerate Li_2O_2

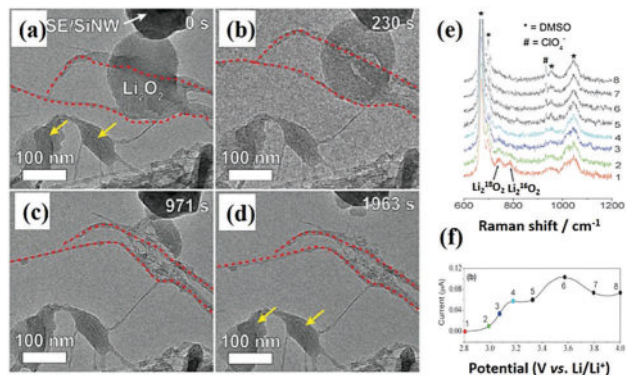


Fig. 12 (a) SEM image of a disc particle aligned orthogonal to the electron beam connected to two sets of MWCNTs (at the middle and bottom of the particle) and also contacted by a solid–electrolyte-coated Si NW (application of a 10 V potential between the MWCNT/Li₂O₂ positive electrode and the Si NW negative electrode initiates the oxidation process); (b–d) SEM images captured at 230, 971 and 1963 s, respectively, showing preferential rapid oxidation occurring at the Li₂O₂/MWCNT interfaces with more gradual oxidation occurring at the top of the particle (during the oxidation process, with no change occurring in the two reference particles (indicated by yellow arrows), excluding the possibility of beam irradiation effects);¹⁴¹ (e) *in situ* SERS spectra collected during a linear potential scan from 2.8 to 4.0 V vs. Li/Li⁺ on a Au electrode passivated by a mixed film of Li₂¹⁸O₂ and Li₂¹⁶O₂ (numbers 1–8 in Fig. 12e and f are the same); (f) current–potential curve of the linear potential scan (scan rate is 2 mV s^{−1}).²⁸ Reprinted with permission from ref. 28 and 141. Copyright 2013, 2016 Wiley-VCH Verlag GmbH & Co. KGaA and American Chemical Society.

decomposition in charge processes (namely OER).¹⁴⁴ Two types of capabilities for the electrolyte were proposed towards Li₂O₂ decomposition, namely the dissolution of solid Li₂O₂ and the chemical oxidation of Li₂O₂ with SRMs.^{5,16,145} In the case of the dissolving solid-phase Li₂O₂ into the solution phase, some specific polar solvents, for example, hexamethylphosphoramide (HMPA) and ionic liquids, showed a capability to dissolve Li₂O₂ in the electrolyte. The dissolved Li₂O₂ would then be diffused and decomposed at the O₂-electrode. The effect of the solvent solubility on Li₂O₂ and the accelerated Li₂O₂ decomposition are discussed in the following electrolyte section.

Except for the solvent effect, some specific additives, *i.e.* SRMs, could potentially sustain the solution-mediated OER process and provide a route to the chemical oxidation of Li₂O₂. SRMs with a redox potential higher than 2.96 V vs. Li⁺/Li can accelerate the OER reaction rate, resulting in a decrease of the charge overpotentials. Moreover, the reduced cell charge potentials will decline the production yield of reactive species (for example, singlet oxygen species).^{139,146} This is also beneficial for the sustainability of cathode reactions. In this case, the initial reaction is the extraction of an electron from Li₂O₂ to the oxidized SRMs, followed by electron transfer from the reduced SRMs to the oxygen electrode. In the section on SRM, we focus on the functions of SRMs for accelerating the Li₂O₂ decomposition reactions, resulting in a decrease in the charge potentials and an increase in cell durability.

To date, the mechanism for Li₂O₂ decomposition is still controversial due to the complicated reaction process and interface. For example, the LiO₂-like species are sometime found on

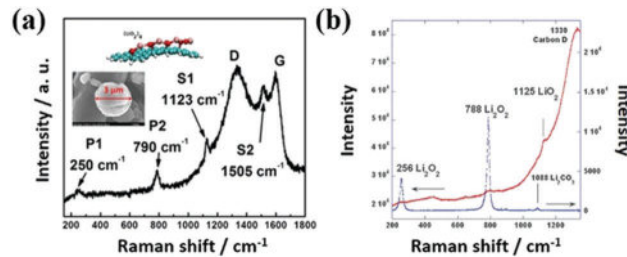


Fig. 13 (a) Raman spectra of the toroids on the surface of the discharged AC cathode at the same discharge capacity of 1000 mA h g^{−1} with different current densities of 0.05 mA cm^{−2} (insets show the morphology of Li₂O₂ and a schematic of LiO₂ clusters on the carbon surface);¹⁴⁷ (b) Raman spectrum at ambient temperature of the discharged AC cathode surface (the separator side) showing the graphite D band, weak Li₂O₂ band and LiO₂ band (red trace) (commercial Li₂O₂ (blue trace) is also shown for comparison; a small amount of Li₂CO₃ impurity is also marked on the blue trace due to the reaction of the commercial Li₂O₂ with CO₂ from air).¹⁴⁸ Reprinted with permission from ref. 147 and 148. Copyright 2013, 2014 Royal Society of Chemistry and American Chemical Society.

the discharge cathode.^{147–149} As shown in Fig. 13, a LiO₂-like component was identified at about 1125 cm^{−1} in the Raman spectra of a carbon surface. The decomposition of LiO₂ products occurs more easily than those of Li₂O₂ in the cell discharge process. Moreover, the evolved electron transfer, Li⁺ diffusion, O₂ release and the electrochemical intermediates at the possible interfaces are difficult to illustrate comprehensively. The initial reaction pathway and interface are probably different with different electrode catalysts and electrolyte components. Thus, it is still necessary to make the great endeavours to reveal a clear description for Li₂O₂ decomposition.

2.3 Mechanism of sudden death in aprotic Li–O₂ cells

The death of aprotic Li–O₂ batteries can commonly occur during discharge processes, and is a big challenge for obtaining long-term cell operation. Exploring and understanding the reason for battery death will provide insights to optimize the battery component, which is beneficial for improving the cell performance and stability. According to the cell operation conditions, the type of battery death can be divided into two situations: one is sudden death during a full discharge and the other is failure during the cycling test. The accumulation of insulating Li₂O₂ and by-product film on the O₂-cathode, as well as undesirable parasitic side products on the Li-anode, can result in a substantial increase in cell electrochemical resistance. This can result in sudden death in the full discharge process and during the discharge cycles.^{150,151}

2.3.1 Sudden death in the full discharge process. When the persistent discharge voltage plateau of the curve turns down sharply, it means that the discharge process is finished, this is the point of so-called battery death. The electrical conductivity of Li₂O₂ has been estimated to be in the range of 10^{−12}–10^{−13} S cm^{−1} (at room temperature),^{152,153} indicating that a thin Li₂O₂ film with a thickness of no more than 10 nm on a porous electrode would block the electron flow.^{87,153} The sudden death during the full discharge is mainly caused by the deposition of this Li₂O₂ film, which fully covers the cathode surface. To achieve a

cell capacity as high as possible, the inhibition of Li_2O_2 film formation to delay the battery sudden death in full discharge is therefore a critical issue.^{150,151,154}

As discussed previously, the conductivity of Li_2O_2 film plays a key role in this phenomenon. Merkle *et al.* studied the major ionic and charge carriers in Li_2O_2 .¹⁵⁶ It was found that the bulk ionic conductivity in Li_2O_2 (10^{-10} – 10^{-9} S cm^{-1} at 100 °C), similar to that of LiFePO_4 (typical cathode materials in a Li-ion battery, 10^{-11} – 10^{-10} S cm^{-1} at 100 °C), could be enhanced by donor doping. Moreover, the electronic conductivity of Li_2O_2 (10^{-12} – 10^{-11} S cm^{-1} at 100 °C), which is much lower than that of LiFePO_4 (10^{-7} – 10^{-6} S cm^{-1} at 100 °C), could be improved by increasing the electron holes. Through first-principles calculations, Monroe *et al.* suggested that doping Co element at equilibrium levels (tens of ppm) can enhance the rate of charge transport by shifting the balance of Li-ion vacancies and hole polarons.¹⁵⁷ Nevertheless, the realization of heteroatom-doping into Li_2O_2 is difficult in the cell operation for a battery process. The related experimental works to delay cell death (which may also decrease OER overpotential) are expected in the future.

In most cases of cell operation conditions, the surface-growth and solution-growth pathways of Li_2O_2 coexist during the discharge process. Fig. 14 presents two examples. After discharging a CNT electrode at a relative low current density (90 mA g^{-1}), both Li_2O_2 toroid and Li_2O_2 film were produced (Fig. 14a and b).¹⁵⁵ Similarly, when the freestanding Co_3O_4 sheets were discharged to 2 V at 102 mA g^{-1} , Li_2O_2 sheets and Li_2O_2 film were formed (Fig. 14c and d).⁹³ The cell sudden death in the full-discharge process was mainly correlated with the formation of a thin Li_2O_2 film, which resulted from the surface-growth pathway. It was inferred that the current density

was one of the critical factors to influence the pathway of Li_2O_2 growth, while a high current density was beneficial for the surface-growth pathway. In order to decrease the current density, the electrode structure, including the specific surface area and pore structure, should be elaborately designed. An electrode with a large specific surface area can effectively decrease the surface current density to produce large Li_2O_2 aggregation through a solution-growth pathway. Moreover, an electrode with a suitable pore structure can provide sufficient space to store large Li_2O_2 aggregations.

It should be noted that the surface-growth mode cannot be excluded entirely just with modulation of the O_2 electrode architecture. In the Li– O_2 battery, the electrode surface is passivated step-by-step with the growth of discharged Li_2O_2 , particularly by the rapidly increased thickness of Li_2O_2 film at the late stage of cell discharge. Moreover, with the coverage of the electrode surface by Li_2O_2 , the solution-growth mode can transform to the surface-growth mode, resulting in the growth of a thick Li_2O_2 film. This indicates that both large Li_2O_2 aggregations and Li_2O_2 films will be formed on the electrode surface. As discussed previously, modulation of the electrolyte solvent and additives with a high DN value can greatly boost the solution-phase growth of Li_2O_2 . Here, delaying the sudden death of the battery is consistent with prompting Li_2O_2 cluster formation through the solution-growth pathway by using specific electrolyte/additives and designing a specific cathode micro-structure for large-sized Li_2O_2 storage. The functional design of the electrolyte and electrode towards delaying the sudden death of battery is discussed in the sections on the O_2 -electrode, electrolyte and soluble redox mediator.

Another point related to sudden death in the full-discharge process is the generation of side products at the cathode/electrolyte and Li_2O_2 /electrolyte interfaces. Although the quantity of by-product is much lower than that of Li_2O_2 in one of the cell cycles, their accumulation can greatly influence the next discharge cycles. Considering their significant effect on the cyclic stability of Li– O_2 cells, we discuss the parasitic chemistry of Li– O_2 batteries in the next section.

2.3.2 Cell death during cell cycling. Different from cell death during full discharge, the continuous accumulation of side products will block electron transfer and passivate the entire electrode. The parasitic reactions occurring on the surface of both the Li-anode and O_2 -cathode are the reason for the generation of side by-products, which can ultimately induce cell death during cell cycling.

2.3.2.1 Cell death from Li-metal corrosion. Due to the highly reactive activity of metallic Li towards the electrolyte components and the crossover O_2 , the side reactions at the lithium anode/electrolyte interface can accelerate the battery failure. Among all the by-products, LiOH is widely regarded as one of the main components in the anode of Li– O_2 cells, and its quantity is increased with the battery life.^{9,63} Cho *et al.* compared the morphologies of a metal Li-anode before and after cycling with a Au/Ni electrode and a 1.3 M (lithium bis(trifluoromethanesulfonyl)imide) (LiTFSI , $\text{LiN}(\text{CF}_3\text{SO}_2)_2$) in tetraethylene glycol

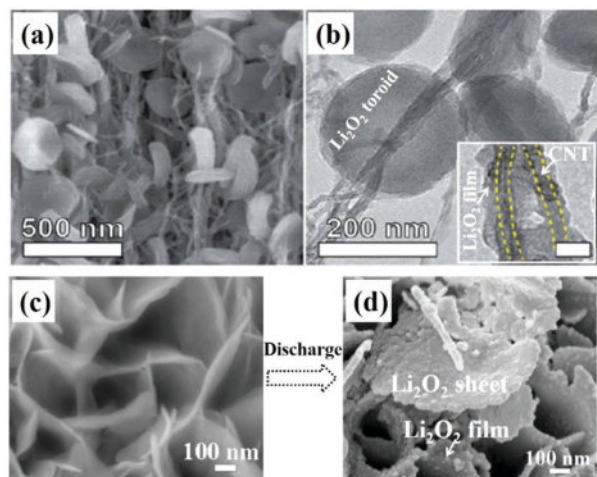


Fig. 14 (a) SEM and (b) TEM micrographs of an electrode discharged at 90 mA g^{-1} to $13\,000 \text{ mA h g}^{-1}$, disc particles and a thin coating of discharge product present on the sidewalls of the CNTs (insets: higher magnification TEM images of CNT sidewalls, indicated by a dashed yellow line).¹⁵⁵ (c) SEM images of Co_3O_4 nanosheets grown on carbon paper; (d) SEM images of Co_3O_4 nanosheet electrodes discharged to 2 V at 102 mA g^{-1} .⁹³ Reprinted with permission from ref. 93 and 155. Copyright 2013, 2017 Wiley-VCH Verlag GmbH & Co. KGaA and American Chemical Society.

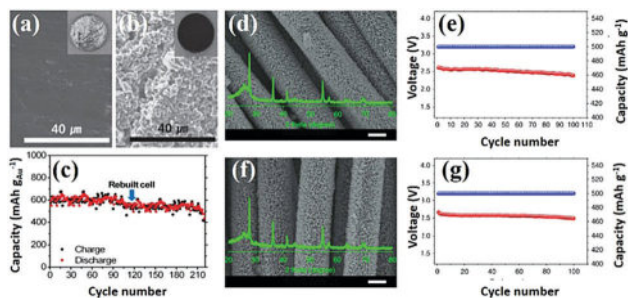


Fig. 15 The morphology change of (a) fresh Li-metal, (b) Li-metal after 110th cycles; (c) the summation cycle graph of the pristine and rebuilt cells ($500 \text{ mA g}_{\text{Au}}^{-1}$) (the rebuilt cell was using the used Au/Ni electrode but with new Li-metal, a new separator, and fresh electrolyte);¹⁵⁸ (d) SEM images of the pristine TiO_2 nanoarrays/carbon textile (NAS/CT) cathode (scale bar, 5 mm; the inset was the corresponding X-ray diffraction pattern); (e) the variation of the terminal discharge voltage of the pristine TiO_2 NAS/CT cathode with a current density of 100 mA g^{-1} ; (f) SEM images of the first-recovered TiO_2 NAS/CT cathode (scale bar, 5 mm); the inset was the corresponding X-ray diffraction pattern; (g) the variation of the terminal discharge voltage of the first-recovered TiO_2 NAS/CT cathode with a current density of 100 mA g^{-1} (the recovered TiO_2 NAS/CT cathode was rinsed with 2 M HCl to remove the residual carbonates).¹⁵⁹ Reprinted with permission from ref. 158 and 159. Copyright 2015 Wiley-VCH Verlag GmbH & Co. KGaA and Nature Publishing Group.

dimethyl ether (TEGDME) electrolyte (Fig. 15a and b).¹⁵⁸ It was clearly seen that a vividly developed black layer was formed after 110 cycles. After rebuilding the battery with the used Au/Ni electrode and a new Li-anode, new separator and fresh electrolyte, another 100 cycles could be performed (Fig. 15c). This indicated that the rapid capacity fading at the late stage of the battery cycle was not due to the Au/Ni electrode but rather due to the corrosion of the Li-anode. This confirmed the passivation of metallic Li towards battery failure, and that the inhibition of LiOH by-product generation should be the key protocol to enhance the sustainability of Li-anodes. Except for LiOH, other Li^+ -Based by-products (lithium alkylcarbonates, Li_2CO_3 , etc.) were also generated, and their influences on the cell performance are discussed in the Li-anode section. Whatever by-products they are, it was concluded that the corrosion of the Li-anode could significantly restrict the long-term cyclic stability of Li-O_2 cells.

2.3.2.2 Cell death from O_2 -electrode passivation. Parasitic reactions at the O_2 -cathode widely exist, resulting in the deposition of insulating and insoluble Li^+ -based by-products. Zhang *et al.* restored a disabled TiO_2 nanoarrays/carbon textile (NAS/CT) with 2 M HCl to remove the residual carbonates.¹⁵⁹ Following this, the recovered battery exhibited a superior cyclic stability to the original one (Fig. 15d and e). It was suggested that the existence of the residual carbonates (originating from CT/electrolyte decomposition) on the cathode surface caused the failure of the battery.

Many works have focused on clarifying the generation process for parasitic by-products by applying *in situ* and *ex situ* techniques. As shown in Fig. 16a and b, Liu *et al.* investigated the discharge process on a carbon cathode by using a spatially

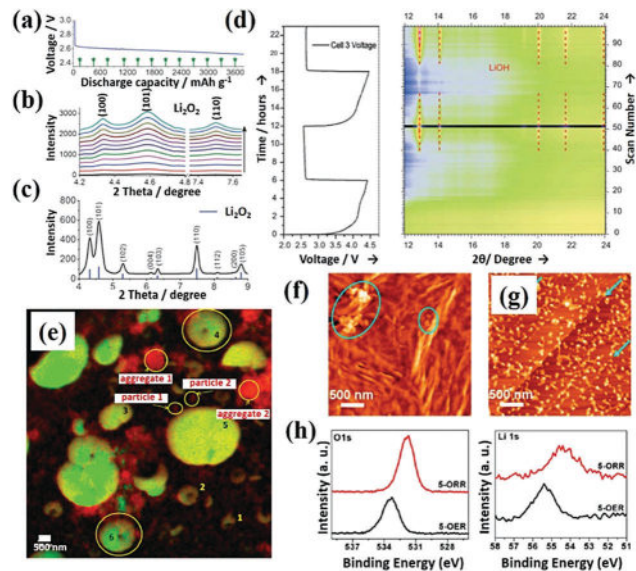


Fig. 16 (a) Voltage profile of a prolonged discharge of a Li-O_2 cell (the markers on the axis indicate the times when the diffraction patterns were recorded); (b) increase in the diffraction intensities of the three strongest Li_2O_2 peaks recorded at the same relative position in the cathode (the vertical arrow indicates the progress of the discharge depth); (c) XRD pattern recorded on the cathode region of an operating Li-O_2 cell after 24 h discharge at a current density of 160 mA g^{-1} ;¹⁶⁰ (d) electrochemical data collected during the first charge of a Li-O_2 cell with the corresponding surface plot of the XRD data (lines corresponding to the Bragg reflections ($\lambda = 0.6161 \text{ \AA}$) are indexed and the discharge/charge rate is 0.07 mA).¹⁶¹ (e) TXM images of carbon-coated Au TEM grid after being fully discharged at 100 mA g^{-1} in a Li-O_2 cell (the images are the result of overlapping three colour maps with intensities proportional to the amounts of Li superoxide (cyan), Li peroxide (green) and carbonate (red));¹⁶² (f) discharged and (g) recharged *in situ* atomic force microscopy images of a highly oriented pyrolytic graphite (HOPG) electrode during the 5-cycle; (h) XPS O 1s (left) and Li 1s (right) binding energy regions of 5-cycled ORR (5-ORR) and 5-cycled OER (5-OER).¹⁶³ Reprinted with permission from ref. 160–163. Copyright 2013, 2014 and 2015 Wiley-VCH Verlag GmbH & Co. KGaA, Royal Society of Chemistry and American Chemical Society.

resolved, real-time synchrotron XRD technique.¹⁶⁰ It was found that the intensities of Li_2O_2 peaks progressed linearly with the increased discharge depth (Super-P/ LiCF_3SO_3 in TEGDME). Combined with the results of the pure Li_2O_2 peaks in the full spectrum after discharge (Fig. 16c), it was seen that the discharge capacity was strongly correlated with the nucleation and grain growth of Li_2O_2 during the first discharge. Ingram *et al.* further found that when the cell was first charged (porous carbon/ LiCF_3SO_3 in TEGDME), the discharge products were transformed from Li_2O_2 to LiOH (Fig. 16d).¹⁶¹ This indicated that the electrolyte could be oxidized, and a proton and subsequently H_2O were generated in the electrolyte during the charge process.

In addition to LiOH, Li^+ -based carbonate is one of the common by-products. Tonti *et al.* observed that the discharge products grew directly on carbon-coated TEM grids by oxidation-state-sensitive full-field transmission soft X-ray microscopy (TXM).¹⁶² As seen in Fig. 16e, although peroxide (green colour) was the main discharge product, the carbonate (red colour) scattered in

many places in the TXM image. Byon *et al.* also investigated the side products of Li–O₂ cells (highly oriented pyrolytic graphite (HOPG)/LiTFSI in TEGDME) by using *in situ* electrochemical atomic force microscopy (EC-AFM).¹⁶³ Although no by-products were observed after the first reduction and oxidation reactions by performing X-ray photoelectron spectroscopy (XPS) measurements, the unintended products were produced in further cell cycles. As indicated in Fig. 16f, the granular products were formed after 5-cycled ORR, while their morphologies were somewhat different from others. XPS results in Fig. 16h revealed O 1s peak (left) at ~531.8 eV arising from the combination of Li₂O₂ and Li₂CO₃ (~532 eV). At the 5-cycled OER electrode, many nanoparticulate products were still not decomposed (Fig. 16g). It also exhibited the further shifted O 1s (~533.2 eV) and Li 1s (~55.4 eV) peaks, involving the generation of Li₂CO₃ and lithium acetate by-products (~533.7 eV for the O 1s peak). These by-products may be related to the oxidation of HOPG and/or electrolyte. Besides, it was well known that carbon was unstable towards Li₂O₂ at high voltage (≥ 3.5 V vs. Li/Li⁺) with a result of Li₂CO₃, especially for hydrophobic carbon. Carbon could also promote the electrolyte decomposition during discharge and charging, giving the increased amounts of Li₂CO₃ and Li carboxylates.^{36,165,166}

To exclude the source of by-products from carbon electrode, Byon *et al.* further investigated the surface chemistry of Li–O₂ cell with nanoporous gold (NPG) as cathode by synchrotron X-ray photoelectron spectra.¹⁶⁴ Fig. 17a displayed a decrease and increase of Au 4f_{7/2} (84 eV), 4f_{5/2} (88 eV) and Ag 3d_{5/2} (368 eV), 3d_{3/2} peaks (374 eV) upon the ORR and OER, which embodied the deposition and decomposition of discharge products on the NPG electrodes, respectively. The O 1s peak at 532.4 eV (Fig. 17c) and Li 1s peaks at 56.3 eV (Fig. 17d) on ORR-2.4 V and ORR-2.0 V correspond to the Li₂O₂ formation after discharge. After the cell was charged, carboxylate and carbonate peaks (C 1s, 289.1 eV and 291.6 eV, Fig. 17b) relative to sp³ carbon still remained with the long tail from Li₂CO₃ (O 1s, over 533.5 eV), respectively. The authors pointed out that the small tails over 533.5 eV in asymmetric O 1s peaks existed on the ORR from O peak (533.6 eV) in Li₂CO₃. With these findings, it can be concluded that carbon-based cathode and electrolyte was both unstable during discharge and charge reaction, especially at high charge potential region.

The electrolyte decomposition was reported to be related with high reactive activity of superoxide (O₂^{•-}, LiO₂) and Li₂O₂ *via* nucleophilic substitution and H⁺ abstraction.^{167–169} In addition to those of O₂/LiO₂ intermediates, singlet oxygen (¹O₂), a strong oxidizing agent, was also detected during battery operation.^{146,170} Wandt *et al.* first reported the formation of ¹O₂ during the charging voltage between 3.55 V and 3.75 V in Li–O₂ batteries.¹⁷⁰ They used 4-oxo-2,2,6,6-tetramethyl-4-piperidone (4-oxo-TEMPO) to trap ¹O₂ to form a stable 4-oxo-TEMPO, which was then detected by *in operando* EPR spectroscopy. The existence of ¹O₂ can well explain the oxidization of carbon above 3.5 V, different from the previous studies that carbon was oxidized by Li₂O₂. Subsequently, Freunberger *et al.* further elucidated the process of ¹O₂ generation by *in operando* fluorescence detection

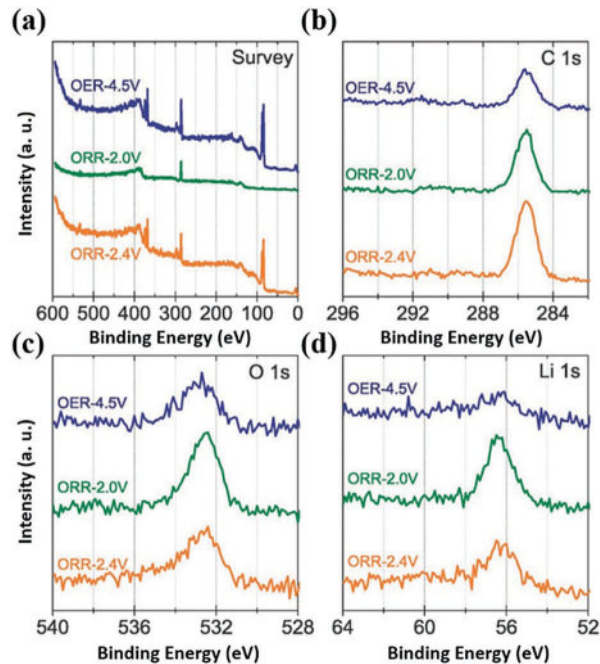


Fig. 17 Synchrotron X-ray photoelectron spectra (photon energy E is about 650 eV) of NPG electrodes with different ORR and OER states *via* CV at a sweeping rate of 1 mV s^{-1} . Spectra in (a) survey, (b) C 1s, (c) O 1s and (d) Li 1s BE region with ORR at 2.4 V (ORR-2.4 V, bottom orange), 2.0 V (ORR-2.0 V, middle green) and OER at 4.5 V (OER-4.5 V, top blue).¹⁶⁴ Reprinted with permission from ref. 164. Copyright 2014 Royal Society of Chemistry.

with 9,10-dimethylantracene as an ¹O₂ probe.¹⁴⁶ It was found that ¹O₂ was generated not only during the discharge process, but also at the initial and high charging voltages. The ¹O₂ quantity at charging process was much higher than that in discharge process. It was confirmed by observing the more serious deviation of O₂/electron ratio at charging process. They further suggested that the formation of ¹O₂ was promoted by proton, identifying the increased quantity of by-products with protic additives. It was proposed that ¹O₂ is probably the dominant source for parasitic reactions in aprotic Li–O₂ batteries.^{171,172} However, this view is new and highly unexpected, and so more evidence should be provided to confirm the origin to the parasitic chemistry.

Except for the superoxide and ¹O₂ in common electrolytes, proton sources, redox chemicals, HOO[•], HOO⁻ and HO[•] appear with electrolyte additives, and are also reactive to electrolyte components.^{47,117,173} As a result, LiOH instead of Li₂O₂ is produced as the main discharge product in some cases.^{16,118,174} It should be noted that the decomposed voltages of Li₂CO₃ and LiOH are about 4.4–4.6 V (*vs.* Li⁺/Li) and 3.8 V (*vs.* Li⁺/Li), respectively,^{175,176} while their oxidation voltages are much higher than those of Li₂O₂. Moreover, the high charge voltage can induce the decomposition of the electrolyte, giving rise to the continuous accumulation of these products during the cyclic test. In order to inhibit the generation of Li⁺-based by-products, the functional design of the O₂ electrode and optimization of the electrolyte and additives are strongly recommended for attaining

a long-term stability of the Li–O₂ battery. This will be discussed in the later sections.

3. Lithium electrode

As an anode material for energy storage/conversion devices, Li-metal has several advantages in terms of its low molar mass (6.94 g mol⁻¹), small ionic radius (0.76 Å) and ultralow redox potential (−3.05 V vs. SHE). Due to these merits, Li-metal-based batteries usually perform with a high mass capacity, fast anion diffusion rate and high discharge voltage. As seen from Table 1, Li-metal-based batteries can perform with higher specific capacities and voltages than those of other metal-based batteries. However, these properties may have their own limitations. First, the ultralow redox potential of Li-metal implies its' high reduction activity. This means that Li-metal can reduce some of the electrolyte components to generate solid products that cannot withstand mechanical deformation and continuous breaks and repairs during the cyclic tests.^{61,177} Goodenough *et al.* proposed the relationship between the electrochemical potentials of the anode (μ_A) and the lowest unoccupied molecular orbital (LUMO) of electrolytes (E_{LUMO}), whereby if $\mu_A > E_{LUMO}$, electrons on the anode tend to transfer to the LUMO of the electrolyte, inducing intrinsic reduction reactions of the electrolyte. Due to the more negative nature of Li-metal, the redox reactions between Li and the electrolyte could not be avoided.^{66,178} Second, the dissolved oxygen crossover from the cathode can also react with metallic Li, and change the ingredients of the SEI in the Li–O₂ battery.^{179–181} The acceleration of Li-metal and electrolyte consumption induces the formation of a thick SEI layer with a high electrical resistance.^{61,62} As a result, metallic Li has a low Coulombic efficiency and sustainability. Third, the electrodeposition of Li-metal during battery recharge is physically unstable towards the formation of rough/dendritic structures on the anode, which are controlled by the surface energy and Li⁺-migration energy of solid products on the Li-metal surface.⁶⁶ The undesirable Li dendrites ultimately result in safety and stability problems during the operation of Li-based batteries.¹⁸² In this part, we focus on the instability and unsustainability of the Li-metal and related strategies in aprotic Li–O₂ batteries.

3.1 Instability nature of Li-metal in Li–O₂ batteries

The chemical stability of Li-metal towards polar and nonpolar solvents should be primary considered for the operation of a

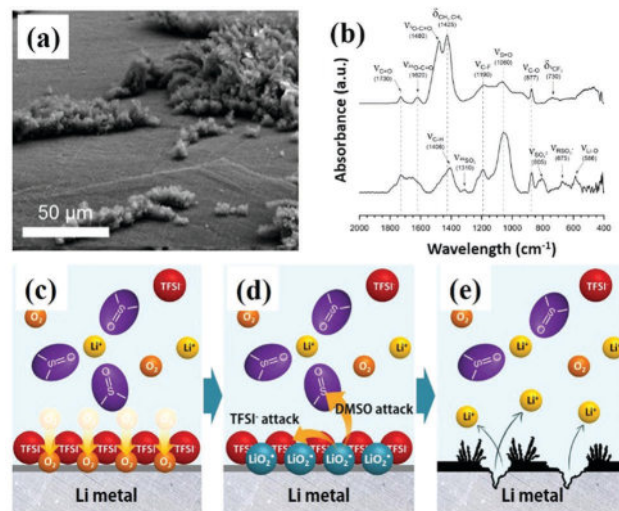


Fig. 18 (a) SEM image of Li-metal immersed in an oxygenated DMSO electrolyte for 30 days; (b) FT-IR spectra of Li-metal stored in a non-oxygenated (top) and an oxygenated DMSO electrolyte (down); (c–e) illustration of the degradation mechanism of the Li surface in an oxygenated DMSO electrolyte ((c) adsorption of TFSI-anions and O₂ molecules diffusing into the native layer of Li-metal, (d) the formation of LiO₂ and nucleophilic attack on the surrounding DMSO solvent and TFSI-anions, (e) precipitation of decomposed compounds forming a moss-like morphology and continuous Li⁺ dissolution and oxidative reactions).⁶¹ Reprinted with permission from ref. 61. Copyright 2014 Elsevier.

stable Li–O₂ battery. Lee *et al.* observed that Li-metal maintained its original flat and clean surface after prolonged storage in polar dimethylsulfoxide (DMSO)-based electrolyte without dissolved O₂. In contrast, rugged and moss-like prolonged deposits were formed on the surface of Li-metal after prolonged storage in an oxygenated electrolyte (Fig. 18).⁶¹ A chemical degradation mechanism was proposed to explain this whereby DMSO was attacked by superoxide species formed through the reaction between Li and O₂, yielding a passivation layer composed of methylsulfinyl carbanion (CH₃SOCH₂⁻) and LiOH. Marinaro *et al.* also found that the existence of O₂ can induce the formation of LiOH on the Li-metal surface in DMSO due to the acid–base reaction between α -hydrogen of DMSO and lithium oxide.⁶³ The formation of a large amount of LiOH led to rapid mass loss and surface passivation of the Li-metal.

The stability of Li-metal in TEGDME, a nonpolar solvent, based electrolyte was analyzed by Curtiss *et al.* with a combination of experiments and density functional theory (DFT) calculations.⁶² Based on the analysis of the Li-anode surface,

Table 1 Theoretical energy density for several batteries based on their cell reactions

Battery	Cell reactions	Cell voltage (V)	Specific capacity (mA h g ⁻¹)	Theoretical energy density (W h kg ⁻¹)
Li-Ion battery	0.5C ₆ Li + Li _{0.5} CoO ₂ = 3C + LiCoO ₂	3.80	102	387
Li–S battery	2Li + S = Li ₂ S	2.24	2615	2615
Na–S battery	2Na + S = Na ₂ S	1.85	687	1273
Li–O ₂ battery	2Li + O ₂ = Li ₂ O ₂	2.96	1168	3456
Na–O ₂ battery	2Na + O ₂ = Na ₂ O ₂	2.33	689	1602
Zn–O ₂ battery	Zn + 1/2O ₂ = ZnO	1.65	658	1086

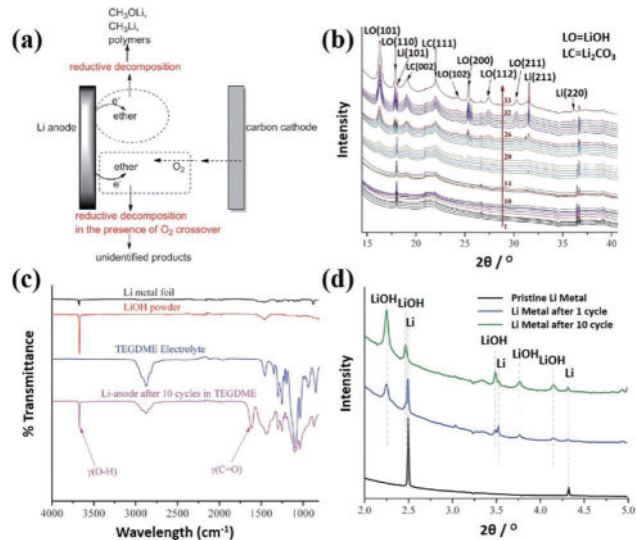


Fig. 19 (a) Possible sources of electrolyte decomposition at the Li-anode in a Li–O₂ battery with an ether-based electrolyte; (b) *in situ* XRD patterns of the Li-anode and LiOH formation during operation; (c) *ex situ* FT-IR spectra of the Li-anode after 10 cycles; (d) high-energy XRD patterns of the Li-anode after 1 and 10 cycles.⁶² Reprinted with permission from ref. 62. Copyright 2013 Wiley-VCH Verlag GmbH & Co. KGaA.

the main products were LiOH and Li₂CO₃, which were generated through reduction and oxygen corrosion reactions in comparison to those of CH₃OLi, CH₃Li and the polymeric Li-salt layers through the direct reaction of ether and Li-metal. The possible reaction paths were also proposed in order to understand the complex reactions between ether-based electrolytes (for example, 1,2-dimethoxyethane (DME) and TEGDME) and the Li-anode under an O₂ environment. As shown in Fig. 19, the reaction between O₂ and TEGDME was proved to be no apparent barrier, inducing the cleavage of the C–O bond of the ethers to form various alkyl radicals, an hydroxide ion and aldehydes. Among these fragments, the hydroxide subsequently reacted with Li⁺ to form LiOH, while other fragments resulted in the generation of lithium alkylcarbonates or Li₂CO₃.

The electrochemical reversibility of the Li-anode in aprotic Li–O₂ batteries was also investigated through spatially and temporally resolved synchrotron X-ray diffraction, as well as by three-dimensional (3D) micro-tomography techniques (Fig. 20).⁹ It was found that a LiOH layer was formed on the Li-anode, and its thickness increased steadily during the discharge and charge processes. This resulted in a limited reversibility of the Li-anode. Nevertheless, the porous channels in the LiOH layer could maintain the transport of Li⁺ until the metallic lithium was completely consumed. The consumption of the lithium and electrolyte accelerate the premature death of Li–O₂ batteries.^{183,184}

3.2 Protection strategies for Li-metal electrodes

To overcome the problems of side reactions between reactive Li-metal and electrolyte components, as well as Li self-dendrite formation (Fig. 21a), several strategies have been proposed.¹⁸⁵ The first one was modification of the SEI layer on the Li-metal,

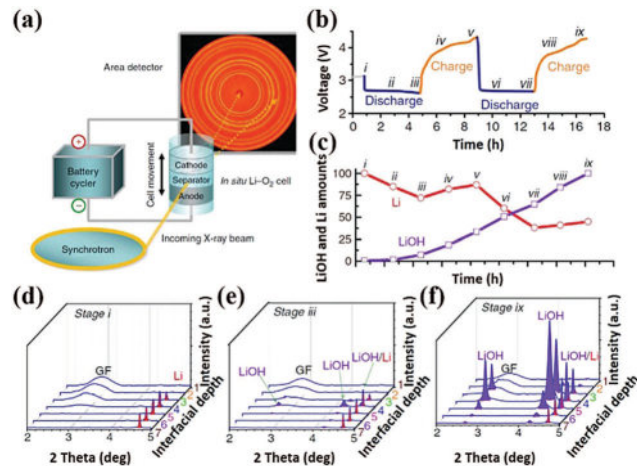


Fig. 20 (a) The experimental set-up for *in operando* μ-XRD study of a Li–O₂ battery under cycling conditions; (b) discharge–charge voltage profile of the *in operando* Li–O₂ cell as a function of cycling time (the stages at which the XRD pattern sets were collected are marked as i, ii, iii... on the curve); (c) the overall change in the amount of LiOH and Li-metal contents at the anode–separator interfacial region as a function of cycling time, individually normalized to the highest points of the respective components (the data collection positions during cycling are the same as those marked in (b)); (d–f) three representative XRD sets taken at the cycling stage i, iii and ix.⁹ Reprinted with permission from ref. 9. Copyright 2013 Nature Publishing Group.

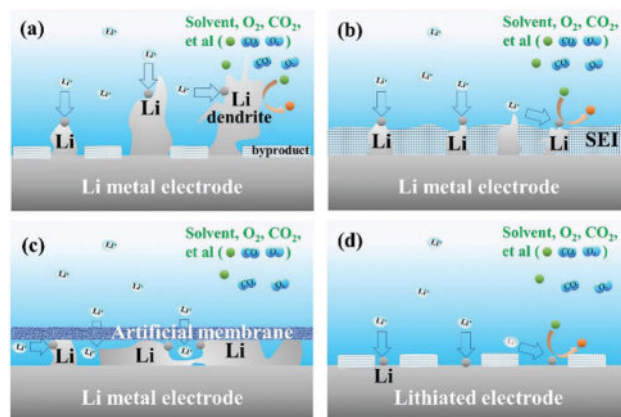


Fig. 21 Schematic illustrations of the remained issues and resolved strategies for sustainable use of Li-electrodes. (a) The dendrite formation and side reaction at Li-electrode; (b) the formation of solid–electrolyte–interface (SEI) layer; (c) insertion of artificial membrane; (d) construction of lithiated composite electrode.

aiming to prohibit Li-dendrite formation and the side reaction between Li-metal and electrolyte during cell cycling (Fig. 21b).¹⁸⁰ The second one was the preparation of an artificially protective film on the Li-metal, which was used to inhibit the side reaction and penetration of Li dendrites across the separator (Fig. 21c).^{181,186} The third one was the use of a lithiated composite or alloy anode that could avoid the formation of Li dendrite (Fig. 21d). The last one was the construction of a solid-state or quasi-solid-state electrolyte, and this part will be discussed in the electrolyte section.

3.2.1 Protection of Li-metal by a solid–electrolyte-interface layer. As aforementioned, Li-metal is thermodynamically unstable towards most organic solvents, functional additives, crossover O₂, CO₂, N₂ and so on. This leads to side reactions and the formation of an SEI layer at the Li-electrode/electrolyte interface, and induces the low Coulombic efficiency of Li-metal. As the formed SEI layer (such as Li alkyl carbonate and Li alkyl species) may not be strong enough to tolerate the rapid morphology changes of the Li-electrode, the formed Li dendrites breakthrough the SEI layer. It is therefore necessary to decrease the electrolyte reactivity or change the ingredient of the SEI layer to improve the Coulombic efficiency of Li-anode.

Having a high concentration of Li-salt in the electrolyte was proved to be an effective strategy to modify the SEI layer for improving the cyclic performance of Li-anodes.¹⁸⁸ Jeong *et al.* found that the high concentration of LiBETI (lithium bis(per-fluoroethylsulfonyl)imide, LiN(SO₂C₂F₅)₂) in the electrolyte (3.27 mol kg⁻¹ LiBETI in polycarbonate (PC)) could lead to the formation of a thick SEI layer more than that formed in a low-concentration medium (1.28 mol kg⁻¹ LiBETI in PC), suppressing Li dendritic formation to some extent. With regard to the solvents, DME was found to be less reactive than other esters and alkyl carbonates. Zhang *et al.* used 4 M LiFSI (lithium bis(fluorosulfonyl)imide, LiNF₂(SO₂)₂) in DME as an electrolyte.¹⁸⁹ As a result, a Cu|Li cell could be cycled at 4 mA cm⁻² for more than 1000 cycles with a Coulombic efficiency of 98.4%. The electrolyte stability was improved and the conciliatory Li dendrite was realized due to the formation of a highly compact and stable SEI layer. Through DFT calculations, high stability of the electrolyte was indicated by the reduced availability of reactive solvent in highly concentrated Li-salt solution, while the Li dendrite growth was due to the increase in Li⁺ concentration during the fast Li plating and stripping. Osaka *et al.* compared the Coulombic efficiency of a Li-anode covered by organic compounds and inorganic compounds (tested in Ar).⁵⁶ It was found that the SEI layer with inorganic compounds, such as Li₂CO₃, Li₂O and LiF, could induce a robust protection against side reactions from DMSO electrolyte solutions in comparison to those of an organic Li-salts-based SEI layer.

To form an inorganic SEI layer, LiNO₃ was thought to be an effective source to produce a stable SEI layer for lithium-based batteries (according to the equation: 2Li + LiNO₃ → Li₂O + LiNO₂). LiNO₃ was first used as an electrolyte additive in Li-S batteries, which was taken act as an inhibitor for blocking electron transport from the Li-anode to the soluble polysulfides released from the sulfur cathode.^{190,191} For Li-O₂ batteries, several research groups also tried to use LiNO₃ for suppressing the rapid and continuous side reactions between the electrolyte and Li-metal.^{192,193} Walker *et al.* pretreated a Li-anode in a solution of LiNO₃/DMA (*N,N*-dimethylacetamide) to form a stable SEI film, and it was found that 1 M LiNO₃ was needed to eliminate any sign of the reaction between DMA and the Li-anode.³⁸ As a result, a Li-O₂ battery with this electrolyte performed more than 80 cycles (2000 h) with only a little increase in overpotential (Fig. 22). Subsequently, J. Uddin, a co-author in

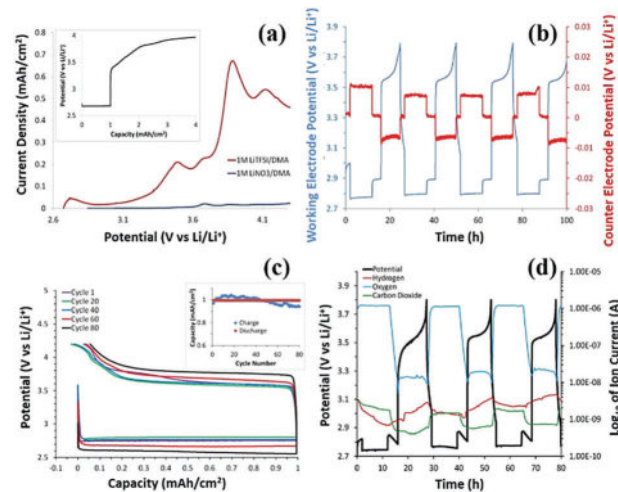


Fig. 22 (a) Linear sweep voltammograms on carbon paper electrodes (the inset was galvanostatic cycling at 0.1 mA cm⁻² of a Li-O₂ cell with 0.5 M LiTFSI/DMA electrolyte); (b) galvanostatic cycling of three-electrode cells utilizing Super-P carbon (C_{sp}) cathode, Li-anode, Li reference electrode, and 1 M LiNO₃/DMA electrolyte (the cell was cycled at a current density of 0.1 mA cm⁻² under 1 atm O₂, with a dwell at open-circuit-voltage between each half cycle); (c) voltage profiles of a Li/1 M LiNO₃-DMA/C_{sp} cell for cycles 1, 20, 40, 60, and 80 operated at 0.1 mA cm⁻² (the inset was plot of charge/discharge capacity by cycle numbers); (d) gas profile of a Li/1 M LiNO₃ DMA (150 μL)/C_{sp} cell cycled at 0.1 mA cm⁻² at room temperature.³⁸ Reprinted with permission from ref. 38. Copyright 2013 American Chemical Society.

the above work, found that LiNO₃ in the electrolyte could be regenerated through the following reactions in a succinct pattern: (1) 2Li + LiNO₃ → LiNO₂ + Li₂O; (2) 2LiNO₂ + O₂ → 2LiNO₃.¹⁹⁴ When the charging potential was beyond 3.6 V vs. Li⁺/Li, the regeneration of LiNO₃ was thermodynamic favoured. This demonstration explained the superior cyclic performance of the LiNO₃/DMA-based Li-O₂ system.

LiNO₃ was also identified as being effective for improving the cyclic stability of the Li-O₂ cell with a DMSO-based electrolyte.¹⁹³ Osaka *et al.* used a highly concentrated LiNO₃ electrolyte with DMSO solvent to produce a stable inorganic SEI film.⁵⁶ In this study, they compared the Coulombic efficiency of the Li-anode with different Li-salts (LiNO₃, LiTFSI, LiClO₄ and LiFSI), as well as the influence of Li-salt concentrations on cyclic stability of the anode. As a result, the LiNO₃-containing electrolytes achieved the highest Coulombic efficiency among the studied Li-salts owing to the presence of an inorganic SEI ingredient. Meanwhile, 4 M LiNO₃/DMSO electrolyte performed with better cyclic stability than that of an electrolyte with a low concentration of Li-salts due to the lack of free DMSO molecules. Although a Li₂O protective layer could be formed on Li-metal with the LiNO₃-containing electrolyte, a CO₂ by-product could be still detected by *in situ* mass spectrometry during the charging process.¹⁹¹ The side reaction on Li-metal cannot be totally inhibited, because Li₂O can also react with some solvents (*e.g.* DMSO), leading to degradation of the SEI stability during cell cycling.⁶³

A combination of Li-salts and other reagents could be also used to make a stable SEI layer on Li-metal for its long-term sustainability.

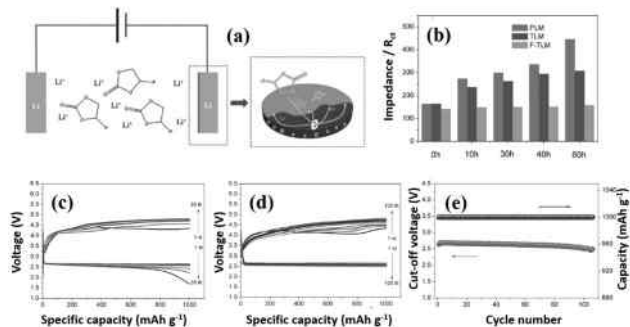


Fig. 23 (a) Schematic illustration for the formation of SEI layer on Li-anode with fluoroethylene carbonate (FEC) electrolyte using an *ex situ* electrochemical strategy; (b) time dependence of the impedance spectra values of the Li–O₂ cells with pristine Li-metal (PLM), Li-metal treated without FEC (TLM) and with FEC (F-TLM) as anode; (c) discharge–charge profiles of Li–O₂ cells with (c) PLM and (d) F-TLM anode; (e) the cycling stability of F-TLM based cell with a fixed capacity of 1000 mA h g^{−1} at a current density of 300 mA g^{−1}.¹⁸⁷ Reprinted with permission from ref. 187. Copyright 2016 Wiley-VCH Verlag GmbH & Co. KGaA.

Zhang *et al.* fabricated an artificial protective film on Li-metal in TEGDME-based electrolyte with fluoroethylene carbonate (FEC) and 1 M LiTf (lithium trifluoromethanesulfonate, LiCF₃SO₃), in which the symmetric Li/electrolyte/Li cell was cycled within a voltage window of 0–0.7 V for several times (1 mV s^{−1}).¹⁸⁷ The cycling performance of Li–O₂ batteries was significantly improved due to the lower amounts of LiOH and smoother Li surface (FEC-Li anode). No Li dendrite was formed in comparison with a battery without an FEC-treated Li-anode (Fig. 23). Choudhury *et al.* operated a Li–O₂ battery with 1 M LiNO₃-DMA electrolyte containing 2-bromoethanesulfonate (Fig. 24), which induced the *in situ* formation of an SEI layer with the lithium ethanesulfonate and soluble LiBr mediator. The as-prepared battery showed a much better cyclability than that of a cell without 2-bromoethanesulfonate. Additionally, the discharge capacity of Li–O₂ cells with 1 M LiNO₃-DMA electrolyte containing 2-bromoethanesulfonate was higher (6.5 mA h) than that of a battery with conventional electrolyte containing 1 M LiTFSI-DME (5.1 mA h) by the same cathode. This was consistent with the observation of large-sized Li₂O₂ structures owing to the solution-mediated nucleation of peroxides by LiBr.¹⁷⁹

3.2.2 Protection of Li-metal by artificial films. Except for the construction of an SEI layer, the fabrication of Li⁺-conductive film on Li-metal surface is considered to be a powerful method to inhibit dendrite issues with Li-anodes.¹⁸¹ Park *et al.* developed a composite protective layer (CPL) composed of Al₂O₃ and polyvinylidene fluoride–hexafluoropropylene (PVdF–HFP) to protect the Li-anode. Al₂O₃ was introduced to offer sufficient strength to suppress dendrite growth in the vertical direction, while PVdF–HFP facilitated the fast Li⁺ transport through CPL by forming a gel–polymer electrolyte. As shown in Fig. 25, the Li–O₂ battery maintained its interfacial resistance at its initial value with the CPL, resulting in 80 stable cycles under the discharge capacity of 1000 mA h g^{−1}. However, the cell without CPL exhibited an increased interfacial resistance, and could only be cycled 40 times at 1000 mA h g^{−1}. In this study,

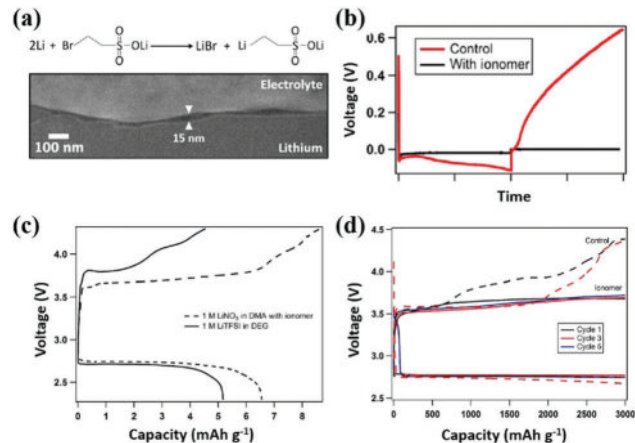


Fig. 24 (a) Schematic image for the reaction of lithium 2-bromoethanesulfonate (Li-BES) with lithium-metal forming LiBr and organometallic Li-salt (upper), and SEM image of the SEI layer between electrolyte and Li-electrode, revealed in a cross section produced by cryo-focused ion beam milling; (b) voltage profile of the Li||stainless-steel cell plotted over time (red line was the profile of control electrolyte (1 M LiNO₃-DMA), and black line was for the same electrolyte enriched with 10 wt% Li-BES); (c) voltage profile for batteries fully discharged and recharged with 1 M LiNO₃-DMA electrolyte containing Li-BES (dash line) and 1 M LiTFSI-diglyme electrolyte (solid line) at a current density of 31.25 mA cm^{−2}; (d) voltage profile of Li–O₂ batteries with a fixed capacity of 3000 mA h g^{−1} and a current density of 0.04 mA cm^{−2} (Solid lines indicated Li-BES-based electrolytes, whereas dashed lines showed the control electrolyte).¹⁷⁹ Reprinted with permission from ref. 179. Copyright 2017 American Association for the Advancement of Science.

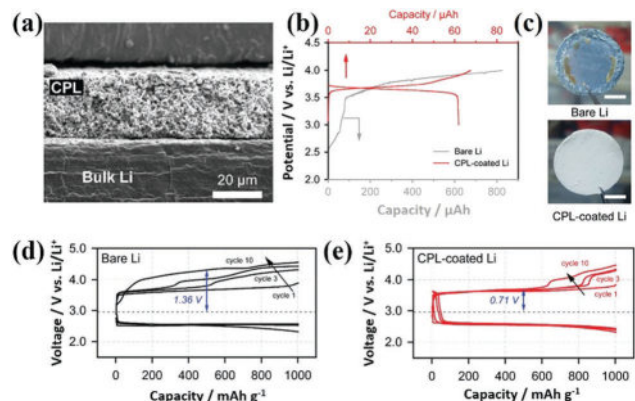


Fig. 25 (a) SEM cross-sectional image of Li-electrode coated with a composite protective layer (CPL); (b) first charge/discharge profiles of carbon paper/Li cells contained 0.05 M 2,2,6,6-tetramethylpiperidiny-1-oxyl (TEMPO) with (red line) and without (grey line) CPL at a current rate of 0.025 mA cm^{−2}; (c) digital pictures of bare Li and CPL-coated Li-electrodes after prolonged storage tests (scale bar, 5 mm); charge/discharge profiles at different cycles of 0.05 M TEMPO-containing Li–O₂ cells without (d) and with (e) CPL.¹⁸⁶ Reprinted with permission from ref. 186. Copyright 2016 Wiley-VCH Verlag GmbH & Co. KGaA.

2,2,6,6-tetramethylpiperidiny-1-oxyl (TEMPO) was used as a redox additive, and CPL (Al₂O₃–PVdF–HFP) could also inhibit the self-discharge reactions between the oxidized TEMPO and Li-metal.¹⁸⁶

Choi *et al.* introduced a poreless polyurethane (PU) separator as an effective solution to inhibit the side reactions initiated

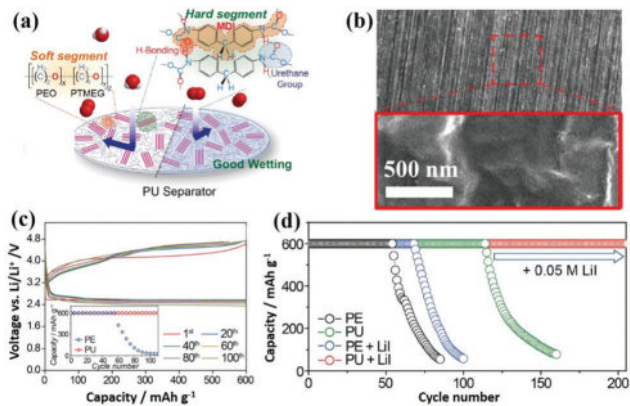


Fig. 26 (a) The molecular structure of poreless polyurethane (PU) separator; (b) SEM images of the PU separators at low (upper) and high (lower) magnifications; (c) the voltage profiles and cycling performance (inset) of the PU cell in the cycle number of 1–110 when measured at 200 mA g^{-1} with a constant capacity of 600 mA h g^{-1} ; (d) the cycling performance of the four cells (PE: polyethylene separator) when measured at a current density of 300 mA g^{-1} at a fixed capacity of 600 mA h g^{-1} .¹⁹⁵ Reprinted with permission from ref. 195. Copyright 2016 Wiley-VCH Verlag GmbH & Co. KGaA.

by moisture, oxygen and the redox mediators transported from the cathode or electrolytes in a Li–O₂ battery (Fig. 26). Despite the nonporosity of the PU membrane, it allowed for decent Li⁺-ion conductivity ($\sim 1.8 \times 10^{-4} \text{ S cm}^{-1}$), even higher than that of conventional porous polyolefin separators ($\sim 1.4 \times 10^{-4} \text{ S cm}^{-1}$), *via* the superior electrolyte uptake and retention. The cycle life of the resultant Li–O₂ battery was extended for an additional 56 cycles compared to a control cell with a porous polyethylene (PE) separator, reaching 110 cycles. Moreover, the effect of the PU separator was validated for Li-metal protection from a LiI redox mediator to extend the cycle life to more than 200 cycles, with a fixed capacity of 600 mA h g^{-1} , which was much better than the cell with the PE separator (68 cycles).¹⁹⁵

Inorganic membranes are also widely adopted to inhibit Li-dendrite formation and side reactions at the Li-electrode, which was also broadly used as the solid-electrolyte for Li–O₂ battery.⁸ Kang *et al.* employed porous anodized alumina oxide (AAO) as an interlayer between the separator and Li-anode, whereby the uniform nanopores in the AAO membrane could facilitate homogeneous plating/stripping of the ions, thus suppressing the surface roughening of metallic Li and improving its cyclic stability remarkably.¹⁹⁶ Park *et al.* designed a bilayer solid film (lithium phosphorous oxynitride/aluminium-substituted lithium lanthanum titanate) with high Li⁺ conductivity, which could prevent Li-metal reacting with the diffused O₂ and other species (such as H₂O, N₂, CO₂). This was beneficial for inhibiting the initiation and growth of Li dendrite.¹⁹⁷ Then in tests, a Li–O₂ cell with this protective layer performed 129 cycles under 1000 mA h g^{-1} . Moreover, several other types of inorganic membranes could be used as the protective layer for Li-metal, and these are presented later in the discussion in the solid-electrolyte part of this review.

3.2.3 Replacement of Li-metal by a lithiated composite.

Construction of large-capacity, lithiated, composite materials,

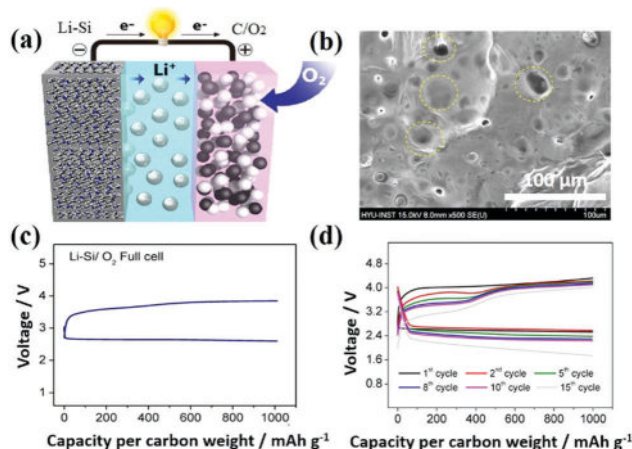


Fig. 27 (a) Schematic image of a Li_xSi–O₂ battery; (b) SEM image of the Li_xSi electrode formed by micro-sized carbon particles containing lithiated silicon particles (yellow circles); (c) voltage profile of the first galvanostatic cycle of Li_xSi–O₂ battery; (d) cyclic voltage profiles of a Li_xSi–O₂ battery with TEGDME–LiCF₃SO₃ electrolyte at 200 mA g^{-1} .⁶⁵ Reprinted with permission from ref. 65. Copyright 2012 American Chemical Society.

for example Li_xSi and Li_xAl, to substitute the metallic Li-anode was thought to be another effective protocol for inhibiting Li dendrite growth. Hassoun *et al.* reported a lithium-ion/O₂ battery for the first time with a lithiated silicon–carbon composite as the anode and Super-P carbon as the cathode. The as-prepared Li_xSi–O₂ battery exhibited similar charge–discharge profiles and overpotentials as those of a conventional Li–O₂ battery. At a fixed capacity of 1000 mA h g^{-1} (a current density of 200 mA g^{-1}), the Li_xSi–O₂ battery could perform about 15 cycles with a slight change of voltage profile (Fig. 27).⁶⁵ This design concept encouraged continuous efforts to develop feasible anodes to replace metallic Li to avoid potential safety problems. Wang *et al.* used a lithiated Al–carbon (Li_xAl–C) composite with a uniform SEI layer as the anode for aprotic Li–O₂ cells.¹⁹⁸ It was found that the Li–O₂ battery with a Li_xAl–C anode generated a lower overpotential of 1.3 V compared to the Li–O₂ battery (1.7 V). The superior performance was attributed to the combination of an SEI layer and lithiated composite, which helped alleviate O₂-attack or air-attack on the anode.

Hassoun *et al.* further fabricated a lithium-ion/O₂ battery employing a nanostructured lithium-alloy (Li_xSn–C) as the anode and an ionic liquid (*N*-butyl-*N*-methyl pyrrolidinium bis(trifluoromethanesulfonyl)imide) as the electrolyte solvent.¹⁹⁹ The battery achieved an intrinsically safer energy storage system, and showed a stable capacity of 500 mA h g^{-1} with a low charge–discharge polarization at a working voltage of 2.4 V (Fig. 28). Unfortunately, the working voltage of the battery decreased progressively, with a consequent deterioration of the cell performance, owing to the side reaction between the Li-anode and crossover O₂ from the cathode. Similarly, Sun *et al.* pointed out that the formation of LiOH at the lithiated anode scaled the loss of lithium sources and induced a decreased potential and poor cycle life of Li–O₂ cells.²⁰⁰

To prohibit the side reactions, Zhou *et al.* recently reported a long-life lithium-ion/O₂ battery with a commercial Si particles-based

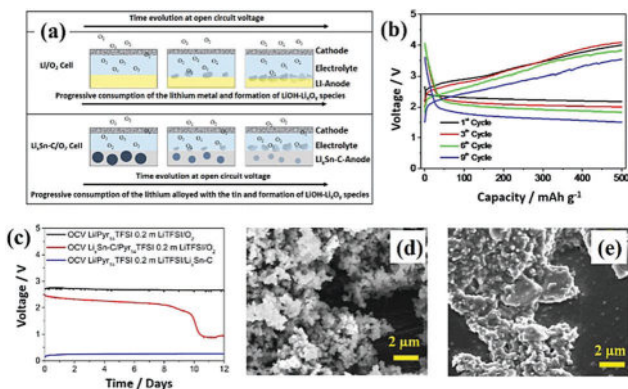


Fig. 28 (a) Schematic images of the reactions occurring at the electrode/electrolyte interphase of the Li/Py₁₄TFSI–LiTFSI/O₂ (upper) and Li_xSn–C/Py₁₄TFSI–LiTFSI/O₂ (bottom) cell in the open-circuit-voltage (OCV) condition in an O₂ atmosphere; (b) galvanostatic cycling and corresponding voltage profile of a Li_xSn–C/Py₁₄TFSI–LiTFSI/O₂ cell (current density: 50 mA g^{−1}) at fixed capacity of 500 mA h g^{−1}; (c) the evolution of OCV of a Li_xSn–C/Py₁₄TFSI–LiTFSI/O₂ cell (red), as well as Li/Py₁₄TFSI–LiTFSI/O₂ (black) and Li/Py₁₄TFSI–LiTFSI/Li_xSn–C (blue, Ar atmosphere) half-cells upon 12 days of storage; SEM micrographs of (d) Li-electrode and (e) prelithiated Sn–C-based electrode after 12 days of storage under OCV conditions (assembled in Li/Py₁₄TFSI–LiTFSI/O₂ and Li_xSn–C/Py₁₄TFSI–LiTFSI/O₂ cell configurations, respectively).¹⁹⁹ Reprinted with permission from ref. 199. Copyright 2015 American Chemical Society.

anode. The anode was protected by a stable SEI layer formed by discharging a Li/Si half-cell in an electrolyte of 1.0 M LiTFSI in FEC/TEGDME (volume ratio, 1 : 4).²⁰¹ As a result, the Li-ion/O₂ cell with this optimized anode achieved as many as 100 discharge/charge cycles with low overpotentials, owing to the combination of the lithiated composite anode and the strong resistibility of the SEI layer towards oxygen crossover effects.

3.3 Short summary and perspective for Li-electrode protection

The use of Li-metal as the anode can help realize the full potential of Li–O₂ batteries, but has limitations as metallic Li suffers from the formation of lithium dendrites and from side reactions caused by O₂, N₂, CO₂, H₂O, and electrolyte components. These issues have been addressed in a number of ways. First, utilizing the reactions between some additives and Li-metal can form a stable SEI layer on the Li-anode to partially prevent metallic Li from taking part in side reactions to some extent. Second, an artificial membrane is an effective approach to inhibit the side reactions and the penetration of Li dendrite across the separator, albeit such a membrane with high stability and Li⁺ conductivity has not been well established yet.

Similar to those in Li-ion batteries, the lithiated composite anode (such as Li_xSi and Li_xSn) with high energy density provides the opportunity to inhibit the dendrite problem as well as to reserve the anode's advantage of high specific energy. However, a decrease in Li source of the original lithiated composite and consumption of the Li source by crossover O₂ reduce the energy density and stability of batteries. More powerful strategies need to be developed to achieve an anode with a long cycle life and high Coulombic efficiency. The combination of constructing an SEI layer and the use of an artificially protective film on the

Li-anode seems to be a promising strategy to meet this standard. With regard to this strategy, it is essential to construct an artificial membrane with high stability and Li⁺-transport efficiency, and for this, some protective films in other Li-based batteries can provide some suggestions for solutions. Moreover, gel-based quasi-solid-state electrolytes with high Li⁺ transport capability may also be suitable for this purpose, which will be discussed in the following section on electrolytes.

4. Oxygen electrode

As the primary site for Li₂O₂ formation and decomposition, the oxygen electrode is the most studied component of a battery and has been the topic of numerous reviews in Li–O₂ batteries.^{13,20,202} Most of these describe the progress made in newly developed cathode materials with no clear classification. In this part, we mainly focus on the function and stability design of cathode materials and pore/surface structures towards Li₂O₂ formation and decomposition in the cell discharge/charge process.

According to the discharge mechanism for Li₂O₂ generation, O₂ electrodes have four main functions: (1) catalyzing Li₂O₂ formation and decomposition at surface active sites (Fig. 29a); (2) transporting Li⁺ and oxygen in porous channels to/from active sites (Fig. 29b); (3) supporting storage space for the Li₂O₂ product (Fig. 29c); (4) inducing growth and morphology evolution of Li₂O₂ at the electrode surface (Fig. 29d). Except for their functionality, the stability of electrode materials towards reactive oxygen species (ROS) should also be evaluated for the long-term stability of Li–O₂ batteries. For these purposes, various kinds of material characteristics, such as catalytic activity and stability, surface atomic structure, pore structures and surface adhesion capability of Li⁺ and oxygen, should be well considered.^{203,204} Since new oxygen electrodes continue to be

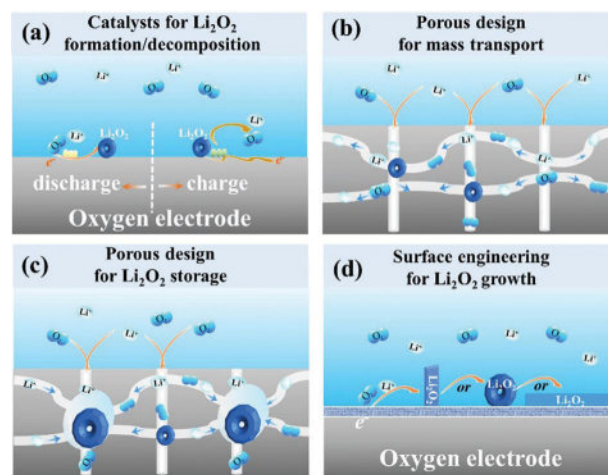


Fig. 29 Schematic illustration for the proposed functionality of the oxygen electrode for Li₂O₂ formation/decomposition. (a) Design of an efficient solid catalyst; (b) pore channel design for fast mass transport; (c) hierarchical porous structure for large Li₂O₂ storage; (d) surface engineering for the induced growth of Li₂O₂ clusters.

constructed with the development of efficient materials, we discuss their progress in terms of material types and structures.

4.1 Carbon materials

Conductive carbon is one of the most attractive cathode materials to accommodate insoluble/insulating Li_2O_2 for $\text{Li}-\text{O}_2$ batteries due to its high electronic conductivity, low mass density, low cost and the facile construction of a porous structure. The low mass density and high electrical conductivity of carbon materials is beneficial for the achievement of a large cell capacity.²⁰⁵ Moreover, the pore structure of carbon electrodes can be easily modulated with the existing techniques, which promote the transport efficiency of Li^+ and oxygen in the channels and support the storage space for Li_2O_2 . Additionally, the electronic structure of carbon materials can be tuned by heteroatom-doping, which is utilized to form the effective active sites for catalyzing the formation and decomposition of Li_2O_2 .⁷⁰ Thanks to these excellent properties, carbon materials are also widely used as a support to exemplify the functionality of other advanced catalysts.^{53,54,206–208} Table 2 summarizes some of the typical carbon materials for $\text{Li}-\text{O}_2$ batteries, while the pore structure, graphitization degree and heteroatom-doping of carbon are highlighted for their functionality and stability.

4.1.1 Carbon structures with good mass transport and Li_2O_2 storage. The pore structure is one of the most important factors to determine the cell capacity of $\text{Li}-\text{O}_2$ batteries. A high pore volume and surface area of the cathode are beneficial for accommodating a large amount of Li_2O_2 product, and providing efficient channels for the transport of Li^+ and oxygen to surface active sites.²⁰⁹ Zhang *et al.* compared the electrochemical performance of $\text{Li}-\text{O}_2$ batteries with several commercial carbon-powder-based cathodes²¹⁰ and found that the pore volume of carbon played an important role in affecting the specific capacity of $\text{Li}-\text{O}_2$ batteries. Ketjenblack (KB) carbon showed the highest pore volume among KB carbon ($7.65 \text{ cm}^3 \text{ g}^{-1}$), ball-milled KB ($0.43 \text{ cm}^3 \text{ g}^{-1}$), BP2000 ($0.84 \text{ cm}^3 \text{ g}^{-1}$), Calgon ($0.55 \text{ cm}^3 \text{ g}^{-1}$), Denda black ($0.54 \text{ cm}^3 \text{ g}^{-1}$) and JMC ($0.24 \text{ cm}^3 \text{ g}^{-1}$), and the corresponding cell showed the best cell capacity. Simultaneously, Hall *et al.* controllably prepared a series of porous carbon aero-gels with different pore volumes for cathode materials.²¹¹ Their results indicated that a larger pore volume provides more space for the formation and storage of Li_2O_2 in the discharge process, and further delivers a higher battery capacity.

Comparably, Zhang *et al.* investigated the effect of the pore-size distribution and pore volume of commercial KB and Super-P carbon on the cell capacity.²¹² Although KB possessed a much higher specific surface area ($1379 \text{ m}^2 \text{ g}^{-1}$) and ten times larger pore volume ($2.61 \text{ m}^3 \text{ g}^{-1}$) than those of Super-P ($54 \text{ m}^2 \text{ g}^{-1}$, $0.23 \text{ m}^3 \text{ g}^{-1}$), the difference in delivered specific capacity was much less (1005 mA h g^{-1} for KB, 635 mA h g^{-1} for Super-P). This indicated that the relationship between the pore volume and the cell capacity could be not simply deduced.

Moreover, the cyclability of $\text{Li}-\text{O}_2$ battery was also influenced by the pore structure. Wang *et al.* constructed porous graphene cathodes with different pore sizes *via* a hard template method (Fig. 30).⁷⁰

Table 2 Performance summary of $\text{Li}-\text{O}_2$ battery with carbon-based electrodes and their operating conditions

Carbon category	Specific design	Discharge voltage (V)	Charge voltage (V)	Limited capacity/ cycles (mA h g^{-1} / times)	Mass and current density ($\text{mg cm}^{-2}/\text{mA g}^{-1}$)	Full discharge capacity (mA h g^{-1})	Electrolyte	Ref.
Pore structure	Porous graphene (250 nm, PG-250)	$\sim 2.70_{\text{PG-250}}^a$ (vs. $\sim 2.65_{\text{nonporous rGO}}^d$)	$\sim 4.30_{\text{PG-250}}^a$ (vs. $\sim 4.50_{\text{nonporous rGO}}^d$)	$500_{\text{PG-250}/20}$ (vs. $500_{\text{nonporous rGO}/10}$)	0.5/200	$\sim 29\,000_{\text{PG-250}}$ (vs. $\sim 8000_{\text{nonporous rGO}}$)	0.1 M LiClO_4 in DMSO	70
	3D mesoporous C (diameter: 35 nm, 3DMC-35)	$\sim 2.80_{\text{3DMC-35}}^d$ (vs. $\sim 2.80_{\text{3DMC-12}}^f$)	$\sim 4.00_{\text{3DMC-35}}^g$ (vs. $\sim 3.30_{\text{3DMC-12}}^f$)	$500_{\text{3DMC-35}/16}$ (vs. $500_{\text{3DMC-12}/6}$)	0.5–1/100	$\sim 65\,000_{\text{3DMC-35}}$	1.0 M LiClO_4 in TEGDME	79
Graphitization degree	Porous C nanocube (diameter: 50 nm, MCC)	$\sim 2.75_{\text{MCC}}^a$ (vs. $\sim 2.75_{\text{CB}}^b$)	$\sim 3.80_{\text{MCC}}^a$ (vs. $\sim 4.20_{\text{CB}}^b$)	$1000_{\text{MCC}/20}$	0.5/200	$\sim 26\,000_{\text{MCC}}$ (vs. $\sim 6000_{\text{CB}}$)	1.0 M LiNO_3 in DMAC	213
	Porous graphene (900 °C/6 h, VTEG-HT)	$\sim 2.70_{\text{VTEG-HT}}^a$ (vs. $\sim 2.75_{\text{VTEG}}^g$)	$\sim 4.20_{\text{VTEG-HT}}^b$ (vs. $\sim 4.50_{\text{VTEG}}^h$)	$1000_{\text{VTEG-HT}/50}$ (vs. $1000_{\text{VTEG}/5}$)	0.25/300	$\sim 19\,800_{\text{VTEG-HT}}$ (vs. $\sim 13\,700_{\text{VTEG}}$)	0.1 M LiClO_4 in DMSO	221
	Graphene nanoplates (GNP)/GO film	$\sim 2.75_{\text{GNP+GO}}^a$ (vs. $\sim 2.6_{\text{rGO}}^d$)	$\sim 4.40_{\text{GNP+GO}}^a$ (vs. $\sim 4.40_{\text{GNP+GO}}^a$)	$1000_{\text{GNP+GO}/16}$	—/200	$\sim 7000_{\text{GNP+GO}}$ (vs. 600_{rGO})	1.0 M LiNO_3 in DMAC	231
	MWNT paper	$\sim 2.60_{\text{MWNT}}^a$	$\sim 4.20_{\text{MWNT}}^a$	$1000_{\text{MWNT}/50}$	—/250	$\sim 34\,600_{\text{MWNT}}$	1.0 M LiNO_3 in DMAC	235
Heteroatom doping	Vertically aligned N/C nanofiber (VA-NCCF)	$\sim 2.80_{\text{VA-NCCF}}^b$ (vs. $\sim 2.70_{\text{CNT-powder}}^b$)	$\sim 3.30_{\text{VA-NCCF}}^b$ (vs. $\sim 3.70_{\text{CNT-powder}}^b$)	$1000_{\text{VA-NCCF}/150}$	0.02/500	$\sim 40\,000_{\text{VA-NCCF}}$	1.0 M LiTFSI in TEGDME	90
	N-Doped graphene/CNT (NGC-CNT)	$\sim 2.75_{\text{NGC-CNT}}$	$\sim 3.70_{\text{NGC-CNT}}$	$1000_{\text{NGC-CNT}/>400}$	0.3/500	$>8500_{\text{NGC-CNT}}$	1.0 M LiTFSI in TEGDME	89
	B-Doped KB carbon (B-KB)	$\sim 2.75_{\text{B-KB}}^b$ (vs. $\sim 2.75_{\text{KB}}^b$)	$\sim 3.90_{\text{B-KB}}^b$ (vs. $\sim 4.10_{\text{KB}}^b$)	$600_{\text{B-KB}/23}$ (vs. $600_{\text{KB}/6}$)	0.1 mA cm^{-2}	$7200_{\text{B-KB}}$ (vs. 3200_{KB})	1.0 M LiTFSI in TEGDME	245

Notes: ^a The full discharge/charge voltages at the half of full capacity. ^b The discharge/charge voltages at the half of limited capacity.

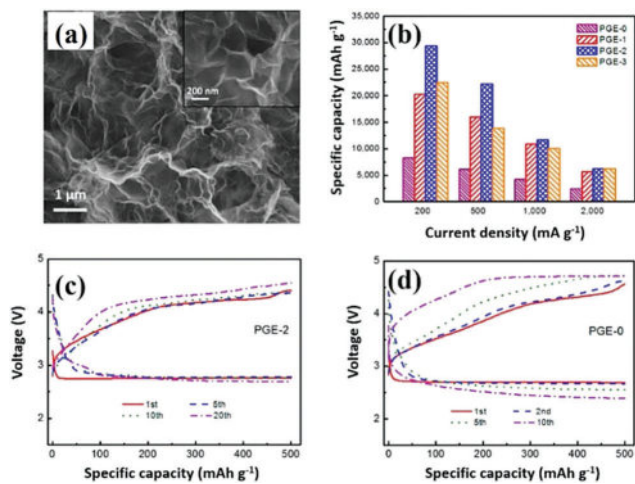


Fig. 30 (a) SEM image of porous graphene (PGE) materials; (b) the discharge specific capacities of Li–O₂ batteries for PGE electrodes with various pore sizes at different current densities; cycling performance of Li–O₂ batteries based on (c) PGE-2 and (d) PGE-0 cathode materials (at a curtailing capacity of 500 mA h g⁻¹ with a current density of 200 mA g⁻¹). (PGE-0: nonporous graphene, PGE-1: pore size about 60 nm, PGE-2: pore size about 250 nm, PGE-3: pore size about 200 nm wide and 400 nm long).⁷⁰ Reprinted with permission from ref. 70. Copyright 2014 American Chemical Society.

They found that all of the porous graphene cathodes displayed a better capacity retention compared to the nonporous graphene during the primary several cycles with the voltage ranging from 2.0 to 4.6 V at 500 mA g⁻¹. The graphene electrode with a pore diameter around 250 nm showed a higher discharge capacity compared to those of graphene with smaller pores (about 60 nm) and larger pores (about 400 nm). The capacity decay during cycling was caused by the volume change in the cathode, which might result from the build-up of excessive Li₂O₂ over the depth of discharge process. This led to a collapse of the cathode architecture. When the discharge capacity was decreased to 500 mA h g⁻¹, the charge/discharge overpotentials of the nonporous graphene electrode were significantly increased at the 10th cycle. In contrast, porous graphene electrodes showed good cycling stability in the initial 20 cycles, demonstrating that the porous structure was one of the most important factors affecting the cell cycling stability.

Wang *et al.* reported a mesoporous carbon nanocubes (MCCs) architecture with main pore sizes of about 50 and 100 nm (Fig. 31), resulting in a good ability for oxygen diffusion and electrolyte impregnation throughout the electrode. This porous structure was also effective for providing sufficient spaces to accommodate the insoluble discharge products.²¹³ Consequently, the cell delivered a high specific capacity of 26 100 mA h g⁻¹ at 200 mA g⁻¹, and operated over 20 cycles steady under a curtailing capacity of 1000 mA h g⁻¹. The positive effect of the pore structure on the cell cyclability was also proved by the construction of three-dimensionally ordered mesoporous (3DOM) carbon cathode by Wang's group, where the discharge current rate was as high as 500 mA h g⁻¹.⁷⁹ As shown in Fig. 32, the 3DOM carbon with a pore diameter of 35 nm could perform

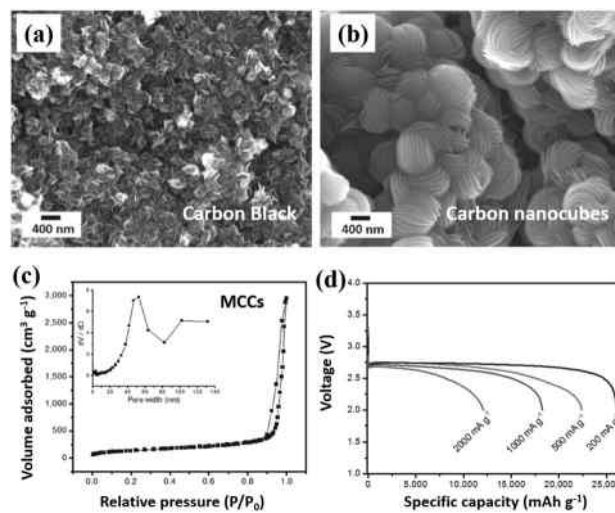


Fig. 31 SEM image of Li₂O₂ particles on the first discharged carbon black (a) and mesoporous carbon nanocubes (MCCs) (b) electrodes with LiClO₄/DMSO electrolyte; (c) the N₂ adsorption/desorption isotherms and pore size distribution of MCCs; (d) discharge curves of Li–O₂ cells with MCC catalysts at different current densities in LiClO₄/DMSO electrolyte.²¹³ Reprinted with permission from ref. 213. Copyright 2015 Wiley-VCH Verlag GmbH & Co. KGaA.

16 cycles at a capacity of 500 mA h g⁻¹, while 3DOM carbon with a pore diameter of 12 nm could only achieve 6 cycles. The cell cyclability was confirmed to be related to the pore size of the carbon; whereby smaller pores with a greater surface-to-volume ratio were more easily clogged than bigger pores. Wang *et al.* developed a kind of ordered hierarchical meso-/macroporous carbon, and the cathode with this carbon achieved 30 cycles without any change in the charge–discharge profiles at the limited capacity of 1000 mA h g⁻¹.²¹⁴ This good performance was ascribed to the sufficient and effective cathode space for O₂ diffusion and Li₂O₂ storage. The composite porous structure composed of abundant mesopores and macropores benefited the storage of Li₂O₂ and the transport of oxygen, and then prolonged the discharge time of the battery. In particular, the large-sized pores were less filled with Li₂O₂ compared to the small-sized pores under the constant capacity mode. This resulted in less resistance and a better structure stability of the cathode, as well as a large cell capacity and superior cyclability.

4.1.2 Carbon materials with good stability. Although porous carbon materials have shown advantages for the construction of Li–O₂ batteries, they usually suffer from decomposition problems, especially those of amorphous carbon, such as KB, Super-P and XC-72.^{210,212,215} These were proved to be riddled with dangling bonds and oxygen-containing surface groups. Consequently, they exhibit poor cyclability when used in Li–O₂ batteries^{100,216,217} as the generated reactive species during battery operation could corrode the carbon electrode, and some of the by-products of this are deposited at the carbon-electrode/Li₂O₂ interfaces.^{36,218} This substantially decreases the cell performance and sustainability. Luntz *et al.* presented theoretical evidence showing that a ~1 monolayer carbonate layer at

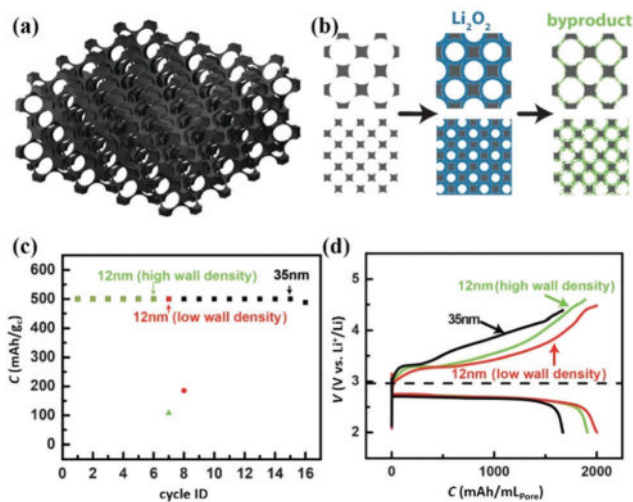


Fig. 32 (a) Schematic images for the structure model of three-dimensionally ordered mesoporous (3DOM) carbon with only the large pores; (b) the simplified 2D representation of the formation and accumulation of by-products on 3DOM carbon with large (top) and small pores (bottom), images show pristine carbon (left), carbon with the Li_2O_2 discharge product (middle), and the product after recharge (right), where green deposits represented by-products that could not be easily decomposed; (c) cycling performance of bare 3DOM carbon with different pore sizes (3DOM carbon with 35 nm pores (black), 12 nm pores with high (green) and low (red) wall densities); (d) discharge/charge profiles normalized to pore volumes with the constrained discharge potential over 2 V vs. Li^+/Li .⁷⁹ Reprinted with permission from ref. 79. Copyright 2015 Wiley-VCH Verlag GmbH & Co. KGaA.

the C- Li_2O_2 interface causes an approximate 10–100 fold decrease in the exchange current density due to the enhanced interfacial resistance.²¹⁹ The accumulation of Li_2CO_3 by-products on the carbon electrode leads to electrode passivation, resulting in a rapid polarization on charging and cell capacity fading on cycling.

Bruce *et al.* found that hydrophilic carbon was less stable and more reactive with superoxide species in the electrolyte compared to hydrophobic carbon.³⁶ This was due to the enrichment of hydrophilic groups on the carbon surface. Additionally, Zhang's group reported that Li_2O_2 preferred to nucleate and grow on the near functionalized lattice defect sites of graphene sheets with functional groups, which they proved by DFT calculations.²²⁰ Therefore, the graphitization degree and the surface functional groups of carbon materials have a strong relationship with the stability of a battery.

Reduced graphene oxide (rGO), which has enriched surface functional groups, is a suitable carbon material to investigate the relationship between the graphitization degree and the stability of battery.^{220–222} Norby *et al.* reported that the content of C(O)O and C=O species increased with the prolonged oxidation time, and this chemical trend in GO could extend to rGO.²²³ When rGO with long-time oxidation was employed as the cathode material for a Li- O_2 battery, it exhibited a higher capacity (11 038 mA h g^{-1}) than that with short-time reduction rGO (6947 mA h g^{-1}). This phenomenon was due to the enriched Li_2O_2 nucleation sites on the long-time oxidated rGO, which was consistent with the DFT results obtained by

Zhang's group.²²⁰ However, the excessive defects could induce parasitic reactions to a large extent, leading to a limited cell cycle life.³⁶ This demonstrates that a decrease in the oxygen-containing functional groups on the carbon surface can improve the cycling stability of Li- O_2 batteries. This concept was further proved by Zhou's group. Here, they reduced the C-O species in a GO material by pretreating the GO at 900 °C under vacuum conditions, whereby the C=O and COOH groups were hardly detected on the rGO surface.²²¹ An as-prepared battery could steadily cycle 50 times at 1000 mA h g^{-1} , with the superior performance of the battery attributed to the reduced surface defects of rGO and the formed porous structure during the synthesis process.

The cycle stability of a battery can be further improved by avoiding the use of a polymer binder, which was proved could be degraded by reactive oxygen species.^{224–230} In this vein, Kang *et al.* developed a paper-like graphene nanoplates/GO film as an oxygen cathode for a Li- O_2 battery. It delivered 10 000 mA h g^{-1} at the current of 100 mA g^{-1} and could be cycled 16 times under 1000 mA h g^{-1} .²³¹ Kang *et al.* also developed porous graphene paper by using the vacuum filtration of a homogeneously mixed aqueous dispersion of a GO and polystyrene colloidal particles template, followed by a heat-treatment process at 1000 °C in a 5% H_2/N_2 atmosphere.²³² The cell discharge capacity with the freestanding electrode was over 12 000 mA h g^{-1} , and the device was shown to be stable for more than 90 stable cycles at 500 mA g^{-1} under 1000 mA h g^{-1} . Compared to the original carbon electrode, the much improved device performance of the freestanding graphene electrode could be attributed to the binder-free property and the reduced surface functional groups after the heat treatment, thus reducing the possibility of side reactions.

CNTs, a kind of carbon with a high graphitization degree, high electrical conductivity and an interconnected porous structure, were believed to be one of the most stable cathode materials for Li- O_2 batteries.^{233,234} Consequently, Kang *et al.* fabricated a freestanding MWCNT fibril, which was drawn from the side wall of MWCNT forests *via* a dry-state spinning process.⁴⁰ As shown in Fig. 33, this MWCNT fibril was perpendicularly stacked on a nickel mesh. The battery made with this fibril cathode showed an enhanced rate capability (stable cycle over 10 times at 2 A g^{-1} when discharged to 2 V) and superior reversibility (60 cycles with the capacity of 1000 mA h g^{-1} at 2 A g^{-1} (note, a relatively high current density)). Zhou *et al.* also presented MWCNT paper with a 3D porous structure. The battery showed a huge specific capacity of 34 600 mA h g^{-1} , and a profile of 50 cycles of continuous discharge/charge with a cut-off capacity of 1000 mA h g^{-1} .²³⁵ The above-mentioned results indicate that carbon materials with a high graphitization degree can reduce the side reactions at the carbon/ Li_2O_2 interface, and thus enhance the battery cycle ability. However, one of the limitations of pure carbon electrodes is their low catalytic activity for cathodic reactions.¹⁶³

4.1.3 Carbon materials with good catalytic activity

4.1.3.1 Nitrogen-doped carbon. Although graphene and CNT have exhibited great potential as cathode materials for

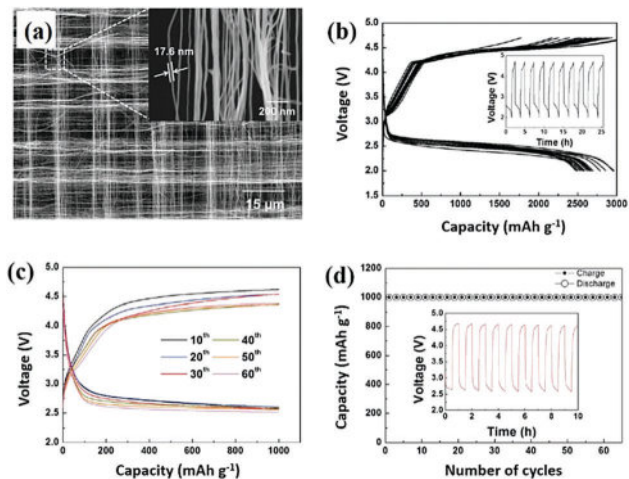


Fig. 33 (a) SEM images of the MWCNT fibril electrode; (b) discharge/charge profiles of the Li–O₂ cells using MWCNT fibril electrodes for 20 cycles at a current rate of 2 A g⁻¹; (c) discharge/charge profiles and (d) cyclability of Li–O₂ cells using an MWCNT fibril electrode at a current rate of 2 A g⁻¹ (inset: voltage vs. time graph of initial 10 cycles).⁴⁰ Reprinted with permission from ref. 40. Copyright 2013 Wiley-VCH Verlag GmbH & Co. KGaA.

Li–O₂ batteries, their catalytic activity towards Li₂O₂ formation/decomposition is relatively low. Heteroatom-doped carbon materials have shown much better catalytic activity due to their tuneable electronic structure compared to pure carbon materials.²³⁶ They have already been demonstrated as efficient four-electron-transfer ORR and OER catalysts in aqueous media.²³⁷ Following along with this idea, they were investigated as cathode catalysts for aprotic Li–O₂ battery.^{67,89,238,239}

Su *et al.* synthesized a mesoporous onion-like carbon (OLC) with and without nitrogen-doping.¹⁰⁸ The cell with the N-OLC electrode exhibited a much improved rate capability and cycle stability (an overpotential of 0.80 V for the 1st cycle and 1.16 V for the 194th cycle) in comparison to the OLC electrode (an overpotential of 1.19 V for the 1st cycle and 1.60 V for the 87th cycle) with a discharge capacity of 1000 mA h g⁻¹ at a current of 0.3 mA cm⁻². These results indicated that the formation of amorphous film-like Li₂O₂ induced by N-OLC was the key factor for the enhancement of the cyclability.

The battery performance could be further improved by modulating the porous structure of N-doped carbon materials for better mass transport and Li₂O₂ storage. Qiu *et al.* reported 3D porous N-doped graphene aero-gel frameworks constructed by interconnecting porous nanocages with the aid of a polystyrene sphere@polydopamine precursor.²⁴⁰ The Li–O₂ battery exhibited a superior rate capability (5978 mA h g⁻¹ at 3.2 A g⁻¹) and cycle stability (70 cycles under 500 mA h g⁻¹ at 300 mA g⁻¹), while the carbon electrode without N-doping could only perform 32 cycles under the same conditions. Zhou *et al.* prepared a hierarchical N-doped carbon material with both a macro-/mesoporous structure as cathodes for Li–O₂ batteries, and the cell showed superior stable cyclability over 160 cycles (600 mA h g⁻¹ at 100 mA g⁻¹).²⁴¹ The improved catalytic performance was investigated with DFT calculations. It was found that the lithiated pyridinic-N provided for excellent O₂ adsorption and

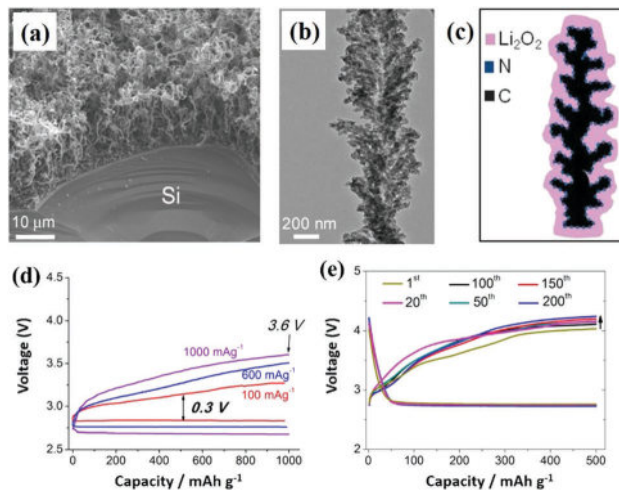


Fig. 34 (a) SEM images of vertically aligned nitrogen-doped coral-like carbon nanofibre (VA-NCCF) array grown on Si wafer; (b) TEM image of an individual VA-NCCF; (c) sketch of Li₂O₂ grown on a coral-like carbon fibre, which tightly holds Li₂O₂ deposited on the rugged VA-NCCF surface; (d) rate capability of VA-NCCF electrode at current densities of 0.1, 0.6 and 1 A g⁻¹; (e) representative discharge/charge curves from the 1st to the 200th cycle (current density: 250 mA g⁻¹, fixed capacity: 500 mA h g⁻¹).⁹⁰ Reprinted with permission from ref. 90. Copyright 2014 American Chemical Society.

activation sites for ORR, while the sites were also beneficial for stabilizing the carbon atom in the discharge process.

Excellent mass transport and Li₂O₂ storage could be realized by using the vertically aligned nitrogen-doped coral-like carbon nanofibre (VA-NCCF) array as the cathode for a non-aqueous Li–O₂ battery (Fig. 34), exhibiting an energy efficiency as high as 90% and a narrow voltage gap of 0.3 V between the discharge and charge plateaus (1000 mA h g⁻¹ at 100 mA g⁻¹), as well as excellent cycle stability over 200 cycles at (500 mA h g⁻¹ at 250 mA g⁻¹).⁹⁰ This outstanding performance was attributed to its high catalytic activity induced by N-doping, optimized oxygen/electron transportation capability and the microporous structure for Li₂O₂ storage in the stainless steel substrate.

4.1.3.2 Other heteroatom-doped carbon. Except for nitrogen, sulfur has also been used as a dopant to modulate the electronic structure of carbon materials, and was investigated as a cathode material for a Li–O₂ battery.²⁴² Chen *et al.* compared the performance of batteries with N-doped and S-doped nanoporous graphene. The N-doped graphene electrode showed better catalytic activity compared to an S-doped graphene electrode, and a double cell capacity was achieved, as shown in Fig. 35. The S-doped graphene could achieve 300 cycles under 1000 mA h g⁻¹ at 300 mA g⁻¹, while the N-doped graphene could only perform 100 cycles under the same conditions.¹⁰⁷ The reason for this was identified as being due to the –C–S–C– and –C=S– structures in S-doped graphene being more stable than the –C–N– in N-doped graphene under electrochemical conditions. The stability of the active sites (related with the doped elements) corresponded to the degeneration rate of the cathode during cycling.

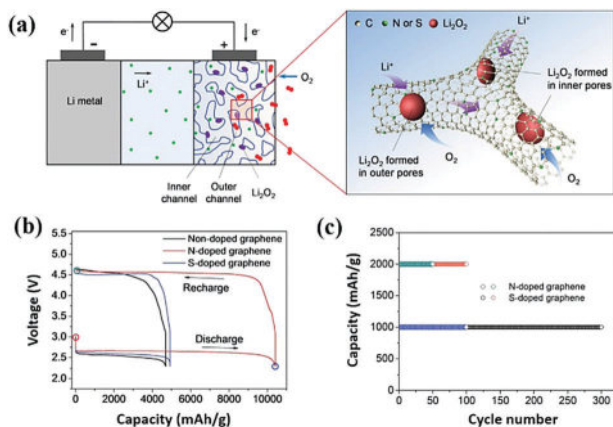


Fig. 35 (a) Schematic representation of nanoporous graphene-based Li–O₂ battery (the high-porosity electrode with heteroatom-doped graphene surfaces and interconnected open pore channels was structurally optimal for the Li–O₂ reactions); (b) discharge–charge profiles of Li–O₂ cells using the nanoporous graphene electrode (the cells were tested at 2.3–4.6 V with a current density of 200 mA g⁻¹); (c) cycling stability of the nanoporous N- and S-doped graphene-based Li–O₂ cells (the electrolyte was 1.0 M LiTFSI/TEGDME).¹⁰⁷ Reprinted with permission from ref. 107. Copyright 2016 Wiley-VCH Verlag GmbH & Co. KGaA.

Several groups calculated the catalytic activity of heteroatom-doped carbon *via* DFT.^{50,88,243–245} Zhou *et al.* investigated ORR and the initial Li₂O₂ nucleation processes on the surface of pristine and N-doped graphene in Li–O₂ batteries. They reported that the in-plane pyridinic-N-doped graphene was more effective for facilitating the nucleation of Li₂O₂ clusters than pristine or graphitic N-doped graphene. This was due to the significant electron transfer from Li₂O₂ to the pyridinic-N sites.⁸⁸ Liu *et al.* systematically investigated X-doped graphene (X = B, N, Al, Si and P) materials as a cathode for Li–O₂ batteries. P-Doped graphene exhibited the highest catalytic activity in reducing the cell charge voltage by 0.25 V, while B-doped graphene had the highest catalytic activity in decreasing the oxygen evolution barrier by 0.12 eV. By combining the two catalytic effects of B- and P-doping, B,P-codoped graphene was demonstrated to have an enhanced catalytic activity in reducing the O₂ evolution barrier by 0.70 eV and the charge voltage by 0.13 V.⁵⁰

Zhao *et al.* performed a first-principles study of graphene, N- and B-doped graphene, and N- and B-codoped graphene as the potential catalysts in non-aqueous Li–O₂ batteries (Fig. 36).²⁴³ As a result, B-doped graphene exhibited the lowest discharge and charge overpotentials in aprotic Li–O₂ batteries. Simultaneously, they found that the codoping of N and B atoms did not enhance the ORR/OER in the presence of lithium atoms, indicating that the synergistic effect in the presence of protons does not occur. The theoretical calculation results confirmed the high catalytic activity of B-doped and B/P-codoped graphene in Li–O₂ batteries.

From these above-mentioned results, it is clear that carbon materials with a high graphitization degree and hierarchical porous structures can achieve better cell performance and prolonged cell cycling life (for example, N-doped porous graphene/CNT

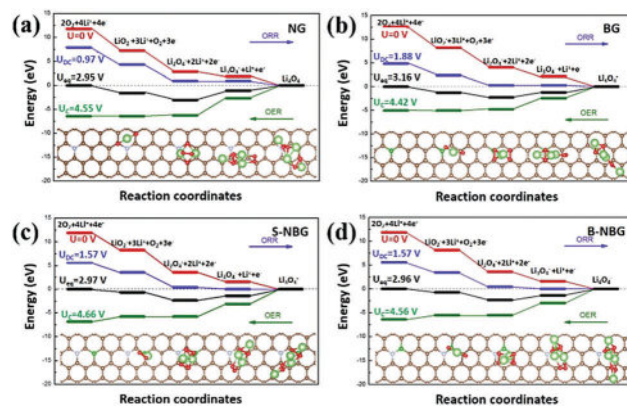


Fig. 36 Free energy diagram of ORR/OER process with the most stable structure of intermediates on (a) nitrogen-doped graphene (NG), (b) boron-doped graphene (BG), (c) separated nitrogen-/boron-doped graphene (S-NBG) and (d) bonded nitrogen-/boron-doped graphene (B-NBG) (the brown, blue, dark green, light green and red spheres indicate C, N, B, Li and O atoms, respectively).²⁴³ Reprinted with permission from ref. 243. Copyright 2016 American Chemical Society.

composites, 3D macro-/mesoporous carbon). However, the carbon materials tend to be quickly oxidized at a charging potential over 3.5 V vs. Li/Li⁺. If the charging potentials could be further reduced through optimizing the cathode catalysts or through the use of electrolyte additives, they would hold great promise for practical implementation in high-performance rechargeable Li–O₂ batteries.

4.2 Precious metal-based catalysts

Noble metal and noble metal oxides, such as Au, Pt, Pd, Ru, RuO₂ and IrO₂, have been investigated as ORR and OER catalysts in Li–O₂ batteries.^{246,247} The previous studies already reveal that most precious-metal-based catalysts are effective for the formation and decomposition of Li₂O₂ products, and Table 3 summarizes some of the typical precious metal materials used for Li–O₂ batteries to date. It can be seen that the performance and stability of precious-metal-based cathodes can be improved through changing the catalyst support and by optimization of the porous structure.²⁴⁸ However, they are not only used for their good catalytic activity, some precious metals or metal oxides, for example monolayer RuO₂ and Ir, have also demonstrated special functionality for the induced growth of crystalline Li₂O₂ or LiO₂.⁸⁰ These are beneficial for decreasing the cell overpotentials and increasing the cell capacity from the viewpoint of the crystal growth sites. In this part, we discuss the above-mentioned characteristics to elucidate the functionality and stability of precious-metal-based cathodes.

4.2.1 Au catalyst. Bruce *et al.* fabricated a 3D nanoporous Au electrode as the cathode of a Li–O₂ battery with a DMSO-based electrolyte. This showed a 95% capacity retention after cycling 100 times with an overpotential of less than 1 V and a discharge capacity of 300 mA h g⁻¹ at 500 mA g⁻¹.²⁴⁹ It was demonstrated that the kinetics of Li₂O₂ oxidation on charging was approximately one order of magnitude faster than on carbon electrodes. Chen *et al.* further developed bi-continuous

Table 3 Performance summary of Li–O₂ batteries with noble-metal-based electrodes and their operating conditions

Metal category	Specific design	Discharge voltage (V)	Charge voltage (V)	Limited capacity/ cycles (mA h g ⁻¹ / times)	Mass and current density (mg cm ⁻² /mA h g ⁻¹)	Full discharge capacity (mA h g ⁻¹)	Electrolyte	Ref.
Au	3D nanoporous Au	~2.60 ^b	~3.40 ^b	320 _{Au} /100	0.15–5.0/500 _{Au}	~320 _{Au}	0.1 M LiClO ₄ in DMSO	249
	Au crystal with high-index (441)	~2.75 ^{a,b} (vs. ~2.65 _{Super P} ^{a,b})	~3.65 ^a , ~3.70 ^b (vs. ~4.20 ^a , ~4.30 _{Super P} ^b)	1000 _C /30	1.0/200 _C , 100 _C ^b	~20 300 _C	1.0 M LiNO ₃ in DMSO	251
	Porous AuNi/NPNI/NiFM	~2.70 ^a	~3.30 ^a (vs. ~3.45 _{Au/NPNI} ^a)	1000 _{Au} /286 (vs. 1000 _{Au/NPNI} /115)	0.1 _{Au} /1000 _{AuNi}	~22 500 _{AuNi}	1.0 M LiTFSI in TEGDME	84
Pt and Pd	Pt/CNT fibril	~2.55 ^a	~3.85 ^a (vs. ~4.30 _{CNT fibril} ^a)	1000 _{Pt+C} /130	0.03/2000 _{Pt+C}	~2500 _{Pt+C}	1.0 M LiPF ₆ in TEGDME	208
	Pd/C(Al ₂ O ₃ coated)	~2.70 ^a	~3.20 ^a (vs. ~4.20 _{Super P} ^a)	500 _{Pt+C} / > 10	—/100 _{Pt+C}	~2750 _{Pt+C}	1.0 M LiCF ₃ SO ₃ in TEGDME	55
	Pd/MnO _x -GeO _y	~2.70 ^{a,b} (vs. ~2.60 _{MnO_x-GeO_y} ^{a,b})	~3.20 ^{a,b} (vs. ~4.25 ^a , ~4.35 _{MnO_x-GeO_y} ^b)	1000 _C /160	0.3/300 _C , 200 _C ^b	~7300 _C	1.0 M LiCF ₃ SO ₃ in TEGDME	257
RuO ₂	Core-shell RuO ₂ /CNTs	~2.75 ^b (vs. ~2.65 _{CNT} ^b)	~3.50 ^b (vs. ~4.40 _{CNT} ^b)	300 _{RuO₂+C} /100	1.0/100 _{RuO₂+C}	~4500 _C	LiTFSI: G3 = 1:5 in TEGDME	264
	RuO ₂ /MWCNTs	~2.75 ^{a,b}	~3.50 ^a (vs. ~4.60 _{CNT} ^a)	1000 _{RuO₂+CNT} /171 (vs. 1000 _{CNT} /10)	0.6/500 ^a , 100 _{RuO₂+C} ^b	~29 900 _{RuO₂+C}	1.0 M LiCF ₃ SO ₃ in TEGDME	83
	RuO ₂ /Mn ₂ O ₃ tube in tube	~2.60 ^b (vs. ~2.50 _{KB} ^b)	~4.250 ^b (vs. ~4.35 _{KB} ^b)	1000 _C -catalyst/120 (vs. 1000 _{KB} /20)	0.5/200 _C -catalyst	~2000 _C -catalyst	1.0 M LiTFSI in TEGDME	271
Ag and Ir	Ag ₁₅ clusters/C (Al ₂ O ₃ coated)	~2.70 ^a	~3.65 ^a (vs. ~4.00 _{Ag clusters} ^a)	1000 _C —	—/100 _C	~3700 _C	1.0 M LiCF ₃ SO ₃ in TEGDME	81
	Ag nanowires	~2.75 ^a	~3.25 ^a (vs. ~3.50 _{Ag particle} ^a)	500 _{Ag} /50	0.8/50 _{Ag}	~17 000 _{Ag}	1.0 M LiTFSI in TEGDME	278
Precious metal alloy	Ir/rGO	~2.75 ^a (vs. ~2.70 _{rGO} ^a)	~3.30 ^a (vs. ~3.90 _{rGO} ^a)	1000 _{Pt+C} /40	—/100 _{Pt+C}	—	1.0 M LiCF ₃ SO ₃ in TEGDME	11
	PtAu/porous N-C	~2.70 ^b (vs. ~2.65 _{N-C} ^b)	~4.00 ^b (vs. ~4.10 _{N-C} ^b)	1000 _C -catalyst/70	—/100 _C -catalyst	~6000 _C -catalyst	1.0 M LiCF ₃ SO ₃ in TEGDME	286
	PdCu nanoparticle	~2.75 ^a	~3.35 ^a (vs. ~3.50 _{Pd nanoparticle} ^a)	~1000 _C /50	0.25 _C /200 _C	~12 000 _C	1.0 M LiCF ₃ SO ₃ in TEGDME	289
	Pt ₃ Co nanocube	~2.70 ^{a,b}	~3.20 ^a , ~3.75 ^b (vs. ~3.30 ^a , ~4.05 _{Pt₃Co} ^b)	10 000 _C /65 (vs. 10 000 _C /40)	0.25 _C /200 _C	~11 000 _C	1.0 M LiCF ₃ SO ₃ in TEGDME	32

Notes: ^a Full discharge/charge voltages at half full capacity. ^b Discharge/charge voltages at half limited capacity.

nanoporous structured Au by introducing secondary nanopores into the ligaments of coarsened nanoporous gold with a two-step de-alloying process.²⁵⁰ The as-prepared cathode possessed high porosity, a large accessible surface area and sufficient mass transport channel for a high cell capacity. More importantly, the devices with such a cathode could perform 120 cycles at a charging voltage of about 3.5 V with a cut-off capacity of 1500 mA h g⁻¹ at 2.0 A g⁻¹.

The OER catalytic activity of Au with various kinds of index facets in a Li-O₂ battery was investigated by Wang's group.²⁵¹ A tris-octahedral Au nanocrystal with high-index (441) facets based cathode was found to show a lower charge-discharge overpotential (0.7–0.8 V) and higher capacity (~20 298 mA h g⁻¹ at 100 mA g⁻¹) than those of crystals with (111) and (100) facets (Fig. 37). High-index facets have a high surface energy due to their large density of atomic steps, ledges and kinks, which could provide dense active sites and high catalytic activity for cathodic reactions.

Conductively porous substrates could be a suitable promoter to increase the Au site density and to support efficient channels for mass transport.²⁵² Xie *et al.* reported a sandwich-structured graphene/Au-nanoparticles/Au-nanosheets catalyst for a Li-O₂ battery.²⁵³ They found that thin-layer Li₂O₂ (below 10 nm) could grow comfortably on the surface of Au nanoparticles located between graphene and Au-nanosheets. The contact area between

graphene and Li₂O₂ was thereby reduced to some extent, resulting in superior cycling performance of 300 times at a current rate of 400 mA g⁻¹ under a fixed capacity of 500 mA h g⁻¹. The super cell cyclic performance was attributed to the substantially decreased side reactions between carbon and Li₂O₂.

The construction of a carbon-free electrode is beneficial for the stability enhancement of Li-O₂ batteries due to the non-existing carbon corrosion. Cho *et al.* developed Au nanoparticles (<30 nm)-coated Ni nanowires as the oxygen electrode for Li-O₂ batteries.¹⁵⁸ The battery could be cycled more than 100 times at 500 mA g⁻¹ without any capacity constraint (about 500 mA h g⁻¹). Sun *et al.* also loaded Au nanoparticles on a vertical-array Ti nanowire with Ti foam as the substrate.²⁵⁴ The Li-O₂ battery with this self-supported cathode exhibited excellent durability (640 cycles) at a high current density of 5 A g⁻¹ within a fixed capacity of 1 A h g⁻¹. The remarkable cyclability was proposed to be related to the high conductivity and stability of the all-metal construction cathode.

Recently, a hierarchical macro-/mesoporous AuNi cathode was developed by Zhang *et al.*, who constructed nanoporous Ni with a nanoengineered AuNi alloy on NiFM (AuNi/NPNI/NiFM) for a Li-O₂ battery. The assembled cell demonstrated the reversible formation and decomposition of Li₂O₂, which induced relatively low overpotentials and a high specific capacity and cycle stability. In particular, an ultrahigh specific capacity of 22 551 mA h g_{AuNi}⁻¹ at a current density of 1.0 A g_{AuNi}⁻¹ and a long-term life (286 cycles) were achieved. These were ascribed to the high surface area and porous structure, which provided a sufficient void volume to house the generated Li₂O₂ and to enable fast mass transport.⁸⁴

4.2.2 Pt and Pd catalysts. Precious Pt and Pd materials have been primarily investigated as OER catalysts for Li-O₂ batteries due to their good activity towards catalyzing the decomposition of Li₂O₂. Porous carbon materials are generally utilized as their support to enhance their metal site density, mass transport and Li₂O₂ storage space.²⁵⁵ Lim *et al.* designed a hierarchically porous Pt/CNT air electrode by embedding Pt nanoparticles on cross-weaving aligned CNT sheets.²⁰⁸ The cell with this cathode exhibited a remarkably cycle stability of over 100 cycles with full discharge/charge at a high current rate of 2 A g⁻¹. This could be attributed to the homogeneous film-like formation of Li₂O₂ by the introduction of Pt particles, as shown in Fig. 38. Zhang *et al.* reported a freestanding Pd-modified hollow spherical carbon deposited onto carbon paper (CP).²¹⁶ The battery was capable of operation at a high rate (5900 mA h g⁻¹ at a current density of 1.5 A g⁻¹) and for a long period (100 cycles at a current density of 300 mA g⁻¹ and a fixed capacity of 1000 mA h g⁻¹). This superior performance could be attributed to the formation of uniform nanosheet-like Li₂O₂ with the aid of Pd.

In order to prevent corrosion of the carbon support under high charge potential in the operation of Li-O₂ batteries, Lu *et al.* designed a Pd-modified carbon cathode *via* an atomic-layer-deposition technique, in which the defect sites of the carbon surface were passivated by sputtering on a thinner layer of Al₂O₃ (Fig. 39).⁵⁵ The Li-O₂ battery with the as-prepared

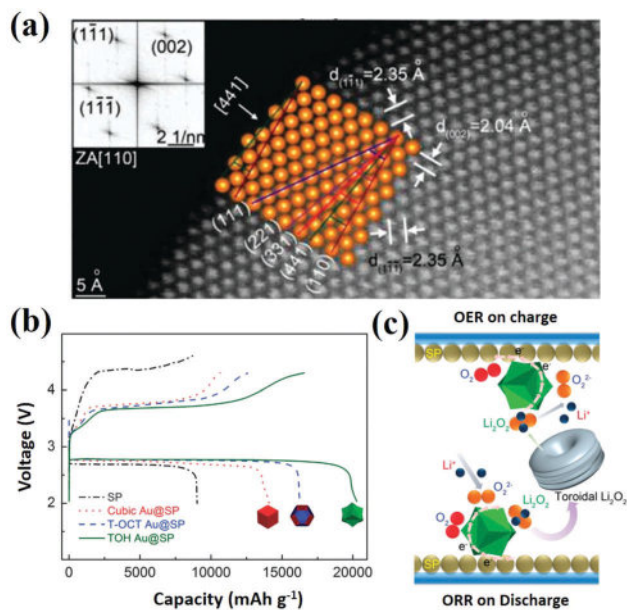


Fig. 37 (a) Atomic resolved HAADF-STEM image of trisoctahedral (TOH) Au NCs taken along the [110] direction, showing the (441) surface, (110) terraces and (001) step (top-left corner inset of (a) was the corresponding indexed FFT pattern along the [110] zone axis; the middle inset of (a) was the simulated atomic arrangement of (110) facets, showing the projected (110) (111), (221), (331) and (441) crystal planes along the [110] direction); (b) the charge-discharge profiles of cubic Au NCs@SP (red dash line), T-OCT Au NCs@SP (blue dash line), TOH Au NCs@SP (green solid line) and bare SP electrodes (black dash line) at 100 mA g⁻¹ in the first cycle; (c) schematic illustration of the proposed Au nanocrystal (NC) catalyst mechanism in Li-O₂ cell.²⁵¹ Reprinted with permission from ref. 251. Copyright 2015 Nature Publishing Group.

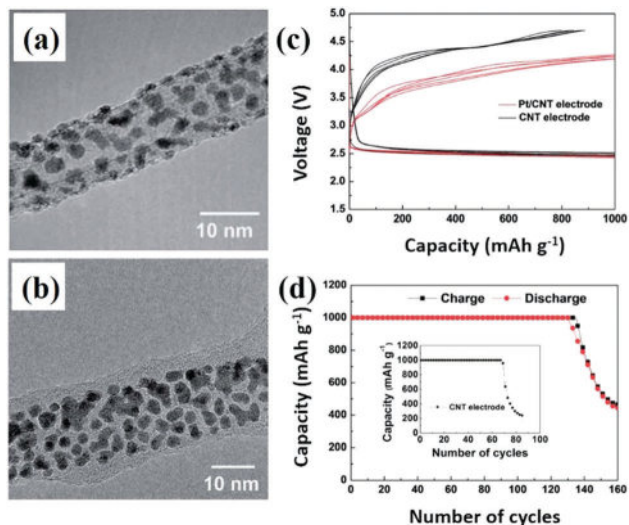


Fig. 38 TEM images of Pt/CNT electrode (a) before and (b) after the first discharge at 1000 mA h^{-1} ; (c) discharge/charge profiles of Li–O₂ cells with the CNT (black line) and Pt/CNT (red line) electrodes at a current rate of 2 A g^{-1} with the limited depth of discharge at 1000 mA h^{-1} ; (d) the corresponding cyclability of Li–O₂ cells shown in (c).²⁰⁸ Reprinted with permission from ref. 208. Copyright 2013 Royal Society of Chemistry.

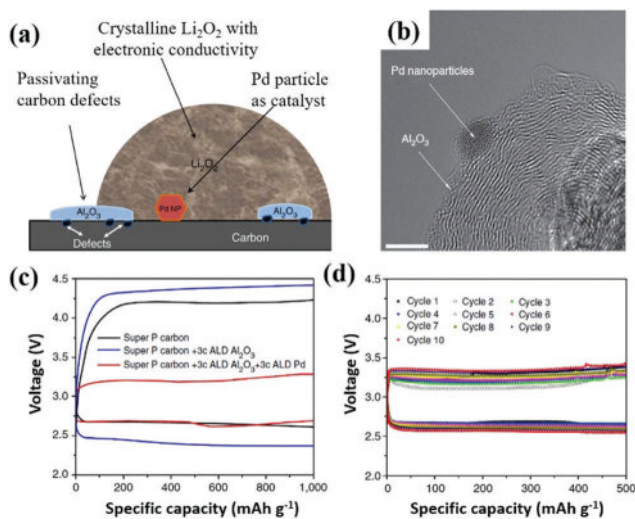


Fig. 39 (a) Schematic of the nanostructured cathode architecture (it showed the deposited Al₂O₃, Pd particles and crystalline Li₂O₂, all of which contributed to lower the overpotential); (b) high-resolution TEM images of Pd nanoparticles decorated carbon with Al₂O₃ layer (scale bars, 4 nm); (c) the discharge/charge profiles of cells based on Super-P carbon (C_{sp}), C_{sp} coated with Al₂O₃; and Al₂O₃-coated C_{sp} with Pd nanoparticles deposition (at a fixed capacity of 1000 mA h^{-1}); (d) the discharge/charge profiles of cells based on Al₂O₃-coated C_{sp} with Pd nanoparticles deposition (electrolyte: TEGDME/LiCF₃SO₃, fixed capacity: 500 mA h^{-1}).⁵⁵ Reprinted with permission from ref. 55. Copyright 2013 Nature Publishing Group.

electrode achieved a low charge overpotential of $\sim 0.2 \text{ V}$ with the assistance of Pd catalysis. The nanocrystalline form of Li₂O₂ with grain boundaries was generated, and the decomposition of carbon materials at the cathode was inhibited by the Al₂O₃ coating to some extent.

Interspersing Pd or Pt on carbon-free porous substrates, for example, MnO_x–GeO_y, TiO₂ and NiO, was proposed to form a stable cathode to avoid carbon corrosion.²⁵⁶ In this regard, Lu *et al.* loaded Pd on the surface of MnO_x–GeO_y nano-membranes as the cathode of Li–O₂ cells.²⁵⁷ Surprisingly, the cell exhibited an extremely low charge voltage of 3.14 V at 70 mA g^{-1} and a prolonged cycle life of 160 cycles (1000 mA h g^{-1} at 300 mA g^{-1}) without apparent degradation. Similarly, Zhao *et al.* loaded Pt nanoparticles on Co₃O₄ nanowires arrays to promote the formation of a tips-bundled structure of Co₃O₄ nanowires instead of the discrete single nanowire, as well as to induce the uniform deposition of a fluffy Li₂O₂ layer on the nanowires surface.²⁵⁸ The battery with the Pt/Co₃O₄ electrode performed over 50 cycles under a fixed capacity of 500 mA h g^{-1} at 100 mA g^{-1} . Sun *et al.* exploited vertical TiO₂ nanotube arrays on Ti foam as a carbon- and binder-free substrate for loading the Pt nanoparticles.²⁵⁹ The battery revealed a good cyclability at high current densities (over 140 cycles at 1 or 5 A g^{-1}) within a wide discharge/charge voltage window (1.5 – 4.5 V).

4.2.3 Ru and RuO₂ catalysts

4.2.3.1 Catalytic activity of Ru-based catalysts. Great efforts have been focused on Ru-based materials as cathode catalysts in Li–O₂ batteries due to their excellent OER activity for decreasing the discharge potential of Li–O₂ batteries.^{260,261} Various carbon substrates, such as CNT, graphene and N-doped graphene, have been used for dispersing Ru or RuO₂ to form cathode materials in Li–O₂ batteries.²⁶² Sun *et al.* successfully prepared Ru-based cathode materials, in which homogeneously distributed metallic Ru and hydrated RuO₂ (RuO₂·0.64H₂O) with an average size below 2.5 nm were deposited exclusively on rGO, respectively.²⁶² The as-prepared battery with the RuO₂·0.64H₂O/rGO material showed a superior activity to that of Ru/rGO hybrids in catalyzing the OER reaction. The average charge potential was significantly reduced to $\sim 3.7 \text{ V}$ at a high current density of 500 mA g^{-1} and it demonstrated stable cycles for 30 times under 5000 mA h g^{-1} (capacity based on carbon + catalyst mass).

Byon *et al.* found that Li₂O₂ uniformly grew on the RuO₂/MWCNTs (RuO₂: 32 wt%) electrodes with a noncrystalline structure, which was responsible for its low OER overpotential.²⁶³ Zhou *et al.* prepared core-shell structured RuO₂/MWCNTs (RuO₂: 86 wt%), which could effectively prevent direct contact between the CNT and Li₂O₂, thus reducing the formation of Li₂CO₃ to some extent.²⁶⁴ The battery showed a high round-trip efficiency of 79% with discharge and charge overpotentials of 0.21 and 0.51 V at 100 mA g^{-1} (capacity on carbon + catalyst mass), respectively. In comparison to Byon's results, the RuO₂/MWCNT (RuO₂: 47 wt%) cathode reported by Zhang *et al.* possessed a feeble surface binding energy towards superoxide species (for example, LiO₂, O₂[−]).⁸³ This promoted the formation of dissolved LiO₂ for the generation of micrometre-sized Li₂O₂ (Fig. 40). The Li–O₂ battery achieved an ultrahigh specific capacity ($29900 \text{ mA h g}^{-1}$ at 200 mA g^{-1}), relatively low overpotentials (0.45 V at a current density of 200 mA g^{-1}) and a long cycle life (171 cycles at a current density of 200 mA g^{-1} and a specific capacity limit of 1000 mA h g^{-1}).

Because of the excellent catalytic activity of RuO₂ for discharge/charge reactions, theoretical calculations were chosen

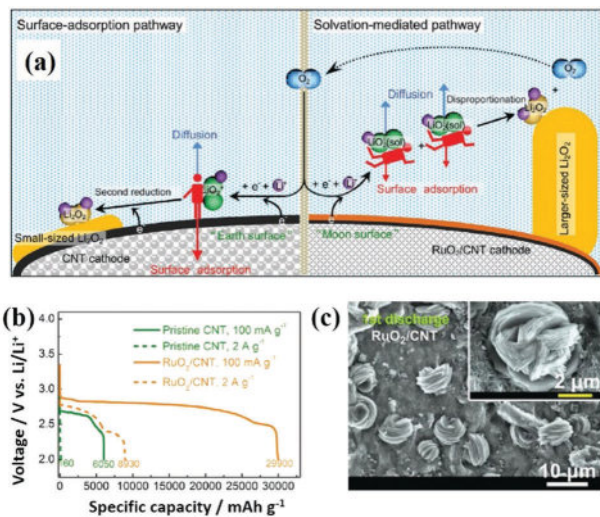


Fig. 40 (a) Schematic image of the Li_2O_2 growth mechanism showing the surface-adsorption pathway followed when the Gibbs free energy for LiO_2^* on the CNT cathode surface exceeds that of the dissolved species, and the solvation-mediated pathway followed when the dissolved species had lower Gibbs free energy than the LiO_2^* on the RuO_2/CNT surface; (b) the rate capability of $\text{Li}-\text{O}_2$ cells with different cathode at current densities of 100 mA g^{-1} and 2 A g^{-1} (green: pristine-CNT, orange: RuO_2/CNT). (c) SEM image of the RuO_2/CNT cathode with Li_2O_2 large cluster after the first discharge at a current density of 200 mA g^{-1} and a specific capacity of 2000 mA h g^{-1} .⁸³ Reprinted with permission from ref. 83. Copyright 2016 Wiley-VCH Verlag GmbH & Co. KGaA.

to clarify the mechanism. One of recent studies showed a large difference in the catalytic activities between crystalline and monolayer RuO_2 for both ORR and OER through DFT calculations.²⁶⁵ The results revealed that the RuO_2 monolayer exhibited a higher catalytic activity than that of rutile RuO_2 . It was explained that the similar lattice structure between monolayer RuO_2 and $\text{Li}_2\text{O}_2(0001)$ surface could induce the formation of Li_2O_2 crystalline with the conductive (0001) surface during the discharge process. Furthermore, the RuO_2 monolayer could attract the remaining Li_2O_2 to its surface spontaneously, maintaining the solid–solid reaction interface during the charge process. This result identified that the monolayer RuO_2 not only functioned as a catalyst for Li_2O_2 formation and decomposition reactions, but also acted as a promoter for the formation of crystallized Li_2O_2 and as an absorber of Li_2O_2 .

4.2.3.2 Ru-Based catalyst with good mass transport and Li_2O_2 storage. The performance of the Ru-based electrode could be further improved by optimization of the nanoporous structure for fast mass transport.^{80,247,266} Zheng *et al.* reported a $\text{Ru}@$ mesoporous graphene-like carbon as a $\text{Li}-\text{O}_2$ battery cathode that delivered 6433 mA h g^{-1} (capacity on carbon + catalyst mass) at a current density of 200 mA g^{-1} . An extremely low charge voltage of 3.20 V and a high discharge voltage of 2.84 V were achieved at a current density of 100 mA g^{-1} .²⁶⁷ Ru-Particles-functionalized graphene aero-gels (Ru-GAs) were also applied as freestanding cathodes for a $\text{Li}-\text{O}_2$ battery.²⁶⁸ This cathode could efficiently enhance the specific cell discharge capacity ($12000 \text{ mA h g}_{\text{carbon}}^{-1}$ at 0.1 mA cm^{-2}), reduce the

charge overpotential (1.25 V) and improve the cycling stability to up to 50 cycles at a curtailing capacity of 500 mA h g^{-1} . Tests by differential electrochemical mass spectrometry (DEMS) indicated that CO_2 was started to be generated from 3.8 V , together with the generation of side products, such as lithium carboxylates and Li_2CO_3 .

The introduction of a hierarchical porous structure into a Ru-based cathode could provide both an efficient mass transport channel and a large deposition space for a high quantity of Li_2O_2 .^{236,269} Liu *et al.* developed a Ru-decorated hierarchically macro-/mesoporous carbon (MmC@Ru) for $\text{Li}-\text{O}_2$ batteries.²⁴⁸ They found that the MmC@Ru cathode presented a high specific capacity of $12400 \text{ mA h g}^{-1}$ at a current density of 200 mA g^{-1} , and an excellent cycling performance for up to 100 cycles at 400 mA g^{-1} (fixed capacity of 1000 mA h g^{-1}). Wang *et al.* constructed a Ru-decorated vertical graphene nanosheets@Ni foam ($\text{Ru-decorated VGNS@NiFM}$) electrode for a $\text{Li}-\text{O}_2$ battery, which exhibited a high discharge capacity of $23864 \text{ mA h g}^{-1}$ at a current density of 200 mA g^{-1} . Moreover, a low charge overpotential of $\sim 0.45 \text{ V}$ and good cyclability of 50 cycles was achieved by Ru-decorated VGNS@NiFM under full charge and discharge conditions in comparison to VGNS@NiFM ($\sim 0.86 \text{ V}$, fast decrease of cell cyclability in 10 cycles), indicating the superior OER activity of the Ru catalyst in the $\text{Li}-\text{O}_2$ battery.²⁷⁰

4.2.3.3 Ru-Based catalyst with good stability. A conductive carbon support might suffer from oxidation under high charge voltages, so as an alternative metal oxide materials could be a good support for the stable Ru-based cathode and could facilitate the increased stability of the electrode in $\text{Li}-\text{O}_2$ batteries. To test this out, Kim *et al.* designed two composite catalysts of $\text{RuO}_2/\text{Mn}_2\text{O}_3$ with a tube-in-tube (RM-FIT) and $\text{RuO}_2/\text{Mn}_2\text{O}_3$ fibre-in-tube (RM-FIT) structures, as shown in Fig. 41.²⁷¹ The RM-FIT catalyst exhibited the combined catalytic activity from both RuO_2 and Mn_2O_3 , resulting in a low cell overpotential gap of 1.48 V at the end of the discharge/charge curves (2000 mA h g^{-1}) and a superior cyclability of 120 cycles under 1000 mA h g^{-1} at 400 mA g^{-1} .

Zhou's group also investigated the $\text{Li}-\text{O}_2$ battery performance with a Ru/MnO_2 catalytic cathode and a TEGDME-based electrolyte containing a trace amount of water.^{45,126} The battery was assembled with LiFePO_4 as the anode in order to avoid the corrosion of metallic Li. As a result, the battery could achieve a low charge overpotential of around 0.3 V in the presence of little water. The excellent cell performance was partially due to the promotion effect of MnO_2 for the formation of LiOH and the high catalytic activity of Ru for the decomposition of LiOH . Subsequently, the TEGDME-based electrolyte was replaced by an ionic-liquid-based electrolyte, and the Li-anode was protected by a commercial lithium superionic conductor (LISICON) film in a $\text{Li}-\text{O}_2$ battery.⁴⁹ As a result, the battery also performed with a low overall overpotential (0.4 V) and achieved a long cycling life of over 95 cycles (1000 mA h g^{-1} , 500 mA g^{-1}).

Moreover, other types of metal oxides, for example nano-structured TiO_2 and NiO , were also demonstrated as advanced supports for Ru-based catalysts.^{272,273} Belharouak *et al.* deposited

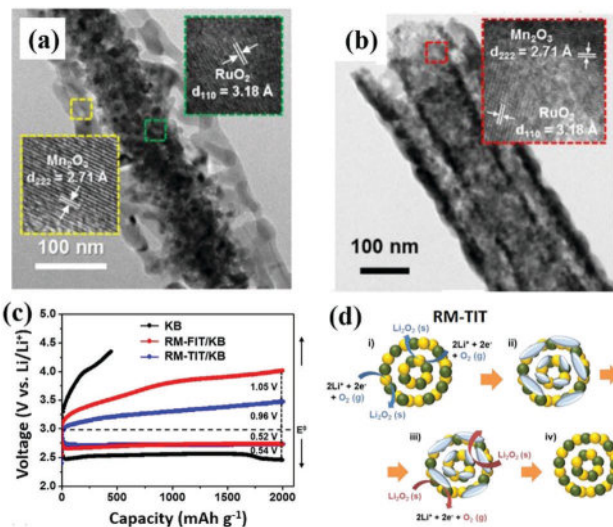


Fig. 41 High-resolution TEM images of (a) RuO₂/Mn₂O₃ fibre-in-tube (RM-FIT) and (b) multi-composite RuO₂/Mn₂O₃ tube-in-tube (RM-TIT); (c) the cell discharge/charge profiles with a limited capacity of 2 A h g⁻¹ at a current density of 100 mA g⁻¹ and voltage window between 2.35 and 4.35 V; (d) the proposed reaction mechanism of RM-TIT electrodes during the operation of Li–O₂ cells, which were represented by four states as (i) on discharging, (ii) discharged state, (iii) on recharging, and (iv) recharged state.²⁷¹ Reprinted with permission from ref. 271. Copyright 2016 American Chemical Society.

a RuO₂ catalyst on a mesoporous TiO₂ support instead of on a carbon substrate, thereby avoiding the side reactions between superoxide species and carbon.²⁷⁴ The cell with the carbon-free RuO₂/TiO₂ electrode exhibited a high catalytic activity towards an overall overpotential below 1 V with a capacity of 2000 mA h g⁻¹ at 100 mA g⁻¹. Over 50 stable cycles were achieved at a limited discharge capacity of 500 mA h g⁻¹. Zhao *et al.* constructed a cathode composed of RuO₂ nanoparticle-decorated NiO nanosheets towards a Li–O₂ battery operated in ambient air. It achieved 200 cycles at 250 mA g⁻¹ under 500 mA h g⁻¹ (based on RuO₂) with a stable Coulombic efficiency of 100% and a high energy efficiency of ~75%.²⁷³ The excellent performance could be attributed to the favourable combination of RuO₂ nanoparticles and NiO nanosheets. This not only catalyzed the OER and ORR reactions, but also promoted the decomposition of side products, including LiOH and LiCO₃.

Other conductive carbon-free materials with good mass transport capability were also proposed as a support for Ru-based catalysts. For example, Peng *et al.* loaded a RuO_x catalyst on freestanding TiN nanotubes as a cathode for a Li–O₂ battery, which then exhibited low overpotentials (below 1 V) and excellent cycle stability over 300 cycles (500 mA h g⁻¹, 150 mA g⁻¹).²⁷⁵ Chen *et al.* incorporated RuO₂ into the pore channels of nanoporous Au, remarkably improving the catalytic activity of RuO₂. The cell exhibited an overall overpotential of 0.71 V at 50 mA g⁻¹ under 300 mA h g⁻¹ (capacity on Au mass, corresponding to ~3600 mA h g⁻¹ based on RuO₂), as well as a relatively stable 50 cycles under this condition.²⁷⁶

4.2.4 Ag catalyst. Metallic Ag was also studied as the electrode catalyst for Li–O₂ batteries. Lu *et al.* evaluated the

effect of Ag particle size on the charge potentials of Li–O₂ cells with a 1 M LiCF₃SO₃/TEGDME-based electrolyte. They found that the Ag-deposited electrode with Ag particles' diameter of 50 μm maintained a very low polarization, corresponding to a charge potential of 3.6 V. In contrast, a Ag-deposited electrode with small Ag particles (<30 μm) only showed low charge potentials in the first charge step. The author suggested that the difference in charge profile might be related with the density of Ag active sites on the as-prepared electrode.²⁷⁷ Aurbach *et al.* compared the performance of Ag nanoparticles and Ag nanowires cathodes in Li–O₂ batteries, whereby the Ag nanowires electrode exhibited a low charge voltage of 3.4 V (500 mA h g⁻¹, 50 mA g⁻¹) and kept the low overpotentials for over 50 cycles. It was proposed that the difference in cell performance was due to the different Li₂O₂ growth morphology on the Ag-based cathode morphology, whereby a corn-on-the-cob-shaped layered Li₂O₂ was generated on the Ag nanowire, while toroidal-shaped Li₂O₂ was generated on the Ag nanoparticles.²⁷⁸

Vajda *et al.* precisely controlled the Ag atom-cluster size (Ag₃, Ag₉, Ag₁₅) on a carbon surface, while the defects on the carbon were passivated by the atomic-layer-deposited Al₂O₃.⁸¹ As shown in Fig. 42, the size of the Ag catalyst could significantly influence the morphology of the discharge products, and the Ag₁₅ particles showed the best cell discharge capacity in the family of Ag₃, Ag₉ and Ag₁₅ clusters. The different morphologies of Li₂O₂ were attributed to the different ORR activities of the Ag_x cluster, in which the Ag₁₅ cluster had a more favourable electron transfer than Ag₃ and Ag₉. This implied that the surface structure of the sub-nanometre cluster cathodes can play a key role in understanding the discharge chemistries in Li–O₂ cells,

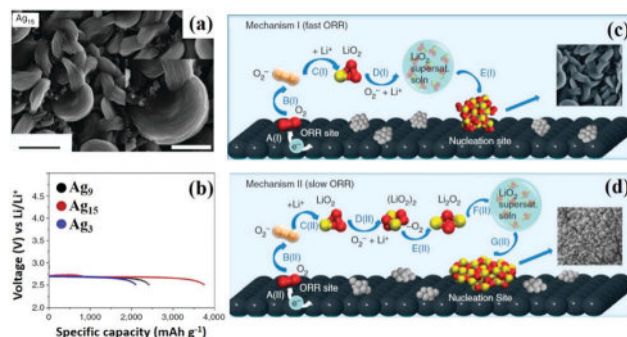


Fig. 42 (a) SEM images of Li₂O₂ products on Ag₁₅-based cathode (scale bar, 1 μm; scale bar of inset image, 500 nm); (b) the first discharge profiles of cells with different Ag cluster catalysts at a cut-off voltage of 2.5 V; (c) and (d) illustration of two discharge reaction mechanisms based on an initial oxygen reduction at an active site followed by solution phase reactions and growth at a surface nucleation site ((c) Mechanism I: step A: electron transfer to O₂; step B: O₂⁻ desorption; step C: Li⁺ reacted with O₂⁻ to form solvated LiO₂; step D: repetition of steps A–C for LiO₂ formation to reach supersaturated LiO₂ solution; step E: surface nucleation and growth of LiO₂ that undergoes disproportionation. (d) Mechanism II: step A: electron transfer to O₂; step B: O₂⁻ desorption; step C: Li⁺ reacted with O₂⁻ to form solvated LiO₂; step D: addition of O₂⁻ and Li⁺ to form LiO₂ dimer; step E: disproportionation to form Li₂O₂ and O₂; step F: repetition of steps A–E for Li₂O₂ formation to reach supersaturated Li₂O₂ solution; step G: surface nucleation and growth of Li₂O₂).⁸¹ Reprinted with permission from ref. 81. Copyright 2014 Nature Publishing Group.

and the tailoring of this structure represents a potential avenue to increase the cell capacities and cycle life.

4.2.5 Ir catalyst. Ir-Based catalysts have excellent OER activity in aqueous media, which indicates their possibility as a catalyst for the cathode of Li–O₂ batteries.²²⁴ Yang *et al.* synthesized a composite consisting of ultrafine IrO₂ homogeneously distributed on KB carbon (IrO₂/KB) as the cathode for a Li–O₂ battery. The corresponding cell achieved an overall overpotential of 0.97 V and 70 cycles without any sharp decay under a limited capacity of 500 mA h g⁻¹, which was a much better performance than that of an IrO₂ + KB-mixture-based cathode (only 30 cycles).²⁷⁹ Furthermore, the discharge products were proved to be Li₂O₂ on the IrO₂/KB-based cathode.

In contrast, the unconventional LiO₂ particle was proved to be the only discharge product in the Li–O₂ cell with Ir/rGO as the cathode, as studied by Curtiss *et al.*¹¹ As shown in Fig. 43, Li–O₂ batteries with the nanorod-like LiO₂ had a low charging voltage of around 3.5 V for the first 39 cycles under 1000 mA h g⁻¹. Additionally, negligible amounts of CO₂ and H₂ gases were generated during the charging process, proving the high reversibility of the cell with LiO₂. The formation of LiO₂ might be due to the similar crystallographic lattice between LiO₂ and Ir₃Li, an intermediate metallic compound occurring during the discharge process. This Ir₃Li can induce the nucleation and growth of the crystalline LiO₂. Simultaneously, the solvent on the LiO₂ surface could further suppress the disproportionation of the crystalline phase, thereby helping guarantee the stability of LiO₂. The different LiO₂ and Li₂O₂ products on IrO₂ and Ir-based cathodes provides a new strategy to tune the discharge products from the growth pathway for a better cell performance.

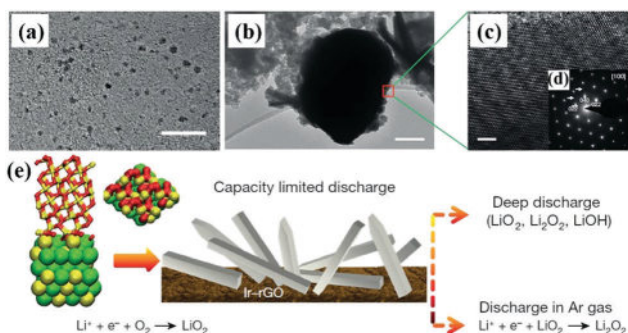


Fig. 43 (a) TEM images of Ir–rGO composite, showing Ir nanoparticles less than 2 nm in size (scale bar, 10 nm); (b) TEM image of an Ir agglomerate after first discharge (scale bar, 200 nm); (c) HR-TEM image of boxed area in (b) (scale bar, 2 nm); (d) the corresponding electron diffraction pattern along the [100] zone axis giving evidence for the formation of an Ir₃Li intermetallic (the indices are diffraction vectors, and a weak superstructure can be observed as indicated by arrows); (e) schematic showing lattice matching between LiO₂ and Ir₃Li, which might be responsible for the LiO₂ product on the Ir–rGO cathode (left: the two structures are the side- and top-views representing epitaxial growth of crystalline LiO₂ in a (111) orientation on a (121) facet of Ir₃Li (yellow: Li, red: O, green: Ir)); centre: the rod-like structures are schematic representations of the crystalline LiO₂ morphology observed in the experiment; right: two subsequent reactions that LiO₂ could undergo either further lithiation in the presence of Ar or further O₂ reduction in the presence of O₂.¹¹ Reprinted with permission from ref. 11. Copyright 2016 Nature Publishing Group.

4.2.6 Comparison of precious metal catalysts. Precious metal catalysts have been demonstrated to have good catalytic activity towards Li₂O₂ formation and decomposition, and thus a comparison of their activity for different catalysts was essential to find the most effective materials. Consequently, Gasteiger *et al.* reported the intrinsic ORR activity of Pd, Pt, Ru, Au and glassy carbon (GC) in a non-aqueous system (LiClO₄ in DME electrolyte). Their ORR activity primarily correlated to their oxygen adsorption energetics, displaying a “volcano-type” trend in the order of Pd > Pt > Ru ≈ Au > GC on bulk surfaces (Fig. 44), which was also confirmed by Xiao *et al.*²⁴⁶ This investigation might be useful for efforts in designing active ORR catalysts for high discharge voltages in Li–O₂ batteries.⁹⁸

Except for their effect on discharge characteristic, the charge profiles of a battery are also influenced by the type of noble metal catalysts.²⁸⁰ Huang *et al.* encapsulated a series of noble metal nanoparticles (Pd, Pt, Ru and Au) inside open-ended CNTs by wet impregnation followed by thermal annealing. The charge overpotential of the as-prepared battery could be as low as 0.3 V with CNT-encapsulated Pd nanoparticles as the cathode materials (LiCF₃SO₃ in TEGDME electrolyte).²⁸¹ DFT calculations revealed that the encapsulation of noble metal nanoparticles on the CNT surface was able to strengthen the electron density of the CNT and avoided the regional enrichment of electron density caused by direct exposure of the nanoparticles on the CNT surface. Lu *et al.* used online electrochemical mass spectrometry to characterize the kinetics of the charge reaction on noble metal catalysts in a Li–O₂ battery.¹³⁵ They found that the aprotic OER was a catalytically active process, and that noble metal catalysts could accelerate the rate of charge reaction *via* solid–solid interactions between the catalyst and the discharge products instead of liquid-phase mediations.

Sun *et al.* also presented a systematic evaluation of Pt, Pd, and Ru nanoparticles supported on rGO as a cathode catalyst for Li–O₂ batteries (LiCF₃SO₃ in TEGDME electrolyte).²⁸² All of these could decrease the charge overpotentials, with the Ru–rGO hybrids exhibiting the most stable cyclability and the lowest charge overpotentials. The experimental results were different from Huang’s result,²⁸¹ and one of the reasons for this might be ascribed to the different growth mechanism between Pt, Pd and Ru materials. It was suggested that Ru nanoparticles facilitated a thin-film-like or particulate Li₂O₂ morphology, and showed stable charge profiles without electrolyte degradation during cycling. In contrast, Pt- and Pd-based catalysts oxidized organic electrolytes electrochemically during cycling, and a fluctuating potential characteristic was observed. It was therefore considered that the activation barrier of Li₂O₂ decomposition on catalysts through electron transfer could not be the reason for the difference in charge characteristics.

For their application in Li–O₂ batteries, the oxidation ability of precious metal catalysts towards electrolyte components needed to be characterized with an aim to achieve a stable cell output. As reported by Sun *et al.*, Pt- and Pd-based catalysts could oxidize organic electrolytes electrochemically during voltage cycling.²⁸² Meanwhile, Gittleson *et al.* also reported that Pt and

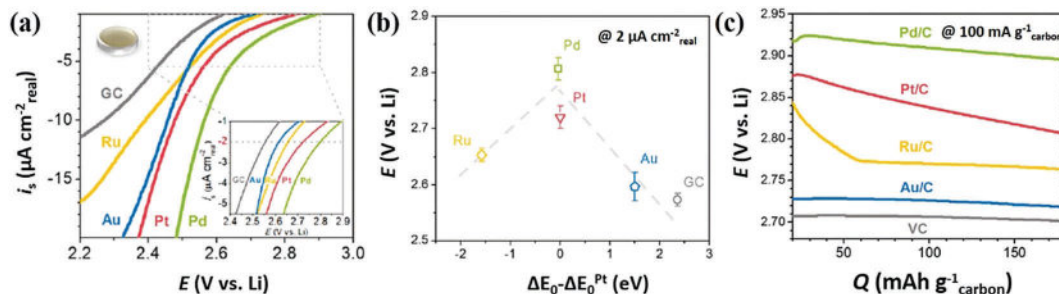


Fig. 44 (a) Background- and IR-corrected (inset) specific ORR polarization curves of polycrystalline Pd, Pt, Ru, Au, and GC surfaces in O₂-saturated 0.1 M LiClO₄/DME at a rotate speed of 100 rpm and a scan rate of 20 mV s⁻¹; (b) aprotic Li⁺-ORR potentials at 2 μA cm⁻² as a function of calculated oxygen adsorption energy (ΔE_{O_2} per oxygen atom relative to an atom in the gas phase), relative to that of Pt; the oxygen adsorption energy on GC was estimated from the oxygen adsorption energy on graphite; error bars represented standard deviations of at least three independent measurements); (c) initial discharge profiles of Li-O₂ cells of Pd/C, Pt/C, Ru/C, Au/C, and Vulcan-C at 100 mA g_{carbon}⁻¹.⁹⁸ Reprinted with permission from ref. 98. Copyright 2015 Wiley-VCH Verlag GmbH & Co. KGaA.

Pd catalysts encouraged Li₂O₂ oxidation at low charging voltage, but further decompose the DMSO electrolyte to produce a large amount of Li₂CO₃. The side products deactivated the electrode surface (occurred to a greater extent with Pt than with Pd), resulting in the quick death of the battery.²⁸³ Combined analysis using differential electrochemical mass spectroscopy (DEMS) and the FT-IR technique revealed an increase in CO₂ evolution during the charging process in the Li-O₂ cells with Pd-CNT cathodes in contrast to what was observed in the cell without a noble metal catalyst. McCloskey *et al.* investigated the efficacy of Au and Pt catalysts in Li-O₂ batteries.²⁸⁴ Both Pt and Au materials accelerated the electrolyte degradation (DME and DME + PC) accompanied by Li₂O₂ decomposition. The calculated ratio of evolved oxygen to consumed oxygen (Au: 0.69; Pt: 0.13) proved that the degradation of the DME-based electrolyte on Pt catalyst was much more serious than it was with the Au catalyst.

4.2.7 Precious metal alloy catalysts. Various kinds of noble metal alloys have been investigated as cathode materials for Li-O₂ batteries^{29,285} and have shown a bifunctional ability for catalyzing the discharge/charge reactions. Pt/Au alloy was reported as a catalyst for a Li-O₂ battery by Shao-Horn's group in the early stage.²⁴ The charge voltages with PtAu/C fell in the range from 3.4 to 3.8 V, which was slightly lower than that obtained with a Pt catalyst. It was proposed that the PtAu nanoparticles exhibited bifunctional catalytic activity, with the Au and Pt atoms on the surface primarily responsible for the ORR and OER kinetics in Li-O₂ cells, respectively. Unfortunately, organic-carbonate electrolytes were proved to suffer from severe decomposition in aprotic Li-O₂ systems.²⁹ Lee *et al.* deposited PtAu nanoparticles on hollow mesoporous N-doped carbon microspheres (HMCMS) to form PtAu/HMCMS materials, which were then used in a Li-O₂ battery together with an ether-based electrolyte.²⁸⁶ This battery exhibited a high reversible capacity of 6000 mA h g⁻¹ (capacity based on catalyst + carbon mass) at 100 mA g⁻¹ with a discharge/charge gap of 1.27 V and a long cycle life over 70 cycles under 1000 mA h g⁻¹. However, the cell still suffered from capacity loss and an overpotential increase within several cycles.

In addition to noble metal alloys, the catalytic activity of noble metals might be increased by alloying with non-noble metals,

because their electronic structure could be adjusted by guest metals.^{287,288} In this vein, Han *et al.* designed a PdCu bimetallic catalyst (7–9 nm) as a cathode material for a Li-O₂ battery, which exhibited a low OER potential of 3.4 V and a superb round-trip efficiency of 80% at 200 mA g_{carbon}⁻¹.²⁸⁹ Moreover, the cell achieved a long cycle life up to 50 cycles without decay of the discharge potential. DFT calculations indicated that there was electron transfer from the underlying Cu atoms to the top-layer Pd atoms, which could weaken the adsorption strength of LiO₂ on the Pd surface. This resulted in a decrease in the discharge/charge overpotentials. DFT calculations towards PtCu catalysis for discharge/charge reactions was further investigated by Chung's group.²⁹⁰ The theoretical calculation showed that the more negatively charged PtCu(111) surface acted as a weakly and positively charged surface for the adsorption of LiO₂ intermediates. This resulted in the weak ionic bonding of the intermediates on the PtCu site. These results indicated that PtCu was a more effective OER catalyst than pure Pt.

Other than PtCu materials, PtCo was also proved as an efficient cathode catalyst in a Li-O₂ battery by Han's group.^{32,291} The battery with Pt₃Co catalyst showed a low overall overpotential of about 0.5 V under 1000 mA h g⁻¹ at 200 mA g⁻¹.³² DFT results suggested that the low OER overpotentials were associated with the reduced adsorption strength of LiO₂ on the outermost Pt catalytic sites. Interestingly, amorphous Li₂O₂ was deposited on the Pt₃Co catalysts, which facilitated the Li₂O₂ decomposition. The authors further investigated the activity of PtCo, Pt₃Co and Pt catalysts *via* first-principle calculations systematically, whereby the PtCo catalyst exhibited remarkably low ORR and OER overpotentials of 0.19 and 0.20 V, respectively. These were considerably lower than those of pure Pt (1.02 and 1.62 V, respectively) and Pt₃Co (1.02 V and 1.13 V, respectively).²⁹² It was thus proposed that alloying Pt with transition metals could be an effective strategy to optimize the adsorption energies of the LiO₂ intermediate, which would be beneficial for a decrease in the overpotentials in Li-O₂ batteries.

In short, noble metal catalysts have already been shown to demonstrate an ability to decrease the overpotentials of cathode reactions, and their activity could be further improved through modulation of the pore structure and surface engineering.

The main concern about noble metal catalysts is the compatibility between the catalysts and organic electrolyte under a wide potential window. One of the possible methods to overcome these issues is to modify the electronic structure of the catalysts, which would potentially decrease their catalytic activity towards oxidation of the electrolyte. Another possibility is the inhibition of electrolyte oxidation, for example, by selection of highly stable solvents or by modification of the electrolyte additives. If the above-mentioned strategies could be successfully developed, precious metal-based catalysts might have a bright future for high-performance Li-O₂ batteries.

4.3 Non-precious-metal-based catalysts

Although noble-metal-based materials exhibit excellent catalytic activity towards Li₂O₂ formation/decomposition, their high-cost and scarcity, as well as their oxidation ability towards organic electrolytes, are hard to overcome in their present state. Thus, the development of efficient non-precious metal catalysts is a possible strategy to resolve these issues due to their cost-effectiveness, earth-abundance and non-oxidation nature of organic compounds.²⁹³ To date, various kinds of non-precious-metal-based materials, such as metal oxides, metal sulfides and nitrides, and perovskites, have been investigated as cathode catalysts for batteries.^{13,53,74,293,294} Some of these have shown high catalytic activity for Li₂O₂ formation and decomposition, and the capability for inducing the growth of Li₂O₂. Moreover, tuning the porous structure of non-precious-metal catalysts can provide the opportunity to obtain a high-performance cathode with an efficient mass transport path and large Li₂O₂ storage space.

4.3.1 Manganese oxide catalysts. Manganese oxide (MnO_x) material is one type of efficient catalyst for use in the cathode of Li-O₂ batteries, ascribed to its' wide structure diversity and excellent activity towards catalyzing both OER and ORR. Depending on the arrangement of the basic MnO₆ structure, Mn-oxide can exhibit different polymorphs, including of α , β , γ , δ , λ - and ϵ -types.^{104,295} The α , β - and γ -types exhibit the tunnel structure of MnO₆ octahedra, while the δ -type possesses a layered structure and the λ -type has a 3D structure. The choice of polymorph of MnO₂ influences the catalytic activity, growth and decomposition pathway of Li₂O₂ in discharge/charge processes. According to these aspects, the following discussion on the catalytic activity of manganese oxides is based on their different polymorphs, where Table 4 summarizes the corresponding parameters of a Li-O₂ battery with typical manganese oxide materials.²⁹⁶

4.3.1.1 α , β , γ -MnO₂ catalysts. Débart *et al.* compared the catalytic activity of MnO_x materials with different crystal structures and morphologies (including α -MnO₂ nanoparticles, α -MnO₂ nanowires, β -MnO₂ nanowires, γ -MnO₂ nanoparticles, Mn₂O₃ nanoparticles and Mn₃O₄ nanoparticles) in Li-O₂ batteries. They found that α -MnO₂ nanowires possessed the best catalytic activity, with a discharging voltage plateau of about 2.7 V, a high specific capacity of 3000 mA h g⁻¹ and a high capacity retention ratio of 50% after 10 cycles (Fig. 45).¹⁰⁴ Additionally, Scott's and Park's groups also investigated the catalytic activity

Table 4 Performance summary of Li-O₂ batteries with MnO_x-based electrodes and their operating conditions

MnO _x	Specific design	Discharge voltage (V)	Charge voltage (V)	Limited capacity/ cycles (mA h g ⁻¹ /times)	Mass and current density (mg cm ⁻² / mA g ⁻¹)	Full discharge capacity (mA h g ⁻¹)	Electrolyte	Ref.
α -MnO ₂	α -MnO ₂ nanorods/ porous carbon [002]-oriented α -MnO ₂ /C	~2.75, ^a ~2.65 ^b	~3.85, ^a ~4.10 ^b	500 _{MnO₂+C} /60	0.6/100 _{MnO₂+C}	~1400 _{MnO₂+C}	1.0 M LiTFSI in TEGDME	299
δ -MnO ₂	δ -MnO ₂ /carbon fiber δ -MnO ₂ /3D- graphene/NiFM	~2.65 ^b (vs. ~2.55 _{[11-2]-oriented α-MnO₂})	~3.60, ^a ~4.10 ^b (vs. ~4.00 _{[11-2]-oriented α-MnO₂})	1000 _C /20 (vs. 1000 _{[11-2]-oriented α-MnO₂/16})	—/200 _C	~11 000 _C (vs. 5000 _C , [11-2]-oriented α -MnO ₂ /C)	1.0 M LiCF ₃ SO ₃ in TEGDME	305
		~2.65 ^b (vs. ~2.55 _{XC-72}) ~2.65 ^b (vs. ~2.40 _{3D-graphene/NiFM})	~3.80, ^a ~4.05 ^b (vs. ~3.80 _{XC-72}) ~4.05 ^b (vs. ~4.40 _{3D-graphene/NiFM})	500 _{MnO₂+C/30} (vs. 500 _{XC-72} /~15) 500 _{MnO₂+C} /130	0.85/100 _{MnO₂+C}	~2000 _{MnO₂+C} (vs. ~1000 _C , XC-72)	1.0 M LiCF ₃ SO ₃ in TEGDME	309
ϵ -MnO ₂	ϵ -MnO ₂ /NiFM	~2.60 ^b	~4.25 ^b	2.2-4.3 V (stop voltages)/120 800 _{MnO₂} /190	0.4/500 _{MnO₂}	3660 _{MnO₂+C} (vs. ~1000 _C , 3D-graphene/NiFM)	0.1 M LiClO ₄ in DME	316
MnO _x (1 < x < 2)	Hierarchical porous ϵ -MnO ₂ MnO _{2-x} sheets/ stainless steel Li _{0.50} MnO ₂ /C	~2.70 ^b	—	—	0.6/500 _{MnO₂}	~6300 _{MnO₂}	1.0 M LiTFSI in TEGDME	318
		~2.80, ^a ~2.75 ^b	~4.00, ^a 4.10 ^b	1000 _{MnO_{2-x}} /150	0.3/200 _{MnO_{2-x}}	~5000 _{MnO₂}	1.0 M LiTFSI in TEGDME	319
		~2.70 ^b (vs. ~2.60 _{MnO₂})	~3.60, ^a ~3.70 ^b (vs. ~4.10 _{MnO₂})	1000 _C /190	100 _C	~7300 _{MnO_{2-x}} ~8000 _C	1.0 M LiTFSI in TEGDME	320
							1.0 M LiTFSI in TEGDME	323

Notes: ^a Full discharge voltages at half full capacity. ^b Discharge/charge voltages at half limited capacity.

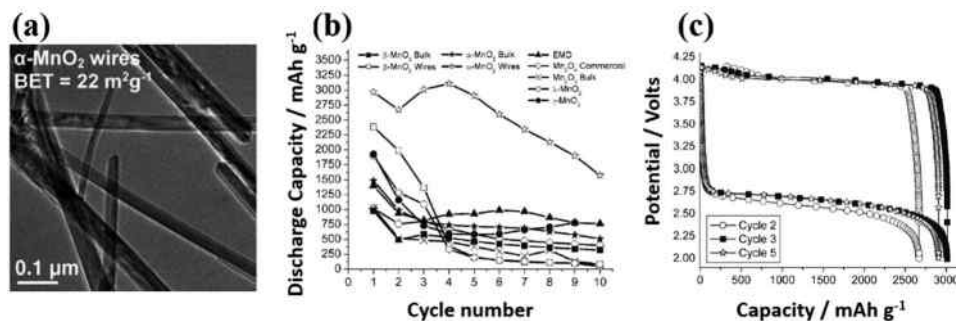


Fig. 45 (a) TEM images of α - MnO_2 nanowire showing their morphologies and surface areas; (b) variation of discharge capacity with cycle number for several electrodes containing manganese oxides (α - MnO_2 in bulk and nanowire form, β - MnO_2 in bulk and nanowire form, γ - MnO_2 , λ - MnO_2 , Mn_2O_3 and Mn_3O_4 ; electrolytic manganese oxide (EMD) was used as a reference material; cycling was carried out at a rate of 70 mA g^{-1} with a cut-off potential of 2 V in 1 atm of O_2 ; capacities are per-gram of carbon in the electrode); (c) variation of potential with state of charge for the α - MnO_2 -nanowires-based electrode (a current density of 70 mA g^{-1} between 2.00 and 4.15 V).¹⁰⁴ Reprinted with permission from ref. 104. Copyright 2008 Wiley-VCH Verlag GmbH & Co. KGaA.

of MnO_2 with different crystalline phases (α -, β -, γ - MnO_2 ;²⁹⁵ α -, β - MnO_2 ²⁹⁷). They found that α - MnO_2 exhibited better catalytic activity than the others. Following the reported results, α - MnO_2 materials were intensively researched by screening the different supports and constructions of porous structures, as well as their possible oxidation ability towards organic electrolytes.

4.3.1.1.1 Catalytic activity of α - MnO_2 . In the reported research, porous carbon materials were always used as the support to deposit α - MnO_2 crystals on for amplifying its activity.²⁹⁸ Amine *et al.* *in situ* deposited α - MnO_2 nanorods on pre-oxidized porous carbon for a Li- O_2 battery, which delivered a specific capacity of 1400 mA h g^{-1} at 100 mA g^{-1} (capacity based on carbon + catalyst mass). The battery could sustain 50 cycles at a limited capacity of 500 mA h g^{-1} , which was much longer than the performances of cells without MnO_2 catalysts.²⁹⁹ Guan *et al.* coated MnO_2 nanoflakes on MWCNTs to inhibit carbon oxidation to some extent, and thereby achieved an improvement in the reversible cell capacity (2200 mA h g^{-1} at 70 mA g^{-1} , capacity on MnO_2 + carbon mass) and energy efficiency (overpotentials below 1 V).³⁰⁰ Zheng *et al.* prepared an *in situ* growth of α - MnO_2 nanorods on graphene nanosheets (GNSs) as a cathode for a Li- O_2 battery. The catalytic activity was determined to be superior to those of mixtures containing GNSs with α - MnO_2 nanorods or α - MnO_2 nanowires, resulting in a high specific capacity and low overpotentials of the battery.³⁰¹ The as-prepared catalyst also exhibited a specific capacity as high as $11520 \text{ mA h g}_{\text{carbon}}^{-1}$ at $200 \text{ mA g}_{\text{carbon}}^{-1}$, and good cyclability over 20 cycles under $3000 \text{ mA h g}_{\text{carbon}}^{-1}$.

The catalytic mechanism of α - MnO_2 towards discharge/charge reactions was evaluated by Kang's and Trahey's groups.^{302–304} Kang *et al.* prepared (002)- and (11-2)-oriented monocrystal α - MnO_2 nanorods to analyze the importance of the surface oxygen sites and metal sites for the catalytic activity in Li- O_2 batteries.³⁰⁵ By combining the experimental and theoretical results, the oxygen sites on the surface were proved to be more important than the metal sites in determining the catalytic activity of α - MnO_2 . As shown in Fig. 46, the specific

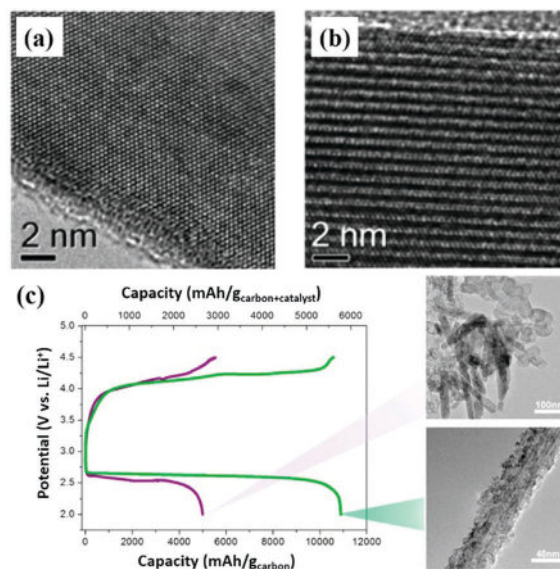


Fig. 46 HR-TEM image of: (a) (002)-oriented and (b) (11-2)-oriented α - MnO_2 nanowires (NWs); (c) the initial discharge-charge curves of Li- O_2 cells using (002)-oriented and (11-2)-oriented α - MnO_2 NWs (the right images show the TEM images of α - MnO_2 NWs with the (11-2)-orientation (top) and (002)-orientation (bottom) after the initial discharge).³⁰⁵ Reprinted with permission from ref. 305. Copyright 2015 American Chemical Society.

capacity of a battery with an (002)-oriented α - MnO_2 nanorod/carbon catalyst was $10000 \text{ mA h g}_{\text{carbon}}^{-1}$, much higher than that with the (11-2)-oriented MnO_2 ($5000 \text{ mA h g}_{\text{carbon}}^{-1}$) battery. The charge potential for (002)-oriented MnO_2 was about 3.5 V at a restricted capacity of 1000 mA h g^{-1} , which was lower than that of the (11-2)-oriented one ($\sim 4.0 \text{ V}$). The superior performance of the (002)-oriented α - MnO_2 material could be attributed to the uniform and abundant surface oxygens from the potentially exposed surfaces ((100), (110), (210) and (310)), which reacted with Li^+ and O_2 in one step.

It was also demonstrated that the storage of Li_2O_2 could be realized in the $2 \times 2 \text{ MnO}_6$ octahedral channel in α - MnO_2 .

Trahey *et al.* demonstrated that the storage of Li_2O_2 in the 2×2 MnO_6 octahedral channel was in agreement with the production of Li_2O_2 and Li^+ intercalation.³⁰⁶ At the same time, the species, including of Li^+ , O_2 and Li_xO_y , could be rapidly transported within the channels, and in this way Li_2O_2 was then deposited on the surfaces. The porous framework of $\alpha\text{-MnO}_2$ provided a large space to accommodate the readily reversible Li_xO_y within the 2×2 tunnels, while the “ $\text{Li}_x\text{O}_y\text{-MnO}_2$ ” structures possibly acted as intermediates during the discharge and charge reactions.

Due to the existing MnO_6 tunnels in $\alpha\text{-MnO}_2$, Li^+ insertion was accompanied with the formation of Li_2O_2 on a MnO_2 -based cathode in a Li-O_2 battery.³⁰² In line with this, Chan *et al.* demonstrated the concept of a hybrid Li-ion/Li-O_2 battery with a $\alpha\text{-MnO}_2$ cathode in coin cells. By performing *in situ* high-energy synchrotron X-ray diffraction tests, the storage of Li_xO_y in “ 2×2 ” MnO_6 tunnels was confirmed experimentally.⁹¹ When the cell was operated under an Ar atmosphere, the lithium insertion/extraction reactions in $\alpha\text{-MnO}_2$ were partially reversible, with the electrode cycling being between ~ 0.35 and ~ 0.80 Li-content per MnO_2 after the first cycle (Fig. 47). In contrast, competitive reactions occurred between lithium insertion and the oxygen reduction under O_2 atmosphere at the cathode, and hence the cell showed the characteristics of both Li-ion and Li-O_2 batteries. This proved that the insertion of Li_xO_y in the “ 2×2 ” tunnels of MnO_2 really occurred.

4.3.1.1.2 $\alpha\text{-MnO}_2$ catalyst towards electrolyte decomposition. Although the $\alpha\text{-MnO}_2$ -based cathode has shown outstanding catalytic activity towards Li_2O_2 formation/decomposition, the degradation of organic electrolytes on such a cathode should be carefully considered.³⁰⁷

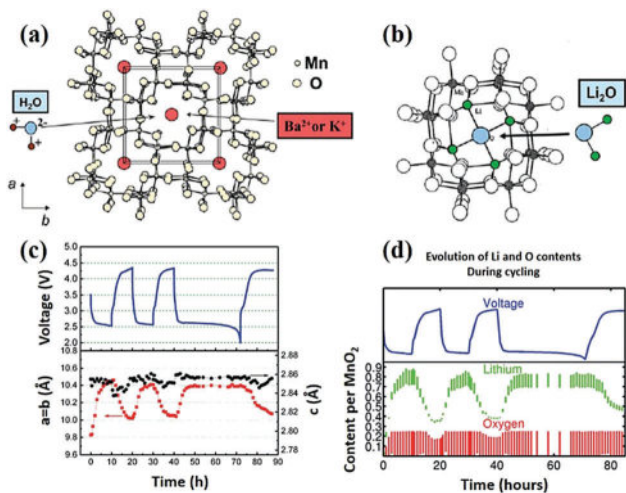


Fig. 47 The structures of $\alpha\text{-MnO}_2$ as represented by the minerals: (a) hollandite (Ba-stabilized) and cryptomelane (K-stabilized) and (b) lithia-stabilized $\alpha\text{-MnO}_2$; (c) three cycles of $\text{Li}/\alpha\text{-MnO}_2\text{-O}_2$ cells (top) during which the lattice parameter of the $\alpha\text{-MnO}_2$ electrode/catalyst were determined, *in situ*, by synchrotron XRD (bottom); (d) the changes of Li (green) and O (red) contents during cycling as deduced from XRD tests and DFT calculation model.⁹¹ Reprinted with permission from ref. 91. Copyright 2015 Royal Society of Chemistry.

Bruce *et al.* showed that the main discharge product was Li_2O_2 , accompanied with Li_2CO_3 , HCO_2Li and CH_3COOLi , with pure carbon as the cathode at the end of the 1st discharge of the battery. In comparison, the main discharge products with $\alpha\text{-MnO}_2$ as the cathode catalyst were Li_2O_2 and LiOH , as shown by powder X-ray diffraction and Fourier transform infrared spectroscopy (FT-IR). However, FT-IR spectra revealed the presence of HCO_2Li , $\text{CH}_3\text{CO}_2\text{Li}$ and Li_2CO_3 at the $\alpha\text{-MnO}_2$ -based cathode.²⁹ The extent of electrolyte degradation accompanied with Li_2O_2 formation on discharge was obviously increased when using $\alpha\text{-MnO}_2$ as the catalyst. Therefore, the negative effect of the $\alpha\text{-MnO}_2$ catalyst on the acceleration of electrolyte degradation should be carefully considered when it is used as a cathode material in Li-O_2 batteries.

4.3.1.2 $\delta\text{-MnO}_2$ catalyst

4.3.1.2.1 Catalytic activity of $\delta\text{-MnO}_2$. $\delta\text{-MnO}_2$ generally tends to crystallize into ultrathin nanosheets in the liquid synthesis process, which is potentially useful to create dense metal sites and porous channels for high catalytic activity and fast mass transport.³⁰⁸ Moreover, these properties could also increase the storage space of Li_2O_2 products. Yan's group prepared two kinds of cathodes: submicron $\delta\text{-MnO}_2$ with a low specific surface area ($31.7 \text{ m}^2 \text{ g}^{-1}$) mixed with KB carbon ($1400 \text{ m}^2 \text{ g}^{-1}$) and core-shell-structured porous $\delta\text{-MnO}_2$ -nanosheets/carbon-fibres ($\delta\text{-MnO}_2/\text{CFs}$) ($117.5 \text{ m}^2 \text{ g}^{-1}$) mixed with XC-72 carbon ($142.7 \text{ m}^2 \text{ g}^{-1}$).^{217,309} At low current densities, the discharge products formed on the KB and XC-72 electrodes both had a toroidal morphology. The morphology of the discharge products though was changed to vertical nanosheets on the $\delta\text{-MnO}_2/\text{KB}$ electrode. In comparison, the discharge products on $\delta\text{-MnO}_2/\text{CFs}$ exhibited micron-sized aggregations assembled with nanorod-like Li_2O_2 randomly dispersed on the electrode surface. This difference indicated that $\delta\text{-MnO}_2$ promoted the transport of superoxide species during the ORR process, whereupon the carbon defect sites acted as the primary nucleation sites for the growth of Li_2O_2 on the $\delta\text{-MnO}_2/\text{KB}$ electrode.^{310,311} When the carbon surface was completely covered by $\delta\text{-MnO}_2$, the lack of nucleation sites resulted in the random distribution of Li_2O_2 aggregations.

Banerjee *et al.* carefully studied the catalytic mechanistic of $\delta\text{-MnO}_2$ monolayers.³¹² In the absence of applied potentials, the $\delta\text{-MnO}_2$ monolayer preferentially reacted with Li ions instead of O_2 molecules to initiate the formation of LiO_2 , and then the discharge products (LiO_2 and Li_2O_2 molecules) strongly interacted with the MnO_2 monolayer *via* the stabilization of Li-O chemical bonds with lattice oxygen atoms. This confirmed that the Li_2O_2 film was homogeneously deposited onto the $\delta\text{-MnO}_2$ surface, where the $\text{Li}_2\text{O}_2/\text{MnO}_2$ interface acted as an electrical conductor. It should be noted that the layered $\delta\text{-MnO}_2$ (birnessite) usually contains a large amount of K^+ (or Na^+ , according to the reactants) and the molecular formula should really be $\text{K}_x\text{MnO}_2 \cdot n\text{H}_2\text{O}$.³¹³ Therefore, the surface of $\delta\text{-MnO}_2$ nanosheets should be negatively charged, such that electrostatic repulsion might exist between the superoxide and $\delta\text{-MnO}_2$.³¹⁴

4.3.1.2.2 $\delta\text{-MnO}_2$ catalyst with good mass transport and Li_2O_2 storage. Loading $\delta\text{-MnO}_2$ nanosheet on 3D porous substrates

could be an effective protocol to increase the exposed catalytically active sites and Li_2O_2 deposition space. Consequently, Wang *et al.* prepared an *in situ* growth of $\delta\text{-MnO}_2$ nanoflakes on GNSs as an electrode catalyst.³¹⁵ The cell discharge and charge overpotentials in a battery using this catalyst decreased by 50 mV and 70 mV at a current density of 100 mA g^{-1} in comparison with that of a GNS electrode, respectively. Moreover, the terminal discharge and charge voltages of the cell were relatively constant at 2.5 V and 4.0–4.5 V during the cycling test under 1000 mA h g^{-1} , respectively. In contrast, the cell with the GNS electrode was polarized to 2 V and 5 V, respectively. The combination of MnO_2 nanoflakes with $\delta\text{-MnO}_2$ nanoflakes/GNS delivered excellent cell performances, which could be ascribed to the high catalytic activity of MnO_2 and the good conductivity and large open space of 3D-GNS to facilitate the catalytic reactions.

Han *et al.* also grew $\delta\text{-MnO}_2$ uniformly on hierarchically porous carbon (HPC) as a cathode for a Li-O_2 battery.³¹⁷ The cell exhibited a low charge overpotential ($\sim 0.68 \text{ V}$ at 100 mA g^{-1} under 1000 mA h g^{-1}) and a good rate capacity (2260 mA h g^{-1} at 5 A g^{-1}) as well as a long cycle stability up to 300 cycles with the controlled capacity of 1000 mA h g^{-1} at 350 mA g^{-1} . The superior performance and stability of cells with $\delta\text{-MnO}_2/\text{HPC}$ could be attributed to its intrinsic ORR/OER catalytic activity, unique architecture, the favourable morphology of Li_2O_2 and the reduced side reactions. Xie *et al.* loaded flower-like $\delta\text{-MnO}_2$ on NiFM/graphene to protect the carbon surface (Fig. 48).³¹⁶ The battery yielded a capacity of 3660 mA h g^{-1} at 0.083 mA cm^{-2} , and sustained 132 cycles at a capacity of 492 mA h g^{-1} and a charge overpotential of about 1 V at a high current density of 0.333 mA cm^{-2} .

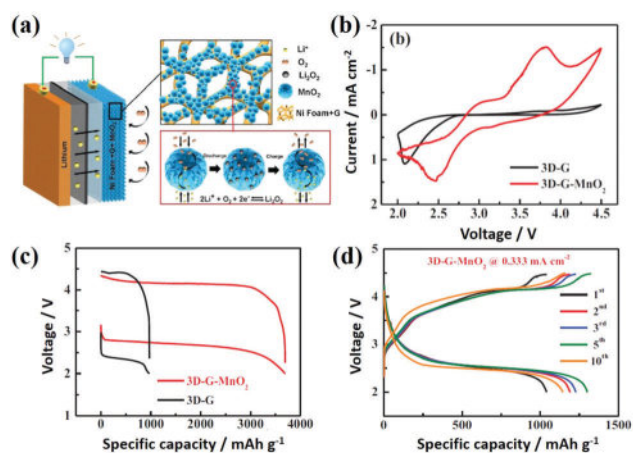


Fig. 48 (a) Schematic illustration for the structure and working mechanism of Li-O_2 battery with three-dimensional graphene/ $\delta\text{-MnO}_2$ /Ni foam (3D-G-MnO₂-NiFM) electrode; (b) CV curves of 3D-G and 3D-G-MnO₂ electrodes between 2.0 and 4.5 V at 0.1 mV s^{-1} ; (c) discharge-charge curves at a current density of 0.083 mA cm^{-2} of Li-O_2 batteries with 3D-G-NiFM electrode and 3D-G-MnO₂-NiFM electrodes at 2.0–4.5 V; (d) cycling performance of Li-O_2 batteries with 3D-G-MnO₂-NiFM electrode under a current density of 0.333 mA cm^{-2} at 2.0–4.5 V.³¹⁶ Reprinted with permission from ref. 316. Copyright 2014 Wiley-VCH Verlag GmbH & Co. KGaA.

4.3.1.3 $\epsilon\text{-MnO}_2$ catalyst. Chen *et al.* electrodeposited $\epsilon\text{-MnO}_2$ on a NiFM substrate as a cathode for a Li-O_2 battery.³¹⁸ The battery exhibited a high rate capability (discharge capacity of 6300 mA h g^{-1} at a current density of 500 mA g^{-1}) and enhanced cyclability (over 120 cycles with a stable capacity of 1000 mA h g^{-1}) without controlling the discharge depth. The charge/discharge overpotential gap of the battery was close to 2 V. The authors further decreased the cell overpotential gap by using hierarchical porous $\epsilon\text{-MnO}_2$ nanostructures on NiFM as the cathode, which was prepared by an oxygen bubble template-assisted electrodeposition route.³¹⁹ The battery with the hierarchical cathode delivered an overpotential gap below 1 V, as well as a capacity of 5000 mA h g^{-1} at 500 mA g^{-1} and over 200 cycles under 800 mA h g^{-1} (500 mA g^{-1}). The superior performance of the $\epsilon\text{-MnO}_2/\text{Ni}$ electrode was proposed to be associated with the 3D nanoporous structures, abundant oxygen defects (structure defects) and the absence of side reactions.

4.3.1.4 Other manganese oxide catalysts. The creation of a Mn(III) or oxygen vacancy is one key strategy to improve the electronic conductivity of MnO_2 , which is beneficial for increasing the exposed active site density.³²⁰ Luo's group studied the catalytic activity of MnO_x on nitrogen-doped carbon (m-N-C) and CNTs.³²¹ The $\text{MnO}_x/\text{m-N-C}/\text{KB}$ electrode delivered a high specific capacity of 7600 mA h g^{-1} at 200 mA g^{-1} and offered lower charge overpotentials compared to that of KB carbon under 800 mA h g^{-1} . The improved cell performance could be attributed to the superior catalytic activity of MnO_x and the facile electron transfer between MnO_x and the carbon substrate. Zhang *et al.* synthesized a series of metal-MOF materials as cathode catalysts for a Li-O_2 battery, in which Mn-MOF-74 endowed the battery with a high specific capacity of 9420 mA h g^{-1} , more than four times higher than those of a cell without the

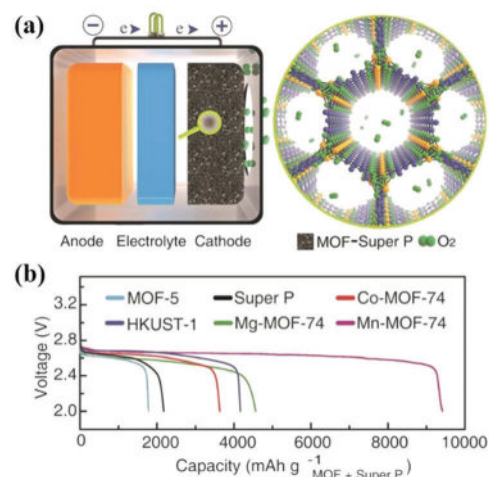


Fig. 49 (a) Schematic illustration of a Li-O_2 cell using MOF-Super-P composite as the O_2 electrode (oxygen molecules relative sizes reduced for clarity); (b) the discharge profiles of Li-O_2 cells using MOF/Super-P-carbon composites and Super-P-carbon under O_2 atmosphere with a current density of 50 mA g^{-1} at room temperature.³²² Reprinted with permission from ref. 322. Copyright 2014 Wiley-VCH Verlag GmbH & Co. KGaA.

MOF support (Fig. 49).³²² *In situ* O₂ and CO₂ evolution measured by DEMS on cell charging indicated a high reversibility of the Li–O₂ battery with the Mn–MOF catalysts.

Zhao *et al.* prepared a MnO_{2–x} nanosheets/stainless steel (SS) electrode with a high content of Mn(III) and oxygen vacancies through an ethanol reduction method.³²⁰ As a result, the cell with the MnO_{2–x}/SS electrode showed a rechargeable capacity of 7300 mA h g^{–1} at a current density of 200 mA g^{–1}, which was 39% higher than that with the MnO₂/SS electrode. In addition, the specific capacities at 400 mA g^{–1} and 800 mA g^{–1} reached 5249 mA h g^{–1} and 2813 mA h g^{–1}, respectively, which were over 30% higher than that of the cell with the MnO₂/SS electrode. Furthermore, the cycling tests showed no change in the discharge/charge overpotentials for 120 cycles, suggesting the good stability of this MnO_{2–x}/SS cathode.

Jin *et al.* presented MnO_x-decorated CeO₂ nanorods *via* an *in situ* redox reaction between KMnO₄ and a Ce(OH)CO₃ nanorod template, which acted as a highly active cathode catalyst for a lithium–air battery.³²⁴ The battery with the MnO_x@CeO₂ catalysts showed good performance, with a high first discharge specific capacity (2617 mA h g^{–1} at 100 mA g^{–1}), a low charge overpotential (about 1 V), good rate capability (1500 mA h g^{–1} at 400 mA g^{–1}) and good cycle stability (only 1.1% voltage loss after 30 circles at a specific capacity of 1000 mA h g^{–1} with 200 mA g^{–1}). The improved performance was proposed to be a result of the enhanced catalytic activity due to the increased electrical conductivity and the mixed valence of Mn.

Cheng *et al.* further studied the ORR and OER catalytic properties of lithiated MnO_x.³²³ The catalytic activity was found to be correlated with the composition of the Li_xMnO₂ electrodes (0 < x < 1) owing to changes in the Mn valence and electronic structure in aprotic Li–MnO₂ cells. As shown in Fig. 50, the modestly lithiated Li_{0.50}MnO₂ exhibited excellent performance with a round-trip efficiency of *ca.* 76%, a high cycling ability of under 1000 mA h g^{–1} at 200 mA g^{–1} for 190 cycles (based on carbon mass) and a high discharge capacity of 10 823 mA h g^{–1} at 100 mA g^{–1}.

4.3.2 Cobalt oxide catalyst. Cobalt oxide (CoO_x) has been confirmed as an effective ORR and OER catalyst in aqueous media,^{325,326} revealing that CoO_x is a potential cathode material in Li–O₂ batteries.^{102,159,327,328} Table 5 summarizes the performance of batteries with typical CoO_x materials, showing a comparison based on the different morphologies, facets and defects, pore structure and active site density of CoO_x.

4.3.2.1 Catalytic activity of CoO_x. As early as 2007, Bruce *et al.* evaluated the catalytic activity of Fe₃O₄, CuO, Fe₂O₃, Pt, NiO and Co₃O₄ towards discharge and charge processes in a Li–O₂ battery (1 M LiPF₆ in propylene carbonate). They reported that the Co₃O₄/Super-P-carbon electrode exhibited good performance from the viewpoint of initial capacity (2000 mA h g^{–1}) and capacity retention (6.5% per cycle).³²⁹ This good battery performance stimulated numerous researchers to further investigate CoO_x as a potential cathode material in Li–O₂ batteries. Consequently, several groups deposited Co₃O₄ nanoparticles on different carbon supports, including rGO and KB, as cathode

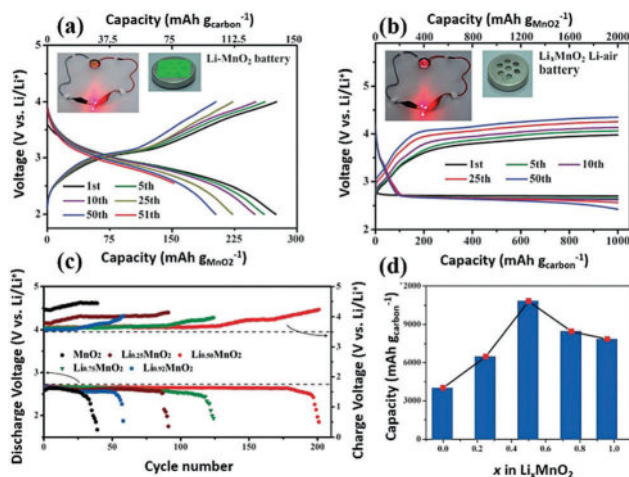


Fig. 50 Discharge/charge profiles of (a) Li–MnO₂ battery and (b) Li–O₂ cell with mesoporous MnO₂-based electrodes (the Li–MnO₂ cell was cycled between 2.0 and 4.0 V for 50 cycles and ceased to a discharged state of Li_{0.50}MnO₂; the same cell was then exposed to air and was discharged and charged at a current density of 100 mA g_{carbon}^{–1}; insets showed photographs of the assembled batteries powering light-emitting diodes); (c) terminal discharge/charge voltage vs. cycle number at a current density of 200 mA g_{carbon}^{–1} and a controlled capacity of 1000 mA h g_{carbon}^{–1}; (d) discharge capacities at 100 mA g_{carbon}^{–1} with a cut-off voltage of 2.2 V.³²³ Reprinted with permission from ref. 323. Copyright 2015 Wiley-VCH Verlag GmbH & Co. KGaA.

materials in a Li–O₂ battery.³³⁰ The Li–O₂ battery with the carbon/Co₃O₄ composite exhibited a lower charge voltage and higher cyclability than the carbon-based cathodes, which was due to their good OER activity. The stability of cobalt-oxide-based cathodes could be improved through decorating dense cobalt oxide on carbon materials, which inhibits the corrosion of carbon materials.

The performance of the CoO_x-based cathode could be improved through modulation of the pore structure, which is beneficial for increasing the active site density and mass transport. Yan *et al.* designed a core–shell structured Co/CoO nanoparticles-decorated carbonized melamine foam-graphene (CMF-G) as the electrode for a Li–O₂ battery (Fig. 51).³³¹ In this CMF-G-Co/CoO cathode, Co/CoO was used as the preservative of carbon and induced Li₂O₂ growth on the surface of the Co/CoO surface instead of on the carbon surface. The cells with this Co/CoO cathode achieved 70 cycles at a current density of 100 mA g^{–1} under a fixed capacity of 500 mA h g^{–1} in contrast to those of CMF-G electrodes with only 20 cycles.

Zhou *et al.* prepared a type of highly graphitic porous carbon–Co₃O₄ (GPC–Co₃O₄) material by executing a two-step annealing of core–shell structured MOFs.³³² The low graphitic carbon cores were selectively removed during the secondary annealing in an air atmosphere, leaving voids in the interior voids due to their lower thermal stability compared with the graphitic carbon shells. When GPC–Co₃O₄ was used as the cathode for a Li–O₂ battery, it exhibited a constant discharge plateau and a slightly increased charging plateau from the current density of 250 mA g^{–1} to 1250 mA g^{–1} at a defined capacity of 500 mA h g^{–1}. Meanwhile, the cell performed with good cycling

Table 5 Performance summary of Li–O₂ batteries with a CoO_x-based electrode and their operating conditions

CoO _x	Specific design	Discharge voltage (V)	Charge voltage (V)	Limited capacity/cycles (mA h g ⁻¹ /times)	Mass and current density (mg cm ⁻² /mA g ⁻¹)	Full discharge capacity (mA h g ⁻¹)	Electrolyte	Ref.
CoO _x	Co/CoO/graphene	~2.75 ^b	~4.25 ^b vs. ~4.05 ^a vs. ~4.25 ^b KB	500 _{CoO_x/C} /70 (vs. 500 _C /10)	0.7/100 _{CoO_x/C}	~5800 _{CoO_x/C} (vs. ~2700 _C , KB)	1.0 M LiCF ₃ SO ₃ in TEGDME	331
CoO _x with facet and defect	Carbon-dotted defective CoO	~2.55 ^a (vs. ~2.50 _{CoO})	—	1000 _C /50 (vs. 1000 _C /30 _(CoO+C))	1.2/200 _C	~5500 _C (vs. ~4000 _C , CoO/C)	1.0 M LiTFSI in TEGDME	333
1D CoO _x with carbon	Co ₃ O ₄ nanofiber/graphene (CNG)	~2.70 ^{a,b} (vs. ~2.60 _{Co₃O₄ particle})	~3.80 ^a vs. ~3.90 ^a vs. ~4.20 _{Co₃O₄ particle}	1000 _{CNG} /80 (vs. 1000 _{Co₃O₄/C} /30 _(Co₃O₄/C))	1.0/200 _{CNG}	~10 500 _{CNG} (vs. ~2000 _{Co₃O₄/C} , Co ₃ O ₄ /C)	1.0 M LiTFSI in TEGDME	335
3D CoO _x with carbon	Co ₃ O ₄ nanosheet/carbon paper	~2.60 ^b (vs. ~2.50 _{Co₃O₄/CP})	~4.20 ^b vs. ~4.40 _{Co₃O₄/CP}	500 _{CoO_x} /50	1.5/100 _{CoO_x}	~2160 _{CoO_x} (vs. ~3300 _{CoO_x} , Co ₃ O ₄ /CP)	1.0 M LiCF ₃ SO ₃ in TEGDME	340
3D CoO _x without carbon	Co ₃ O ₄ nanowire/Ni foam	~2.80 ^b (vs. ~2.80 ^{a,b})	~3.90 ^b (vs. 4.30 _{Co₃O₄/KB}) vs. ~3.40 ^{a,b} (vs. ~3.95 _{Co₃O₄})	1 mA h _{CoO_x} / > 10	~1.88/0.05 mA cm ⁻²	~4530 _{CoO_x} (vs. ~2700 _{CoO_x} , Co ₃ O ₄ /CP)	1.0 M LiClO ₄ in DMSO	197
				1000 _{CoO_x} /160	0.33/100 _{CoO_x}	~11 000 _{CoO_x}	0.5 M LiClO ₄ in DMSO	346

Notes: ^a Full discharge/charge voltages at half full capacity. ^b Discharge/charge voltages at half the limited capacity.

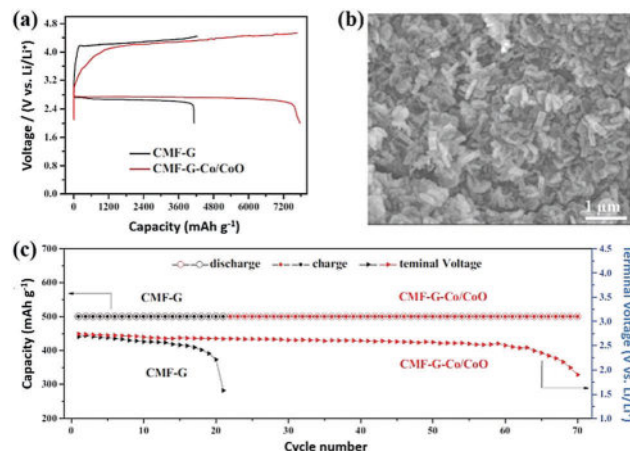


Fig. 51 (a) Charge–discharge curves of Li–O₂ batteries with CMF-G or CMF-G-Co/CoO sample at 50 mA g⁻¹; (b) SEM images of the fully discharged CMF-G-Co/CoO electrodes; (c) the cyclability of CMF-G-Co/CoO and CMF-G electrodes at 100 mA g⁻¹ with a limited capacity of 500 mA h g⁻¹.³³¹ Reprinted with permission from ref. 331. Copyright 2016 Wiley-VCH Verlag GmbH & Co. KGaA.

stability over 50 cycles with constant charge/discharge terminal voltages. The good performance could be attributed to the high electron conductivity and high graphitization degree of GPC, the superb catalytic performance of Co₃O₄ and the meso-/macroporous structure of the material.

4.3.2.2 Catalytic activity of CoO_x with different facets and defects. It was reported that the catalytic activity of CoO_x was related to its exposed crystal faces.³²⁷ Su *et al.* synthesized single-crystalline Co₃O₄ nanoparticles with different exposed crystal planes.³³³ The correlation between the different Co₃O₄ crystal planes and the reduced charge–discharge overpotentials followed the trend: (100) < (110) < (112) < (111). This was related to the density of dangling bonds of Co³⁺ ions, as calculated through the DFT method. Liu *et al.* also confirmed this concept. Co₃O₄ octahedra with an exposed (111) plane showed much higher specific capacity, cycling performance and rate capability than the Co₃O₄ cube with an exposed (001) plane in a Li–O₂ battery. They attributed the different performance to the richer Co²⁺ on the (111) plane of Co₃O₄ octahedra instead of the Co³⁺ effect reported in Su's work.³³³

The generation of oxygen vacancies on the surface of CO_x could be another strategy to increase its catalytic activity, essentially due to the increased electrical conductivity and promoted formation of Li₂O₂. Liu *et al.* prepared carbon-dotted defective CoO with oxygen vacancies (CoO/C) to further enhance the electrocatalytic activity of CoO.³³⁴ In comparison with carbon or oxygen-vacancies-only CoO, the CoO/C-based cathode had a better cycling stability (50 cycles for the CoO/C-based cathode vs. 30 cycles for the CoO-based cathode under 1000 mA h g⁻¹ at 200 mA g⁻¹), initial capacity (7000 mA h g⁻¹ vs. 5100 mA h g⁻¹ at 100 mA g⁻¹) and rate capability as well as a low charge overpotential. This could be attributed to the synergetic effect of the dotted carbon species and oxygen vacancies, which enhanced the mobility of e⁻ and Li⁺ and bound them to O₂ and Li₂O₂.

4.3.2.3 Theoretical analysis of CoO_x catalysts. Cui *et al.* investigated the critical role of CoO on the OER process during Li-O_2 battery operation.³³⁶ Through DFT calculations, they found that the intermediate LiO_2 tended to adsorb on the CoO surface rather than the carbon surface. Thus, the $\text{CoO}/\text{Super-P}$ cathode exhibited a much longer cycle life over 300 times ($1000 \text{ mA h g}_{\text{carbon}}^{-1}$ at 0.04 mA cm^{-2}) that of pure carbon. Meanwhile, first-principles calculations indicated that $\text{Co}_3\text{O}_4(111)$ had a lower activation barrier for O_2 desorption compared to $\text{Co}_3\text{O}_4(001)$ in the OER, which was very important to refresh the active sites. To further identify the catalytically active sites of Co_3O_4 for the OER process in Li-O_2 batteries, a (100) faceted Co_3O_4 cube enclosed by only a Co^{2+} site and a (112) faceted Co_3O_4 plate with an exposed Co^{3+} site were studied as catalysts for Li-O_2 batteries.³³⁷ It was found that the Co^{3+} site played a crucial role in determining the adsorption properties of the reactants, and that the Co_3O_4 plate enabled a high round-trip efficiency and cyclic stability, as well as having an influence on the Li_2O_2 morphology.

Zhu *et al.* constructed an interfacial model to study the decomposition mechanism of Li_2O_2 on Co_3O_4 surfaces.³³⁸ The computational results indicated that the O-rich $\text{Co}_3\text{O}_4(111)$ with a relatively low surface energy had a high catalytic activity in reducing the O_2 desorption barrier and the charge overpotential, which was due to the fast electron transfer from the Li_2O_2 layer to the underlying catalyst surface. Meanwhile, the basic sites on the $\text{Co}_3\text{O}_4(110)$ surface induced Li_2O_2 decomposition into Li_2O and a dangling Co-O bond, leading to a high charge overvoltage in subsequent cycles. The calculations for transition-metal-doped $\text{Co}_3\text{O}_4(111)$ indicated that the p-type doping of $\text{Co}_3\text{O}_4(111)$ exhibited significant catalytic activity in decreasing both the charging overpotential and O_2 desorption barrier.

4.3.2.4 Cobalt oxide catalyst with good mass transport and Li_2O_2 storage. The construction of one-dimensional (1D) Co_3O_4 materials might be a good protocol to further improve their catalytic activity, mass transport efficiency and Li_2O_2 storage ability.³³⁹ For instance, Jeon *et al.* prepared a hybrid film with electrospun 1D Co_3O_4 nanofibres immobilized on both sides of 2D graphene nanoflakes (GNFs) to construct a cathode for a Li-O_2 battery (Fig. 52), which could then deliver a high discharge capacity of $10\,500 \text{ mA h g}^{-1}$ and a long-term cyclability for 80 cycles with a limited capacity of 1000 mA h g^{-1} at 200 mA g^{-1} .³³⁵ This good battery performance could be attributed to the improved catalytic activity of 1D Co_3O_4 nanofibres with a large surface area and facile electron transport *via* the interconnected GNFs.

The construction of a 3D-structured Co_3O_4 electrode might provide a more efficient transport channel and open space for Li_2O_2 formation and decomposition. Zhang *et al.* directly grew Co_3O_4 nanosheets with pore diameters of about 4–8 nm on CP ($\text{CP}/\text{Co}_3\text{O}_4$).³⁴⁰ A cell with the $\text{CP}/\text{Co}_3\text{O}_4$ electrode delivered 2159 mA h g^{-1} at 100 mA g^{-1} and over 40 stable cycles under 500 mA h g^{-1} . Simultaneously, film-like Li_2O_2 was observed during the cycling test. Yan *et al.* prepared different types of Co_3O_4 nanoarrays on CP, including single-crystal Co_3O_4 rectangular nanosheets, polycrystal nanowires and single-crystal hexagonal nanosheets.³⁴¹ A Li-O_2 battery with Co_3O_4 rectangular nanosheets exhibited the best electrocatalytic performance among all of the nanostructured electrodes, such as a high specific capacity (1300 mA h g^{-1} at 50 mA g^{-1}) and good cycling stability over 54 cycles at 100 mA g^{-1} . The high performance of the battery was related to the porous structure (mesopores on the surface), large specific surface area ($230 \text{ m}^2 \text{ g}^{-1}$) and high activity of the exposed (112) plane. In this work, the charging

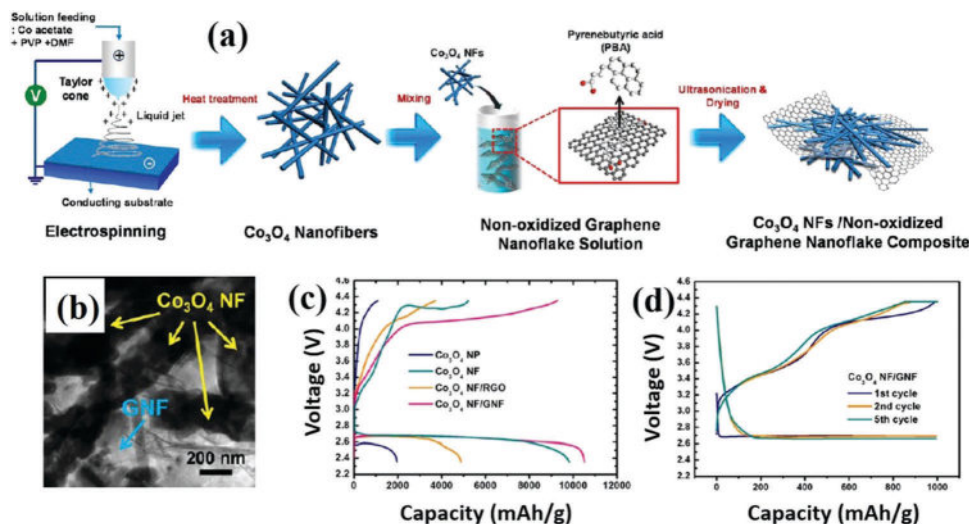


Fig. 52 (a) Schematic illustration for the synthetic procedures of Co_3O_4 nanofibre/graphene nanoflake (NF/GNF) composite; (b) TEM images of Co_3O_4 NF/GNF composite; (c) initial charge/discharge curves of cells with Co_3O_4 nanoparticle (NP), Co_3O_4 nanofibre (NF), Co_3O_4 nanofibre/reduced graphene oxide (NF/RGO) composite, and Co_3O_4 NFs/GNF composite in a voltage window between 4.35 and 2.35 V at a current density of 200 mA g^{-1} ; (d) charge and discharge behaviour of Co_3O_4 NF/GNF composite at the 1st, 2nd, 5th cycles under fixed capacity of 1000 mA h g^{-1} as in the voltage window between 4.35 and 2.00 V at a current density of 200 mA g^{-1} (capacity on catalyst + carbon + binder mass).³³⁵ Reprinted with permission from ref. 335. Copyright 2013 American Chemical Society.

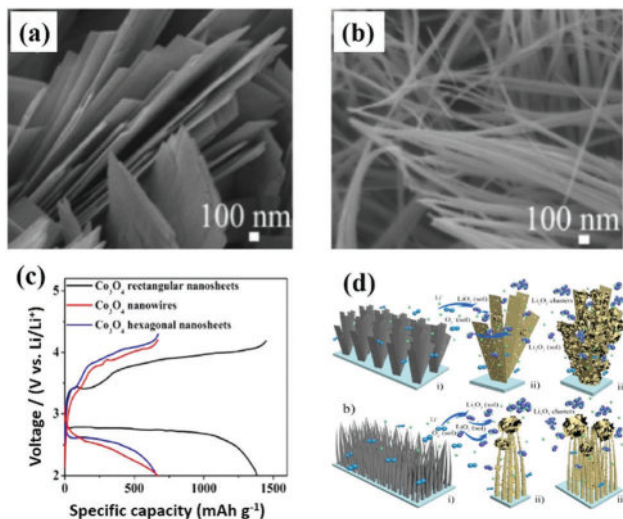


Fig. 53 SEM images of Co_3O_4 (a) nanosheets and (b) nanowires on carbon paper; (c) discharge/charge profiles of Li– O_2 batteries with Co_3O_4 rectangular nanosheets, nanowires, and hexagonal nanosheets at a current density of 50 mA g^{-1} ; (d) schematic illustration for the formation of Li_2O_2 product on the surfaces of Co_3O_4 nanosheet and nanowire electrodes.³⁴¹ Reprinted with permission from ref. 341. Copyright 2016 American Chemical Society.

potentials were found to be affected by the evolved Li_2O_2 morphology. As shown in Fig. 53, Li_2O_2 can be uniformly nucleated on single Co_3O_4 nanosheets, with the homogeneously large flower-like Li_2O_2 embedded between the nanosheets. During the charging process, the film-like Li_2O_2 can be easily decomposed, resulting in a low charging voltage below 3.5 V. In contrast, the decomposition of the large flower-like Li_2O_2 cluster needs a higher charging voltage (3.8 V). On the nanowire electrode, Li_2O_2 was mainly produced at the top region of the nanowires, while a similar flower-like morphology was formed on the surface of nanowires. Corresponding to the profiles, there was only one charging plateau for the nanowire sample.

4.3.2.5 Cobalt oxide catalyst with good stability. Good stability of the oxygen electrode in the presence of active intermediates is essential to produce a reversible Li– O_2 battery, and for this, porous nickel foam (NiFM) has been widely used as a current collector to construct a stable carbon-free CoO_x -based cathode. 1D cobalt oxide nanostructures, for example nanorods and nanowires, were grown on NiFM for fast mass transport in a Li– O_2 battery.²⁶⁸ Cui *et al.* uniformly and vertically grew Co_3O_4 nanorods on NiFM with diameters around 250 nm and a loading mass of about 8 mg cm^{-2} .³⁴² A cell with such a $\text{Co}_3\text{O}_4/\text{NiFM}$ electrode delivered 1880 mA h g^{-1} at 0.1 mA cm^{-2} with a charging voltage of 3.6 V. Then, Kim *et al.* grew Co_3O_4 nanowires on NiFM by a facile hydrothermal reaction (1.88 mg cm^{-2}), and the assembled cell achieved a high specific capacity of 4500 mA h g^{-1} at 0.05 mA cm^{-2} and a low charging voltage of about 3.5 V at an initial capacity of 0.5 mA h (0.1 mA cm^{-2} discharged to 1 mA h).¹⁹⁷ Interestingly, this cathode showed better cycle stability at a high current density (0.3 mA cm^{-2}) than at a low current density (0.1 mA cm^{-2}). The authors explained that Li_2O_2

produced in the top region of the nanowires array preferentially tended to form a large crystallite structure, where clustering of the nearby Li_2O_2 -coated NWs was useful for minimizing the surface energy of the Li_2O_2 crystallite to form a pointed-tip-brush-like structure. Under the condition of a high current density, Li_2O_2 tended to form a film closely covering the nanowires surface, resulting in an easier decomposition of Li_2O_2 and a better cycle stability.

Two-dimensional (2D) Co_3O_4 nanostructures, for example nanosheets and nanoflowers, were also grown on NiFM for their better Li_2O_2 storage in Li– O_2 batteries. Sun *et al.* investigated the influence of the pore structure of freestanding Co_3O_4 nanosheet on the cell performance.³⁴³ A battery constructed with the $\text{Co}_3\text{O}_4/\text{NiFM}$ electrode realized a high capacity of 2460 mA h g^{-1} , and performed more than 35 discharge/charge cycles with a capacity limitation of 1000 mA h g^{-1} . The enhanced performance was attributed to the macroporous channels surrounded by the Co_3O_4 nanosheet and the optimized mesopores in the flakes.

Chen *et al.* studied the influence of the thickness of freestanding Co_3O_4 nanosheets (NiFM substrate) on the electrochemical performance of Li– O_2 batteries.⁷¹ A battery based on these nanosheets with a thickness of 5 nm and surface mesopores of 2–10 nm exhibited a higher (200 mA g^{-1} , $11000 \text{ mA h g}^{-1}$) capacity and much longer cycle life (80 cycles under 500 mA h g^{-1}) than nanosheets with a thickness of about 40 nm (7000 mA h g^{-1}). It was found that the initially formed morphology of Li_2O_2 was thin films that stuck closely to the nanosheets. Then, as the films became thicker, a plate-like shape was formed upon the continued discharge to higher capacities. The hierarchical porous structure of the Co_3O_4 -nanosheets-based electrode was suggested to be the reason for the high capacity of this Li– O_2 battery.

Lee *et al.* systematically compared the performances of batteries with different nanostructured Co_3O_4 materials, such as nanosheets, nanoneedles and nanoflowers, on NiFM as cell cathodes.³⁴⁴ They found that the discharging voltage (around 2.75 V) and charging voltage (around 3.5 V) exhibited the same tendency, but the specific capacity was strongly dependent on the Co_3O_4 nano-architectures. The capacity decreased in the order of: nanosheet (1127 mA h g^{-1}) < nanoflower (1930 mA h g^{-1}) < nanoneedle (2280 mA h g^{-1}), which was different to that found in Yan's results.³⁴¹ This difference could possibly be explained by the different crystalline state and morphology of the Co_3O_4 nanosheets in the two reports. Moreover, the nanoneedle-like Co_3O_4 could sustain 50 cycles without any obvious change in the discharge/charge profiles under 500 mA h g^{-1} at 100 mA g^{-1} . This good performance could possibly be attributed to the nanostructured Co_3O_4 electrode having dense metal active sites, as well as a large amount of open space for Li_2O_2 storage.

To improve the conductivity of the CoO_x nanostructure, Wen *et al.* presented a core-shell structured nanosheet-like array with a metallic cobalt core and a cobalt oxide shell.³⁴⁵ As shown in Fig. 54, the core-shell-structured electrodes delivered a high discharge capacity of over $10000 \text{ mA h g}^{-1}$ at 100 mA g^{-1} with a

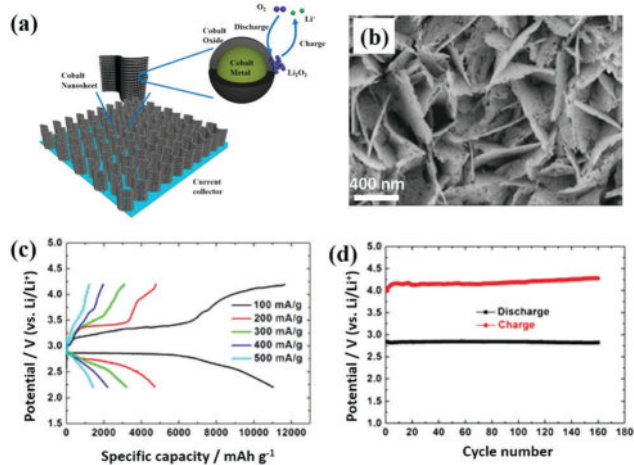


Fig. 54 (a) Schematic illustration of the core-shell structured Co@CoO_x based electrode during the discharge/charge process of Li-O₂ battery; (b) SEM image of Co@CoO_x nanostructured electrode; (c) discharge/charge curves of Co@CoO_x electrode at different current densities within the voltage window of 2.2–4.2 V (vs. Li⁺/Li); (d) the terminal voltage against the cycle number with Co cathode at 100 mA g⁻¹ and a capacity limitation of 1000 mA h g⁻¹.³⁴⁵ Reprinted with permission from ref. 345. Copyright 2016 American Chemical Society.

relatively low charging voltage below 3.5 V in the initial charge process, as well as outstanding cycle stability over 160 cycles (under 1000 mA h g⁻¹ at 100 mA g⁻¹).

4.3.3 Nickel oxide catalyst. As a type of efficient OER catalyst in aqueous media, nickel oxide has also been used as a cathode material in Li-O₂ batteries. He *et al.* developed mesoporous NiO nanosheets with a single-crystalline structure for use as a catalyst in an aprotic Li-O₂ battery.³⁴⁶ The recharge voltage plateau of a cell with the NiO-based electrode was ~3.95 V (1260 mA h g⁻¹ at 100 mA g⁻¹), and no obvious performance decay was observed even after 40 cycles with the limited capacity of 500 mA h g⁻¹. NiO nanosheets also exhibited good activity for the decomposition of Li₂O₂ (charge potential below 4 V) and Li₂CO₃ (above 4 V) as assessed through data analysis from X-ray photoelectron spectroscopy and gas chromatography-mass spectrometry analyses.

Wagemaker *et al.* presented NiO nanoseed crystallites as an electrode material to control the size and morphology of Li₂O₂ product.³⁴⁷ They showed that the hybrid hexagonal NiO nanoparticles and activated carbon electrode acted as seed crystals for the equiaxed growth of Li₂O₂, which was confirmed by elemental mapping scanning electron microscopy equipped with energy-dispersive X-ray spectroscopy. The experimental results and theoretical calculations identified that small amounts of NiO (~5 wt%) particles could act as the preferential sites for Li₂O₂ nucleation, effectively reducing the average size of the primary Li₂O₂ crystallites and promoting the growth of crystalline Li₂O₂. This observed phenomenon was due to the low interfacial energy for the formation of NiO-Li₂O₂.

The performance of the nickel-oxide-based cathode could be further improved by optimization of the porous structure. Chen *et al.* exploited Ni-based metal-organic frameworks as the

cathode catalysts in Li-O₂ batteries.³⁴⁸ They found that the as-prepared Ni-MOFs possessed a 3D micro-/nanostructure, open catalytic sites and a large specific surface area (1225 m² g⁻¹), which guaranteed the rapid transfer of O₂ and effective contact between the electrolyte and catalytic sites. Consequently, the battery with Ni-MOF catalysts exhibited an extremely high capacity of 9000 mA h g⁻¹ (0.12 mA cm⁻², capacity based on the mass of Ni-MOFs, VC-72, and binder), a high round-trip efficiency of 80% (600 mA h g⁻¹ at 0.12 mA cm⁻²) and a respectable cycling of 170 cycles without any obvious voltage drop.

4.3.4 Iron oxide catalyst. As a type of transition metal oxide, iron oxide has also been investigated as a cathode material for discharge/charge reactions in Li-O₂ batteries.^{134,285,349,350} Yan *et al.* prepared Fe₂O₃-nanocluster-decorated graphene as an oxygen electrode for a Li-O₂ battery, which delivered a discharge capacity of 8290 mA h g⁻¹ (capacity based on C + Fe₂O₃ + Li₂O₂ mass) and a round-trip efficiency of 65.9% in comparison to the corresponding parameters of 5100 mA h g⁻¹ and 57.5% for a pure graphene electrode. The good cell performance was proposed to be due to the high catalytic activity of Fe₂O₃ for oxygen reduction. However, the charging plateau of the battery was over 4.0 V.³⁵¹

To improve the catalytic activity of the iron-oxide-based electrode, a combination of conductive Fe metal and iron oxide was proposed for the cell cathode to take advantage of their better electrical conductivity. Wen *et al.* synthesized Fe@Fe₂O₃ core-shell nanowires as an oxygen electrode catalyst for Li-O₂ batteries.³⁵² The charging plateau of such a battery was reduced to 3.8 V and the cycle life was improved to 40 cycles under 1000 mA h g⁻¹ at 100 mA g⁻¹ (capacity based on Fe@Fe₂O₃ mass). The excellent properties of the Fe@Fe₂O₃ catalysts were attributed to their high surface area (53.2 m² g⁻¹) and electrical conductivity. Similarly, Amine *et al.* deposited core-shell the Fe@Fe₃O₄ nanocomposite on porous carbon as a cathode material for Li-O₂ batteries.³⁵³ As a result, the battery with this cathode could sustain 50 cycles under 500 mA h g⁻¹ at 100 mA g⁻¹ (capacity based on Fe/Fe₃O₄ + carbon mass).

4.3.5 Titanium oxide catalyst. TiO₂ is a semiconductor with low electrical conductivity, but this could be largely increased through generating oxygen vacancies in TiO₂ materials. It could therefore potentially be applicable as a cathode material for Li-O₂ batteries.^{354,355} Nazar *et al.* used a reduction method to produce metallic-Ti₄O₇ as a cathode material for a Li-O₂ battery.³⁵⁶ With this set-up, the OER occurred mainly within the charge potentials of 3.0–3.5 V due to the high electron conductivity and the formation of self-passivated sub-stoichiometric metal oxide layer. Wu *et al.* proposed an attractive TiO₂ material with sufficient oxygen vacancies as the cathode³⁵⁷ and demonstrated that the adsorption and dissociation of oxygen were facilitated due to the presence of defects, whereby the battery could sustain 372 cycles at a current density of 0.5 mA cm⁻² with a fixed specific capacity of 0.1 mA h cm⁻².

3D nanostructured TiO₂ has a big surface area and a porous channel suitable for the growth of a large quantity of Li₂O₂, which is beneficial for increasing the cell capacity. Zhang *et al.* fabricated a flexible Li-O₂ battery based on a cathode with TiO₂

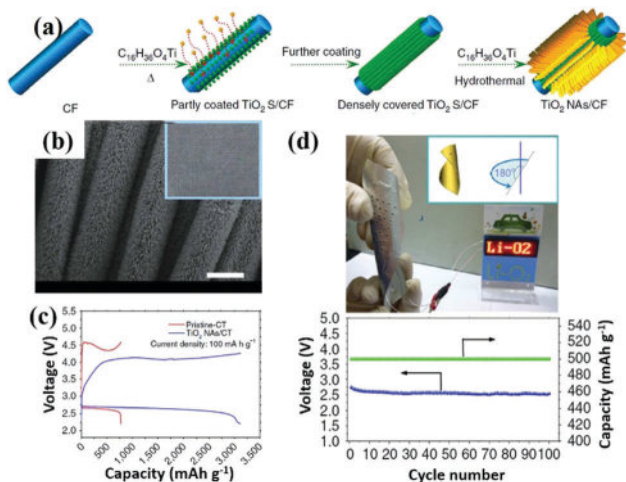


Fig. 55 (a) Scheme for the fabrication and structure of the TiO₂ nanowire arrays/carbon paper (NAs/CP) cathode; (b) SEM image and photograph (inset) of the obtained TiO₂ NAs/CP cathode (scale bar, 10 μm); (c) discharge/charge profiles of the Li-O₂ cells with pristine-CP and TiO₂ NAs/CP cathodes at a current density of 100 mA g⁻¹ (the cathodes were discharged with the cut-off voltage limited to 2.2 V and then recharged with the equivalent discharge capacity); (d) the performance of a Li-O₂ battery twisted to 180° (the corresponding variation of terminal discharge voltage vs. cycle number of Li-O₂ cells with TiO₂ NAs/CP cathode are shown at the bottom).¹⁵⁹ Reprinted with permission from ref. 159. Copyright 2013 Nature Publishing Group.

nanowire arrays (TiO₂/NA) directly grown onto CP.¹⁵⁹ Compared with the pristine-CP cathode, the discharge voltage and charge voltage of a Li-O₂ battery with the TiO₂ NA/CP cathode was higher by 160 mV and lower by 495 mV, respectively. Interestingly, the flexible Li-O₂ battery could be bent to 180° (Fig. 55), 360° or even more stringent conditions, while the cell terminal discharge voltage remained almost identical to the original one (about 2.5 V).

4.3.6 Other single metal oxide catalysts. In addition to the above-mentioned oxides, other types of single metal oxides, for example Cr₂O₃, CeO₂ and Cu₂O, have also been used as cathode materials for Li-O₂ batteries, whereupon these have exhibited specific characteristics for advanced Li-O₂ batteries.³⁵⁸ For example, Zhang *et al.* synthesized a hierarchical Cr₂O₃ octahedron decorated porous carbon (Cr₂O₃/OPC) cathode derived from a Cr-based metal-organic framework precursor.³⁵⁹ The Li-O₂ battery with the as-prepared cathode exhibited a discharge capacity of up to ~4800 mA h g⁻¹ at 0.1 mA cm⁻², a charging voltage plateau of 3.9 V and a cycle life of over 50 cycles at a fixed capacity of 800 mA h g⁻¹ (capacity based on Cr₂O₃ + carbon mass). Li *et al.* used an electrospinning technique combined with a pyrolysis method to prepare hexagonal close-packed Cr₂O₃ nanotubes.³⁶⁰ The synthesized mesoporous Cr₂O₃ nanotubes (Cr₂O₃-NT) with a surface area of 53.4 m² g⁻¹ were then applied as the catalysts for the oxygen electrode of a Li-O₂ battery, which then showed an astonishingly capacity of 8279 mA h g⁻¹ at 50 mA g⁻¹, and excellent cyclic stability of up to 50 cycles under 1000 mA h g⁻¹ at 100 mA g⁻¹ with a charging voltage of 3.78 V (capacity based on carbon mass). These results

highlighted the superior catalytic activity of Cr₂O₃-NT as the oxygen electrode, and could be attributed to their intrinsic catalytic activity together with their sophisticated 3D porous structure.

Byon *et al.* found an unexpected growth of Li₂O₂ film with a thickness of ~60 nm on CeO₂ nanoparticles decorated on a 3D CNTs electrode (50 mA g⁻¹).³⁵⁸ The growth of the Li₂O₂ film was divided into two steps: the initial Li₂O₂ nucleation process, based on the strong binding energy between the surface oxygen vacancies of CeO₂ NPs (diameter ≤ 5 nm) and the reactive oxygen species (e.g. O₂, O₂⁻ and O₂²⁻); the second step was related to the subsequent film growth of up to 40 nm. The thickness of the Li₂O₂ film was further increased up to ~60 nm with the addition of trace amounts of H₂O, which enhanced the solution free energy. In comparison to toroidal Li₂O₂ formed mainly from Li₂O(sol), the thick Li₂O₂ films were proposed to be beneficial for the higher reversibility and rapid surface decomposition during recharge.

Sun *et al.* developed self-supported cubic Cu₂O films with a Cu foam plate as the support through an electrochemical method, and this was then used as a cathode catalyst in Li-O₂ batteries.³⁶¹ It was shown that the discharge and charge voltages of the Cu₂O films cathode were about 2.5 V and 3.6 V under 1000 mA h g⁻¹ at 0.5 A g⁻¹, respectively, showing the better OER activity and higher stability than with carbon and Cu₂O powder catalysts. Furthermore, XPS analysis of the Cu₂O cathode indicated that there was no change in the Cu₂O materials before and after the cycling tests, leading to a long cycle life of the battery of over 100 times without any evident decay.

4.3.7 Binary metal oxides catalysts. Binary metal oxides, especially spinel oxides, have attracted a great deal of research interest with various applications in magnetism, electronics and catalysis, as well as energy storage and conversion.³⁶² The electronic conductivity of single metal oxides and the electronic structure of their metal sites can be tuned by the insertion of a second metal and oxygen defects, which are beneficial for an enhanced electron transfer ability and for optimizing the adsorption energetics of the intermediates.³⁶³ Table 6 summarizes a comparison of some cell parameters based on typical binary metal oxide materials, mainly based on the effects of the structure diversity and stability on the cell performance.

4.3.7.1 Nickel-cobalt oxide catalysts

4.3.7.1.1 Catalytic activity of NiCo₂O₄. Shao-Horn *et al.* compared the catalytic performance of Co₃O₄ and NiCo₂O₄ nanowires for discharge/charge reactions in a Li-O₂ battery.³⁶⁴ A NiCo₂O₄-based Li-O₂ battery delivered reduced overpotentials and enhanced cycling stability in comparison to Co₃O₄ nanowires, which was possibly due to the improved surface electrical conductivity of NiCo₂O₄. He *et al.* further prepared NiCo₂O₄ nanoparticles decorated on the surface of N-doped rGO with a high loading amount, which ensured the materials had a high oxide density for OER, and this prevented the side reactions between the N-rGO and Li₂O₂.³⁶⁵ Consequently, the battery fabricated with these materials exhibited a high full discharge/charge capacity at 200 mA g⁻¹ (about 7000 mA h g⁻¹, capacity based on carbon mass)

Table 6 Performance summary of Li–O₂ batteries with binary metal oxides-based electrodes and their operating conditions

Binary spinel oxides	Specific design	Discharge voltage (V)	Charge voltage (V)	Limited capacity/cycles (mA h g ⁻¹ /times)	Mass and current density (mg cm ⁻² /mA g ⁻¹)	Full discharge capacity (mA h g ⁻¹)	Electrolyte	Ref.
1D-NiCo ₂ O ₄ /carbon	NiCo ₂ O ₄ particles/ N-rGO	~2.75 ^a	~3.90 ^d	1000 _{CoO_x} /110	0.8/200 _{electrode}	~7000 _{NiCo₂O₄+C}	1.0 M LiTFSI in TEGDME	365
3D NiCo ₂ O ₄	3D foam-NiCo ₂ O ₄ / SP-carbon	~2.80 ^{a,b} (vs. ~2.70 _{SuperP})	~3.80 ^a , ~3.95 ^b (vs. ~4.05 ^a , ~4.25 _{SuperP})	1000 _C /80 (vs. 1000 _{SuperP} /15)	—/200 _C	~10 100 _C (vs. ~7000 _C , Super P)	1.0 M LiCF ₃ SO ₃ in TEGDME	51
	NiCo ₂ O ₄ nanowire/ carbon textile	~2.70 ^b (vs. ~2.60 _{NiCo₂O₄ spheres})	~3.70 ^a , ~3.85 ^b (vs. ~3.95 ^a , ~3.70 _{NiCo₂O₄ spheres})	1000 _{CoO_x} /200	—/200 _{CoO_x}	~4200 _{NiCo₂O₄} (vs. ~3500 _C , NiCo ₂ O ₄ -spheres(C))	1.0 M LiTFSI in TEGDME	368
	Prelithiated NiCo ₂ O ₄ nanowire/C-fabric	~2.65 ^b (vs. ~2.40 _{pure NiCo₂O₄})	~4.05 ^b , ~4.25 _{pure NiCo₂O₄}	> 1000/100	0.35/0.1 mA cm ⁻²	~29 000 _{NiCo₂O₄} (vs. ~1300 _{NiCo₂O₄} , pure NiCo ₂ O ₄)	1.0 M LiTFSI in TEGDME	369
MnCo ₂ O ₄	MnCo ₂ O ₄ /hierarchical porous P/C	~2.70 ^b (vs. ~2.60 _{P/C})	~4.15 ^b (vs. ~4.25 _{P/C})	1000/50	0.13/200	~13 000 _{NiCo₂O₄+P/C-binder} (vs. ~3800 _{P/C-binder})	1.0 M LiTFSI in TEGDME	377
	MnCo ₂ O ₄ nanowire/ Ni foam	~2.75 ^b (vs. ~4.00 _{KB})	~3.40 ^b (vs. ~4.00 _{KB})	1000 _{CoO_x} /120	0.8/100 _{CoO_x}	~10 500 _{NiCo₂O₄} (vs. ~3800 _C)	1.0 M LiTFSI in TEGDME	379

Notes: ^a Full discharge/charge voltages at half full capacity. ^b Discharge/charge voltages at half limited capacity.

and a low overpotential (0.7 V) during a long cycling test (110 cycles) under 1000 mA h g⁻¹.

4.3.7.1.2 NiCo₂O₄ catalyst with good mass transport and Li₂O₂ storage. Wang *et al.* synthesized a self-assembled 3D foam-like NiCo₂O₄ catalyst with starch as the template.⁵¹ When it was subsequently used as a cathode material with a Super-P carbon support, the battery showed a high round-trip efficiency of 70% (overall potential of about 1.17 V, 200 mA g⁻¹, full discharge), a high discharge capacity of 10 137 mA h g⁻¹ at a current density of 200 mA g⁻¹ and a long cycle life over 30 cycles under 1000 mA h g⁻¹ (capacity based on carbon mass). The good cell performance was due to the 3D porous structure of NiCo₂O₄ materials, which facilitate better mass transport and Li₂O₂ storage. He *et al.* designed a hierarchical porous hybrid film with NiCo₂O₄ nanoparticle-decorated mesoporous N-doped carbon nanofibres (NCO@NCF).³⁶⁶ The Li–O₂ battery fabricated with this NCO@NCF electrode exhibited a low charging overpotential of 0.85 V (1000 mA h g⁻¹ at 200 mA g⁻¹), excellent rate capability and outstanding cycling stability (close to 100 cycles under 1000 mA h g⁻¹, capacity based on carbon mass), resulting from its structural and material superiority.

He *et al.* also synthesized a kind of needle-like mesoporous NiCo₂O₄ nanowire arrays uniformly coated on flexible CP.³⁶⁷ As a result, the fabricated battery exhibited a low overall overpotential of about 0.9 V under 1000 mA h g⁻¹ at 200 mA g⁻¹, a long cycle life over 200 cycles and a superior rate capability (almost overlapping discharge/charge profiles from 200 mA g⁻¹ to 1000 mA g⁻¹). In addition, the battery showed good flexibility, whereby it could be folded and flexed to some extent. Zhang *et al.* also grew NiCo₂O₄ nanowires on CP as the electrode for a Li–O₂ battery.³⁶⁸ After the electrode underwent a pre-lithiation process, the size of the NiCo₂O₄ nanoparticles was reduced from 20–30 nm to a uniformly distributed domain of ~2 nm, resulting in a significant improvement of the catalytic activity in the cell (Fig. 56). At the optimized pre-lithiated voltage (0.5 V) for preparing NiCo₂O₄, the as-assembled Li–O₂ batteries demonstrated an initial capacity of 29 280 mA h g⁻¹ and retained a stable capacity of >1000 mA h g⁻¹ after 100 full cell cycles. Fu *et al.* prepared NiCo₂O₄ nanowires arrays on CP as the cathode for a Li–O₂ battery, which delivered 1000 mA h g⁻¹ at 18 mA g⁻¹ and stable cycle performance over 10 cycles without any capacity restriction.³⁶⁹ In this work, large flower-like Li₂O₂ was also observed in the top region of the nanowires. The special morphology of Li₂O₂ was contributed to the high surface charge density and high O₂ concentration in the tip region in comparison to those in other parts of the nanowire.

Except for micro-sized CP, porous NiFM has also been investigated as a current collector to construct a carbon-free NiCo₂O₄ cathode that could avoid carbon corrosion, which is important for the cathode sustainability.^{370,371} Yu *et al.* synthesized the hierarchical porous NiCo₂O₄ nanowires on Ni substrate as the cathode for a Li–O₂ battery,³⁷² which delivered a capacity of 1500 mA h g⁻¹ at 0.05 mA cm⁻² and a charging

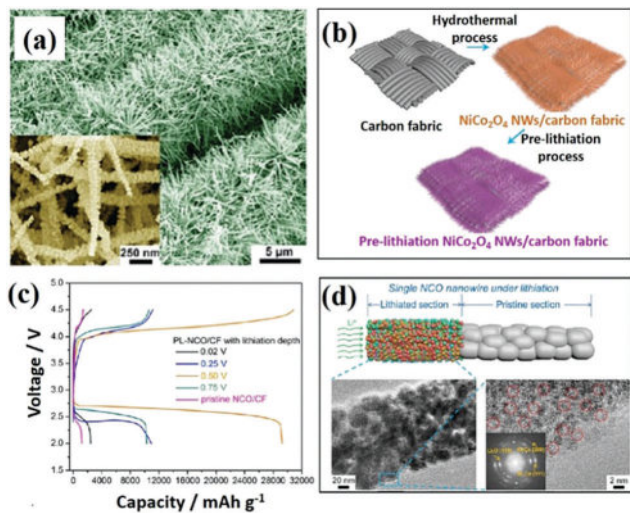


Fig. 56 (a) SEM images of NiCo_2O_4 nanowires (NCO-NWs) grown on carbon fabric (CF) (the inset shows the high-magnification SEM image of NCO-NWs); (b) schematic illustration of the total fabrication of prelithiated (PL) NCO-NWs/CF composite films; (c) discharge/charge profiles of cells with the pristine NCO-NWs/CF and the as-prepared PL-NCO-NWs/CF oxygen electrodes with different lithiation depths (0.02, 0.25, 0.50 and 0.75 V); (d) schematic illustration of NCO-NWs under lithiation and TEM images of the selected lithiation areas (the inset shows the fast Fourier transform pattern of prelithiated NCO).³⁶⁸ Reprinted with permission from ref. 368. Copyright 2016 American Chemical Society.

voltage below 4 V. The capacity retention ratio of the battery was still maintained 50% after the 70th cycle without any capacity restriction. Wen *et al.* developed wave-like NiCo_2O_4 anchored to a Ni substrate.³⁷³ After discharging at a current density of 40 mA g^{-1} , the Li-O_2 battery fabricated with this cathode delivered 7004 mA h g^{-1} with a charging voltage lower than 3.6 V (capacity based on NiCo_2O_4 mass). The high capacity was correlated with the large micrometre-sized Li_2O_2 on the cathode surface. Also, the battery with this electrode could be cycled 100 times under 500 mA h g^{-1} at 100 mA g^{-1} , demonstrating the superior characteristic of the wave-like NiCo_2O_4 material.

4.3.7.2 Manganese-cobalt oxide catalysts. The partial substitution of Co with Mn in CoO_x to form MnCo_2O_4 was identified to increase the catalytic activity of cobalt sites through changing the absorption bond strength of oxygen intermediates for ORR in alkaline solution.³⁷⁴ Since there are some similarities for ORR and OER processes in aqueous and non-aqueous electrolytes, MnCo_2O_4 might be a potential candidate as a catalyst for Li-O_2 batteries.

Xie *et al.* synthesized multi-porous MnCo_2O_4 microspheres with a diameter of $2.5\text{--}3.5 \mu\text{m}$.³⁷⁵ The quasi-hollow porous structure maximized the availability of catalytic sites and facilitated the diffusion of electrons and reactants. A Li-O_2 battery fabricated with the $\text{MnCo}_2\text{O}_4/\text{Super-P}$ electrode exhibited a decreased charging voltage from 4.2 V (Super-P electrode) to 3.9 V under full discharge to 2 V at 200 mA g^{-1} and an enhanced cycle life (50 cycles under 1000 mA h g^{-1} , capacity based on carbon mass) in comparison to that of a battery with just a Super-P carbon electrode.

The construction of a porous structured cathode was proved to have dense active sites and sufficient transport paths for O_2 and electrolyte.³⁷⁶ Consequently, Yang *et al.* anchored MnCo_2O_4 on P-doped hierarchical porous carbon (P-HPC) to form $\text{MnCo}_2\text{O}_4/\text{P-HPC}$ material.³⁷⁷ The $\text{MnCo}_2\text{O}_4/\text{P-HPC}$ electrode had an excellent ability for the transport of electrons, Li^+ and O_2 , as well as a large storage space for the Li_2O_2 product. As a result, a battery fabricated with such an electrode delivered a high discharge capacity of $13150 \text{ mA h g}^{-1}$ at a current density of 200 mA g^{-1} and over 200 cycles under 1000 mA h g^{-1} at 200 mA g^{-1} (capacity based on $\text{MnCo}_2\text{O}_4 + \text{carbon} + \text{binder}$ mass).

To improve the stability of the MnCo_2O_4 cathode, Park *et al.* constructed a freestanding MnCo_2O_4 nanoneedle array on a Ni substrate, producing a huge specific capacity over $10000 \text{ mA h g}^{-1}$ (100 mA g^{-1}) and a low charging voltage of about 3.5 V at an initial 7000 mA h g^{-1} for the fabricated battery.³⁷⁹ The low charge overpotentials were ascribed to the amorphous and film-like Li_2O_2 , which covered entirely and closely the nanoneedle array. It was pointed that the redox couples of $\text{Mn}^{2+}/\text{Mn}^{3+}$ and $\text{Co}^{2+}/\text{Co}^{3+}$ could yield oxygen vacancies on the surface of the catalyst, facilitating oxygen adsorption during the ORR process. In addition, a cell with the MnCo_2O_4 electrode performed with a long cycle life, with 120 cycles under 1000 mA h g^{-1} at 100 mA g^{-1} . A similar concept for constructing a hierarchical structured MnCo_2O_4 cathode for better mass transport and Li_2O_2 storage was also revealed by Sun *et al.*³⁸⁰ They reported a high cell discharge capacity of $12919 \text{ mA h g}^{-1}$ at 0.1 mA cm^{-2} and excellent rate capability (capacity based on MnCo_2O_4 mass).

4.3.7.3 Pyrochlore-type metal oxide catalysts. Pyrochlore has the chemical formula $\text{A}_2\text{B}_2\text{X}_6\text{Z}_{1-\delta}$, and it has already been shown to have good performance as a bifunctional catalyst for ORR/OER in alkaline media.³⁸¹ Its catalytic capability is believed to originate from the variable-valence characteristics of B cations and oxygen vacancies. The properties of pyrochlore suggest that it can be used as a catalyst in Li-O_2 batteries.³⁸²

Narzar *et al.* synthesized a hybrid composite of metallic mesoporous $\text{Pb}_2\text{Ru}_2\text{O}_{6.5}$ and KB carbon ($\text{Pb}_2\text{Ru}_2\text{O}_{6.5}/\text{KB}$) for cathode materials for a Li-O_2 battery. The battery showed a high capacity of $10000 \text{ mA h g}^{-1}$ at 70 mA g^{-1} (capacity based on carbon mass) as well as low charge overpotentials.³⁸³ The excellent catalytic activity of the $\text{Pb}_2\text{Ru}_2\text{O}_{6.5}$ materials could be explained by the high fraction of surface oxygen vacancies, their unique porosity, which enables good diffusion to the active sites, and the nanoscale network with metallic conductivity. The author further synthesized PbRuO and BiRuO catalysts for a Li-O_2 battery. These materials showed intriguing OER properties for Li-O_2 cells, producing rechargeable capacities well over $10000 \text{ mA h g}^{-1}$ (capacity based on carbon + catalyst + binder + O_2 mass). The specific capacity and energy efficiency of the cell was enhanced remarkably in comparison to that of the original carbon cathode.³⁸² The good catalytic behaviour was facilitated by the significant concentration of surface active sites afforded by the material's high surface area and intrinsic variable redox states and *via facile* electron transport owing to their conductive character.

4.3.7.4 Other binary metal oxide catalysts. Other binary metal oxides, such as ZnCo_2O_4 , CoFe_2O_4 and NiFe_2O_4 , have also been reported as catalysts for Li-O_2 systems.^{57,384–387} For instance, Guan *et al.* compared the catalytic activity of CoFe_2O_4 and NiFe_2O_4 towards discharge and charge reactions, and a cell with such a $\text{CoFe}_2\text{O}_4/\text{CNT}$ cathode showed a slightly enhanced performance compared to a $\text{NiFe}_2\text{O}_4/\text{CNT}$ cathode. This was probably due to the high spin for Co^{2+} in an oxygen-atom-ligand field associated with the easy formation of a stable ion pair with the superoxide species.³⁸⁸ After mixing with KB carbon, the $\text{CoFe}_2\text{O}_4/\text{KB}$ electrode exhibited a stable cycle performance over 30 cycles under 430 mA h g^{-1} at 200 mA g^{-1} (capacity based on carbon mass).

The pore structure of CoFe_2O_4 catalysts was further optimized for their good mass transport and Li_2O_2 storage space. Kim *et al.* used the colloidal crystal template method to prepare three-dimensionally ordered macroporous CoFe_2O_4 catalysts as a cathode for a Li-O_2 battery, the assembled cell showed a high discharge capacity of $11\,658 \text{ mA h g}^{-1}$, and exhibited cycling stability over 47 cycles at a limited capacity of 500 mA h g^{-1} (capacity based on carbon mass).³⁸⁹

4.3.8 Perovskite catalysts. Perovskite has the general formula ABO_3 , where the A site is occupied by an alkaline earth element, and the B site is occupied by a transition metal element with a six-coordination number to oxygen atoms. Perovskites with good ionic and electronic conductivity have emerged as highly active electrode materials for various kinds of energy devices, such as solid-oxide fuel cells, electrolysis cells, oxygen sensors and transport membranes.^{390,391} In this vein, perovskites were also applied as a catalyst in aprotic Li-O_2 batteries,^{74,392} and Table 7 shows the performance in Li-O_2 batteries of some typical perovskite materials by comparing the different chemical and porous structures.

4.3.8.1 ABO_3 -type perovskites. Cheng *et al.* prepared an interconnected porous CaMnO_3 nanostructure and used it as the cathode catalyst in a Li-O_2 battery.³⁹³ The CaMnO_3 -based electrode enabled better cyclability and a 620 mV smaller discharge-recharge voltage gap compared that of the pure carbon cathode at a current rate of $50 \text{ mA g}_{\text{carbon}}^{-1}$. The improved performance was attributed to its high catalytic activity and porous nanostructure. Shui *et al.* developed a hybrid catalyst composed of LaNiO_3 and $\text{g-C}_3\text{N}_4$, ensuring a high $\text{Ni}^{3+}/\text{Ni}^{2+}$ ratio and a high content of absorbed hydroxyl on the catalyst surface, which could promote the ORR and OER processes.³⁹⁴ Consequently, the fabricated battery showed a higher capacity (5500 mA h g^{-1} at 50 mA g^{-1} , capacity based on catalyst mass), lower overpotentials (below 4 V at the first charging voltage under 500 mA h g^{-1}) and a better cycling stability (65 cycles) compared to the performances achieved with XC-72 carbon and LaNiO_3 catalysts.

Zhang *et al.* further synthesized a 3D ordered macroporous LaFeO_3 material as a catalyst for use in a Li-O_2 battery (KB carbon support) (Fig. 57). The battery showed good cell performances, including a low overpotential with a charging voltage of 1 V , a high specific capacity ($12\,000 \text{ mA h g}^{-1}$ at 0.025 mA cm^{-2}) and

Table 7 Performance summary of Li-O_2 batteries with perovskite-based electrodes and their operating conditions

Perovskite category	Specific design	Discharge voltage (V)	Charge voltage (V)	Limited capacity/cycles (mA h g^{-1} /times)	Mass and current density ($\text{mg cm}^{-2}/\text{mA g}^{-1}$)	Full discharge capacity (mA h g^{-1})	Electrolyte	Ref.
ABO_3	Porous $\text{CaMnO}_3/\text{C}_{\text{XC-72}}$	$\sim 2.60^a$ (vs. $4.30_{\text{XC-72}}^d$) $\sim 2.70^{a,b}$	$\sim 3.65^a$ (vs. $4.20_{\text{XC-72}}^a$)	$500_{\text{C}}/80$	$\sim 50_{\text{C}}$	$\sim 5200_{\text{C}}$	1.0 M LiTFSI in TEGDME	393
$(\text{A}_{x-1-x})\text{BO}_3$	3D macroporous $\text{LaFeO}_3/\text{C}_{\text{KB}}$	$\sim 2.70^a$ $\sim 2.70^b$	$\sim 4.10^{a,b}$ (vs. 4.20^a , 4.25_{KB}^b)	$1000_{\text{C}}/124$	0.025^a , 0.1^a , $0.75/0.1^a$, 0.025^b , 0.4000_{KB}	$\sim 12\,000_{\text{C}}$ (vs. $10\,500_{\text{C}}$, KB)	1.0 M LiTFSI in TEGDME	378
	$\text{La}_{0.5}\text{Sr}_{0.5}\text{CoO}_{3-x}$ nanotubes/ C_{KB}	$\sim 2.70^a$	$\sim 3.85^b$ (vs. 4.20_{KB}^b)	$500_{\text{C}}/50$ (vs. $500_{\text{KB}}/13$)	0.025^b , 0.4000_{KB}	$\sim 5900_{\text{C}}$ (vs. 4000_{C} , KB)	1.0 M LiTFSI in TEGDME	400
	$\text{La}_{0.75}\text{Sr}_{0.25}\text{MnO}_3$ nanotubes/ C_{KB}	$\sim 2.70^a$	$\sim 4.20^a$	$1000_{\text{C}}/120$ (vs. $1000_{\text{KB}}/43$)	$0.9/0.1^a$	$\sim 11\,000_{\text{C}}$ (vs. 8000_{C} , KB)	1.0 M LiTFSI in TEGDME	402
	$(\text{A}_{x-1-x})\text{(B}_x\text{B}_{1-x})\text{O}_3$	$\sim 2.70^{a,b}$	$\sim 4.20^b$ (vs. $\sim 4.40_{\text{XC-72}}^b$)	$500_{\text{catalyst}}/50$	0.025^b , 0.50_{catalyst}	$\sim 5400_{\text{C}}$	$1.0 \text{ M LiCF}_3\text{SO}_3$ in TEGDME	350

Notes: ^a Full discharge/charge voltages at half full capacity. ^b Discharge/charge voltages at half limited capacity.

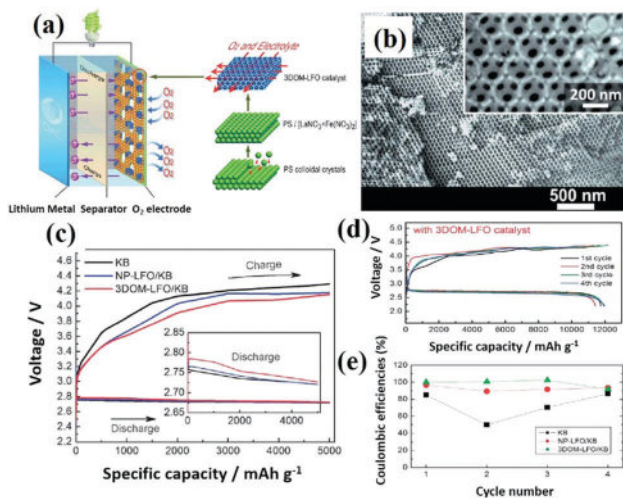


Fig. 57 (a) Schematic illustration for the preparation of three-dimensionally ordered macroporous LaFeO₃ (3DOM-LFO) catalyst and structure of the Li–O₂ batteries; (b) SEM images of 3DOM-LFO after calcination at 600 °C (the inset shows the magnified image); (c) first charge/discharge curves of Li–O₂ cells with pure KB carbon, NP-LFO/KB, and 3DOM-LFO/KB electrodes at a current density of 0.025 mA cm⁻² (the inset shows the magnified voltage region of (c)); (d) cyclability and (e) Coulombic efficiency of Li–O₂ cells with (1) pure KB, (2) NP-LFO/KB and (3) 3DOM-LFO/KB electrodes at a current density of 0.025 mA cm⁻².³⁷⁸ Reprinted with permission from ref. 378. Copyright 2014 Royal Society of Chemistry.

cycle stability up to 124 cycles (1000 mA h g⁻¹ at 0.15 mA cm⁻², capacity based on carbon mass).³⁷⁸

4.3.8.2 (A_xA_{1-x}')BO₃-type perovskites. The ABO₃ structure can accommodate cation substitution in a wide range by partially substituting at the A site with another element to give an (A_xA_{1-x}')BO₃ composition.^{395,396} The electronic structure of active metal sites can be varied systematically using the partial replacement or doping of second metal sites with different valences or ionic radii. These properties are considered to be critical factors for their good catalytic activity towards OER and ORR.^{236,397–399}

Mai *et al.* synthesized mesoporous perovskite La_{0.5}Sr_{0.5}CoO_{2.91} (LSCO) nanowires, and investigated their intrinsic ORR and OER activity in an aprotic Li–O₂ system. The mesoporous LSCO nanowires showed a low peak-up potential and a high limiting diffusion current for ORR. Consequently, the as-prepared cathode exhibited an ultrahigh capacity of 11 000 mA h g⁻¹ at 50 mA g⁻¹ (capacity based on carbon mass), which was one order of magnitude higher than that of LSCO nanoparticles. The excellent electrochemical catalytic activity was proposed to be due to the high active site density and continuous disorderly-piled pore channels for oxygen transport.²¹⁵

In order to achieve good mass transport and Li₂O₂ storage, Wang *et al.* further developed hierarchical meso/macroporous La_{0.5}Sr_{0.5}CoO_{3-x} nanotubes (HPN-LSC).⁴⁰⁰ The HPN-LSC/KB electrode displayed excellent performance towards both discharge and charge processes for Li–O₂ batteries, which showed a high specific capacity of about 5900 mA h g⁻¹ (capacity based on carbon mass) with a low overall overpotential of 1.14 V,

and an excellent cycle stability, sustaining 50 cycles at a current density of 0.1 mA cm⁻² with an upper limit capacity of 500 mA h g⁻¹.

Except for the equal ratio of A and A' cations in (A_{0.5}A_{0.5}')BO₃, changing the mole ratio of A and A' cations might give the possibility for having a different electronic structure of the active site in the (A_xA_{1-x}')BO₃ material for catalyzing the discharge/charge reactions in Li–O₂ batteries.^{285,401} Consequently, Zhang *et al.* reported La_{0.75}Sr_{0.25}MnO₃ porous nanotubes (LSM-PNT) fabricated through combining the electrospinning technique with a heating method, and then used these as a cathode catalyst for a Li–O₂ battery.⁴⁰² The battery exhibited a higher capacity (11 000 mA h g⁻¹ at 0.025 mA cm⁻¹, capacity based on carbon mass) and much longer cycle life (120 cycles at 0.15 mA cm⁻¹) than with KB carbon (8000 mA h g⁻¹ and 43 cycles), respectively. The excellent performance of the LSM-PNT-based cathode was speculated to be due to the facile pathway for electronic and mass transport, as well as the dense active sites.

Lee *et al.* prepared a hollow-structured La_{0.6}Sr_{0.4}CoO_{3-δ} perovskite sphere as a cathode material for a Li–O₂ battery, and the cell delivered a deep discharge capacity of 4895 mA h g⁻¹ (capacity based on carbon mass) with high Coulombic efficiency (82%). It also showed a 53% excess specific capacity compared to the particulate morphology, which could be ascribed to the fast mass transport and large Li₂O₂ storage space.⁴⁰³

4.3.8.3 (A_xA_{1-x}')(B_xB_{1-x}')O₃-type perovskites. The electronic structure of the B site in the (A_xA_{1-x}')BO₃ structure can also be modulated by partially substituting the B cation with another element to give (A_xA_{1-x}')(B_xB_{1-x}')O₃ compositions.^{395,396} Xin *et al.* compared the catalytic performance of Ni-doped La_{0.8}Sr_{0.2}Mn_{0.6}Ni_{0.4}O₃ and undoped La_{0.8}Sr_{0.2}MnO₃.³⁵⁰ The results revealed that the battery with the La_{0.8}Sr_{0.2}Mn_{0.6}Ni_{0.4}O₃ catalyst delivered a better electrochemical performance, including the specific capacity (5360 mA h g⁻¹ vs. 4400 mA h g⁻¹, capacity on carbon mass), overpotential (1.33 V vs. 1.62 V) and cycle life (79 cycles vs. 30 cycles), compared to that achieved with La_{0.8}Sr_{0.2}MnO₃. The improved performance was due to the formation of sufficient oxygen vacancies by replacing Mn with the Ni cation.

4.3.9 Metal carbide/nitride/sulfide/selenide catalyst

4.3.9.1 Metal carbides. Metal carbides possess the advantages of a high electronic conductivity, low cost, non-toxic, relatively low density and good stability towards nucleophilic attack by superoxide species. They have consequently been utilized as alternative lightweight supports to carbon in electrodes for metal–air batteries.⁴⁰⁴ It was found that metal carbides have a better catalytic activity for aqueous ORR relative to carbon.⁴⁰⁵ Some metal carbides, such as titanium carbide, molybdenum carbide and iron carbide, were also investigated as cathode materials for Li–O₂ batteries (Table 8), with the results reported in discussions of their intrinsic catalytic activity.⁴⁰⁶

4.3.9.1.1 Titanium carbide. Bruce *et al.* investigated the feasibility of utilizing TiC as a cathode material to substitute for the traditional carbon materials.⁶ Remarkably, the TiC cathode greatly reduced the side reactions compared with carbon, and also exhibited a better reversible formation/decomposition of

Table 8 Performance summary of Li–O₂ batteries with carbide-based electrodes and their operating conditions

Carbide category	Specific design	Discharge voltage (V)	Charge voltage (V)	Limited capacity/ cycles (mA h g ⁻¹ /times)	Mass and current density (mg cm ⁻² /mA g ⁻¹)	Full discharge capacity (mA h g ⁻¹)	Electrolyte	Ref.
TiC	TiC particle/C	~2.60 ^b	~3.50 ^b	350 _C /100	4/5 mA cm ⁻²	~350 _{TiC}	0.5 M LiClO ₄ in DMSO	6
Mo ₂ C	TiC/meso-porous carbon	~2.75 ^a	~4.05 ^b (vs. ~4.30 _{SuperP} ^b)	500 _{TiC+c} /90	0.2/100 _C	~3460 _{TiC+c}	LiCF ₃ SO ₃ ; TEGDME (1:4)	406
	Mo ₂ C/CNT composite	~2.70 ^b	~3.20 ^c (vs. ~3.90 _{CNT} ^c)	500 _{TiC+c} /150	1.1/100 _{Mo₂C/CNT}	—	1.0 M LiCF ₃ SO ₃ in TEGDME	206
Fe ₃ C	Fe/Fe ₃ C/3D N-graphene	~2.85 ^b (vs. ~2.75 _{SuperP} ^b)	~4.15 ^b (vs. ~4.28 _{SuperP} ^b)	800 _{Catalyst+c} /30	1.0/100 _{Catalyst+c}	~7150 _{Catalyst+c} (vs. ~3600 _C , Super P)	1.0 M LiTFSI in TEGDME	412

Notes: ^a Full discharge/charge voltages at half full capacity. ^b Discharge/charge voltages at half limited capacity.

Li₂O₂ compared to nanoporous gold (>98% capacity retention after 100 cycles, compared with 95% for nanoporous gold). The main charging plateau of TiC-based batteries was below 4 V even after 100 cycles at 0.5 mA cm⁻² (about 500 mA h g⁻¹) without capacity limitation. This stability might originate from the presence of stable TiO₂ (along with some TiOC) on the surface of TiC after the first discharge. In comparison, although a TiO₂ layer was also formed on the TiN surface, the as-prepared Li–O₂ battery showed larger discharge and charge overpotentials than those of TiC-based devices. These resulted from the lower electrical conductivity of TiN. This research proved the effectiveness of utilizing carbides in the development of high-performance Li–O₂ batteries.

The influence of a passivated TiO₂ film on the activity of TiC cathodes was studied by Nazar's group.⁴⁰⁶ In this work, commercial Li₂O₂ with a crystallite size of about 200–800 nm was pre-filled in cathode materials and charged directly. It was found that the TiC-based cathode could oxidize the bulk Li₂O₂ crystallites at a much lower overpotential in comparison to carbon. Oppositely, the TiC and TiN cathodes with insulating TiO₂ surface layers (thickness of only 3 nm) could not perform the charge reaction in Li–O₂ batteries.

Niu *et al.* further investigated the adsorption and deposition characteristics of Li₂O₂ on a Ti-terminated TiC(111) surface and TiO-terminated TiC(100) surface.⁴⁰⁷ They found that Li₂O₂ reassembled into a saturated periodic two atomic layer coating, in which each O atom was bonded to three Ti atoms to form an O layer equivalent to the layer formed by O₂ surface oxidation. Li atoms located on the top and the growth of Li₂O₂ could be continuously grown *via* a surface mechanism to cover the electrode surface with lattice parameters, almost identical to those of the standard Li₂O₂ unit cell.⁴⁰⁷ On the TiC(100) surface, the Li₂O₂ adsorption layout (two Li₂O₂ clusters) was similar to that of the O₂Li₃O₄ layers in the Li₂O₂ crystal structure, and subsequently Li₂O₂ may grow on the TiC(100) surface with a dihedral angle between 11.4° and 22.4°, and strains inside the Li₂O₂ could induce conductivity.⁴⁰⁸ This supported the experimental findings and explained the reason for the superior stability and low OER overpotential of the TiC electrode.

4.3.9.1.2 Molybdenum carbide. Except for TiC-based materials, Mo₂C has also been developed as an OER catalyst in Li–O₂ batteries.⁴⁰⁹ Curtiss *et al.* dispersed Mo₂C nanoparticles onto CNTs as the cathode catalyst in a Li–O₂ cell, and charged it with a low voltage below 3.5 V under a fixed capacity of 500 mA h g⁻¹ at 100 mA g⁻¹.²⁰⁶ As shown in Fig. 58, the Mo₂C-based cell achieved a long cycle life over 100 cycles, and even close to 50 cycles under a confined capacity of 1000 mA h g⁻¹ at 200 mA g⁻¹. Moreover, the cell also showed an excellent rate capability. Through DFT calculations, the high OER activity of Mo₂C could be attributed to the formation of metallic non-crystalline MoO₃-like layers on the Mo₂C nanoparticles along with the CNTs.

Nazar *et al.* further investigated the reversibility of carbon-free Mo₂C in Li–O₂ batteries.⁴¹⁰ They found that a thin native oxide layer (MoO_{2+x}) existed on the prepared Mo₂C surface,

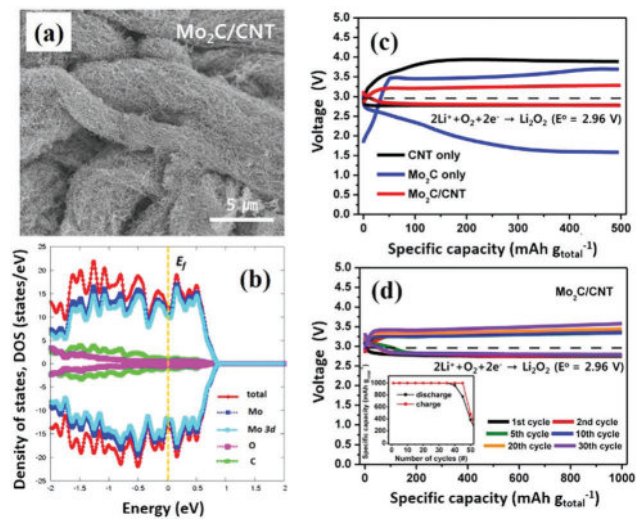


Fig. 58 (a) SEM images of (a) $\text{Mo}_2\text{C}/\text{carbon nanotube}$ ($\text{Mo}_2\text{C}/\text{CNT}$); (b) the electronic density of states (e-DOS) around the Fermi-level (E_f) for $\text{Mo}_2\text{C}/\text{CNT}$ material (the light-blue region was the Mo 3d projected e-DOS that dominated the e-DOS around the Fermi-level); (c) the first discharge/charge profiles of $\text{Li}-\text{O}_2$ batteries with pristine-CNT, Mo_2C , $\text{Mo}_2\text{C}/\text{CNT}$ electrodes with a fixed capacity of 500 mA h g^{-1} at a current density of 100 mA g^{-1} ; (d) cycling performance of $\text{Li}-\text{O}_2$ batteries with $\text{Mo}_2\text{C}/\text{CNT}$ electrodes with a fixed capacity of 1000 mA h g^{-1} and at a current density of 200 mA g^{-1} .²⁰⁶ Reprinted with permission from ref. 206. Copyright 2015 American Chemical Society.

and that this oxide layer was then converted into Li_xMnO_3 through the reaction of Li_2O_2 and $\text{MoO}_{2+\delta}$ ($x\text{Li}_2\text{O}_2 + 2\text{MoO}_{2+\delta} \rightarrow 2\text{Li}_x\text{MoO}_3$) after discharge. During the charging process, Li_2O_2 and Li_xMoO_3 were proposed to be simultaneously oxidized owing to their close redox potentials. During this process, fresh surface was exposed upon electrochemical charge by releasing Li_xMoO_3 into the electrolyte, inducing at the low charging voltage below 3.5 V at $100 \mu\text{A cm}^{-2}$.

In order to obtain a better mass transport efficiency, Yan *et al.* prepared $\text{MoO}_2/\text{Mo}_2\text{C}$ -nanocrystal-decorated N-doped carbon foam ($\text{MoO}_2/\text{Mo}_2\text{C}@\text{NCF}$) by using recombinant proteins to achieve the self-assembly of meal precursors and to provide a carbon source for Mo_2C formation.⁴¹¹ The as-prepared $\text{MoO}_2/\text{Mo}_2\text{C}@\text{NCF}$ electrode showed superior electrocatalytic activity in both the ORR and OER processes, with a high round-trip efficiency of 89.1% ($2.77 \text{ V}/3.11 \text{ V}$) at 100 mA g^{-1} , as well as exceptional rate performances and good cyclability in a $\text{Li}-\text{O}_2$ battery (120 cycles under 500 mA h g^{-1} and 40 cycles under 5000 mA h g^{-1} at a high rate of 1 A g^{-1} , capacity based on $\text{MoO}_2/\text{Mo}_2\text{C} + \text{carbon mass}$). This desirable performance was attributed to the hierarchical porous structure of NCF for large Li_2O_2 storage space and the good OER and ORR catalytic activity of $\text{MoO}_2/\text{Mo}_2\text{C}@\text{NCF}$.

4.3.9.1.3 Other metal carbides. The superior catalytic activity of TiC and Mo_2C encouraged the development of other metal carbides for the cathode of $\text{Li}-\text{O}_2$ cells. Zhang *et al.* designed Fe/ Fe_3C -decorated 3D porous N-doped graphene (F-PNG) using metal-organic frameworks (MOFs) as the structure-directing material.⁴¹²

A $\text{Li}-\text{O}_2$ battery with the F-PNG cathode exhibited a high discharge capacity of 7150 mA h g^{-1} at 0.1 mA cm^{-2} (capacity based on $\text{Fe}/\text{Fe}_3\text{C} + \text{carbon mass}$), a discharge voltage plateau of 2.91 V and a charge voltage plateau of 3.52 V at 0.1 mA cm^{-2} . The superior performance of the F-PNG electrode was proposed to be due to the good catalytic activity of $\text{Fe}/\text{Fe}_3\text{C}$ particles and due to the 3D porous N-doped graphene facilitating better mass transport and Li_2O_2 storage.

4.3.9.2 Metal nitrides. Transition metal nitrides have a high electronic conductivity and good electrochemical activity, which enable them to be widely used in the electrochemistry field.^{413,414} They have been demonstrated to be efficient catalysts in replacing noble metals for aqueous ORR in fuel cells.⁴¹⁵ Zhou *et al.* presented TiN nanoparticles supported on Vulcan XC-72 carbon as a cathode catalyst for a $\text{Li}-\text{O}_2$ battery.⁴¹⁶ The as-prepared TiN electrode showed better OER and ORR catalytic activity in comparison to Vulcan XC-72 carbon. The assembled battery presented a discharge-charge voltage gap of 1.05 V at 50 mA g^{-1} (capacity on carbon mass).

In addition to TiN material, CoN has also been investigated as a cathode catalyst for $\text{Li}-\text{O}_2$ batteries. Wang *et al.* performed the nitridation of Co_3O_4 to improve its electron density and Fermi energy, which consequently increased the electron-transport capability of the generated CoN material.⁴¹⁷ The densely packed Li_2O_2 could be formed on the obtained CoN nanoarrays after discharge, and Li_2O_2 was decomposed at a low charging voltage (below 4 V at 100 mA g^{-1}). This was due to the high electron conductivity of CoN and the electron migration between the half-metallic Li_2O_2 nanoparticles (Fig. 59). Simultaneously,

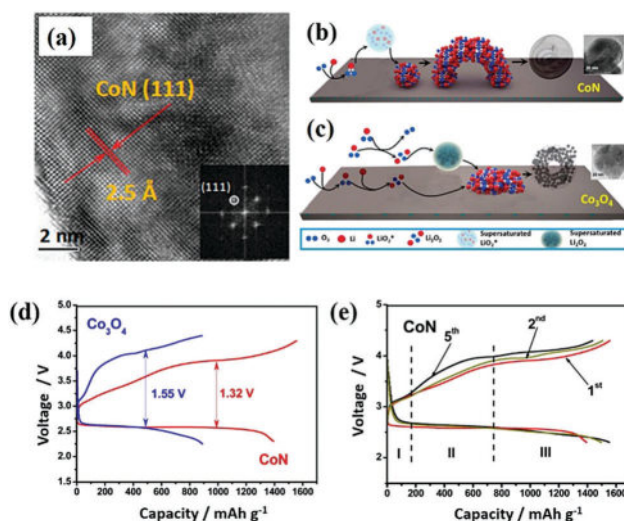


Fig. 59 (a) TEM images of as-synthesized CoN nanorods and corresponding fast Fourier transform pattern (inset); illustration of two discharge reaction mechanisms based on an initial oxygen reduction at an active site followed by solution-phase reactions and growth at a surface nucleation site of (b) CoN and (c) Co_3O_4 catalysts; (d) the initial discharge/charge profiles of cells with Co_3O_4 and CoN based electrodes; (e) the discharge/charge profiles of the 1st, 2nd, and 5th cycles of CoN electrodes (the cell discharge/charge and cycling test were performed within a voltage window of $2.3-4.3 \text{ V}$ at a current density of 100 mA g^{-1}).⁴¹⁷ Reprinted with permission from ref. 417. Copyright 2016 American Chemical Society.

the CoN nanoarrays performed with a better capacity retention than the Co₃O₄ electrode within the voltage range 2.3–4.3 V.

4.3.9.3 Metal sulfides and selenides. Metal sulfides and selenides have been revealed to have efficient and stable activity towards catalyzing ORR and OER in aqueous media.^{418,419} Consequently, attempts to exploit such materials as possible catalysts for Li–O₂ batteries have been made by several groups (Table 9).^{420–422}

Curtiss *et al.* investigated the catalytic activity of MoS₂ for ORR and OER in a Li–O₂ system with an ionic liquid, namely 1-ethyl-3-methylimidazolium tetrafluoroborate (EMIM-BF₄), as the electrolyte solvent.⁴²¹ In this system, MoS₂ performed with a remarkable round-trip efficiency of 85% and good cyclability to 50 cycles at a fixed capacity of 500 mA h g⁻¹ (0.1 mA cm⁻², capacity based on MoS₂ mass). It was also shown that the coverage of Mo edge by the EMIM⁺ ions tended to form isolated Mo sites, which prevented O₂ dissociation and enabled O₂ adsorption as determined through DFT calculations. In addition, EMIM-BF₄ facilitated the dissolution of O₂⁻. The above-mentioned merits led to the formation of Li₂O₂ *via* a solution-mediated mechanism, which facilitated the increase in cell capacity.

Yu *et al.* further synthesized 3D MoS_x nanosheets decorated on hydrothermally reduced graphene (3D MoS_x/HRG) for better mass transport.⁴²³ The Li–O₂ batteries based on this MoS_x/HRG aero-gel cathode showed a high initial discharge capacity up to 6678.4 mA h g⁻¹ at a current density of 0.05 mA cm⁻², and a good cycling capability with a cut-off capacity of 500 mA h g⁻¹ (capacity based on MoS_x + HRG mass) at a current density of 0.1 mA cm⁻². The good performance was ascribed to the good catalytic activity of MoS_x nanosheets and the unique 3D meso-/microporous architecture for mass transport.

Except for MoS_x materials, Gu *et al.* developed a binary core–shell structured CoSe₂/CoO nanocomposite as a cathodic catalyst for a Li–O₂ cell.⁴²⁴ The battery with CoSe₂/CoO achieved an enhanced cycle performance in a full-discharge mode (50% retention of the first discharged capacity after the 30th cycle for CoSe₂/CoO/Super-P, about the 12th cycle for CoO/Super-P and about the 6th cycle for Super-P). This improvement was ascribed to the much stronger binding energy of LiO₂ onto the CoO surface (–2.7 eV to –13.4 eV based on different crystal lattices) compared to the corresponding values for carbon materials (0.1 to 0.3 eV based on pristine and OH-functionalized graphite sheets). This could prevent the formation of Li₂CO₃ on the electrode surface. Moreover, the existence of CoSe₂ affected the electronic structure of the Co-metal site of CoO, inducing a superior cell cycling performance compared to that of the pure CoO catalyst.

The construction of metal sulfide/selenide with a porous architecture was proposed to further improve the performance of Li–O₂ batteries. A 2D Co₃S₄ nanosheet prepared *via* a simple hydrothermal process was employed as the cathode catalyst in a Li–O₂ battery.⁴²⁵ The nanosheet assembled with the core–shell structure Co₃S₄ nanoparticles had rich mesopores in the plane, which facilitated mass transport in the Li–O₂ battery. Consequently, the battery with the as-prepared cathode exhibited a high reversible

Table 9 Performance summary of Li–O₂ batteries with nitride/carbide-based electrodes and their operating conditions

Catalyst category	Specific design	Discharge voltage (V)	Charge voltage (V)	Limited capacity/cycles (mA h g ⁻¹ /times)	Mass and current density (mg cm ⁻² /mA g ⁻¹)	Full discharge capacity (mA h g ⁻¹)	Electrolyte	Ref.
Nitride	TiN particles/C _{XC-72}	~2.70 ^a	3.75 ^a (vs. 4.30 _{XC-72} ^a)	1000/—	0.3–0.5/50, ^a 500 ^b	~6400 _C (vs. ~4000 _C , XC-72)	LiTFSI in TEGDME (1:5)	416
	CoN nanorods/C	~2.60 ^b	~3.80 ^b (vs. ~4.10 _{Co₃O₄} ^b)	2.3–4.3 V (stop voltages)/50	—/100 _{CoNHC}	~1400 _{CoNHC} (vs. ~900 _{Co₃O₄+C} , Co ₃ O ₄ /C)	1.0 M LiTFSI in TEGDME	417
Sulfide	MoS ₂ nanoflake	~2.70 ^a	~3.60 ^a	500 _{MoS₂} /50	0.2/0.1 mA cm ⁻²	~1200 _{MoS₂}	0.1 M LiTFSI in EMIM-BF ₄	421
	3D-MoS _x /graphene	~2.70 ^b	~4.20 ^b	500 _{MoS₂+C} /30	—/0.05 mA cm ⁻²	~6680 _{MoS₂+C} (vs. ~4000 _C , graphene)	1.0 M LiTFSI in TEGDME	423
	Co ₃ S ₄ nanosheet/C	~2.70 ^{a,b}	~3.60 ^b (vs. ~4.20 _{KB} ^b)	500 _{Co₃S₄+C} /25	1.0/100	~6000 _{Co₃S₄+C} (vs. ~3100 _C , KB)	1.0 M LiTFSI in TEGDME	425
	NiS flower/C	~2.65 ^a	~4.20 ^a	900 _C /30	1.5–2.0/75	~6700 _C (vs. ~2600 _C , Super P)	1.0 M LiTFSI in TEGDME	426

Notes: ^a Full discharge/charge voltages at half full capacity. ^b Discharge/charge voltages at half limited capacity.

capacity of 5917 mA h g⁻¹ at 0.1 mA cm⁻² and could stably be cycled for over 25 times.

Yuan *et al.* compared the catalytic activity of flower-like and rod-like NiS materials for the cathode of Li–O₂ batteries.⁴²⁶ The flower-like NiS catalyst material gave a higher capacity of 6733 mA h g⁻¹ and lower charge voltage of 4.24 V at 75 mA g⁻¹ and quite stable cycling performance (900 mA h g⁻¹, capacity based on carbon mass) in comparison to the batteries with rod-like NiS and pure Super-P carbon. This was due to the flower-like architecture providing more space for storage of the discharge products and efficient channels for O₂ diffusion.

4.4 Short summary and perspective for oxygen electrodes

Oxygen electrodes are an essential part of Li–O₂ batteries, and provide critical functionality for catalyzing Li₂O₂ formation/decomposition, mass transport, Li₂O₂ storage and the induced evolution of Li₂O₂ clusters. Recent efforts have been devoted to promote the functionality of the oxygen electrode, including the development of efficient catalysts for catalyzing Li₂O₂ formation/decomposition, the development of a mesoporous structure for fast mass transport, surface engineering for the induced growth of large Li₂O₂ clusters and crystals, and the development of hierarchical macro-/mesoporous structures for a large amount of Li₂O₂ storage. Equally important, the stability of the cathode itself and the cathode towards electrochemically oxidizing organic electrolytes have been carefully evaluated for the improved sustainability of Li–O₂ batteries. All of these are essential points to consider to improve the performance and stability of Li–O₂ batteries.

Carbon materials have shown a number of advantages due to their high electrical conductivity and easy construction of various porous structures, which are effective for fast electron transfer and mass transport. In particular, hierarchical meso-/macrostructured carbon electrodes have demonstrated excellent ability for mass transport and Li₂O₂ storage. Strategies to improve the graphitization degree of carbon and heteroatom-doping are proposed to increase their stability further and improve their catalytic activity for Li₂O₂ formation and decomposition. However, the low catalytic activity of carbon and its easy oxidation at high charge potentials seriously limit the performance and stability of Li–O₂ cells based on carbon electrodes.

Numerous works have been focused on the development of precious metal catalysts to increase their catalytic activity towards Li₂O₂ formation/decomposition. Some of these even enable the Li–O₂ battery to operate below 3.5 V at a confined charge capacity. Another advantage for some precious metal catalysts is that they can function as the substrate to induce Li₂O₂ particles with a larger size. For example, a RuO₂ monolayer and Li₂O₂(0001) surface show a similar lattice structure, which induces the formation of exposed crystalline Li₂O₂ with a conductive (0001) surface during discharge. The Ag₁₅ cluster catalyst has shown the ability to induce the growth of toroid Li₂O₂ in a high quantity, while Ir₃Li can induce the nucleation and growth of crystalline LiO₂. These properties of specific precious metal catalysts make them applicable in high-performance Li–O₂ batteries.

One of the challenges for precious metal catalysts, though, is their oxidation activity towards organic electrolytes, which deteriorates the cyclability of Li–O₂ batteries. For example, Peng's group found that noble metal catalysts were the most effective at reducing the charge overpotential but they accelerated the decomposition of the electrolyte.²⁶⁰ Furthermore, the cost and scarcity of precious metals may be an obstacle for their application and broader use in Li–O₂ batteries.

Non-precious metal catalysts, such as metal oxides/nitrides/carbides, provide the chance for the construction of cost-effective oxygen electrodes. They have shown good activity towards catalysing Li₂O₂ formation/decomposition. Furthermore, carbon-free cathodes with non-precious metal catalysts do not suffer the fatal drawback of carbon corrosion, and further they can improve the cycle stability of Li–O₂ batteries. Several types of metal oxides, such as MnO_x, CoO_x and MnCoO_x, have also shown the capability to induce the growth of large Li₂O₂ clusters by surface engineering. For instance, the δ-MnO₂/carbon-based electrode exhibits micron-sized aggregations assembled with nanorod-like Li₂O₂ on the electrode surface. This indicates that δ-MnO₂ promotes the transport of superoxide species during the ORR process, while the carbon defect sites act as the primary nucleation sites for the growth of Li₂O₂ in the δ-MnO₂/KB electrode.³⁰⁹ However, the use of this type of cathode material comes at the cost of sacrificing capacity and energy density due to their high mass densities. The construction of non-precious-metal-catalyst electrodes with high porosity and low mass density may be a good strategy to increase the active site density and to open up intrinsic pore channels for efficiently catalyzing Li₂O₂ formation and decomposition, fast mass transport, and to facilitate a large space for Li₂O₂ storage, which are all useful aspects for the construction of a high-performance and stable Li–O₂ battery.

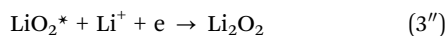
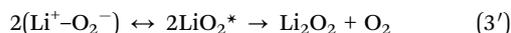
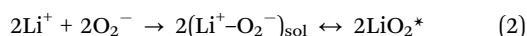
Except for non-precious metal oxides, metal carbides/nitrides/sulfides have also demonstrated good catalytic activity for discharge/charge reactions. Some of them have shown better catalytic activity compared with metal oxides, possibly ascribed to their good electrical conductivity in bulk. Specific metal carbides/sulfides/nitrides, such as Mo₂C, MoS and CoN, have shown unique properties for effectively catalyzing Li₂O₂ formation/decomposition, resulting in low charge potentials and a high cell capacity for Li–O₂ batteries. In particular, the Mo₂C/CNT-based cathode has shown a charge potential lower than 3.5 V for at least 30 cycles.²⁰⁶ Although possible reasons for their advanced properties have been proposed, it is still hard to fully understand their ultralow charge potentials. If the mechanism is clarified, it may provide a good chance to obtain an excellent cathode for high-performance Li–O₂ batteries.

Although various advanced materials and structures have been built to enhance the performance and cyclability of the cathode in Li–O₂ batteries, most of the research to date has paid the most attention to the cell parameters at small current rates (≤1 A g⁻¹, current density on total cathode material amount). As discussed in Section 2.2.2.2, the discharge/charge current rates have a strong impact on the mass transport rate, resulting in different product morphology, overpotential, capacity, rate capability, cyclability, as well as the conversion efficiency.

As one of the main high-capacity battery candidates, more efforts should be paid to investigate the effects of current rates on the cell performance from the viewpoint of high power-density energy conversion devices.

5. Electrolyte

The current state for developing advanced non-aqueous electrolytes is concentrated on screening stable aprotic solvents and functional additives for achieving high-performance and stable Li-O₂ batteries.^{15,25,29} There are three steps for Li₂O₂ formation recognized in the discharge process: the first step is the oxygen reduction reaction based on going from O₂ to the O₂⁻ intermediate (formula (1)), followed by the formation of a solvated Li⁺-O₂⁻ ionic pair ((Li⁺-O₂⁻)_{sol}) and/or adsorbed LiO₂ intermediates (LiO₂* in the second step (formula (2)), and finally in step 3, (Li⁺-O₂⁻)_{sol} and LiO₂* are finally converted to Li₂O₂ (formula (3')) or LiO₂* combines with Li⁺ and electrons to generate Li₂O₂. In the charge step, Li₂O₂ is possibly oxidized to Li⁺ and O₂ directly (formula (4)).



With regard to the above-mentioned mechanism, the electrolytes are essential in four functions: (1) for transport of Li⁺ ions between the Li-anode and oxygen-electrode (Fig. 60a);⁴²⁷ (2) for the dissolution and transport of O₂ molecules for the formation of Li₂O₂ product (Fig. 60b);⁴²⁸ (3) they act as the medium for stabilizing Li⁺-O₂⁻ intermediates, which is beneficial for

developing large Li₂O₂ clusters (Fig. 60c);⁵ (4) for Li₂O₂ decomposition (Fig. 60d). To meet these functions, the corresponding characteristics of solvents and additives, such as water absorbability, volatile rate, viscosity, polarity, ionic conductivity, solubility, and the diffusion rate of oxygen and Li⁺, and the chemical and electrochemical stability of non-aqueous electrolytes need to be evaluated.⁴²⁹

5.1 Stability and Li⁺ transport efficiency of electrolyte solvents

The first function of the electrolyte is Li⁺ transport between the Li-anode and air-cathode, which is mainly controlled by the polarity and viscosity of the electrolyte. In order to achieve a high rate and stable transport of Li⁺ ions in the electrolyte, three points related to the organic solvents should be considered: (1) the solvent should have a good solubility for lithium-salt, so that Li⁺ can be transported with high efficiency; (2) the solvent should be compatible with the Li-anode, which can inhibit the side reactions; (3) the solvent should be inert to nucleophilic attack by superoxide species, which avoids degradation within the working potential range.^{15,430}

In this part, we discuss the present advances made in the efforts to search for solvents with good solubility and a fast transport rate of Li⁺. Since these properties are mainly controlled by the phase state of solvents, the discussion will be divided into three parts: (1) liquid electrolytes with organic solvents, such as carbonate, acrylamide, sulfoxide, ether and pyrrolidinone;^{25,44,431} (2) quasi-solid electrolytes with ionic liquids and/or polymer gels;⁴³² (3) solid-state electrolytes with polymers, inorganic ceramics and/or molten salts.⁴³³⁻⁴³⁵ In addition, the electrochemical stability and decomposition mechanism of organic solvents initiated by superoxide species will be clarified where possible.

5.1.1 Carbonate-based electrolytes. Organic carbonates, such as ethylene carbonate (EC), propylene carbonate (PC), dimethyl carbonate (DMC) and ethyl methyl carbonate (EMC), are widely used as electrolyte solvents for lithium-ion batteries due to their good capability for Li⁺ transport.⁴³⁶⁻⁴³⁸ Accordingly, these carbonates have been studied as solvents for Li-O₂ batteries too.⁴⁴ The first aprotic Li-O₂ battery with EC and PC as electrolyte solvents was pioneered by Abraham and Jiang in 1996, following which carbonates were widely studied.

Laino T. *et al.* investigated the reactivity of lithium peroxide versus PC, and found that Li₂O₂ irreversibly decomposed carbonate solvents, leading to the generation of alkyl carbonates. They also found that a crystalline surface of Li₂O₂ exhibited an enhanced reactivity compared to that of a carbonate solvent.⁴⁴ Careful investigation of the discharge products in PC electrolyte was done by Curtiss L. A. and Amine K. *et al.*⁴³⁹ They demonstrated that the discharge products were Li₂CO₃ and lithium oxide. The decomposition of Li₂CO₃ took place at a higher potential than Li₂O₂, which could be responsible for the observed high overpotentials when using a PC-based electrolyte. Due to their serious instability and the resulting cell deterioration, carbonate-based Li-O₂ batteries are rarely investigated now.

5.1.2 Sulfoxide-based electrolytes. Due to the instability of carbonate-based electrolytes, much effort has been devoted to

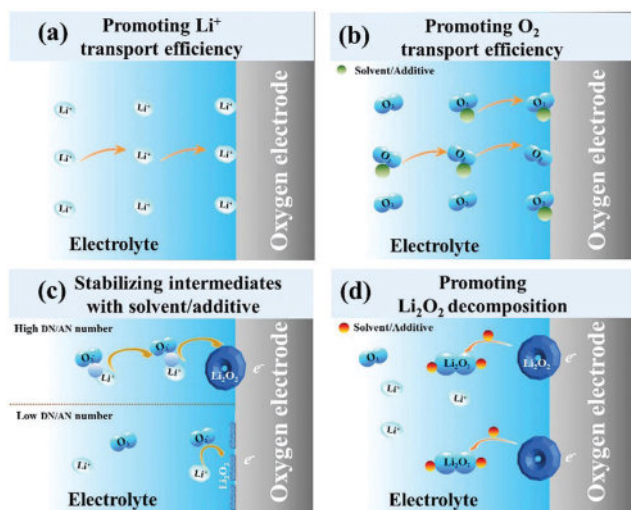


Fig. 60 The functionality of the electrolyte for Li₂O₂ formation and decomposition: (a) promotion of Li⁺ transport efficiency; (b) promotion of O₂ transport efficiency; (c) stabilization of the intermediates; (d) enhancement of Li₂O₂ decomposition.

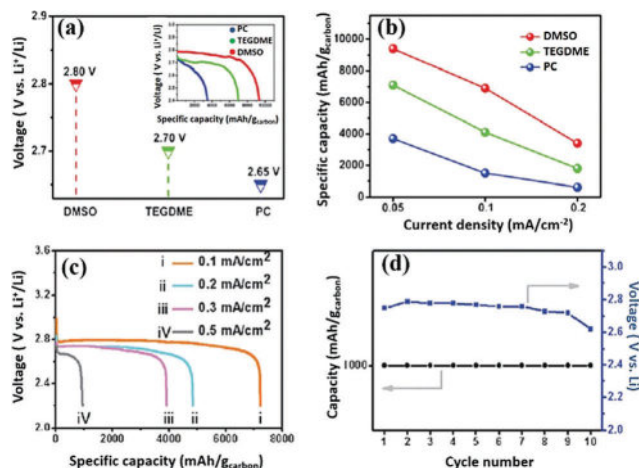


Fig. 61 (a) Discharge voltage plateau, (b) rate capacity of Li–O₂ batteries with KB carbon cathodes and DMSO, TEGDME and PC-based electrolytes at different current densities; (c) discharge curves of Li–O₂ batteries with DMSO based electrolyte at different current densities; (d) cyclic voltage and capacity versus cycle number by controlling the current density at 0.1 mA cm⁻².⁴³¹ Reprinted with permission from ref. 431. Copyright 2012 Royal Society of Chemistry.

the adoption of alternative novel electrolytes for aprotic Li–O₂ batteries. Sulfoxides have a high Lewis basicity and donor number (29.8), which is one type of good medium for aprotic Li–O₂ batteries.^{56,431,440–442} Zhang *et al.* used dimethyl sulfoxide (DMSO) as an electrolyte solvent in a rechargeable Li–O₂ battery with LiTFSI salt. The battery exhibited high capacities of 7200 and 3900 mA h g⁻¹ at 0.1 and 0.3 mA cm⁻², respectively, indicating a good rate capability (Fig. 61). By restricting the discharge depth to 1000 mA h g⁻¹ at 0.1 mA cm⁻², such a Li–O₂ battery showed a stable performance of 10 cycles, which confirmed the good feasibility and efficiency of DMSO for Li–O₂ batteries.⁴³¹ The same group reported tetramethylene sulfone as the electrolyte solvent for Li–O₂ batteries, which showed a discharge voltage plateau of 2.7 V. This was slightly lower than that of DMSO-based batteries. The specific discharge and charge capacity were 7735 and 6305 mA h g⁻¹ at a current density of 0.1 mA cm⁻², respectively, which were comparable to those of DMSO-based devices.⁴⁴³

The decomposition mechanism of DMSO-based electrolyte was investigated by Baltruschat's group.⁴⁴⁴ By using DEMS and an electrochemical quartz crystal microbalance technique, the evolved quantities of CO₂ were found to be linearly dependent on the quantities of O₂ reduced in the cathodic sweep. The superoxide species was formed in the discharge reaction, which was then the active species for the decomposition of DMSO. Moreover, Wittstock *et al.* investigated the generation of superoxides and peroxides species in DMSO-based electrolyte during discharge and charge reactions. Here, 4-chloro-7-nitrobenzo-2-oxa-1,3-diazole (NBD-Cl) was used as a fluorescence probe to detect the soluble O₂^{•-} intermediate.⁴⁴⁵ They found that O₂^{•-} intermediates could be observed in both charge/discharge processes, resulting in decomposition of the solvent and electrolyte additives, as well the loss of cell capacity.⁴⁴⁶ Furthermore,

DMSO could react with Li-metal anode chemically. Consequently, the ultimate application of DMSO solvent should be carefully evaluated in Li–O₂ batteries.⁶

5.1.3 Amide-based electrolytes. Amides are one of key polar solvents that can resist chemical degradation at the O₂ electrode. Bruce *et al.* reported that DMF solvent was more stable than organic carbonates towards attack by O₂^{•-}. They showed that Li₂O₂ was generated in a relatively high purity condition with an *N,N*-dimethylformamide (DMF)-based electrolyte in the first discharge, and was then completely removed on the subsequent charge.²⁵ However, their results also showed that the degree of side reactions increased upon cycling together with the accumulation of Li₂CO₃, HCO₂Li and CH₂CO₂Li at the cathode. The generated LiO₂ and O₂^{•-} species attacked the CO group of the amide, yielding a tetrahedral intermediate. The subsequent reactions generate a series of by-products, such as Li₂O₂, Li₂CO₃, CH₃CO₂Li, HCO₂Li, CO₂, H₂O and NO, which were proved by PXRD patterns, FT-IR, HNMR and DEMS (Fig. 62) measurements.

Other types of amides, for example *N,N*-dimethylacetamide (DMA) and dimethylpyrrolidine (NMP), do not have CO groups in their chains,^{25,447} which might mean they have good stability in the operation of a Li–O₂ battery.^{38,448} Consequently, Walker *et al.* investigated DMA as a solvent for a Li–O₂ cell without any protective membrane for the Li-anode. They found that the reaction between Li and DMA generated soluble species that were electrochemically active above 3.4 V. In order to prevent this side reaction, a SEI layer was produced by cycling the Li-electrode in LiNO₃/DMA electrolyte, and the overpotential and capacity of cell were found to remain mostly unchanged in the charge and discharge profile in the first 1000 h of operation. The stability of this battery system might be attributed to the inertness of the amide core towards Li-metal, and also because the protective SEI film could form and inhibit the side reactions.³⁸

Tokur also tried to use a hybrid of PVdF, polyethylene oxide and aluminium oxide with NMP as a hybrid electrolyte

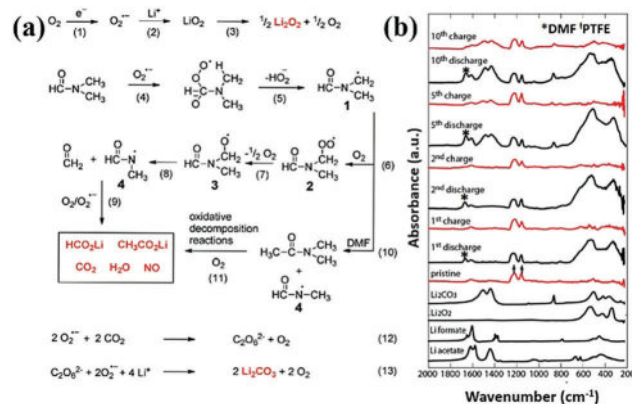


Fig. 62 (a) Proposed mechanism for the discharge reactions in a Li–O₂ battery; (b) FT-IR spectra of Super-P carbon/PTFE composite electrodes cycled in 0.1 M LiClO₄/DMF electrolyte at a current density of 70 mA g_{carbon}⁻¹ (spectra in red correspond to the pristine electrode and electrodes at the end of charge after the indicated number of cycles).²⁵ Reprinted with permission from ref. 25. Copyright 2012 American Chemical Society.

for a Li–O₂ battery. A small amount of polymer and ceramic were selected as the additives to prevent clogging of the porous structure of the cathode. With the composite electrolyte, the Li–O₂ battery was capable of operating over 35 cycles with a capacity of 2.54 mA h and a Coulombic efficiency close to 100%. In particular, the addition of Al₂O₃ nanoparticles into the polymer-supported NMP electrolyte contributed good ionic conductivity and cycling stability to the cell, and hence were used as a promoter for stabilizing the cell performance.⁴⁴⁸ Wang *et al.* used a hybrid of NMP, TBA⁺ClO₄[−] and LiClO₄ as the electrolyte of a Li–O₂ battery. The battery exhibited a first cycle efficiency of approximately 97%, demonstrating their potential use in Li–O₂ batteries. They also observed that the decomposition of NMP occurred on the air electrode during the recharging process. When the cell was cycled between 2.0 V and 4.1 V five times, both the capacity and efficiency decreased to approximately 70% and 10%, respectively.⁴⁴⁹

Kim and Kang *et al.* used an *in situ* DEMS technique to compare the stability of DMA and TEGDME-based electrolytes by detecting the gas products upon Li–O₂ battery operation. The quantitative DEMS data clearly showed that the energy efficiency of the TEGDME-based cell was lower than 71.0%, the oxygen reduction efficiency at discharge was lower than 92% and the carbon dioxide rate was just higher than 6% during five cycles. However, DMA exhibited a 19% greater oxygen efficiency at charge, 5.1% lower CO₂ generation and 5% higher energy efficiency than TEGDME during the first cycles. These results indicated that DMA might be a more desirable solvent for Li–O₂ batteries.³⁰ Although the cycling ability of Li–O₂ batteries based on an amide electrolyte was good, the stability of amide solvents towards superoxide attack and the degradation mechanism should be clarified to develop a stable amide-based Li–O₂ battery.

5.1.4 Ether-based electrolytes. Ether-based solvents have the advantages of a good solubility for Li⁺ and O₂ and chemical inertia to attack by superoxide species, which is why they have

been broadly studied as an electrolyte component in Li–O₂ batteries.^{450,451} Lots of ethers, such as TEGDME, DME, 1,3-dioxolane and 2-methyltetrahydrofuran, have been reported as electrolyte solvents.⁴⁵² These have been shown to be capable of operating with a Li-metal anode and to be stable to oxidation potentials in excess of 4.5 V vs. Li/Li⁺. In the case of higher molecular weight solvents, such as TEGDME, they have low volatility (boiling point: 275–276 °C).

Sun and Scrosati reported that a TEGDME-based electrolyte with LiCF₃SO₃ salt in a Li–O₂ battery showed a relatively stable operation for 50 and 30 cycles at a capacity of 3000 mA h g_{carbon}^{−1} and 4000 mA h g_{carbon}^{−1}, respectively (Fig. 63). Equally importantly, the cell could be operated under capacity levels as high as 5000 mA h g_{carbon}^{−1} with an average discharge voltage of 2.7 V, leading to a very high energy density of 13 500 W h g^{−1}.⁴ Bruce P. G. *et al.* investigated the stability of ether-based electrolytes with LiPF₆ as the lithium-salt in a Li–O₂ battery. They found that Li₂O₂ was formed on the first discharge, accompanied by ether decomposition, to give a mixture of Li₂CO₃, HCO₂Li, organic lithium-salt, polyethers/esters, CO₂ and H₂O (Fig. 64).²⁹

The possible mechanism for the degradation of ether initiated by the superoxide species was provided by Freunberger *et al.* they proposed that the degradation reaction began with hydrogen abstraction from the β-methylene carbon by superoxide or other strong bases, such as Li₂−_xO, and then subsequent reactions led to the generation of lithium- and alkyl carbonates.²⁹ Curtiss and Amine *et al.* tried to investigate the mechanism for proton or hydrogen abstraction from the terminal α-methyl carbon. Tri(ethylene glycol)-substituted trimethylsilane, dubbed 1NM3, was synthesized as the probe solvent to check the mechanism.⁴³⁹ An increased stability of the 1NM3-based electrolyte was observed, although only one of the glycol termini was protected, indicating that the β-hydrogen of the ether might be the site attacked by the superoxide species.

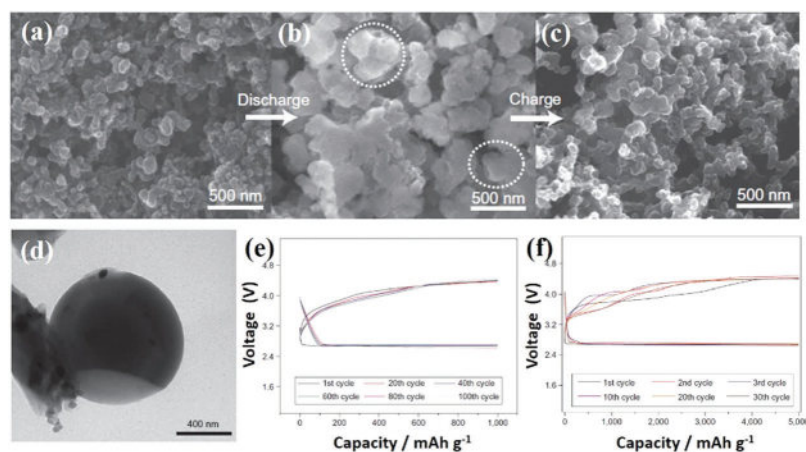


Fig. 63 SEM images of an oxygen electrode: (a) before discharge, (b) in the discharge state and (c) in the reverse charged state of a Li–O₂ cell with TEGDME–LiCF₃SO₃ electrolyte; (d) TEM images of an oxygen electrode with Li₂O₂ toroid in the discharge state with TEGDME–LiCF₃SO₃ electrolyte; the discharge–charge curves of cells using TEGDME–LiCF₃SO₃ electrolyte and a plain carbon electrode (e) at a current density of 1 A g^{−1} and a charge voltage limit of 4.4 V; (f) cycling response of a lithium/TEGDME–LiCF₃SO₃/O₂ battery with the voltage profiles of 30 cycles at a capacity limit of 5000 mA h g_{carbon}^{−1} under a current density of 500 mA g_{carbon}^{−1}.⁴ Reprinted with permission from ref. 4. Copyright 2012 Nature Publishing Group.

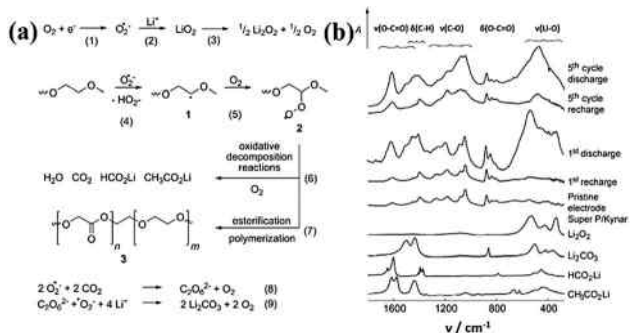


Fig. 64 (a) Proposed mechanism for the discharge reactions and the possible degradation mechanism of ethers initiated by superoxide species in a 1 M LiPF₆/TEGDME-based Li–O₂ battery. (b) FT-IR spectra of a Super-P/Kynar cathode cycled in 1 M LiPF₆/TEGDME under 1 atm O₂ between 2 and 4.6 V versus Li/Li⁺ (the reference spectra for Li₂O₂ (small peaks are due to impurities at 1080, 1450, and 1620 cm⁻¹), Li₂CO₃, HCO₂Li and CH₃CO₂Li, as well as for the pristine electrode (*i.e.* before cycling), are shown; the peaks in the pristine electrode arise from the Kynar binder).²⁹ Reprinted with permission from ref. 29. Copyright 2011 Wiley-VCH Verlag GmbH & Co. KGaA.

Also, 2,3-dimethyl-2,3-dimethoxybutane (DMDMB), where all of the β -hydrogen on carbon was substituted by methyl groups, was synthesized by Nazar L. F., while possible hydrogen abstraction was eliminated (Fig. 65). The electrolyte composed of DMDMB and LiTFSI salt formed a stable [(DMDMB)₂Li]TFSI complex, which inhibited the formation of lithium formate,

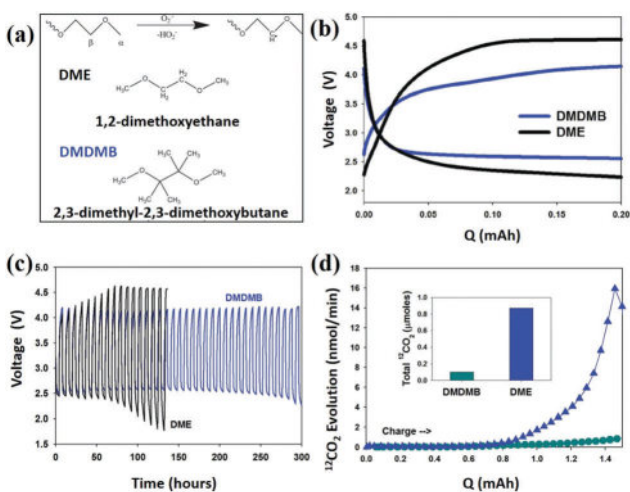


Fig. 65 (a) Proposed initial hydrogen abstraction step of glymes by superoxide during cell discharge and the structures of 1,2-dimethoxyethane (DME) and 2,3-dimethyl-2,3-dimethoxybutane (DMDMB); (b) The discharge-charge curve of the 10th cycle for the [(DMDMB)₂Li]TFSI and [(DME)₂Li]TFSI electrolytes at a current density of 50 $\mu\text{A cm}^{-2}$; (c) the overall voltage vs. time plots of Li–O₂ batteries with DME (black) and DMDMB (blue) electrolytes at 50 $\mu\text{A cm}^{-2}$ using Li-metal anode and TiC cathode (a capacity cut-off of 0.2 mA h (4 h discharge or charge maximum), was applied, along with a lower voltage limit of 1.75 V and upper voltage limits of 4.2 V (DMDMB) and 4.65 V (DME)); (d) comparison of the ¹²CO₂ evolution from DME (blue triangles) and DMDMB (teal circles) electrolytes by differential electrochemical mass spectrometry during galvanostatic charge at 0.25 mA of ¹³C cathode (the cells were firstly discharged to 1 mA h in O₂ at 0.25 mA).³¹ Reprinted with permission from ref. 31. Copyright 2015 Wiley-VCH Verlag GmbH & Co. KGaA.

dimethyl oxalate and lithium carbonate in the discharge process. Consequently, no CO₂ was evolved even with a charge potential over 4.0 V, which was clarified by DEMS technique. Compared to DME-based electrolytes, much less decomposition product was deposited on the electrode surface. After the cell with the TiC cathode was cycled for over 300 h, only a little change in overpotential was observed.³¹

The concept for removing the β -hydrogen from the ether molecular chain was confirmed by Aurbach *et al.*, who synthesized 2,4-dimethoxy-2,4-dimethylpentan-3-one as a solvent to resist nucleophilic attack and hydrogen abstraction by superoxide species. With a discharge cell capacity close to 7 mA h, they found that only a negligible amount of solvent was degraded after prolonged cycling of their Li–O₂ battery. This confirmed that a solvent without β -protons on the carbon should have a high resistance to reactive species in comparison to the common ether solvents.⁴⁵³

5.1.5 Quasi-solid-state and solid-state electrolytes. A Li–O₂ battery with a liquid electrolyte presents a number of technical challenges, in particular associated with: (1) solvent evaporation; (2) the ingress of penetrating gas (such as CO₂, H₂O, O₂) crossover from the cathode; (3) safety issues and side reactions initiated by Li dendrite and electrolyte components. Quasi-solid-state and solid-state electrolytes might provide an effective method to address these issues.^{454–456} Moreover, quasi-solid-state and solid-state electrolytes can offer additional benefits in scalability and processability for Li–O₂ batteries, as proven with their application in lithium-ion batteries.⁴⁵⁴

5.1.5.1 Ionic-liquid-based quasi-solid-state electrolytes. Ionic liquids show several advantages over traditional aprotic solvents, such as negligible vapour pressure, high ionic conductivity, non-flammability and a large and stable potential window.⁴⁵⁷ The general cations of ionic liquids are imidazolium, pyridinium, quaternary-ammonium and quaternary-phosphonium ions, while the anions are halide, tetrafluoroborate and hexafluorophosphate ions.¹³² The characteristics of ionic liquids can be tuned due to the diversity of anions and cations, which provide the opportunity to screen a stable and efficient quasi-solid-state electrolyte for Li–O₂ batteries.

Kuboki *et al.* were the first to use an ionic liquid, 1-ethyl-3-methylimidazolium bis(trifluoromethylsulfonyl)amide (EMITFSI), as the electrolyte solvent for a Li–O₂ battery. In their study, EMITFSI had a high conductivity and hydrophobic property, while the assembled cell showed a high discharge capacity of 5360 mA h g⁻¹. The battery could work for 56 days in ambient air, and no negative effect of the discharge behaviour was observed with a change of humidity.⁴⁵⁸ As it has a similar chemical structure to EMITFSI, 1-butyl-3-methylimidazolium bis(trifluoromethylsulfonyl)amide (BMITFSI) was also tested as an electrolyte solvent for a Li–O₂ battery. The operation of the cell could reach 75 days for 10 cycles without the overpotential changing in the discharge/charge process.⁴²⁹

Zhou and Watanabe's groups recognized that TFSI⁻-anion-based ionic liquids, for example 1-methyl-3-propyl-imidazolium bis(trifluoromethylsulfonyl)amide (MPITFSI) and trihexyl-tetradecylphosphonium bis(trifluoromethanesulfonyl)amide,

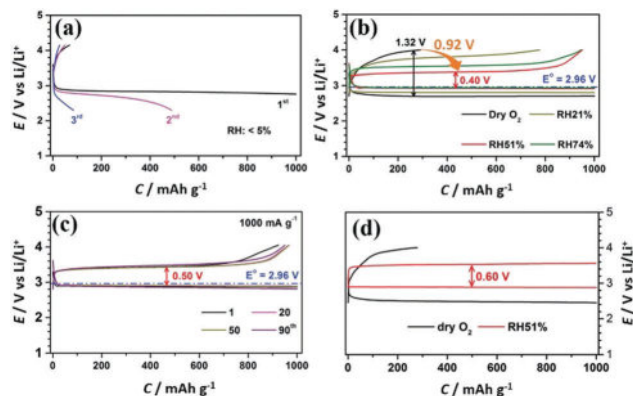


Fig. 66 (a) Initial 3 cycles of the discharge–charge profiles for a TEGDME-based Li–O₂ battery at a room-humidity (RH) of <5% at 500 mA g⁻¹; (b) discharge–charge profiles of MPITFSI-based Li–O₂ batteries in an O₂ atmosphere with various RHs at 500 mA g⁻¹; (c) discharge–charge profiles of the selected cycles at 1000 mA g⁻¹ with a RH of 51%; (d) initial discharge–charge profiles of Li–O₂ batteries in a dry O₂ atmosphere and in a humid O₂ atmosphere with a RH of 51% at 250 mA g⁻¹ (the cell configuration in (a, b, c) was (EMD/RuO₂/SP)/electrolyte/LiFePO₄, and the cell configuration in (d) was (EMD/RuO₂/SP)/electrolyte/LISICON-membrane/electrolyte/Li; EMD: electrolytic manganese oxide).⁴⁹ Reprinted with permission from ref. 49. Copyright 2016 Wiley-VCH Verlag GmbH & Co. KGaA.

might have suitable hydrophobic properties due to their enriched F-atoms, which should make them applicable in an O₂ atmosphere with high humidity for use in Li–O₂ batteries.^{456,459} Their Li–O₂ battery with a MnO₂/RuO₂/carbon cathode and MPITFSI-electrolyte demonstrated a high discharge potential of 2.94 V and a low charge potential of 3.34 V. Such a cell system could be consecutively discharged and charged for 218 cycles at 500 mA g⁻¹ and for 95 cycles at 1000 mA g⁻¹, thus showing its superior rechargeability and rate capability. More importantly, the cell could be operated at a room humidity of over 50% in an O₂ atmosphere, which opened up the reality of a Li–O₂ battery operating as a practical Li–air battery (Fig. 66).⁴⁹

Except for an independent solvent, an ionic liquid could be used as an additive in a liquid solvent to improve the cyclability of Li–O₂ batteries. Park *et al.* used a hybrid of *N*-propyl-*N*-methylpyrrolidinium bis(trifluoromethanesulfonyl)imide (Pyr₁₃-TFSI) and PC as co-solvents for the electrolyte of a Li–O₂ battery. The bulky Pyr₁₃⁺ cation had a soft acidity, which could neutralize the soft base O₂^{•-}. The attack of superoxide radicals on PC could then be alleviated by the existence of Pyr₁₃⁺ cations. The tested cell with a 1:1 ratio of PC and Pyr₁₃-TFSI electrolyte retained 94.6% of its initial capacity after 70 cycles, which was in contrast to the results of a cell with pure PC, which showed a 75% loss of capacity after 70 cycles.⁴⁶⁰ Scrosati B. *et al.* also reported a hybrid solvent by mixing *N*-methyl-*N*-butyl-pyrrolidinium bis(trifluoromethane sulfonyl)imide (Pyr₁₄-TFSI) and TEGDME (mole ratio, 1:1) for the electrolyte of a Li–O₂ battery. The presence of Pyr₁₄-TFSI in the electrolyte decreased the overpotentials of the charge reaction, due to their effect of increasing the kinetics and promoting the reversibility of OER.⁴⁶¹

A series of ester-functioned ionic liquids were tested as additives to a TEGDME electrolyte for a Li–O₂ battery.⁴⁶² One of the

pyrrolidinium-cation-based ionic liquids, namely ethyl-*N*-methylpyrrolidinium-*N*-acetate bis(trifluoromethanesulfonyl)imide, exhibited a lower viscosity, higher ionic conductivity and good stability over a wide potential window than those of imidazolium, piperidinium and morpholinium-cation-based ionic liquids. The mixed electrolytes also showed better capacity and decreased overpotentials compared to a pure TEGDME-based electrolyte, which was due to their enhanced ionic conductivity and inhibited degradation of TEGDME.⁴⁶²

5.1.5.2 Gel-polymer based quasi-solid-state electrolytes. Gel-polymer electrolytes are composed of a polymer matrix swollen with a liquid electrolyte that can provide ionic conductivity close to that of a liquid electrolyte, while at the same time eliminating the problem of potential electrolyte leakage in Li–O₂ batteries. Furthermore, gel-polymer electrolytes can efficiently restrain oxygen diffusion to the Li-anode and electrolyte evaporation.^{432,463} These advantages ensure gel-polymer electrolytes have a promising future for stable and high-performance Li–O₂ batteries.

Abraham reported the first demonstration of a quasi-solid-state Li–O₂ battery with a polyacrylonitrile (PAN)-based gel-electrolyte, which contained a mixture of PAN, EC, PC and LiPF₆ (weight percent, 12:40:40:8). The cells showed specific energies between 250 and 350 W h kg⁻¹.⁹⁴ The same author replaced PAN by PVdF–HFP by plasticizing the copolymer with a solution of LiSO₃CF₃ (LiN(SO₂CF₃)₂ or LiPF₆) in oligomeric poly(ethylene glycol) dimethyl ether (PEGDME). A capacity of 1262 mA h g_{carbon}⁻¹ was achieved at the voltage cut-off of 2.0 V, similar to that of the cell using a PAN polymer-based gel-electrolyte.⁴⁶⁴

Yahya synthesized a gel-polymer electrolyte composed of 50% epoxidised natural rubber polymer, a liquid carbonate plasticizer and 35% LiCF₃SO₃ salt. The ionic conductivity of the gel-polymer electrolyte with 10% PC achieved 4.92 × 10⁻⁴ S cm⁻¹ at room temperature, which is even better than that of electrolytes with a high content of PC. The capacity and power density of a cell with a PC plasticized gel-polymer delivered 62 mA h and 29.7 W h kg⁻¹, respectively.⁴⁶⁵ However, carbonate solvents are known to be easily decomposed at high charge potentials, and the cell stability is therefore quite low.

Ether-type solvents were proved to have a better stability than those of carbonates in Li–O₂ batteries, which might make them more suitable for the preparation of stable gel-polymer electrolytes. Liao *et al.* reported a gel-electrolyte composed of PVdF–HFP, cellulose acetate, TEGDME and LiTFSI. The assembled Li–O₂ battery could be charged and discharged continuously between 2.0 and 4.5 V (*vs.* Li/Li⁺) for 530 h (about 11 cycles). When a confined capacity of 500 mA h g⁻¹ at a current density of 0.05 mA cm⁻² was employed in the cycling tests, the battery maintained 40 stable cycles. In contrast, the liquid electrolyte battery exhibited a continuous discharge voltage decay and lasted for only 30 cycles.⁵² A similar electrolyte component for Li–O₂ batteries was also reported by Zhang and Wang *et al.*, where the tested cell showed a relatively stable 50 cycles at a limited capacity of 500 mA h g⁻¹.⁴⁶⁶

Except for ether-type solvents, ionic liquids have also been used as the components to form gel-polymer electrolytes due to their good stability. Lee *et al.* reported a gel-polymer-based electrolyte, which contained *N*-methyl-*N*-butyl-pyrrolidinium bis(trifluoromethanesulfonyl) imide (Pyr₁₄-TFSI), PVdF-HFP and LiTFSI.⁴⁶⁷ The cell capacity value was equivalent to 2525 mA h g⁻¹ at a current density of 228 mA g⁻¹, and the cell could be cycled for at least 30 cycles with a capacity of 10 mA h. The primary results indicated that ionic liquids might be a good choice for the gel-polymer electrolyte of Li-O₂ batteries. A similar gel-polymer electrolyte for a lithium-ion oxygen battery was also demonstrated by Hassoun *et al.*, in which PVdF-HFP was substituted by poly(ethylene glycol)500-dimethylether (PEG500DME). When the Li-metal was substituted by a Li-Sn-C anode, the battery with a PEG500DME-based electrolyte could be operated for 15 stable cycles at a limited capacity of 100 mA h g⁻¹.⁴⁶⁸

Although the above-mentioned gel-polymer electrolyte showed an enhanced cycling performance compared to that of liquid electrolytes, the presently used liquid solvents, such as carbonates, ethers or ionic liquids, can still possibly decompose during battery operation. With this in mind, more stable liquid solvents and plasticizers should be developed for ensuring a stable output of quasi-solid-state Li-O₂ batteries.

5.1.5.3 Polymer-based solid-state electrolytes. Solid-state polymer electrolytes do not contain organic solvents, so using such electrolytes in the assembled Li-O₂ battery may provide a feasible solution to the safety issues and allow flexible processability compared to batteries with liquid electrolytes.^{33,435} The solid-state polymer electrolytes are generally prepared by dispersing lithium salts into a polymer matrix, such as polyacrylonitrile (PAN), poly(carbonate-ether), poly(ethylene oxide) (PEO)¹³⁹ or PVdF-HFP.⁴⁷⁰ PEO has been known as a solid-state Li⁺ conductor for more than 30 years, and researchers have made great efforts to increase the ionic conductivity, reduce the operation temperature and improve the mechanical stability of PEO-based electrolytes.⁴⁷¹

Scrosati proposed a solid-state electrolyte with PEO, ZrO₂ and LiCF₃SO₃ for a Li-O₂ battery without any cathode catalyst. The overpotential gap of the assembled cell was about 400 mV, which was much lower than that of liquid-electrolyte-based Li-O₂ batteries. However, the cell power density was relatively low, and the battery failed to reach current densities higher than 20 μA cm⁻². This could possibly be ascribed to the low ionic conductivity of PEO-based electrolytes at room temperature.¹³⁹ Ein-Eli *et al.* fabricated a similar solid polymer electrolyte for a Li-O₂ battery, which could work at 80 °C.³³ The PEO-based Li-O₂ cell showed a higher cell discharge voltage by 80 mV and a charge voltage lower by 400 mV in comparison to that of the cell with an ethylene-glycol-dimethyl-ether-based liquid electrolyte at 80 °C. When the cell was discharged at a current density of 0.1 mA cm⁻², the specific discharge capacity was 1481 mA h g_{carbon}⁻¹. Also, the polymeric cell was stable after 40 cycles at a current density of 0.2 mA cm⁻². By combining insights from the electrochemical studies and other characterization techniques, the decomposition products were confirmed

to be a mixture of lower-molecular-weight PEO, esters, formates, oxymethylene, methyl methanoate and water.

Except for PEO, polycarbonate was also investigated as an electrolyte candidate for the preparation of solid-state Li-O₂ batteries. Wang *et al.* prepared a low-molecular weight poly(carbonate-ether)-based electrolyte with LiBF₄ salt in a Li-O₂ battery, which demonstrated a high ionic conductivity (1.57 mS cm⁻¹) due to the relatively low glass transition temperature of the polymer. The obtained cell capacity (at 0.1 mA cm⁻², about 2200 mA h g⁻¹) was comparable to that of the TEGDME/LiBF₄ liquid electrolyte (at 0.1 mA cm⁻², about 2600 mA h g⁻¹).⁴³⁷

5.1.5.4 Inorganic-ceramic-based solid-state electrolyte. Inorganic ceramic materials have a relatively high Li⁺ conductivity compared to solid polymer electrolytes, which allows them to be used as both an electrolyte and membrane for conducting Li⁺ and blocking O₂ permeation to the Li-anode in Li-O₂ batteries.⁴⁵⁴ Compared to those of pure polymeric solid-state electrolytes, there is no degradation process between the interface of the O₂ electrode and the ceramic electrolyte. The above merits make these good candidates for solid-state Li-O₂ batteries.

Kumar and Abraham *et al.* first suggested the use of an inorganic ceramic conductor for an all-solid-state Li-O₂ battery with PEO polymer film as the separator, which could be used in a temperature range from 45 °C to 105 °C. The glass ceramic membrane electrolyte was constructed by Li₂O, Al₂O₃, GeO₂ and P₂O₅ composite oxides. The cell was discharged and charged for 40 cycles at 75 °C and 85 °C with current densities of 0.1 mA cm⁻² and 0.05 mA cm⁻², thus showing good thermal stability and rechargeability.⁴⁷²

Zhou *et al.* further used a Li_{1-x}Al_x(TiGe)_{2-x}Si_yP_{3-y}O₁₂ ceramic electrolyte to improve the performance of the solid-state Li-O₂ battery (Fig. 67). The Li_{1-x}Al_x(TiGe)_{2-x}Si_yP_{3-y}O₁₂ had a high ionic conductivity and thermal stability, while the assembled cell showed a capacity of 300 mA h g⁻¹ in subsequent discharge-charge cycles at a current density of 10 mA g⁻¹. Unfortunately, a poor cycling ability of the cell was observed. The low cycling capacity could be ascribed to the deterioration of the CNT cathode,

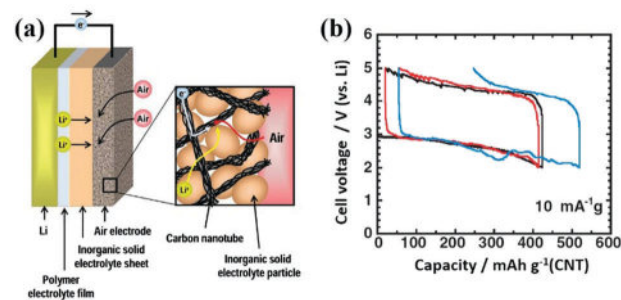


Fig. 67 (a) Schematic diagram of a solid-state lithium-air battery using a Li-anode, polymer electrolyte (PE) film, inorganic ceramic electrolyte (CE) sheet and air electrode composed of CNT and solid-electrolyte particles; (b) charge-discharge curves of the solid-state Li/PE/CE/CNT cell with a weight ratio *x* of 5 (*x* is the weight ratio of CE and CNT particles on the air cathode; black, red and blue lines represent the 1st, 2nd and 3rd cycles, respectively).⁴⁶⁹ Reprinted with permission from ref. 469. Copyright 2012 Wiley-VCH Verlag GmbH & Co. KGaA.

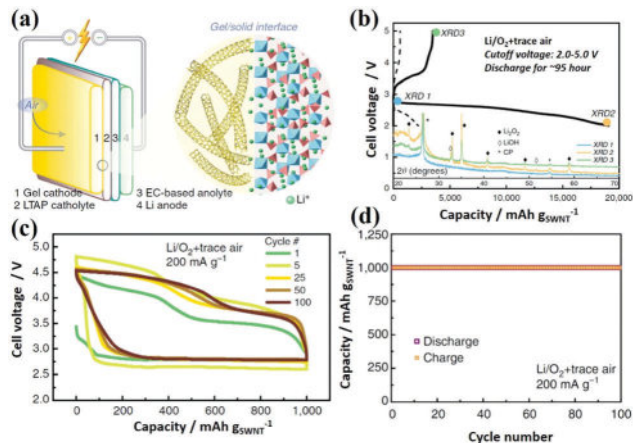


Fig. 68 (a) Schematic illustration of the proposed Li-air cell with LiTFSI-modified crosslinked network gel (CNG) cathode; (b) discharge-charge performance and XRD analysis of Li-air batteries without LiTFSI-modified CNG; (c) discharge-charge curves and (d) cycling profiles of Li-air cell with LiTFSI-modified CNG under a fixed capacity of 1000 mA h g_{SWNT}^{-1} for 100 cycles for 100 cycles.⁸ Reprinted with permission from ref. 8. Copyright 2013 Nature Publishing Group.

coarsening of the discharge products (*i.e.* LiOH, Li₂O₃ or Li₂CO₃) or irreversible deposition of the large amount of discharge products.⁴⁶⁹ Further improvements in this cell should be done to achieve a stable air cathode and to decrease the interface resistance between the electrolyte and electrode. The same author further constructed a Li-O₂ battery by using these ceramic electrolytes and a cross-linked network gel (GNG) air cathode, which consisted of single-walled CNTs and 1-ethyl-3-methylimidazolium bis(trifluoromethylsulfonyl)imide (Fig. 68). The CNG electrode had superior 3D tri-continuous passages of electrons, ions and oxygen, which enabled the three-phase cathodic reaction to occur independent of liquid electrolyte permeation. The discharge and charge capacity reached 56 800 mA h g^{-1} and 53 900 mA h g^{-1} (capacity based on CNT mass), respectively, with a Coulombic efficiency of 95%. More important, the cell sustained the repeated cycling for 100 cycles with a limited discharge capacity of 2000 mA h g^{-1} .⁸

Park *et al.* reported a bilayer lithium phosphorous oxynitride/aluminium-substituted lithium lanthanum titanate solid-electrolyte for a Li-O₂ battery. Due to the high ionic conductivity of 2.25×10^{-4} S cm^{-1} and good stability of the electrolyte in the tested electrochemical window, the cell exhibited excellent charge-discharge cycling stability with a long-life span of 128 cycles at a limited capacity of 1000 mA h g^{-1} . However, it should be noted that 5 μ L of organic electrolyte was used between the Li-anode and solid-electrolyte to decrease the interfacial resistance, so in fact, it cannot really be called a true all-solid-state Li-O₂ battery.¹⁹⁷

Sun *et al.* demonstrated garnet ceramic (Li_{6.4}La₃Zr_{1.4}Ta_{0.6}O₁₂) as a solid electrolyte for a Li-O₂ battery, which was assembled with a composite cathode consisting of garnet powder, Li-salt, polypropylene carbonate and active carbon. The resulting batteries showed a discharge capacity of 20 300 mA h g_{carbon}^{-1} and could be cycled 50 times while maintaining a cut-off capacity of 1000 mA h g_{carbon}^{-1} at 20 μ A cm^{-2} and 80 °C.⁴⁵⁴

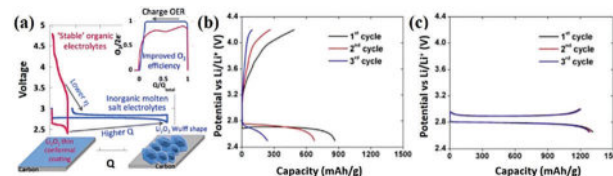


Fig. 69 (a) Comparison of the voltage and pressure profiles of a Li-O₂ battery measured in liquid and inorganic molten-salt electrolytes; the discharge/charge profiles of a cell with: (b) LiClO₄-DMSO electrolyte at 30 °C between the cut-off voltages of 2.5 and 4.2 V, and (c) LiNO₃-KNO₂-CsNO₃ molten salt electrolyte at 120 °C between the cut-off voltages of 2.65 and 3.0 V (cathode: Super-P carbon/PTFE, 95:5 wt%; electrolyte volume: 150 μ L; carbon mass: \sim 4 mg cm^{-2} ; current density: \sim 80 mA g_{carbon}^{-1}).⁴⁷³ Reprinted with permission from ref. 473. Copyright 2016 American Chemical Society.

5.1.5.5 Molten-salt-based solid-state electrolytes. Research into molten salt electrolytes for lithium-ion batteries and thermal batteries can be traced back to the 1970s, where they were first found to be stable for primary cells and rechargeable cells but with a limited cycle life. Giordani and Addison from Liox Power Company showed a moderate temperature Li-O₂ battery by using a lithium anode, a molten LiNO₃-KNO₂-CsNO₃ electrolyte and a porous carbon cathode with a high energy efficiency and improved rate capacity (Fig. 69). The discharge product, Li₂O₂, was stable and moderately soluble in the molten salt electrolyte at high temperature, which enabled the easy operation of the discharge/charge processes. This resulted in an overpotential gap as low as 50 mV, but the cell capacity was relatively low due to the low O₂ solubility in the electrolyte. The cycling stability of the molten-salt-based Li-O₂ battery was also not good, which could be ascribed to the degradation of the carbon-based cathode.⁴⁷³

5.2 Stability of Li-salts

Except for evaluating the stability of aprotic solvents, the electrochemical stability of Li-salts, another critical component in the electrolyte, should also be well clarified to achieve the long-term stability of a Li-O₂ battery. Chalasani and Lucht found that LiBF₄, lithium bis(oxalato)borate (LiBOB, Li(C₂O₄)₂B) and LiTFSI were chemically stable in the presence of Li₂O₂, while LiPF₆ tended to generate OPF₂OLi and LiF.⁴⁷⁴ Veith investigated the electrochemical stability of the TEGDME-based electrolyte with LiBF₄, LiClO₄ and LiTFSI salts by using XPS, Raman spectra and ¹⁹F-NMR techniques. Analysis of the discharge products on the cathode indicated that all three Li-salts underwent similar decomposition, which was likely due to superoxide species (or reactive oxygen species) reacting with the counter-anion of the Li-salts. LiClO₄ appeared to be less reactive than those of Li-salts with the F element.⁴⁷⁵

Calvo *et al.* also compared the stability of LiPF₆ and LiBF₄ in two types of solvents: DMSO and acetonitrile. In an acetonitrile-based electrolyte, LiBF₄ showed less decomposition than that of LiPF₆, which was proved by XPS analysis.⁴⁷⁶ Xu and Zhang *et al.* studied the performance and stability of seven Li-salts, including LiBF₄, LiBr, LiBOB, Li(C₂O₄)₂, LiPF₆, LiTFSI, LiTF and LiClO₄, in TEGDME-based electrolytes (Fig. 70). The cell discharge capacity

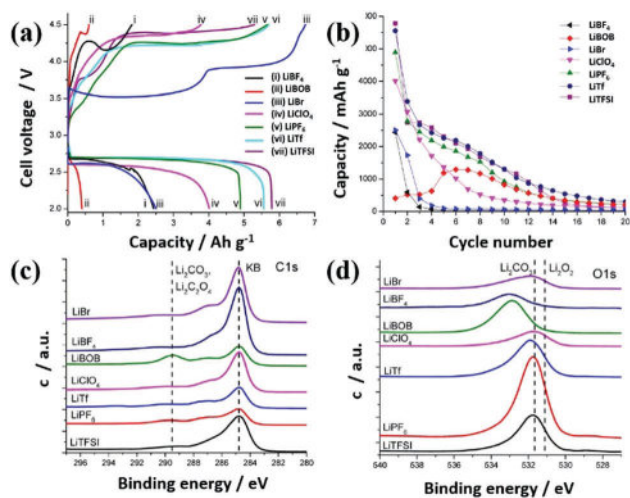


Fig. 70 (a) First cycles of the discharge–charge voltage profiles and (b) cycling stability of Li–O₂ batteries with different electrolytes at a current density of 0.05 mA cm⁻²; XPS (c) Li 1s and (d) O 1s spectra of the discharge products with various electrolytes (KB carbon loading: 1 mg cm⁻²; current collector: carbon paper).⁴⁷⁷ Reprinted with permission from ref. 477. Copyright 2013 American Chemical Society.

decreased in the order of LiTFSI > LiTf ≈ LiPF₆ > LiClO₄ > LiBF₄. LiBr, LiBOB and LiClO₄ were found to be stable during cell cycling. In contrast, minor signs of salt decomposition were observed in LiTFSI-, LiTf- and LiPF₆-based electrolytes during the cell discharge process. LiBF₄ and LiBOB were unstable and consequently accompanied with a large amount of side products. It could be deduced that the salt anions had a non-negligible effect on the cell stability.⁴⁷⁷

5.3 Electrolytes with good O₂ transport efficiency

The second function of the electrolyte is O₂ transport for Li₂O₂ formation.⁴²⁸ The Li₂O₂ formation reaction is suggested to occur at the three-phase interface of the solid/liquid/gas (electrode, electrolyte and oxygen).⁴⁷⁸ Since an abundance of Li⁺ ions could be easily achieved by modulation of the electrolyte components, the transport efficiency of O₂ plays the dominant role in the determination of the reaction rate, especially in the high current density region. O₂ transport efficiency in an electrolyte is mainly controlled by the polarity and viscosity of the solvents. Additionally, functional additives can also be used to regulate these properties.^{428,479}

Read *et al.* investigated the O₂ solubility, viscosity and ionic conductivity in the different electrolytes.⁴²⁸ They found that these properties were greatly influenced by the polarity of the solvent and additives, the intermolecular interaction with the electrolyte components and the concentration of Li-salts. The Bunsen solubility coefficient was used to quantitatively evaluate O₂ solubility in the electrolyte, where it was found that solvents with low polarity have a higher Bunsen coefficient (high O₂ concentration) than solvents with high polarity. Moreover, an increase in Li⁺-salt concentration would decrease oxygen solubility (low Bunsen coefficient). For example, the discharge capacity of a Li–O₂ battery with a 1 M LiPF₆-based

PC : DME (1 : 1) electrolyte was lower than that of a Li–O₂ battery with 0.5 M LiPF₆-based PC : DME (1 : 1) electrolyte, due to their different oxygen concentrations.⁴²⁸

Except for the solvents and Li-salt, some low-polarity molecules could act as promoters to increase O₂ concentration in the electrolyte, with fluorine-containing molecules being one type of such reagent. Oyaizu and Nishide *et al.* used perfluorohexyl bromide (PFB) as an oxygen-uptake component in the TEGDME-based electrolyte with LiTFSI or LiPFOS (lithium perfluorooctanesulfonate, LiSO₃(CF₂)₇CF₃) salt. Similar to that of the PFB reagent, BrC₆F₁₃ had a low polarity and high miscibility with TEGDME in the presence of LiPFOS salt, and O₂ enrichment could be realized with increasing the BrC₆F₁₃ content in the electrolyte. This resulted in an enhanced discharge capacity of the Li–O₂ battery.⁴⁸⁰ Other F-containing molecules, for example tris(2,2,2-trifluoroethyl)phosphate (TTFP) and nonafluorobutyl ether (MFE), could also be O₂ takers for increasing the specific capacity and rate capability of Li–O₂ batteries, although the addition of TTFP caused a little increase in the viscosity and a decrease in the ionic conductivity.

The perfluoro-chemicals as O₂ carriers were important for O₂ solubility in high-polarity solvents, for example DMSO and DMF, while they had a relatively low O₂ solubility but high DN value for the growth of large Li₂O₂ particles. When 1,2-(1,1,2,2-tetrafluoroethoxy) ethane (FE1) and DMSO were used as the co-solvent (volume ratio: 1:1) in a Li–O₂ battery, the cell discharge capacity was 11 744 mA h g_{carbon}⁻¹ at 25 mA g_{carbon}⁻¹ in comparison to that of pure DMSO-based electrolyte (814 mA h g_{carbon}⁻¹). The improved cell capacity was attributed to the increased solubility of O₂ as a result of the fluorinated reagents in the electrolyte.^{449,479} The above-mentioned results emphasize that the perfluoro-chemicals are important for improving O₂ accessibility in high-polarity solvents, and can expand the working voltage window at a high current density.⁴⁸¹

5.4 Electrolytes for Li₂O₂ formation

The third function of an electrolyte is tailing the stability of solvated Li⁺–O₂⁻ and LiO₂* intermediates. As referred to previously, two types of discharge paths, namely surface-phase growth (at cathode surface) and solution-phase growth (in electrolyte), are proposed for Li₂O₂ formation in a discharge process (Fig. 71). The stability of solvated Li⁺–O₂⁻ and LiO₂* intermediates was considered to be a controllable factor for these two paths. A good stability of solvated Li⁺–O₂⁻ prefers Li₂O₂ formation through solution-phase growth, resulting in a large quantity of Li₂O₂ product and a high cell capacity.^{5,145} In this vein, continuous efforts have been concentrated on the screening of solvents, Li-salts and other additives for stabilizing the solvated Li⁺–O₂⁻ intermediate to form large Li₂O₂ clusters.

5.4.1 The effects of the solvent. Numerous researchers have shown that the stability of solvated Li⁺–O₂⁻ intermediates is influenced by the type of solvents, resulting in a big difference in cell performance.^{5,85} In 2010, Abraham investigated the effect of different solvents and supporting cations on the nature of the reduction products and the cell rechargeability. TBA⁺PF₆⁻ was introduced as an additive in the electrolyte without Li⁺ ions.

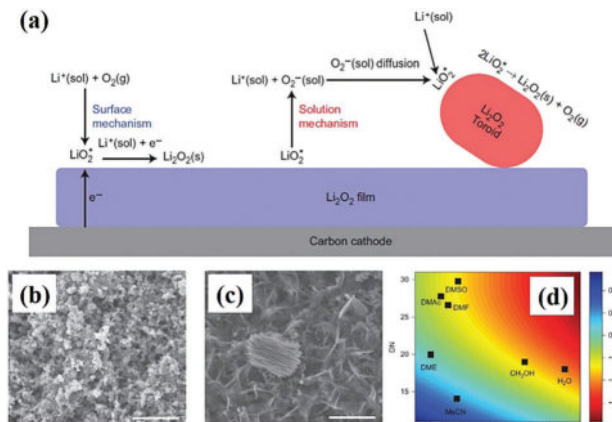


Fig. 71 (a) Proposed mechanism for the growth of Li_2O_2 toroids in the presence of water (the deposition of Li_2O_2 in a $\text{Li}-\text{O}_2$ cell is shown schematically to proceed via a surface-growth process that occurs on a nucleated film of Li_2O_2 through the sequential transfer of solvated Li^+ ($\text{Li}^+(\text{sol})$) and an electron (e^-) to the intermediate species LiO_2^* , eventually forming Li_2O_2 . The electron must therefore tunnel through the nucleated Li_2O_2 film as indicated, and this process is limited by the electronic conductivity of Li_2O_2 . The presence of a solvent (water in our experiments) solvates LiO_2^* to $\text{Li}^+(\text{sol})$ and then the solvated O_2^- ($\text{O}_2^-(\text{sol})$) triggers a solution pathway leading to the growth of toroids, as shown schematically. $\text{O}_2^-(\text{sol})$ is adsorbed as LiO_2^* on the growing toroidal particle, ultimately disproportionating to form Li_2O_2 . Thus, $\text{O}_2^-(\text{sol})$ acts as a redox shuttle and leads to the formation of large particles, thereby circumventing the conductivity limitations in the surface growth); SEM images of a Vulcan-carbon cathode discharged to a capacity of 1 mA h using nominally anhydrous (<30 ppm) 1 M LiTFSI/DME electrolyte in the (b) absence and (c) presence of 4000 ppm water (scale bars, 1 μm); (d) quantitative basis for solvent selection for high-capacity $\text{Li}-\text{O}_2$ batteries (the free energy of dissolution for LiO_2^* into $\text{Li}^+(\text{sol})$ and $\text{O}_2^-(\text{sol})$ in different solvents as a function of the Gutmann acceptor and donor numbers (AN and DN); the free energy plot is normalized relative to that of pure DME; DMF, dimethyl acetamide (DMAc) and DMSO have high DN values and are thus capable of stabilizing Li^+ . Water and methanol, on the other hand, have high AN values and thus stabilize O_2^- .¹⁶ Reprinted with permission from ref. 16. Copyright 2015 Nature Publishing Group.

It was found that O_2^- was stabilized by the TBA^+ anion to form a $\text{TBA}^+-\text{O}_2^-$ complex, due to the strong electron-accepting ability of TBA^+ . This phenomenon could be explained by Pearson's hard-soft acid-base (HSAB) theory.⁸⁵ It was shown that aprotic ORR was a highly reversible one-electron process involving the O_2/O_2^- couple in TBA^+ -containing electrolytes. In contrast, O_2 reduction proceeds in a stepwise fashion to form O_2^- , O_2^{2-} and O^{2-} products in Li^+ -containing electrolytes, which is a kinetically irreversible or quasi-reversible reaction. Similarly, the bond strength between Li^+ and different solvents should also follow HSAB theory, which is related to the basicity of solvents, or more accurately, the electron-donating ability from oxygen atoms (that is, the donor number (DN)). The bond strength between Li^+ and the solvent was followed in the order: $\text{DMSO} > \text{MeCN} > \text{DME} > \text{TEGDME}$.⁸⁵ Therefore, the stability of $\text{Li}^+(\text{solvent})_n-\text{O}_2^-$ ion pairs was determined by the stabilization degree of solvated Li^+ . Solvents with a high DN value appeared to provide a higher degree of stability for intermediates, while solvents with a low DN value have a lower degree stability for intermediates.⁸⁵

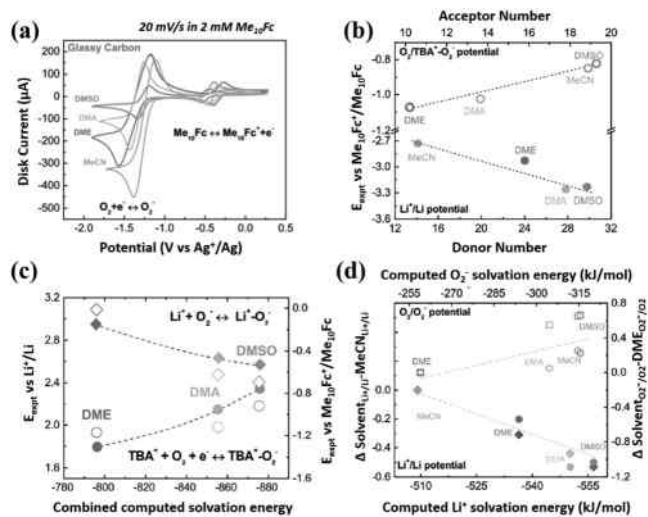


Fig. 72 (a) Steady-state CVs of $\text{O}_2/\text{TBA}^+-\text{O}_2^-$ and $\text{Me}_{10}\text{Fc}^+/\text{Me}_{10}\text{Fc}$ redox reactions collected at 20 mV s^{-1} in O_2 -saturated electrolytes containing 2 mm Me_{10}Fc in 0.5 M TBAClO_4 in DME, 0.1 M TBAClO_4 in DMA, and DMSO, obtained with an Ag/Ag^+ reference electrode and Ni foam counter electrode; (b) experimental standard $\text{O}_2/\text{TBA}^+-\text{O}_2^-$ and Li^+/Li redox potentials vs. $\text{Me}_{10}\text{Fc}^+/\text{Me}_{10}\text{Fc}$ plotted against acceptor and donor numbers of each solvent; (c) comparison of standard experimental (open hexagons) and calculated (open squares) O_2/O_2^- redox potentials, and experimental (filled circles) and calculated (filled diamonds) Li^+/Li redox potentials against computed Li^+ and O_2^- solvation energies of each solvent (all Li^+/Li and O_2/O_2^- potentials were plotted with respect to MeCN and DME, respectively); (d) the relationship between standard redox potentials of $\text{O}_2/\text{TBA}^+-\text{O}_2^-$ (circles) and $\text{O}_2/\text{Li}^+-\text{O}_2^-$ (diamonds) vs. Li^+/Li (filled symbols) and $\text{Me}_{10}\text{Fc}^+/\text{Me}_{10}\text{Fc}$ (open symbols), and the total solvation energy for Li^+ and O_2^- ions calculated from a mixed cluster-continuum model for each solvent.¹⁴⁵ Reprinted with permission from ref. 145. Copyright 2016 Wiley-VCH Verlag GmbH & Co. KGaA.

In addition to DN, the acceptor number (AN) of a solvent also plays a critical role in the ORR process in $\text{Li}-\text{O}_2$ batteries. Shao-Horn *et al.* measured the standard potentials of $\text{O}_2/\text{Li}^+-\text{O}_2^-$ and O_2/O_2^- experimentally, and also calculated them with a mixed cluster-continuum model of ion solvation (Fig. 72). They found that the standard $\text{O}_2/\text{TBA}^+-\text{O}_2^-$ potentials increased with a greater AN, and the Li^+/Li redox potentials decreased with a greater DN. Furthermore, the increase in O_2^- and Li^+ solvation degree (expressed by $\text{O}_2/\text{TBA}^+-\text{O}_2^-$ redox potentials) improved the solubility of Li^+-O_2^- in the electrolyte. This is highly important for suppressing the surface nucleation rates or trigger solution-phase growth of Li_2O_2 . This observation indicated that although the combined computed solvation energy was dominated by the Li^+ solvation energies (scaling with DN), the solvation energies of O_2^- (scaling with AN) were also important for increasing the cell capacity. This highlighted the importance of the interplay between ion-solvent and ion-ion interactions in understanding and controlling the intermediate species energetics, reaction product morphology, discharge capacity and solvent stability in aprotic $\text{Li}-\text{O}_2$ batteries.¹⁴⁵

5.4.2 The effects of additives

5.4.2.1 Lithium-salt. Yamada and Zhou *et al.* prepared aprotic electrolytes with different molar ratios of LiTf and TEGDME (or DME) solvent. The best cycling stability for a $\text{Li}-\text{O}_2$ battery

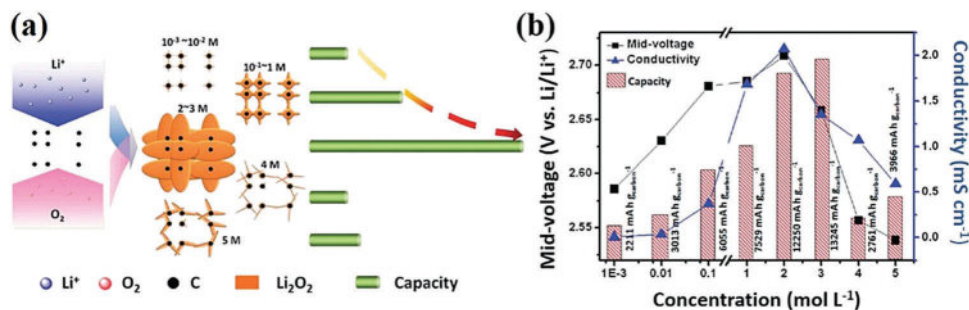


Fig. 73 (a) Schematic illustration of the cell discharge capacities and Li_2O_2 morphologies influenced by Li^+ concentrations in the electrolyte; (b) the concentration dependence of the mid-voltages (corresponding to the midpoint voltage of the discharge process), conductivities and discharge capacities in LiTFSI–TEGDME electrolytes.⁴⁸⁴ Reprinted with permission from ref. 484. Copyright 2014 Royal Society of Chemistry.

was obtained with the molar ratio of 1:5 for LiTf:TEGDME in the electrolyte. The high stability of electrolytes could be explained by the competition for accessibility of $\text{O}_2^{\bullet-}$ radicals between solvated Li ions and TEGDME molecules.⁴⁸² Xu and Zhang also investigated the effect of LiTFSI concentrations on the cycling stability of a Li– O_2 battery with DME-based electrolytes. The cell with 3 M LiTFSI showed a high cycling stability under both full discharge and charge (2.0–4.5 V) under capacity-limited conditions (1000 mA h g^{-1}). It was suggested that the C–H bond scission of DME molecule became more robust with highly concentrated Li-salts present in the electrolyte.⁴⁸³

Wang and Hu systematically investigated the effect of Li^+ concentrations on the discharge capacity of a Li– O_2 battery with TEGDME/LiTFSI electrolytes (Fig. 73).⁴⁸⁴ They found that an increase in Li^+ concentration could result in a larger cell discharge capacity, with the discharge capacity volume achieved at the highest value with 3 M LiTFSI. It was explained that Li_2O_2 tended to grow on the carbon surface in the dilute electrolytes *via* a surface-growth pathway, while the solution-mediated growth had a leading effect at higher Li^+ -ion concentrations.⁴⁸⁴ Consequently, concentrated Li^+ ions could generate the tri-dimensional Li_2O_2 cluster, resulting in the high cell capacity.

The negative effect of Li^+ concentration on the cell stability was also studied by conducting a combined experimental and computational study. By varying the Li^+ concentrations in a DME + LiTFSI electrolyte, Garcia *et al.* identified two different failure mechanisms for the cell chemistry based on the decomposition of the anion in the electrolyte. High Li^+ concentrations could increase the amount of decomposition products coming from both the solvent and Li-salt in the electrolyte, as exemplified by high levels of H_2 production and low O_2 production at the onset charge step with DEMS tests. This finding was contrary to the above-mentioned results that high-concentration LiTFSI in DME-based electrolytes provided additional stability to Li– O_2 batteries. Therefore, the effect of Li^+ concentration on cell performance and stability remain to be fully explained.⁴⁸⁵

In addition to the effect of Li^+ cations, McCloskey *et al.* also demonstrated that anions of the Li-salt played a critical role in promoting the solubility of the intermediates during the discharge of a Li– O_2 battery. The promoted toroid-shaped formation and the enhanced cell capacity were observed by utilizing an increased ratio of LiNO_3 in the LiNO_3 -LiTFSI/DME-based electrolyte.

This was ascribed to the high DN number of NO_3^- species, as previously discussed. The authors developed a generalized model for the predicted Li^+ solvation shell occupation and the resulting stability of Li^+ in the electrolyte, which could be a guiding principle to develop promising electrolytes for high-capacity and long-life Li– O_2 batteries (Fig. 74).⁵

Aurbach *et al.* also showed that the morphology and quantity of Li_2O_2 were significantly influenced by the level of

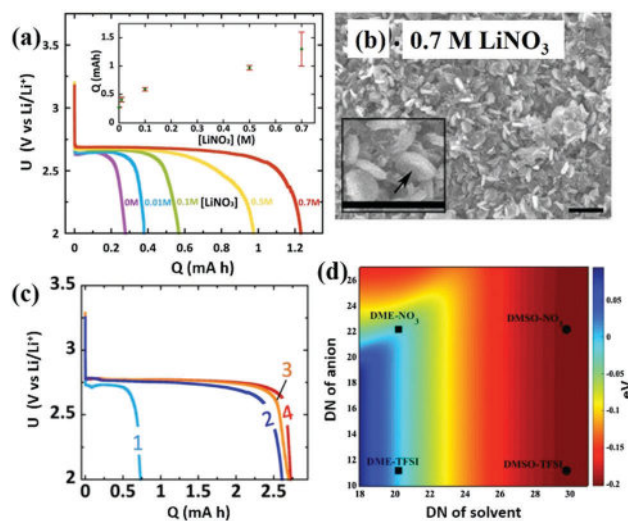


Fig. 74 (a) Representative discharge profiles of Li– O_2 cells at a current density of $450 \mu\text{A cm}^{-2}$ under a 1.5 atm O_2 atmosphere to a 2 V cut-off (the inset shows the capacity dependence on LiNO_3 concentration); (b) SEM image of discharged cathodes from cells using 0.3 M LiTFSI and 0.7 M LiNO_3 (cells were discharged to 0.9 mA h cm^{-2} at $45 \mu\text{A cm}^{-2}$ with a 2 V cut-off voltage, and all the cells had at least a 0.5 mA h cm^{-2} capacity (scale bars, 1 μm); (c) discharge profiles ($45 \mu\text{A cm}^{-2}$, 2 V cut-off) for cells with DMSO and DME-based electrolytes (labels correspond to discharges of the cells using the following electrolytes: 1. 1 M LiTFSI in DME, 2. 0.5 M LiNO_3 :0.5 M LiTFSI in DME, 3. 1 M LiTFSI in DMSO and 4. 0.5 M LiNO_3 :0.5 M LiTFSI in DMSO); (d) contour plot showing the free energy of Li^+ for electrolytes with varying DN of the solvent and salt anion, in kcal mol^{-1} (The free energy was normalized relative to those of DME and 1 M LiTFSI; the electrolyte was considered to be a 50 : 50 mixture of LiTFSI and a salt consisting of Li^+ and the labelled salt anion in the labelled solvent; the blue region corresponds to those electrolytes incapable of triggering the solid-surface path, whereas the red region correspond to those that can trigger the solution-mediated process).⁵ Reprinted with permission from ref. 5. Copyright 2015 National Academy of Sciences.

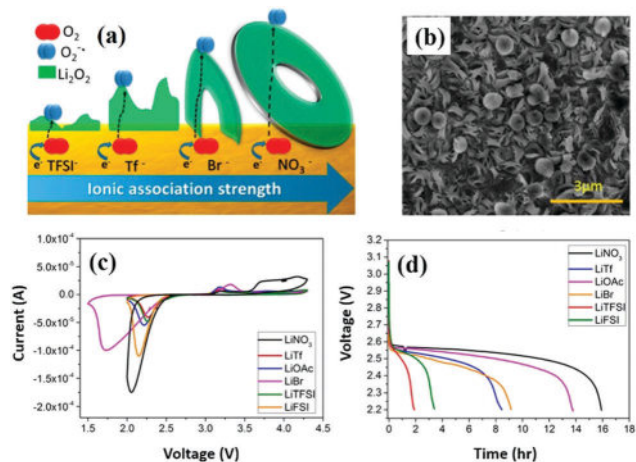


Fig. 75 (a) Schematic illustration for the proposed mechanism of Li_2O_2 formation modulated by the Li^+ dissociation level with different cations; (b) SEM image of discharged gold cathodes with toroid-shaped particles of diameter about 600–800 nm in 1 M LiNO_3 in DME; (c) CVs (5 mV s^{-1}) of 1 M LiX in DME under an O_2 atmosphere; (d) discharge curves ($3 \mu\text{A cm}^{-2}$) of 1 M LiX in DME (gold and Li-metal were used as the counter and reference electrodes, respectively).¹¹² Reprinted with permission from ref. 112. Copyright 2016 American Chemical Society.

Li^+ ion dissociation, which was controlled by the counter-anion in the low DN solvents. The Li^+ association strength in DME-based electrolytes was contrary to the ionic conductivity of the electrolyte. The ionic conductivity (mS cm^{-1}) trend of 1 M LiX (X denoted as the anion) in 30°C was as follows: $\text{FSI}^- (10.66) > \text{TFSI}^- (9.46) > \text{Tf}^- (2.94) > \text{Br}^- (1.21) > \text{NO}_3^- (0.87) > \text{OAc}^- (0.13)$. Consequently, the Li^+ association strength of LiX was as follows: $\text{FSI}^- < \text{TFSI}^- < \text{Tf}^- < \text{Br}^- < \text{NO}_3^- < \text{OAc}^-$. 1 M LiTFSI and LiFSI DME-based electrolyte had a Li_2O_2 layer structure with a small thickness, while the 1 M $\text{LiNO}_3/\text{LiOAc}$ -DME-based electrolyte had toroid-shaped particles with a high thickness. The cell with the Li_2O_2 toroid morphology had the larger amount of Li_2O_2 and larger cell discharge capacity (Fig. 75). This work suggested that the use of lowly dissociated Li-salts in low DN solvent would follow a surface-growth mechanism of Li_2O_2 , forming a uniform and thin layer that blocked the electrode after reaching coverage of a few monolayers.¹¹² In contrast, the use of highly associated salts in a low DN solvent would follow a solution-growth mechanism of Li_2O_2 , allowing a prolonged ORR that formed thick and irregular Li_2O_2 deposits. The latter morphology enabled a relatively long electron transfer process, since the coverage of the surface did not block it uniformly.

5.4.2.2 Protic reagents. Many recent reports have shown that the fortuitous ingress of protic chemicals, such as water and phenol, is responsible for the enhanced cell capacities, suggesting that the solution-phase pathway for Li_2O_2 generation is promoted through the addition of protic additives.^{45,115} Aetukuri and Visvanathan *et al.* investigated the effect of water on the growth of the Li_2O_2 toroid structure. A significant increase in cell discharge capacity was observed in the presence of a trace amount of water in the electrolyte. Water that allowed for the

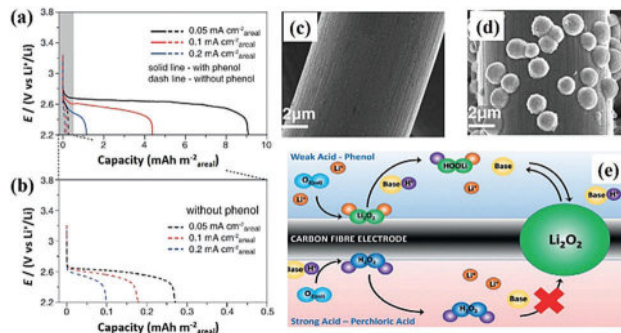


Fig. 76 (a) Load curves of O_2 reduction at a gas diffusion electrode discharged in 1 M $\text{LiTFSI}/\text{TEGDME}$ electrolyte with (solid lines) and without (dashed lines) 30 mM phenol under O_2 at various areal current densities from 0.05 mA cm^{-2} to 0.2 mA cm^{-2} ; (b) enlarged section of the load curves recorded without phenol in (a); SEM images showing the Li_2O_2 morphologies on discharge (c) without and (d) with 30 mM phenol in 1 M $\text{LiTFSI}/\text{TEGDME}$ electrolyte under O_2 ; (e) schematic comparing the action of strong and weak acids during discharge in $\text{Li}-\text{O}_2$ cells. With a strong acid (weak conjugate base), the major product was H_2O_2 , and the exchange of H^+ and Li^+ was inhibited by the poor base. With a weak acid (strong conjugate base), the major product was Li_2O_2 , and the exchange of H^+ between Li_2O_2 and the conjugate base was facile, enabling the phase-transfer catalyst and a solution mechanism.¹¹⁵ Reprinted with permission from ref. 115. Copyright 2017 Wiley-VCH Verlag GmbH & Co. KGaA.

increased solubility of LiO_2 could produce the large Li_2O_2 toroid, which was the key to obtaining large discharge capacities.¹⁶

Phenol is one type of protic reagents that was considered might present a similar function as a trace amount of water in $\text{Li}-\text{O}_2$ batteries. Bruce *et al.* reported that the addition of weak acid phenol to a TEGDME-based electrolyte within a battery was capable of promoting the discharge process *via* a solution mechanism.¹¹⁵ The cell discharge capacity was over 9 mA h cm^{-2} , which was a 35-fold increase in capacity compared to the battery without phenol (Fig. 76). The proton of the phenol functioned as a phase-transfer catalyst, which converted the insoluble Li_2O_2 to its soluble protonated analogue and was subsequently redeposited again from solution to form large Li_2O_2 clusters. This resulted in the high capacity and high rate of $\text{Li}-\text{O}_2$ batteries.

5.4.2.3 Ammonium salts. Hammond *et al.* showed that one of ammonium ions, namely tetrabutylammonium, could act as an additive to support Li_2O_2 formation in $\text{Li}-\text{O}_2$ batteries without any Li-salts.⁴⁸⁶ During the discharge process, a TBA-salt-based electrolyte in the presence of Li-metal can support the formation of Li_2O_2 , where TBA^+ could temporarily complex the superoxide in solution before Li^+ from the oxidized Li-metal combined to form Li_2O_2 . During charging, the electrochemical-induced transformation of TBA^+ to tributylamine at 3.55 V resulted in the formation of tributylamine oxide intermediate in the presence of O_2 and Li_2O_2 , which was responsible for the improved Li_2O_2 oxidation. Consequently, a decreased charging potential (500 mV) was observed compared to that with Li-salts.

The effect of ammonium ions on the discharge behaviour of $\text{Li}-\text{O}_2$ batteries was also investigated by Nakanishi *et al.*¹²⁰ They compared the discharge performance of batteries with three ammonium-salt-based electrolytes, including $\text{NH}_4^+\text{TFSI}^-$,

TBA⁺TFSI⁻ and tetraethylammonium TFSI (TEA⁺TFSI⁻). They found that the ammonium salts could increase the cell discharge capacity compared to that in the absence of ammonium salts. The batteries with NH₄⁺TFSI⁻ showed the highest cell discharge capacity among the batteries with three types of ammonium salts. This was ascribed to the ammonium ions functioning as promoters for the solution-mediated formation of Li₂O₂, which resulted in the formation of toroidal Li₂O₂ particles.

5.5 Electrolytes for Li₂O₂ decomposition

The fourth function of an electrolyte is for tailing the Li₂O₂ decomposition reaction, while Li₂O₂ is possibly decomposed to Li⁺ and O₂ directly. Although the reaction mechanism is not well established, the reaction rate of Li₂O₂ decomposition is likely correlated with the bond strength of Li-O and the solubility of Li₂O₂ in the electrolyte. The reaction rate of Li₂O₂ decomposition would be increased if the electrolyte components could improve the solubility of Li₂O₂ to some extent.¹⁴³ Tuning the properties of electrolyte solvents and additives, for example their polarity and electron affinity, provides the opportunity to accelerate Li₂O₂ decomposition reactions.¹¹⁶

5.5.1 The effects of the solvents. Some solvents not only function as an intermediates stabilizer, but also as the medium for dissolving Li₂O₂ in the electrolyte. Peng *et al.* demonstrated one of the amides, namely hexamethylphosphoramide (HMPA), as an electrolyte solvent for a Li-O₂ battery, which could also dissolve Li₂O₂, Li₂CO₃ and LiOH up to 0.35, 0.36 and 1.11 × 10⁻³ M, respectively (Fig. 77). The passivation/clogging of the O₂ cathode upon discharge could be considerably alleviated, and the kinetics of Li₂O₂ oxidation on recharge substantially improved. More importantly, the oxidation of Li₂O₂ in HMPA electrolyte can proceed well below 3.5 V, and thereby the decomposition of carbon electrode and electrolyte was effectively suppressed. Compared to

ether-based Li-O₂ batteries, better cell capacity, rate capability, voltaic efficiency and cycle life were achieved for the HMPA-based Li-O₂ cells.⁴⁸⁷

5.5.2 The effects of additives. Meini and Gasteriger *et al.* checked the effect of water on the cell charge capacity, the overpotential and the starting activation potential. No change in the discharge potential was found in the presence of a little water, which meant that the Li₂O₂ seemed to be stable in this condition. However, the activation charge peak potential and overpotential of the Li-O₂ battery were substantially decreased, which might be explained as being due to a shuttle mechanism existing for Li₂O₂ from the surface of Li₂O₂ particles to the cathode in the presence of water and protons.^{488,489}

Zhou *et al.* also studied the dependence of the charge potential and capacity on the concentration of water in a DMSO-based electrolyte in a lithium-ion O₂ battery, which used Ru/MnO₂/Super-carbon and LiFePO₄ as the cathode and anode, respectively (Fig. 78).⁴⁵ The charge potential plateau was significantly reduced from 3.65 V to 3.20 V in the presence of 120 ppm water. This confirmed the oxidation of LiOH, which was quickly converted from the primary discharged Li₂O₂. A higher concentration of water in the electrolyte would increase the charge potential and decrease the capacity, due to the high surface coverage of LiOH by-products on the cathode.⁴⁵ The authors further used DFT calculations to simulate the charge process of Li₂O₂ surface adsorbed with a single H₂O molecule. They demonstrated that a water molecule could spontaneously adsorb on the Li₂O₂ surface, which would thereby decrease the energy barrier for the elementary charge steps. The intrinsic charge overpotential of the Li-O₂ battery was reduced from 0.45/0.16 V to 0.31/0.09 V on the (001)/(110) surface of Li₂O₂, respectively.

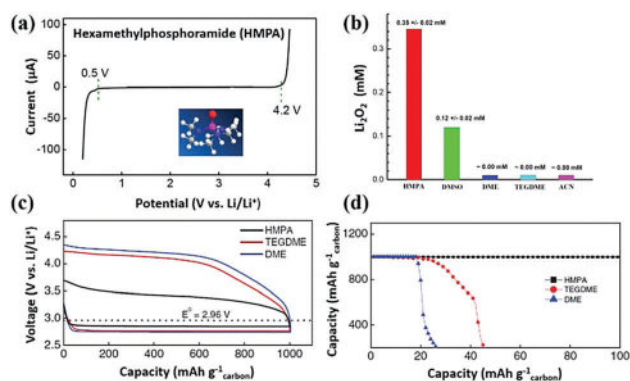


Fig. 77 (a) Linear potential scan conducted at a glassy carbon electrode in a hexamethylphosphoramide (HMPA)-based electrolyte with 0.1 M LiClO₄ (the inset shows the molecular structure of HMPA); (b) saturated concentrations of dissolved Li₂O₂ in HMPA, DMSO, DME, TEGDME and CAN solvents; (c) load curves of Li-O₂ batteries containing HMPA and ethereal electrolytes with a curtailed capacity of 1000 mA h g_{carbon}⁻¹ at a current density of 200 mA g_{carbon}⁻¹; (d) cycling profiles of Li-O₂ batteries under the same test conditions in (c).⁴⁸⁷ Reprinted with permission from ref. 487. Copyright 2017 Wiley-VCH Verlag GmbH & Co. KGaA.

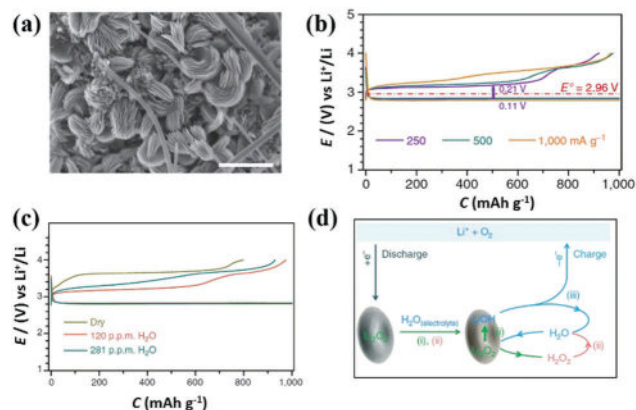


Fig. 78 (a) SEM images of the discharged cathodes with a Li₂O₂ toroid morphology in a DMSO-based electrolyte with 120 ppm H₂O; (b) discharge/charge profiles of Li-O₂ cells with Ru/MnO₂/SP at the 10th run with varied current densities from 250 to 500 and 1000 mA g⁻¹; (c) discharge/charge profiles of the Li-O₂ cells at the 5th cycle with Ru/MnO₂/SP cathode containing 120 and 281 ppm of H₂O (current density: 500 mA g⁻¹); (d) proposed reaction mechanism for the growth of Li₂O₂ toroid with water (i) spontaneous process; (ii) promoted over MnO₂ particles in Ru/MnO₂/SP; and the oxidation of LiOH (iii) at low charge overpotentials over Ru nanoparticles.⁴⁵ Reprinted with permission from ref. 45. Copyright 2015 Nature Publishing Group.

The reduced charge potentials originated from the low energy barriers in the initial charge step, due to the stronger interaction between H_2O and Li_2O_2 .

Furthermore, Zhou *et al.* found the Li_2O_2 formation through the ' $\text{O}_2 \rightarrow \text{HO}_2^- \rightarrow \text{H}_2\text{O}_2 \rightarrow \text{Li}_2\text{O}_2$ ' pathway with a water content in the range of 0.5% to 30% (v/v) in TEGDME-based electrolyte involved a direct two-electron reduction instead of a typical one-electron pathway ' $\text{O}_2 \rightarrow \text{O}_2^- \rightarrow \text{LiO}_2^- \rightarrow \text{Li}_2\text{O}_2$ '.⁴⁹⁰ The authors suggested that this process avoided the formation of highly reactive superoxides, thus reducing the side reactions during the cell operation. Moreover, the charging overpotential could also be decreased to 0.5 V due to the chemical equilibrium between Li_2O_2 and the soluble peroxides. Very recently, the same authors optimized the H_2O content to establish a hydrate-melt electrolyte (The molar ratio of components in the electrolyte $\text{LiTFSI}:\text{LiBETI}:\text{H}_2\text{O} = 7:3:20$).⁴⁹¹ The charging overpotential was further decreased as low as 0.2 V with the discharge product of Li_2O_2 . The authors attributed the low charging polarization of the "hydrate-melt-based battery" to the oxidation of pure Li_2O_2 , in comparison to the high charging potentials of aprotic $\text{Li}-\text{O}_2$ batteries with some Li^+ -based by-products at the oxygen electrode.

The proposed pathway ' $\text{O}_2 \rightarrow \text{HO}_2^- \rightarrow \text{H}_2\text{O}_2 \rightarrow \text{Li}_2\text{O}_2$ ' suggested that the positive effect of water on the charging process was correlated with the solvent/additives. For instance, Li_2O_2 is always detected as a discharge product in ether-based electrolytes regardless of the water content (without any other kinds of additives),^{117,173,491} while LiOH and Li_2O_2 usually coexist with the invasion of moisture in DMSO-based electrolyte.⁴⁹²⁻⁴⁹⁴ To explain this difference, Shao-Horn *et al.* conducted DFT calculations to confirm the effect of water on the discharge products. They found that solvents with a low water solvation energy and a high dissociation constant ($\text{p}K_{\text{a}}$) of solvated water, for example DME, could impose a high thermodynamic barrier for reaction between superoxide and water, and thus yielded mainly Li_2O_2 ,¹⁶⁸ while solvents with a low $\text{p}K_{\text{a}}$ for water solvation, for example DMSO and MeCN, could induce deprotonation by the attack of O_2^- , finally resulting in the formation of LiOH through " $\text{O}_2 \rightarrow \text{HOO}^\bullet \rightarrow \text{HOO}^- \rightarrow \text{LiOH}$ ".

Similar to the effect of water, an organic H_2O_2 compound (urea hydrogen peroxide) was introduced as an electrolyte additive in a $\text{Li}-\text{O}_2$ battery, while the charge potential was decreased significantly (to ~ 3.26 V) and only a slight increment of the charge plateau was observed after 50 cycles at a limited capacity of 1000 mA h g^{-1} . Moreover, the corrosion of Li -metal by urea hydrogen peroxide was limited. The good cell performance and stability was due to the decomposition of Li_2O_2 and LiOH assisted by the addition of urea hydrogen peroxide and the inhibition of undesired H_2O corrosion of the Li -electrode.¹¹⁶

Although the successful use of water for better $\text{Li}-\text{O}_2$ batteries has been identified, the introduction of water or other proton additives inevitably induces a reaction with the lithium anode. Moreover, protic chemicals, including water, can be oxidized at high charge potentials and thus will be rapidly consumed.¹¹⁷ Moreover, some other radical reactive species, such as HOO^\bullet and HOO^- , can be formed by the introduction of

proton sources,^{495,496} which can trigger possible side reactions in the aprotic electrolyte. Thus, proton additives should be carefully evaluated and systematically studied if they are to be considered as suitable additives to improve the capacity or reduce the overpotentials.

5.6 Short summary and perspective for electrolytes

The investigation of aprotic electrolytes in $\text{Li}-\text{O}_2$ batteries is still in its infancy, and much effort is still being done to increase the cell performance and stability. The ideal electrolyte should meet the demands of the above-mentioned four functions: fast Li^+ and O_2 transport rate, good solubility for Li_2O_2 formation, good capability to stabilize the Li^+-O_2^- intermediate for Li_2O_2 formation and the ability to dissolve Li_2O_2 for accelerating its decomposition. Equally important, the electrolyte components should have a high enough resistance to attack by reactive species to enable their long-term stability.

Liquid solvents, such as acrylamide, sulfoxide and ether, have shown good mass transport efficiency and stability within a wide voltage window. Some have demonstrated a possibility to achieve a high cell performance. In particular, ether-type solvents are one of the most suitable media for $\text{Li}-\text{O}_2$ batteries due to their good O_2 dissolution ability, their inert nature to Li -metal and as they are electrochemically stable at a high charge potential region. One of the concerns for the present developed liquid solvents is their instability initiated by reactive superoxide species. This issue may be alleviated through modification of their chemical structure or by the addition of additives to inhibit the generation of superoxide species by decreasing the charge potential. Another remaining concern for liquid solvents is their flammability and volatility, which might be obstacles in an open system of $\text{Li}-\text{O}_2$ batteries.

Quasi-solid-state and solid-state electrolytes provide an opportunity to solve the flammability and volatility issues from liquid solvents. Several gel-polymer and ionic-liquid-based electrolytes have already shown a possibility for good-performance $\text{Li}-\text{O}_2$ batteries. However, their high viscosity and instability towards reactive species are also obstacles for achieving a stable output of the battery. Much effort should be paid to synthesizing stable and low viscosity quasi-solid-state electrolytes for highly efficient and stable batteries.

One of the key functions for an electrolyte is to act as a stabilizer for Li^+-O_2^- intermediates, which is critical for the solution-phase growth of Li_2O_2 . Solvents with a low polarity, for example DME and TEGDME, have a high Li^+ -ion transport efficiency and O_2 solubility. But the low DN/AN values of such solvents limit their ability to stabilize the solvated Li^+-O_2^- intermediates. In contrast, solvents with polarity, for example DMSO, have high DN/AN values to stabilize the solvated Li^+-O_2^- intermediates. But here, their low O_2 solubility and instability towards Li -metal become the key challenges during cell operation. The selection of functional additives may be a good strategy to compensate for the limitations of solvents, such as PFC molecules for the enrichment of O_2 in DMSO-based electrolyte, a redox mediator for stabilizing the intermediates in ether-based electrolytes (this will be discussed later) or the

formation of an SEI layer with LiNO_3 on Li-metal in DMSO-based electrolyte, and so on.

Another function of the electrolyte is accelerating the Li_2O_2 decomposition reaction. Some electrolyte solvents and additives, for example HMPA and water, show specific properties to dissolve Li_2O_2 and decrease the energy barriers of Li_2O_2 decomposition. The stronger the interaction between the specific components of the electrolyte and Li_2O_2 , the lower the energy barriers in the Li_2O_2 decomposition reaction. Consequently, the intrinsic cell charge potentials are substantially reduced. Except for the electrolyte, the effect of operating temperatures on the charge potentials of Li– O_2 battery might provide some options for a further improvement of cell performance.^{473,497}

6. Redox mediator

As mentioned previously, bulky Li_2O_2 is an insulating material and is insoluble in most aprotic solvents under general conditions, which is one of the main reasons for the slow kinetics of discharge/charge reactions. However, the further development of advanced solid catalysts seems to be difficult for accelerating the rate of the Li_2O_2 formation and decomposition reactions. This is due to the insufficient charge transfer and the limited contact area between Li_2O_2 and the catalysts.¹³⁸ Consequently, the initial charge potentials of a battery were increased quickly in the charging profiles, resulting in decomposition of the electrolyte and cathode.¹³⁹

The introduction of SRMs in the electrolyte provides a potential route to solve these issues. This could accelerate Li_2O_2 formation in the discharge process (namely ORR), and promote Li_2O_2 decomposition in the charge process (namely OER).¹⁴⁴ The decreased overpotentials of OER and ORR were also effective for lowering the content of reactive superoxide species, resulting in a better cell durability. SRMs are a special type of additives, with quite different functionality from those mentioned in Sections 5.4.2 and 5.5.2 of the electrolyte chapter. SRMs with redox activities could donate/accept electrons to O_2 and from Li_2O_2 chemically, thus acting as “catalysts” for Li_2O_2 formation and decomposition. Similar to the more common additives, SRMs can surround the exposed Li_2O_2 surface, and consequently, the contact area between the SRM, O_2 and Li_2O_2 is substantially increased compared to that with the use of solid catalysts and Li_2O_2 (Fig. 79).^{142,143} From the viewpoint of the additive and catalyst functions, SRMs can be called “liquid catalysts” in Li– O_2 batteries. Therefore, the related positive and negative effects are discussed within this chapter.

The OER and ORR activity of SRMs was strongly correlated their physicochemical properties, such as their midpoint potential, molecular weight, polarity and concentration in solvents. Among all of the properties, the midpoint potential of SRMs plays the dominant role in their functionality. The gap between an SRM's midpoint potential and $\text{Li}_2\text{O}_2/\text{O}_2$ (2.96 V) is small, and the OER and ORR overpotentials were small. According to this dominant factor, they were divided into ORR and OER SRMs, and we will discuss their current progress with this classification.

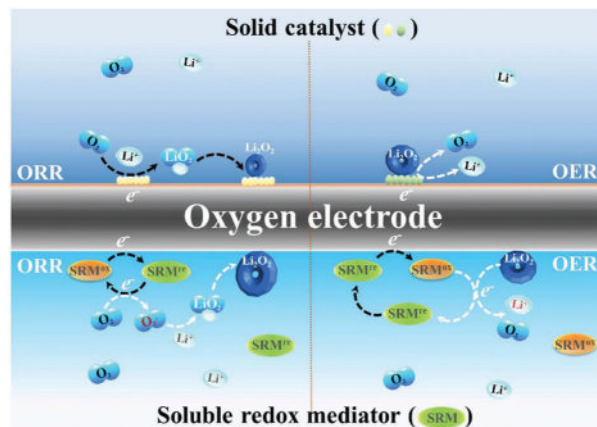


Fig. 79 Schematic illustrations for the Li_2O_2 formation and decomposition process with the assistance of a solid catalyst (upper) and soluble redox mediator (SRM, bottom).

6.1 SRMs for Li_2O_2 formation

The equilibrium potential of Li_2O_2 formation ($\text{O}_2 + 2\text{Li}^+ + 2e^- \leftrightarrow \text{Li}_2\text{O}_2$) was 2.96 V vs. Li/Li^+ , while SRMs with low midpoint potentials (≤ 2.96 V vs. Li^+/Li) could potentially function as an O_2 reducer and electron carrier from the cathode to Li_2O_2 , resulting in ORR proceeding chemically. Moreover, some SRMs could also act as a stabilizer for Li^+-O_2^- intermediates, similar to high DN solvents, which shifted the Li_2O_2 generation pathway from solid-phase growth to solution-phase growth. This induced the enhanced ORR kinetics, resulting in an increase in the cell discharge potential and capacity (Fig. 79).⁵⁰⁰

When the midpoint potential of SRMs was lower than 2.96 V vs. Li^+/Li , their reduced form could react with O_2 to generate O_2^- chemically, and O_2^- then combined with Li^+ to produce LiO_2^* or Li^+-O_2^- intermediates. Finally, the intermediates were disproportionated to Li_2O_2 solid. The oxidized form of SRMs could be regenerated through electron exchange with the cathode. Owen *et al.*⁴⁹⁸ were the first to use ethyl viologen ditriflate ($\text{EtV}^{2+}(\text{OTf}^-)_2$) with a midpoint potential of 2.40 V vs. Li^+/Li as an SRM to catalyze the ORR. As shown in Fig. 80, EtV^{2+} accepted one electron from the cathode to form the reduced form of EtV^+ ,

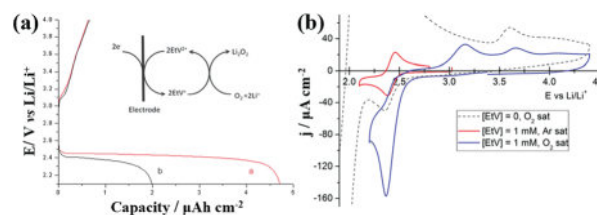


Fig. 80 (a) The galvanostatic discharge and charge of cells with a glassy carbon electrode in O_2 -saturated 0.1 M $\text{LiTFSI}/\text{Py}_{14}\text{TFSI}$ with (1) and without (2) 2 mM EtV^{2+} (the inset shows the redox shuttle action of EtV^{2+} , displacing the formation pathway of Li_2O_2 from the electrode surface to the solution, $j = 20 \text{ mA cm}^{-2}$); (b) cyclic voltammograms of 1 mM EtV^{2+} in (red) Ar-saturated and (blue) O_2 saturated BMPTFSI on 3 mm glassy carbon discs at a scan rate of 50 mV s^{-1} (CV of BMPTFSI without EtV^{2+} at O_2 is shown with a dashed line).^{498,499} Reprinted with permission from ref. 498 and 499. Copyright 2013, 2015 Royal Society of Chemistry and Elsevier.

and then EtV^+ reduced O_2 to O_2^- accompanied with the regeneration of EtV^{2+} through an electrochemical reduction reaction. It was also proposed that EtV^{2+} reacted with superoxide species to some extent, although controlling $(\text{EtV}(\text{OTf})_2)$ at a low concentration and Li^+ at a high concentration could alleviate the degradation of EtV^{2+} initiated by superoxide attack. The same authors further fabricated a $\text{Li}-\text{O}_2$ battery with $\text{EtV}(\text{OTf})_2$ in a $\text{Py}_{14}\text{TFSI}$ -based electrolyte (0.1 M LiTFSI), in which the cell discharge overpotentials were decreased a little in comparison to those without $\text{EtV}(\text{OTf})_2$.⁴⁹⁹ Moreover, the cell capacity was enhanced from $2 \mu\text{A h cm}^{-2}$ to $4.7 \mu\text{A h cm}^{-2}$. It was also found that $\text{EtV}(\text{OTf})_2$ not only reduced O_2 to O_2^- , but also reduced O_2^- to O_2^{2-} . As a result, the superoxide lifetime was drastically decreased, and the cell durability could be increased. However, the midpoint potential of viologen molecules was much smaller than 2.96 V vs. Li^+/Li , showing the decreased charge overpotential was limited.

The influence of the midpoint potential for SRMs on the discharge potentials of a battery was studied by Nakanishi *et al.*, who selected quinone (Q) molecules as probes to check their ORR activity in aprotic solvents.⁵⁰¹ They found that there was a linear correlation between the onset potentials of the ORR and the midpoint potential of the quinone derivatives ($Q_{\text{ox}}/Q_{\text{re}}$) (Fig. 81). However, the redox potentials of $Q_{\text{ox}}/Q_{\text{re}}$ were not very close to the theoretical thermodynamic potential of Li_2O_2 formation, and Q_{re} could not reduce O_2 to yield Li_2O_2 effectively.

With this guidance, Bruce *et al.* introduced 2,5-di-*tert*-butyl-1,4-benzoquinone (DBBQ) with the midpoint potential of 2.63 V vs. Li^+/Li as an ORR catalyst in a weakly solvating (low DN solvent) electrolyte.⁷⁵ DBBQ endowed the system with a higher discharge voltage of around 2.7 V (0.1 mA cm^{-2}) than that of a $\text{Li}-\text{O}_2$ battery without DBBQ (Fig. 82). Remarkably, DBBQ increased

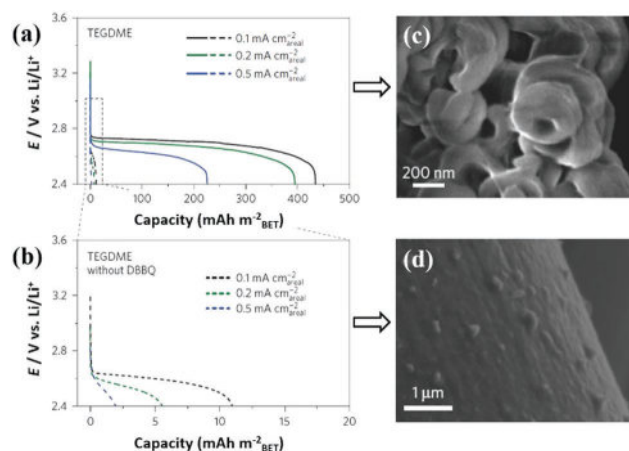


Fig. 82 (a) Load curves for oxygen reduction at a gas diffusion electrode discharged in $\text{LiTFSI}/\text{TEGDME}$ with DBBQ (solid lines) and without DBBQ (dashed lines) under O_2 at various areal current densities; (b) enlarged section of the load curves recorded without DBBQ in (a); SEM images of the (upper) toroid-like and (bottom) film-like Li_2O_2 morphologies on discharge in 1 M $\text{LiTFSI}/\text{ethers}$ (c) with and (d) without DBBQ.⁷⁵ Reprinted with permission from ref. 75. Copyright 2016 Nature Publishing Group.

the cell capacity 80- to 100-fold in comparison to a $\text{Li}-\text{O}_2$ battery without DBBQ, originating from the significantly enlarged size of Li_2O_2 particles. It was proposed that $\text{Li}^+-\text{DBBQ}-\text{O}_2^-$ was formed as the intermediate in solution instead of LiO_2^* on the cathode, changing the Li_2O_2 formation pathway from solid-phase growth to solution-phase growth. The solution-phase pathway could support Li_2O_2 deposition form large clusters, and inhibit the generation of a dense Li_2O_2 film by the solid-phase pathway. This induced a substantial increase of cell capacity.

Except for viologen and quinone molecules, some redox radicals were also investigated as ORR SRMs in a $\text{Li}-\text{O}_2$ battery. Ratera and Tonti *et al.* examined the ORR activity of tris(2,4,6-trichlorophenyl)methyl (TTM) radical with the midpoint potential of 2.6 V vs. Li^+/Li in a $\text{Li}-\text{O}_2$ battery.⁵⁰² The battery with the TTM radical could deliver a capacity two times (7.5 A h g^{-1}) larger than the one without TTM at 0.1 mA cm^{-2} (TEGDME -based electrolyte and Super-P based cathode), as well as a little lower ORR overpotentials. The authors also proposed synthesizing several molecules with different functional groups in the TTM family, which could possibly suggest a bright future for their application in $\text{Li}-\text{O}_2$ batteries with better performance.

Details of the presently developed ORR soluble redox mediators are shown in Table 10. Except for the strong effect of the midpoint potentials, the concentrations and molecular weight of the SRMs also had an impact on the increased degree of the capacity. The high concentration of SRMs can reduce oxygen through a chemical route as much as possible, while the low molecular weight of SRMs can provide fast diffusion kinetics to revive itself as soon as possible.

6.2 SRMs for Li_2O_2 decomposition

SRMs with a high midpoint potential ($\geq 2.96 \text{ V vs. Li}^+/\text{Li}$) could potentially function as a Li_2O_2 oxidizer and electron carrier

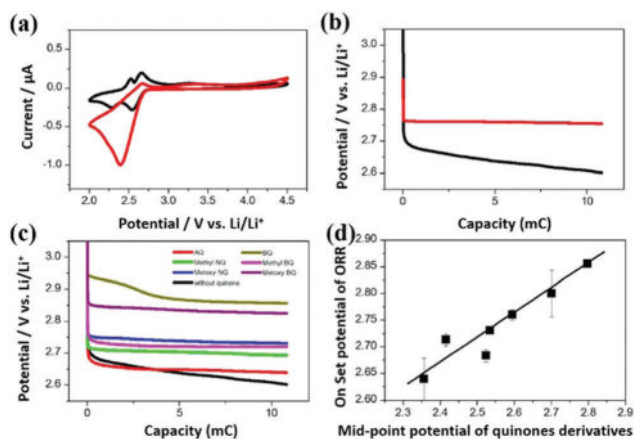


Fig. 81 (a) CV of three-electrode cells in the presence of 1 mM naphthoquinone under O_2 -bubbled (red curve) or Ar -bubbled (black curve) condition; (b) cathodic chronopotentiograms of $\text{Li}-\text{O}_2$ battery in the presence (red curve) and absence (black curve) of 1 mM naphthoquinone; (c) cathodic chronopotentiograms of cell with various quinone derivatives (1 mM); (d) onset potentials of the ORR plotted against the midpoint potential of quinone derivatives ($Q_{\text{ox}}/Q_{\text{sem}}$).⁵⁰¹ Reprinted with permission from ref. 160. Copyright 2014 American Chemical Society.

Table 10 Application of ORR SRMs in aprotic Li–O₂ systems

SRM ($M_w/g\ mol^{-1}$, concentration)	Cathode	Electrolyte	Midpoint potential (V vs. Li/Li)	Discharge voltage (V)	Improved capacity	Current density	Ref.
EtV ²⁺ [(OTf) ⁻] ₂ (466, 2 mM)	Glassy carbon	0.1 M LiTFSI in Py ₁₄ TFSI	~2.42	~2.42 (vs. 2.39 w/o SRM)	2.5-fold	20 $\mu A\ cm^{-2}$	499
DBBQ (220, 10 mM)	Carbon paper	1 M LiTFSI in TEGDME	~2.63	~2.72 (vs. 2.61 w/o SRM)	80-fold	0.2 mA cm_{gold}^{-2}	75
TTM (553, 1 mM)	Super P	1 M LiOTf in TEGDME	~2.60	~2.65 (vs. 2.55 w/o SRM)	2-fold	0.1 mA cm_{gold}^{-2}	502

M_w , molecular weight.

from Li₂O₂ to the cathode, resulting in the decomposition of Li₂O₂ chemically and a decrease in the charge potential.^{503–507} Importantly, the decreased charge potentials effectively inhibit the generation of active superoxide species and by-products. As a result, the cell durability is promoted.

Bruce *et al.* presented the first demonstration of tetrathiafulvalene (TTF) as an OER SRM to catalyze the decomposition of Li₂O₂ in Li–O₂ batteries (Fig. 83).⁵⁰³ With the addition of TTF in the electrolyte (1 M LiClO₄ in DMSO), the battery exhibited suppressed charge potentials from 3.9 V to 3.4 V, as well as a much improved rate capability and superior cyclic stability. When LiFePO₄ was applied as an anode material to avoid the side reaction between Li-anode and TTF, the charge overpotentials could be sustained without any obvious change even at 100 cycles. Afterwards, Whittingham *et al.* studied the chemical and electrochemical stability of a TTF-containing battery with the LiFePO₄ anode by utilizing an *in situ* synchrotron XRD technique.⁵⁰⁸ Unfortunately, TTF chemically reduced Fe³⁺ and induced lithiation of FePO₄ in the presence of Li⁺. Recently, Chen *et al.* used a TTF-based DMSO electrolyte for a Li–O₂ battery with nanoporous graphene as the cathode. The porous cathode offered an efficient pathway for charge transfer, TTF oxidation and diffusion. As a result, the charge potential of the battery with the TTF redox mediator was decreased by about 0.66 V in comparison to that of the battery without TTF, while the cell could cycle 100 times at a capacity of 2000 mA h g⁻¹ at a current density of 2 A g_{carbon}⁻¹.⁵⁰⁶

After the first demonstration of TTF for the advancement of Li–O₂ batteries, other OER SRMs with better stability were developed.¹⁰⁶ For example, Janek *et al.* investigated the OER catalytic activity of TEMPO in a Li–O₂ battery.¹⁰⁵ TEMPO possessed a redox potential of about 3.7 V vs. Li⁺/Li (Fig. 84),

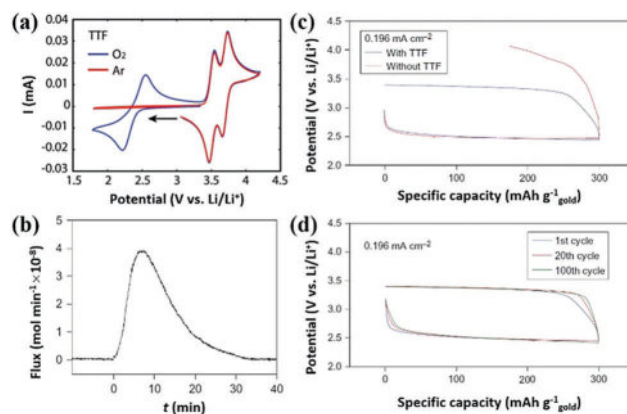


Fig. 83 (a) Cyclic voltammetry of tetrathiafulvalene (TTF) dissolved in 0.1 M TBAClO₄/DMSO electrolytes cycled under an O₂ (blue curves) and Ar (red curves) atmosphere at a gold electrode (current density: 100 mV s⁻¹); (b) the evolved O₂ as determined by mass spectrometry after mixing the oxidized forms of TTF and excess Li₂O₂ in 1 M LiClO₄/DMSO electrolyte; (c) charge–discharge profiles of Li–O₂ batteries with a limited capacity of 300 mA h g_{Au}⁻¹ at a current density of 0.196 mA cm⁻²; (d) charge–discharge curves of cells with TTF at a current density of 0.196 mA cm⁻² for the 1st, 20th and 100th cycles.⁵⁰³ Reprinted with permission from ref. 503. Copyright 2013 Nature Publishing Group.

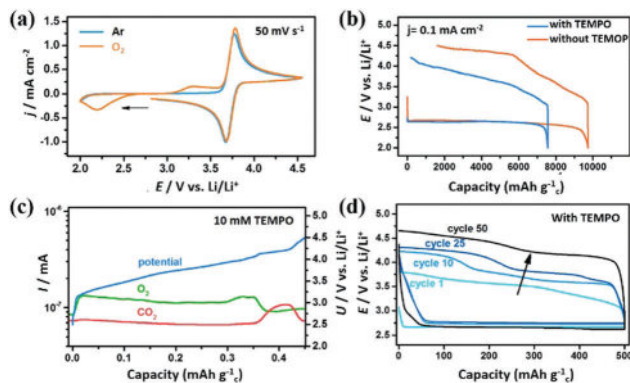


Fig. 84 (a) Cyclic voltammogram of 1 M LiTFSI/DME electrolyte with 10 mM TEMPO under an Ar and O₂ atmosphere; (b) full cycle of the Li–O₂ cell with and without 10 mM TEMPO using a KB carbon cathode (current density: 0.1 mA cm⁻²); (c) differential electrochemical mass spectrometry analysis of evolved gases during the charging of cells with 10 mM TEMPO ($j = 0.1 \text{ mA cm}^{-2}$); (d) cyclability of Li–O₂ cells with TEMPO in 0.1 M LiTFSI/DME electrolyte at 0.1 mA cm⁻².¹⁰⁵ Reprinted with permission from ref. 105. Copyright 2014 American Chemical Society.

which enabled the battery to achieve a $\sim 400 \text{ mV}$ lower OER overpotential and $\sim 14\%$ higher Coulombic efficiency than those of the battery without TEMPO. It was found that the per cent of released CO₂ could be decreased with the aid of TEMPO, and the battery performed with superior cyclic stability at a limited capacity of $500 \text{ mA h g}_{\text{carbon}}^{-1}$. The same authors further investigated the influence of the TEMPO concentration on the battery performance. The cell capacity was derived from the combination of a Li–O₂ battery and a redox-flow battery.⁵⁰⁹ To achieve this design, they applied a Li⁺ selective solid-electrolyte membrane to avoid the side reactions between the Li-anode and TEMPO. With a 1 M TEMPO-based electrolyte in the Li–O₂/redox-flow cell, it could deliver a capacity of $\sim 27 \text{ mA h mL}^{-1}$ and a Coulombic efficiency of 96% at a current density of 0.05 mA cm^{-2} .

In addition to TEMPO derivatives, phenothiazine derivatives have also been proved to be promising SRM candidates for Li–O₂ batteries.^{510–513} Typically, the OER activity of 10-methyl-10*H*-phenothiazine (MPT) with a redox potential of about 3.7 V vs. Li⁺/Li was investigated by Zhou's group.^{510,511} The addition of MPT distinctly reduced the charging potentials by more than 800 mV and thus, the battery had a much improved cycling stability. However, Kim *et al.*'s investigations showed that the catalytic activity of MPT was degraded after a certain number of cycles, leading to an increase in the overpotential during cell cycling. The failure of such a type of Li–O₂ battery was due to the irreversible decomposition of MPT on Li-metal even when there was a stable SEI layer on the Li-anode. This observation emphasized that the protection of Li-metal from attack by the electrolyte components was crucial for promoting the Li₂O₂ decomposition with SRMs.⁵¹²

In addition to pure organic molecules, transition metal complexes,^{514,515} such as metal porphyrins^{501,516} and metal phthalocyanines,^{501,517} have been investigated for OER SRMs in Li–O₂ batteries. The midpoint potentials of transition metal

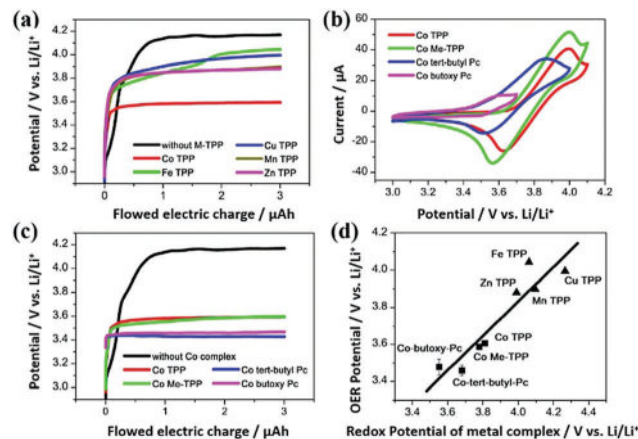


Fig. 85 (a) Anodic chronopotentiograms obtained in the presence and absence of 1 mM metal *tert*-butylphthalocyanine (M-TPP) using a Li₂O₂-formed GC electrode in an Ar atmosphere; (b) cyclic voltammograms obtained in the presence of 1 mM cobalt complexes using pristine GC electrode in an Ar atmosphere (scan rate: 10 mV s^{-1}); (c) anodic chronopotentiograms obtained in the presence and absence of 1 mM cobalt complexes using a Li₂O₂-formed GC electrode in an Ar atmosphere; (d) onset potentials of OER plotted against the redox potential of M(III)/M(II) in transition metal complexes.⁵²⁷ Reprinted with permission from ref. 527. Copyright 2014 American Chemical Society.

complexes could be well tuned by their core-metals and substituted groups, which is potentially useful for decreasing the cell charge potential.⁵⁰¹ Nakanishi *et al.* studied the OER property of several metal porphyrins and phthalocyanine in a Li–O₂ battery (Fig. 85).⁵⁰¹ Among all the metal complexes tested, cobalt *tert*-butylphthalocyanine (Co-TTP) exhibited the best catalytic activity for Li₂O₂ decomposition. The charging potential was decreased from 4.1 V to 3.4 V at $1 \mu\text{A cm}^{-2}$ with the Co-TTP complex. *tert*-Butyl cobalt phthalocyanine (tb-CoPc) was also investigated as an OER catalyst in a Li–O₂ battery, while the charging potentials was decreased from 4.0 V to 3.5 V.⁵¹⁷ This confirmed that the charging potentials were strongly associated with the midpoint potential of the SRMs.

Ryu *et al.* proved that an iron porphyrin molecule (Fe-PP, Fig. 86) – a heme cofactor in blood – could function as an SRM for efficient OER and ORR in aprotic Li–O₂ batteries.⁵¹⁸ The Fe-PP complex not only enabled charge transfer between the insulating Li₂O₂ products and the electrode with high efficiency, but also acted as an oxygen carrier for binding oxygen species with its Fe³⁺ centre. As a result, the cell achieved a lower polarization and longer cycle life in comparison to the cell without Fe-PP. The macrocyclic compounds coordination with the polyvalent metal, for example iron porphyrin, probably had a bifunctional catalytic effect for both ORR and OER, since Fe⁺, Fe²⁺ and Fe³⁺ could coexist in the chemicals. Shen and Huang *et al.* proved iron phthalocyanine (FePc) could serve as a bifunctional redox catalyst with the midpoint potentials of Fe²⁺/Fe⁺ and Fe³⁺/Fe²⁺ centred at 2.5 V vs. Li⁺/Li and 3.65 V vs. Li⁺/Li, respectively.⁵¹⁹ They proposed a two-step redox mechanism as “(FePc–O₂) ↔ (FePc–O₂)[–] ↔ (FePc–LiOOli)” during the ORR and OER process. Here, FePc could chemically reduce O₂ and oxidize Li₂O₂ through redox chemical reactions. A Li–O₂ battery

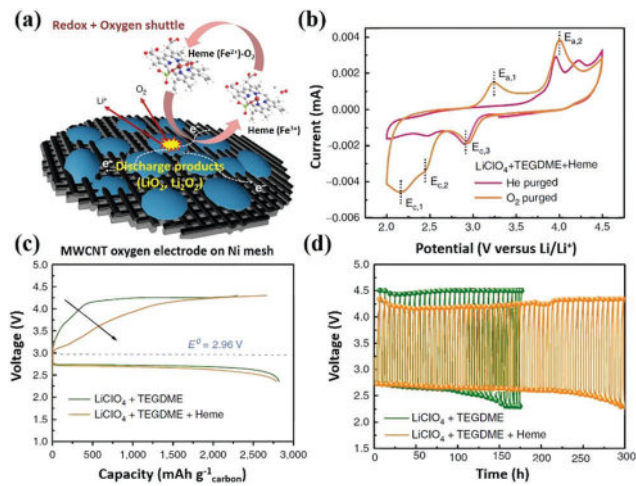


Fig. 86 (a) Schematic illustration of an oxygen electrode charged Li–O₂ cell with an electrolyte containing heme (Fe-PP) molecules; (b) CVs of the electrolyte containing 1 M LiClO₄, TEGDME and Fe-PP under a He and O₂ atmosphere at a scan rate of 5 mV s⁻¹; (c) initial charge/discharge curves of cells with the MWCNT electrode and (1) 1 M LiClO₄ + TEGDME or (2) 1 M LiClO₄ + TEGDME + Fe-PP in a voltage window between 4.30 and 2.35 V at a current density of 100 mA g⁻¹; (d) voltage versus time curves of batteries at a current density of 200 mA g⁻¹ under the same conditions as (c).⁵¹⁸ Reprinted with permission from ref. 518. Copyright 2016 Nature Publishing Group.

with FePc performed with a two times larger capacity (full-discharge mode) and lower OER overpotential of 400 mV (at 1000 mA h g⁻¹) compared to batteries without FePc.

In addition to organic SRMs, several inorganic reagents, such as LiI and LiBr, have been developed to catalyze the OER in aprotic Li–O₂ cells.^{425,449–457,520} Kang *et al.* first used LiI as an SRM in a Li–O₂ cell, exhibiting a reduced OER potential from 4.3 V to 3.3 V with CNT fibril as the cathode at a current rate of 2 A g⁻¹ with a limited capacity of 1000 mA h g⁻¹ (Fig. 87).⁶⁹ Consequently, the battery with the I⁻/I₃⁻ redox couple achieved an excellent cyclic stability of close to 900 cycles at a fixed capacity of 1000 mA h g⁻¹. It was also found that the cell performance with SRMs was significantly related to the applied cathode. A CNTs electrode could perform better in terms of the electron-transfer property than KB electrode, and therefore offered lower OER overpotentials. After that, numerous reports used LiI SRMs combined with different cathode materials, such as rGO, nori-derived carbon, polydopamine-modified CNTs or polyimide-coated carbon.^{521–523} All of these combinations exhibited a better performance than those of a battery with single SRMs or that was possible through cathode design.

Due to the highly positive effects of the LiI redox couple on the decrease of cell charging polarization, many researchers investigated the reaction chemistry of LiI in aprotic Li–O₂ batteries. Aurbach *et al.* found that LiI could accelerate the electrolyte degradation (1 M LiCF₃SO₃ in TEGDME) and produce LiOH as the main discharge product in a high concentration (0.1–1 M), while LiOH cannot be decomposed by the I₃⁻/I⁻ and I₂/I₃⁻ couples.⁵²⁴ At a low concentration (0.01 M), Li₂O₂ becomes the dominant product, and can be oxidized

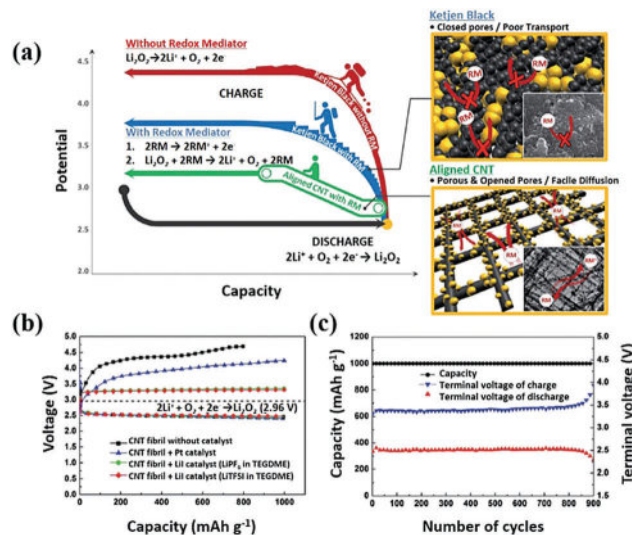


Fig. 87 (a) Schematic illustration of the role of a redox mediator (RM) in a Li–O₂ battery using KB carbon and aligned-CNT-fibril electrodes; (b) discharge/charge profiles of CNT fibril electrodes without a catalyst, with Pt catalyst and with LiI catalyst at a discharge depth of 1000 mA h g⁻¹ and a current rate of 2000 mA g⁻¹; (c) cyclability and terminal voltages of cells with the CNT fibril electrodes and LiI catalyst.⁶⁹ Reprinted with permission from ref. 69. Copyright 2014 Wiley-VCH Verlag GmbH & Co. KGaA.

by the I₂/I₃⁻ couple. This result was in accordance with Zhou's report.¹⁷³

In addition to the use of an independent additive, Grey *et al.* used LiI and H₂O as co-additives and rGO as the cathode to achieve an outstanding battery performance. The battery had a low charging voltage of about 3 V (1 A g⁻¹ at a limited capacity of 8 A h g⁻¹) and superior cycling stability for over 500 cycles at 5 A g⁻¹ (5 A h g⁻¹).⁵²⁵ The authors proposed that the better performance could be attributed to the catalytic decomposition of LiOH by LiI, and the interconnected macroporous network of rGO, which was beneficial for the formation of large-sized LiOH aggregations. Wang *et al.* proved that LiOOH was also a stable discharge product with 50 mM LiI and 1–20% water (v/v) in DME (0.5 M LiTFSI) and found it could be oxidized by the I₃⁻/I⁻ couple below 3.5 V.⁴⁷ They also found that LiOH could be decomposed at about 3.85 V with LiI and water. Zhou *et al.* suggested that the quantity of Li₂O₂ in the discharge product increased with the improved water content in the 1 M LiI/TEGDME-based electrolyte, owing to the buffer effect of water towards the nucleophilic attack of superoxide species.¹⁷³ In this case, Li₂O₂ and LiOH coexisted after discharge, while Li₂O₂ could be decomposed by the I₂/I₃⁻ couple and LiOH remained on the cathode after charging. Shao-Horn *et al.* further investigated the influence of the water/LiI ratio on the reaction chemistry of a Li–O₂ cell. When the molar ratio of H₂O/LiI was lower than 5, LiOH was the major product due to the shifting of the reaction equilibrium (Li₂O₂ + H₂O ↔ H₂O₂ + 2LiOH) to the right side by the consumption of H₂O₂ by LiI (3LiI + H₂O ↔ LiI₃ + 2LiOH).¹⁷⁴ In contrast, at a high H₂O/LiI ratio (12, 24 and 134), LiOOH·H₂O was formed and disproportionated to LiOH·H₂O as the final discharge product. It was suggested that LiI accelerated

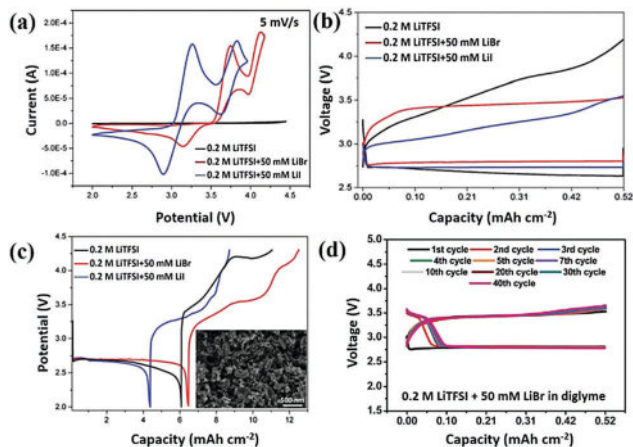


Fig. 88 (a) Cyclic voltammetry (5 mV s^{-1}) of (1) 0.2 M LiTFSI/DME (black curve), (2) 0.2 M LiTFSI/DME containing 50 mM LiBr (red curve) and (3) 0.2 M LiTFSI/DME containing 50 mM LiI (blue curve) on Pt working electrodes under an Ar atmosphere; the 1st discharge/charge profiles of Li-O_2 cells with different DME electrolytes at (b) a limited capacity (0.052 mA cm^{-2}) for 10 h and (c) an unlimited capacity (the inset shows the typical toroid deposits of Li_2O_2); (d) discharge/charge profiles of Li-O_2 cells with $0.2 \text{ M LiTFSI} + 50 \text{ mM LiBr}$ in DME electrolytes during prolonged galvanostatic cycling (current density: 0.052 mA cm^{-2}).⁵²⁸ Reprinted with permission from ref. 528. Copyright 2016 Royal Society of Chemistry.

the superoxide-related nucleophilic attack towards the electrolyte or promoted Li_2O_2 transformation, which probably hampered the battery cycle life.

Up to now, it is still controversial to say whether LiOH could be decomposed by LiI or not. Theoretically, the redox potential of the LiOH/O_2 couple is 3.82 and $3.42 \text{ V vs. Li}^+/\text{Li}$ in acidic and basic conditions, respectively, which are much higher values than that of the I_3^-/I^- couple. The I_3^-/LiOH reaction to produce O_2 in a charge process seems unfeasible.^{8,175} However, the redox chemicals may arise from the existence of derived intermediates, for example IO^- and IO_3^- , and consequently more effort should be done to show evidence for the chemical oxidation of LiOH by the LiI -containing system.⁵²⁶

Similar to the I^-/I_3^- redox couple, other halide cation couples also have similar OER functionality. Aurbach and Sun *et al.* used LiBr as an OER SRM in a Li-O_2 battery, and demonstrated a pronounced improvement in the charge characteristics at higher charging rates.⁵²⁸ The battery achieved over 40 stable cycles with negligible overpotential deviations, owing to the efficient decomposition of Li_2O_2 by LiBr (Fig. 88). They also stated that Br_2 was formed above $4 \text{ V vs. Li}^+/\text{Li}$, and it could decompose the Li_2CO_3 by-products.

6.3 SRMs for both Li_2O_2 formation and decomposition

Due to their independent function for promoting the discharge/charge reactions in Li-O_2 batteries, ORR and OER SRMs could be simultaneously used to accelerate both Li_2O_2 formation and decomposition reactions.^{27,529} Bruce *et al.* demonstrated that the dual mediators DBBQ and TEMPO could be used to promote both Li_2O_2 formation and decomposition in solution (Fig. 89). The as-prepared battery showed capacities of $2 \text{ mA h cm}_{\text{areal}}^{-2}$

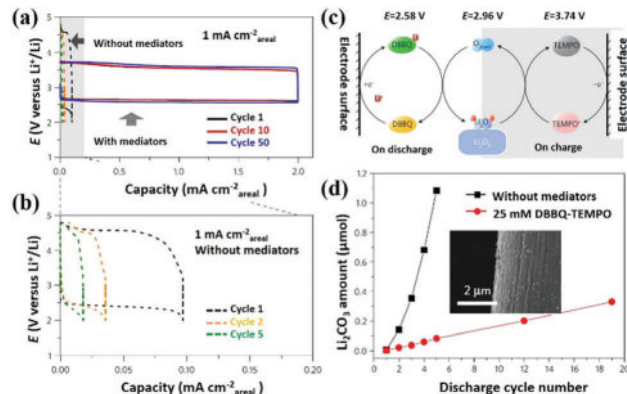


Fig. 89 (a) Discharge-charge curves of a battery using gas-diffusion-layer-based porous carbon electrodes and $0.3 \text{ M LiClO}_4/\text{DME}$ with $25 \text{ mM DBBQ}/25 \text{ mM TEMPO}$ (solid lines) and without DBBQ-TEMPO (dashed lines); (b) enlarged section of the discharge-charge curves recorded without DBBQ-TEMPO in (a); (c) schematics of the positive electrode reactions on discharge and charge in the presence of DBBQ and TEMPO ; (d) amounts of $\text{Li}_2^{13}\text{CO}_3$ in the ^{13}C -carbon cathodes at the end of discharge on each cycle (determined by subjecting the electrodes to acid to liberate $^{13}\text{CO}_2$ from the $\text{Li}_2^{13}\text{CO}_3$), the inset of (d) shows SEM images of the GDL-based porous carbon electrodes using $0.3 \text{ M LiClO}_4/\text{DME}$ electrolyte with $25 \text{ mM DBBQ}/25 \text{ mM TEMPO}$ at the end of the 10th charge.⁵³⁰ Reprinted with permission from ref. 530. Copyright 2017 Nature Publishing Group.

at $1 \text{ mA cm}_{\text{areal}}^{-2}$ with a low polarization on charge/discharge (3.6 V and 2.7 V), which were much better results than those of batteries without SRMs ($\sim 0.1 \text{ mA h cm}_{\text{areal}}^{-2}$, 4.0 V and 2.5 V). Because Li_2O_2 was formed and decomposed in solution within low charge potentials (3.6 V), the generation of Li_2CO_3 by-product and carbon instability were significantly reduced ($< 0.008\%$ decomposition per cycle compared with 0.12% without SRMs). Moreover, it was hypothesized that $40 \text{ mA h cm}_{\text{areal}}^{-2}$ at rates of $1 \text{ mA cm}_{\text{areal}}^{-2}$ could be achieved with gas diffusion electrodes, which were equal to a practical cell with $500\text{--}600 \text{ W h Kg}^{-1}$.⁵³⁰

A Li-O_2 battery with redox couples and a separate gas diffusion tank (GDT) instead of a cathode current collector could separate the current collection and discharge-product accumulation, which prevented the surface passivation and pore clogging of Li_2O_2 products. This battery was named a redox-flow Li-O_2 battery (RF Li-O_2 battery).⁵²⁹ Zhu *et al.* used EtV^{2+} and LiI as ORR and OER redox catalysts in a RF Li-O_2 battery (Fig. 90), and the primary cell delivered a high capacity of over 40 mA h in the presence of 10 mM ethyl viologen (EV^{2+}) at a current density of 0.125 mA cm^{-2} .²⁷ Although these two types of redox mediators functioned reasonably well in the RF Li-O_2 battery, they suffered corrosion problems and presented large overpotentials for the oxidation of Li_2O_2 , as well as an unstable nature upon prolonged cycling. The same authors reported a new pair of redox molecules, namely tris(4-[2-(2-methoxyethoxy)ethoxy]phenyl)amine (TMPPA) and DBBQ , as OER and ORR catalysts to tackle these issues.⁵²⁹ As reported previously, DBBQ and TMPPA molecules presented the redox reactions at around 2.63 and $3.63 \text{ V vs. Li/Li}^+$, respectively, located in the upper and bottom of the $\text{O}_2/\text{Li}_2\text{O}_2$ equilibrium potential. With DBBQ as the ORR SRM,

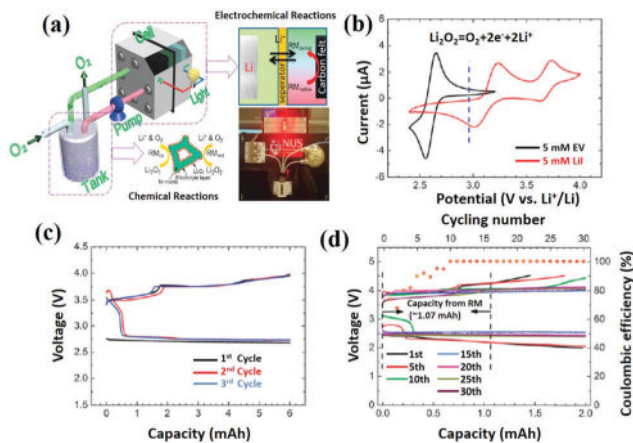


Fig. 90 (a) Schematic illustration of the configuration and working process of an RF Li–O₂ battery (the cell stack constitutes a Li-anode and carbon felt cathode (2 × 2 cm²), separated by a membrane; a gas diffusion tank was then connected to the cathodic compartment through a pump; during the discharge process, oxygen flowed into the tank and was reduced to form Li₂O₂, while the electrolyte fluid containing the redox mediators and Li⁺ circulated between GDT and the cell; the photo at the lower-right corner shows an RF Li–O₂ battery powering three light-emitting diodes); (b) CVs of the TEGDME electrolyte with ethyl viologen or Lil (the equilibrium potential of Li₂O₂/O₂ is indicated for reference); (c) discharge/charge curves of an RF Li–O₂ battery in the first 3 cycles (a current density of 0.05 mA cm⁻²); (d) discharge/charge curves and Coulombic efficiency of RF Li–O₂ batteries employing a PVdF-Nafion membrane at different cycle numbers (current density: 0.125 mA cm⁻², electrolyte: 1.0 M LiTFSI/TEGDME containing 10 mM EV²⁺/10 mM I⁻).²⁷ Reprinted with permission from ref. 27. Copyright 2015 Royal Society of Chemistry.

a volumetric energy density as large as 7090 W h L⁻¹ could be attained if only the volume of the GDT tank was considered. Unfortunately, they found that the DBBQ molecule could undergo certain changes in the high-voltage region (above 3.5 V).⁵²⁹ It remains therefore essential to search for OER SRMs with good stability and a low midpoint potential (at least ≲3.5 V Li/Li⁺) for decreasing the charging potentials, which would be beneficial for the inhibition degradation of the SRMs under high voltages.

6.4 Short summary and perspective for SRMs

In short, the introduction of SRMs could substantially enlarge the catalytic sites for Li₂O₂ formation/decomposition, which is benefit for the increased reaction kinetics at the oxygen electrode (Tables 10 and 11). The active and stable SRMs should meet the following criteria: (1) their redox potential should be close to the equilibrium potential of O₂/Li₂O₂, which is essential for catalyzing Li₂O₂ formation/decomposition; (2) the chemical and electrochemical stability of the SRM should be high enough to tolerate the reactive species, especially in the harsh superoxide-containing environment; (3) their solubility in organic electrolytes should be high enough for fast Li₂O₂ formation/decomposition; (4) their molecular weight should be as low as possible for their fast diffusion kinetics.

To screen SRMs with the above-mentioned standards, many challenges still remain. First, SRMs with better chemical and electrochemical stability are essential to achieve stable ORR and OER sustainably.^{526,528} Second, the redox potentials of

Table 11 Application of OER SRMs in aprotic Li–O₂ systems

SRM (M _w /g mol ⁻¹ , concentration)	Cathode	Electrolyte	Midpoint potential (V vs. Li ⁺ /Li)	Charging voltage (V)	Decreased overpotential/limited capacity	Current density	Ref.
TTF (204, 10 mM)	Nanoporous gold	1 M LiClO ₄ in DMSO	~3.60	~3.40	500 mV/300 mA h g ⁻¹	78 μA cm ⁻²	503
TEMPO (156, 10 mM)	KB (~0.4 mg cm ⁻²)	0.1 M LiTFSI in DME	~3.70	~3.60	400 mV/—	0.1 mA cm ⁻²	509
MPT (213, 100 mM)	Super P (~0.13 mg cm ⁻²)	1 M LiCF ₃ SO ₃ in TEGDME	~3.70	~3.60	800 mV/1000 mA h g ⁻¹	150 mA g ⁻¹	511
Fe-PP (620, 2.3 mM)	MWCNTs (—)	1 M LiClO ₄ in TEGDME	~3.60	~3.90	300 mV/2800 mA h g ⁻¹	100 mA g ⁻¹	519
I ⁻ /I ₃ ⁻ (127, 50 mM)	CNT (<0.1 mg cm ⁻²)	1 M LiTFSI in TEGDME	~3.30	~3.30	1 V/1000 mA h g ⁻¹	2000 mA g ⁻¹	69
Br ⁻ /Br ₃ ⁻ (80, 10 mM)	KB (0.4 mg cm ⁻²)	1 M LiTFSI in DME	~3.50	~3.60	400 mV/500 mA h g ⁻¹	500 mA g ⁻¹	528

M_w, molecular weight.

SRMs should be close to 2.96 V vs. Li/Li⁺, which is beneficial for decreasing the ORR and OER overpotentials. Third, the side reaction between SRMs and the Li-anode can induce a short-circuit and self-discharge of the battery, as well as a rapid failure of the Li-anode and SRMs. Consequently, some protective methods are proposed to solve the above-mentioned obstacles, for example, a Li⁺ selective solid-electrolyte membrane and negatively charged polymer separator,^{69,509,531} a pretreated Li-anode with carbonate-based electrolyte^{105,507} and replacement of the counter electrodes.⁵¹¹ However, these cannot solve all these problems thoroughly and some new issues will also arise. With regard to these challenges, a combination of advanced electrode, electrolyte and SRMs may be a good strategy to achieve a stable and high-performance battery.

7. Conclusion and perspective

The rate and sustainability of electrochemical reactions at the electrode of aprotic Li-O₂ batteries are the critical factors to determine the cell energy density, capacity, rate capability, stability and so on. The lack of fundamental understanding between the material/structure of electrodes/electrolytes and the electrode reaction kinetics limits the rapid development of high-performance and stable Li-O₂ batteries. In this review article, we tried to illustrate the discharge/charge mechanism at the anode and cathode of Li-O₂ batteries, and paid great attention to clarifying the influence of the electrode and electrolyte material/structure functionality on the stability and rate of the electrode reactions, which is beneficial for the synthesis and optimization of advanced materials/structures for high-performance Li-O₂ batteries.

For the Li-electrode part, the construction of an SEI layer with inorganic Li-salts and a protective Li⁺ conductive film on the Li-electrode as well as substitution of the Li-metal by Li-alloy are proposed to solve the issues of Li dendrite formation and to overcome issues with the side reactions. We comprehensively discuss these effective protocols for protection of the Li-metal to enable the stable long-term operation of Li-O₂ batteries. The safety issues, self-discharge and rapid decay of the Li-anode can be partially resolved with an independent strategy. However, it is clear that the sole optimization method cannot settle all of the challenges associated with the Li-anode. A combination of two-to-three methods may have the opportunity to achieve a persistent and stable Li-anode for the sustainable energy output of Li-O₂ batteries.

For the oxygen electrode part, their improved functionalities are identified as being key to accelerate the reaction kinetics through the design of efficient solid catalysts, a porous structure and *via* surface engineering.²⁰ First, the cathode architecture with a suitable pore structure has been proven to be highly important for better mass transport and to give a large space for Li₂O₂ storage. Second, the construction of advanced catalysts may provide the opportunity for effectively catalyzing Li₂O₂ formation and decomposition, and inducing the efficient growth of large Li₂O₂ particles through surface engineering. Third,

the present Li₂O₂ formation reaction seems to occur at the two-phase interface (electrode/electrolyte), because the accessible O₂ is dissolved in the electrolyte. The construction of a three-phase interface between the electrode, electrolyte, and O₂ for better Li₂O₂ formation/decomposition reactions is definitely essential for achieving a high cell capacity and rate capability.^{8,532}

For the electrolyte part, liquid, quasi-solid and solid electrolytes with different mass transport abilities and electrochemical stabilities have been screened for high-performance and stable Li-O₂ batteries.¹⁴⁶ Ether-type electrolytes may be one of the most stable electrolytes among this family. Additionally, ionic-liquid and polymer-gel electrolytes offer an increased stability against superoxide species, and overcome the main shortages of the liquid-type electrolyte in Li-O₂ batteries, as well as inhibiting the side reactions and dendrite growth at the Li-electrode.⁵²⁰ One of the functions of the electrolyte is the tuneable formation of the Li⁺-O₂⁻ intermediates, while solvents and additives with a specific electron affinity can provide the opportunity for stabilizing the intermediates for the growth of large Li₂O₂ clusters.^{5,481,486} Additionally, some solvents and additive also possess a specific functionality for increasing the charge reaction kinetics. To compensate the shortage of single solvents or additives, a proper integration of electrolyte components with different functionalities, such as additives for increasing the O₂ and Li₂O₂ solubility, additives for inhibition of the side reactions^{142,515} and solvents and additives for stabilizing the intermediates and solubility of Li₂O₂, may provide the chance for an acceleration of the ORR and OER reactions in Li-O₂ batteries.¹⁵

SRM is a special kind of additive, which functions as an electron transporter, oxygen carrier and intermediates stabilizer for enhancement of the OER and ORR kinetics in Li-O₂ batteries.⁵¹⁸ It should be noted that the electrochemical reaction kinetics for the Li₂O₂ solid to O₂ and Li⁺ are contrary to the potential gap between the midpoint potentials of the SRMs and 2.96 V vs. Li⁺/Li. It seems that a decrease in the overpotentials and an increase in the electrochemical kinetics of OER and ORR cannot be simultaneously achieved by using SRMs alone. However, this contradiction can be settled by further understanding the effect of OER redox mediators on the cell performance, for example, the use of additional chemicals to accelerate electrochemical ORR and OER.^{143,293}

Besides achieving fast and sustainable Li₂O₂ formation and decomposition reactions, another essential point that should be carefully considered is the avoidable generation of some by-products (for example, LiOH, Li₂CO₃) due to the side reactions.¹³⁸ Li⁺-Based by-products are generally difficult to be decomposed due to their high equilibrium potentials, which can induce pore clogging of the cathode and lead to sudden death of the battery. One of the strategies to resolve this issue is the development of efficient additives to decompose them. For example, SRMs with multiple redox couples may have an opportunity to independently decompose them. Another strategy is to inhibit their generation during cell cycling. For example, the development of efficient and stable electrolytes can tolerate the attack by reactive species for generating negligible by-products. In addition, the combination of advanced solvents and functional

additives provides an opportunity to reduce the charge potentials, which could have a high impact to weaken the degradation of the electrolyte.

Although the present designs of advanced materials and structures seem to be effective for promoting and sustaining the electrochemical reactions at the anode and cathode, the achievement of fast and sustainable reactions in Li–O₂ batteries is not so simple. For example, one of biggest challenges for Li–O₂ batteries is their rate capability, that is to say, the devices should work at high current rates. Most recent efforts have only focused on research at relatively low current rates ($\leq 1 \text{ A g}^{-1}$, the amount of total cathode materials). At high current rates, the efficiencies of mass transport and electron transfer, including Li⁺ transport through the interface and electrolyte, O₂ transport to the two-phase/three-phase interfaces, electron transfer between the electrode and O₂/Li₂O₂, and so on, strongly affect the rates of Li₂O₂ formation and decomposition. Independent studies on the individual parts are far away from achieving high-performance and stable Li–O₂ batteries. Much effort should be done to seriously understand the essential points for the fast and sustainable Li₂O₂ formation/decomposition reactions in Li–O₂ batteries.

In summary, the present achievements have already shown that the functional design of a material and structure play important roles in the increased kinetics and stable output of electrochemical reactions. From an academic point of view, the high and stable energy output of a Li–O₂ battery should be established on the fast and stable electrochemical reaction at their independent electrodes. However, it is clear that a straightforward solution to solve the sole problem associated with a single cell module seems to be ineffective. A holistic approach with a combination of several parts has the chance to solve this obstacle. For instance, the safety problem at the Li-metal electrode may be solved with the combination of an SEI membrane, a Li⁺ conductive membrane and optimal electrolytes; while the decomposition of electrolytes under high charge potentials may be solved through optimization of the solvents and the use of additives, and cathode materials; fast O₂ transport may integrate the optimized solvents and additives, as well as the surface/interface architecture of the oxygen electrode.

Although most of these challenges still exist and hinder the rapid development of Li–O₂ batteries, a deep understanding of the electrode reaction process is critical for the progress of this new-generation battery system. The combination and optimization of advanced electrodes, electrolytes and membranes should provide powerful solutions to solve all of the remaining issues in Li–O₂ batteries. After the fundamental question of electrode reactions are answered and the efficient materials and surface/interface structure are constructed, it is believed that Li–O₂ batteries will finally reach commercial application in the next decades.¹³⁹

List of abbreviations

AN	Acceptor number
CNTs	Carbon nanotubes
CT	Carbon textile

3D	Three-dimensional
DEMS	Differential electrochemical mass spectroscopy
DFT	Density functional theory
DN	Donor number
DMSO	Dimethylsulfoxide
DME	1,2-Dimethoxyethane
DMA	<i>N,N</i> -Dimethylacetamide
DMF	<i>N,N</i> -Dimethylformamide
FT-IR	Fourier transform infrared spectroscopy
LiTFSI	Lithium bis(trifluoromethanesulfonyl)imide
LiBETI	Lithium bis(perfluoroethylsulfonyl)imide
LiFSI	Lithium bis(fluorosulfonyl)imide
LiTf	Lithium trifluoromethanesulfonate
LiBOB	Lithium bis(oxalato)borate
LiPFOS	Lithium perfluorooctanesulfonate,
(Li ⁺ –O ₂ [–]) _{sol}	Solvated Li ⁺ –O ₂ [–] ionic pair
MWCNT	Multi-walled carbon nanotube
NAs	Nanoarrays
NMP	Dimethylpyrrolidine
ORR	Oxygen reduction reaction
OER	Oxygen evolution reaction
PC	Polycarbonate
PVdF	Polyvinylidene fluoride
rGO	Reduced graphene oxide
SEI	Solid–electrolyte–interface
SRM	Soluble redox mediator
TBA ⁺	Tetrabutylammonium
XPS	X-ray photoelectron spectroscopy

Conflicts of interest

There are no conflicts to declare.

Acknowledgements

We acknowledge Prof. Zhongqun Tian at Xiamen University, China, for his valuable discussion for manuscript edition. This work was supported by National Natural Science Foundation of China (U1604122, 21773055, 51702086, 21203055), Program for Science & Technology Innovation Talents in Universities of Henan Province (18HASTIT004), and the “1000 Youth Talents Plan” of China.

References

- 1 M. K. Debe, *Nature*, 2012, **486**, 43–51.
- 2 L. Grande, E. Paillard, J. Hassoun, J. B. Park, Y. J. Lee, Y. K. Sun, S. Passerini and B. Scrosati, *Adv. Mater.*, 2015, **27**, 784–800.
- 3 S. Chu and A. Majumdar, *Nature*, 2012, **488**, 294–303.
- 4 H. G. Jung, J. Hassoun, J. B. Park, Y. K. Sun and B. Scrosati, *Nat. Chem.*, 2012, **4**, 579–585.
- 5 C. M. Burke, V. Pande, A. Khetan, V. Viswanathan and B. D. McCloskey, *Proc. Natl. Acad. Sci. U. S. A.*, 2015, **112**, 9293–9298.

- 6 M. M. O. Thotiyl, S. A. Freunberger, Z. Q. Peng, Y. H. Chen, Z. Liu and P. G. Bruce, *Nat. Mater.*, 2013, **12**, 1049–1055.
- 7 K. Song, D. A. Agyeman, M. Park, J. Yang and Y.-M. Kang, *Adv. Mater.*, 2017, **29**, 1606572.
- 8 T. Zhang and H. Zhou, *Nat. Commun.*, 2013, **4**, 1817.
- 9 J.-L. Shui, J. S. Okasinski, P. Kenesei, H. A. Dobbs, D. Zhao, J. D. Almer and D.-J. Liu, *Nat. Commun.*, 2013, **4**, 2255.
- 10 D. Oh, J. Qi, Y.-C. Lu, Y. Zhang, Y. Shao-Horn and A. M. Belcher, *Nat. Commun.*, 2013, **4**, 2756.
- 11 J. Lu, Y. Jung Lee, X. Luo, K. Chun Lau, M. Asadi, H.-H. Wang, S. Brombosz, J. Wen, D. Zhai, Z. Chen, D. J. Miller, Y. Sub Jeong, J.-B. Park, Z. Zak Fang, B. Kumar, A. Salehi-Khojin, Y.-K. Sun, L. A. Curtiss and K. Amine, *Nature*, 2016, **529**, 377.
- 12 R. Van Noorden, *Nature*, 2014, **507**, 26–28.
- 13 Z. Ma, X. X. Yuan, L. Li, Z. F. Ma, D. P. Wilkinson, L. Zhang and J. J. Zhang, *Energy Environ. Sci.*, 2015, **8**, 2144–2198.
- 14 B. D. McCloskey, J. M. Garcia and A. C. Luntz, *J. Phys. Chem. Lett.*, 2014, **5**, 1230–1235.
- 15 Y. Li, X. Wang, S. Dong, X. Chen and G. Cui, *Adv. Energy Mater.*, 2016, **6**, 1600751.
- 16 N. B. Aetukuri, B. D. McCloskey, J. M. Garcia, L. E. Krupp, V. Viswanathan and A. C. Luntz, *Nat. Chem.*, 2015, **7**, 50–56.
- 17 X. H. Yao, Q. Dong, Q. M. Cheng and D. W. Wang, *Angew. Chem., Int. Ed.*, 2016, **55**, 11344–11353.
- 18 D. Geng, N. Ding, T. S. A. Hor, S. W. Chien, Z. Liu, D. Wu, X. Sun and Y. Zong, *Adv. Energy Mater.*, 2016, **6**, 1502164.
- 19 N. Feng, P. He and H. Zhou, *Adv. Energy Mater.*, 2016, **6**, 1502303.
- 20 Z. W. Chang, J. J. Xu, Q. C. Liu, L. Li and X. B. Zhang, *Adv. Energy Mater.*, 2015, **5**, 1500633.
- 21 D. Aurbach, B. D. McCloskey, L. F. Nazar and P. G. Bruce, *Nat. Energy*, 2016, **1**, 16128.
- 22 P. G. Bruce, S. A. Freunberger, L. J. Hardwick and J. M. Tarascon, *Nat. Mater.*, 2012, **11**, 19–29.
- 23 J. Z. Zhu, F. Wang, B. Z. Wang, Y. W. Wang, J. J. Liu, W. Q. Zhang and Z. Y. Wen, *J. Am. Chem. Soc.*, 2015, **137**, 13572–13579.
- 24 Y. C. Lu, Z. C. Xu, H. A. Gasteiger, S. Chen, K. Hamad-Schifferli and Y. Shao-Horn, *J. Am. Chem. Soc.*, 2010, **132**, 12170–12171.
- 25 Y. Chen, S. A. Freunberger, Z. Peng, F. Barde and P. G. Bruce, *J. Am. Chem. Soc.*, 2012, **134**, 7952–7957.
- 26 S. M. Dong, X. Chen, K. J. Zhang, L. Gu, L. X. Zhang, X. H. Zhou, L. F. Li, Z. H. Liu, P. X. Han, H. X. Xu, J. H. Yao, C. J. Zhang, X. Y. Zhang, C. Q. Shang, G. L. Cui and L. Q. Chen, *Chem. Commun.*, 2011, **47**, 11291–11293.
- 27 Y. G. Zhu, C. K. Jia, J. Yang, F. Pan, Q. Z. Huang and Q. Wang, *Chem. Commun.*, 2015, **51**, 9451–9454.
- 28 J. W. Wang, Y. L. Zhang, L. M. Guo, E. K. Wang and Z. Q. Peng, *Angew. Chem., Int. Ed.*, 2016, **55**, 5201–5205.
- 29 S. A. Freunberger, Y. H. Chen, N. E. Drewett, L. J. Hardwick, F. Barde and P. G. Bruce, *Angew. Chem., Int. Ed.*, 2011, **50**, 8609–8613.
- 30 D. W. Kim, S. M. Ahn, J. Kang, J. Suk, H. K. Kim and Y. Kang, *J. Mater. Chem. A*, 2016, **4**, 6332–6341.
- 31 B. D. Adams, R. Black, Z. Williams, R. Fernandes, M. Cuisinier, E. J. Berg, P. Novak, G. K. Murphy and L. F. Nazar, *Adv. Energy Mater.*, 2015, **5**, 1400867.
- 32 B. G. Kim, H.-J. Kim, S. Back, K. W. Nam, Y. Jung, Y.-K. Han and J. W. Choi, *Sci. Rep.*, 2014, **4**, 4225.
- 33 M. Balaish, E. Peled, D. Golodnitsky and Y. Ein-Eli, *Angew. Chem., Int. Ed.*, 2015, **54**, 436–440.
- 34 F. Y. Cheng and J. Chen, *Nat. Chem.*, 2012, **4**, 962–963.
- 35 D. C. Lin, Y. Y. Liu and Y. Cui, *Nat. Nanotechnol.*, 2017, **12**, 194–206.
- 36 M. M. O. Thotiyl, S. A. Freunberger, Z. Q. Peng and P. G. Bruce, *J. Am. Chem. Soc.*, 2013, **135**, 494–500.
- 37 T. Liu, Z. Liu, G. Kim, J. T. Frith, N. Garcia-Araez and C. P. Grey, *Angew. Chem., Int. Ed.*, 2017, **56**, 16057–16062.
- 38 W. Walker, V. Giordani, J. Uddin, V. S. Bryantsev, G. V. Chase and D. Addison, *J. Am. Chem. Soc.*, 2013, **135**, 2076–2079.
- 39 S. W. Lee, C. Carlton, M. Risch, Y. Surendranath, S. Chen, S. Furutsuki, A. Yamada, D. G. Nocera and Y. Shao-Horn, *J. Am. Chem. Soc.*, 2012, **134**, 16959–16962.
- 40 H. D. Lim, K. Y. Park, H. Song, E. Y. Jang, H. Gwon, J. Kim, Y. H. Kim, M. D. Lima, R. O. Robles, X. Lepro, R. H. Baughman and K. Kang, *Adv. Mater.*, 2013, **25**, 1348–1352.
- 41 H. D. Lim, B. Lee, Y. Bae, H. Park, Y. Ko, H. Kim, J. Kim and K. Kang, *Chem. Soc. Rev.*, 2017, **46**, 2873–2888.
- 42 Z. Lyu, Y. Zhou, W. Dai, X. Cui, M. Lai, L. Wang, F. Huo, W. Huang, Z. Hu and W. Chen, *Chem. Soc. Rev.*, 2017, **46**, 6046–6072.
- 43 L. Luo, B. Liu, S. Song, W. Xu, J.-G. Zhang and C. Wang, *Nat. Nanotechnol.*, 2017, **12**, 535.
- 44 T. Laino and A. Curioni, *Chem. – Eur. J.*, 2012, **18**, 3510–3520.
- 45 F. Li, S. Wu, D. Li, T. Zhang, P. He, A. Yamada and H. Zhou, *Nat. Commun.*, 2015, **6**, 7843.
- 46 D. Sharon, D. Hirsberg, M. Afri, F. Chesneau, R. Lavi, A. A. Frimer, Y. K. Sun and D. Aurbach, *ACS Appl. Mater. Interfaces*, 2015, **7**, 16590–16600.
- 47 Y. G. Zhu, Q. Liu, Y. Rong, H. Chen, J. Yang, C. Jia, L.-J. Yu, A. Karton, Y. Ren, X. Xu, S. Adams and Q. Wang, *Nat. Commun.*, 2017, **8**, 14308.
- 48 K. J. Zhang, L. X. Zhang, X. Chen, X. He, X. G. Wang, S. M. Dong, L. Gu, Z. H. Liu, C. S. Huang and G. L. Cui, *ACS Appl. Mater. Interfaces*, 2013, **5**, 3677–3682.
- 49 S. C. Wu, J. Tang, F. J. Li, X. Z. Liu, Y. Yamauchi, M. Ishida and H. S. Zhou, *Adv. Funct. Mater.*, 2016, **26**, 3291–3298.
- 50 X. D. Ren, B. Z. Wang, J. Z. Zhu, J. J. Liu, W. Q. Zhang and Z. Y. Wen, *Phys. Chem. Chem. Phys.*, 2015, **17**, 14605–14612.
- 51 L. L. Liu, J. Wang, Y. Y. Hou, J. Chen, H. K. Liu, J. Z. Wang and Y. P. Wu, *Small*, 2016, **12**, 602–611.
- 52 L. M. Leng, X. Y. Zeng, P. Chen, T. Shu, H. Y. Song, Z. Y. Fu, H. S. Wang and S. J. Liao, *Electrochim. Acta*, 2015, **176**, 1108–1115.
- 53 G.-H. Lee, S. Lee, J.-C. Kim, D. W. Kim, Y. Kang and D.-W. Kim, *Adv. Energy Mater.*, 2017, **7**, 1601741.
- 54 H. Yadegari, M. N. Banis, A. Lushington, Q. Sun, R. Y. Li, T. K. Sham and X. L. Sun, *Energy Environ. Sci.*, 2017, **10**, 286–295.

- 55 J. Lu, Y. Lei, K. C. Lau, X. Y. Luo, P. Du, J. G. Wen, R. S. Assary, U. Das, D. J. Miller, J. W. Elam, H. M. Albishri, D. Abd El-Hady, Y. K. Sun, L. A. Curtiss and K. Amine, *Nat. Commun.*, 2013, **4**.
- 56 N. Togasaki, T. Momma and T. Osaka, *J. Power Sources*, 2015, **294**, 588–592.
- 57 X. B. Cheng, T. Z. Hou, R. Zhang, H. J. Peng, C. Z. Zhao, J. Q. Huang and Q. Zhang, *Adv. Mater.*, 2016, **28**, 2888–2895.
- 58 R. Khurana, J. L. Schaefer, L. A. Archer and G. W. Coates, *J. Am. Chem. Soc.*, 2014, **136**, 7395–7402.
- 59 Q. Lu, Y.-B. He, Q. Yu, B. Li, Y. V. Kaneti, Y. Yao, F. Kang and Q.-H. Yang, *Adv. Mater.*, 2017, **29**, 1604460.
- 60 K. Liu, D. Zhuo, H.-W. Lee, W. Liu, D. Lin, Y. Lu and Y. Cui, *Adv. Mater.*, 2017, **29**, 1603987.
- 61 H. Lee, D. J. Lee, J.-N. Lee, J. Song, Y. Lee, M.-H. Ryou, J.-K. Park and Y. M. Lee, *Electrochim. Acta*, 2014, **123**, 419–425.
- 62 R. S. Assary, J. Lu, P. Du, X. Luo, X. Zhang, Y. Ren, L. A. Curtiss and K. Amine, *ChemSusChem*, 2013, **6**, 51–55.
- 63 M. Marinaro, P. Balasubramanian, E. Gucciardi, S. Theil, L. Jorissen and M. Wohlfahrt-Mehrens, *ChemSusChem*, 2015, **8**, 3139–3145.
- 64 P. Bhattacharya, E. N. Nasybulin, M. H. Engelhard, L. Kovarik, M. E. Bowden, X. H. S. Li, D. J. Gaspar, W. Xu and J. G. Zhang, *Adv. Funct. Mater.*, 2014, **24**, 7510–7519.
- 65 J. Hassoun, H.-G. Jung, D.-J. Lee, J.-B. Park, K. Amine, Y.-K. Sun and B. Scrosati, *Nano Lett.*, 2012, **12**, 5775–5779.
- 66 X.-B. Cheng, R. Zhang, C.-Z. Zhao and Q. Zhang, *Chem. Rev.*, 2017, **117**, 10403–10473.
- 67 G. Wu, N. H. Mack, W. Gao, S. G. Ma, R. Q. Zhong, J. T. Han, J. K. Baldwin and P. Zelenay, *ACS Nano*, 2012, **6**, 9764–9776.
- 68 J. H. Lee, R. Black, G. Popov, E. Pomerantseva, F. H. Nan, G. A. Botton and L. F. Nazar, *Energy Environ. Sci.*, 2012, **5**, 9558–9565.
- 69 H. D. Lim, H. Song, J. Kim, H. Gwon, Y. Bae, K. Y. Park, J. Hong, H. Kim, T. Kim, Y. H. Kim, X. Lepro, R. Ovalle-Robles, R. H. Baughman and K. Kang, *Angew. Chem., Int. Ed.*, 2014, **53**, 3926–3931.
- 70 B. Sun, X. D. Huang, S. Q. Chen, P. Munroe and G. X. Wang, *Nano Lett.*, 2014, **14**, 3145–3152.
- 71 F. Wu, X. X. Zhang, T. L. Zhao, R. J. Chen, Y. S. Ye, M. Xie and L. Li, *J. Mater. Chem. A*, 2015, **3**, 17620–17626.
- 72 Y. Cao, S. R. Cai, S. C. Fan, W. Q. Hu, M. S. Zheng and Q. F. Dong, *Faraday Discuss.*, 2014, **172**, 215–221.
- 73 Y. Cao, M. S. Zheng, S. R. Cai, X. D. Lin, C. Yang, W. Q. Hu and Q. F. Dong, *J. Mater. Chem. A*, 2014, **2**, 18736–18741.
- 74 Y. B. Yang, W. Yin, S. T. Wu, X. D. Yang, W. Xia, Y. Shen, Y. H. Huang, A. Y. Cao and Q. Yuan, *ACS Nano*, 2016, **10**, 1240–1248.
- 75 X. Gao, Y. Chen, L. Johnson and P. G. Bruce, *Nat. Mater.*, 2016, **15**, 882–888.
- 76 X. Guo, B. Sun, D. W. Su, X. X. Liu, H. Liu, Y. Wang and G. X. Wang, *Sci. Bull.*, 2017, **62**, 442–452.
- 77 S. J. Kang, T. Mori, S. Narizuka, W. Wilcke and H.-C. Kim, *Nat. Commun.*, 2014, **5**, 3937.
- 78 G. Tan, L. Chong, R. Amine, J. Lu, C. Liu, Y. Yuan, J. Wen, K. He, X. Bi, Y. Guo, H.-H. Wang, R. Shahbazian-Yassar, S. Al Hallaj, D. J. Miller, D. Liu and K. Amine, *Nano Lett.*, 2017, **17**, 2959–2966.
- 79 J. Xie, X. H. Yao, Q. M. Cheng, I. P. Madden, P. Dornath, C. C. Chang, W. Fan and D. W. Wang, *Angew. Chem., Int. Ed.*, 2015, **54**, 4299–4303.
- 80 M. Abu Sayeed, T. Herd and A. P. O'Mullane, *J. Mater. Chem. A*, 2016, **4**, 991–999.
- 81 J. Lu, L. Cheng, K. C. Lau, E. Tyo, X. Luo, J. Wen, D. Miller, R. S. Assary, H.-H. Wang, P. Redfern, H. Wu, J.-B. Park, Y.-K. Sun, S. Vajda, K. Amine and L. A. Curtiss, *Nat. Commun.*, 2014, **5**, 4895.
- 82 S. Zhang, G. Wang, J. Jin, L. Zhang, Z. Wen and J. Yang, *Nano Energy*, 2017, **36**, 186–196.
- 83 J.-J. Xu, Z.-W. Chang, Y. Wang, D.-P. Liu, Y. Zhang and X.-B. Zhang, *Adv. Mater.*, 2016, **28**, 9620–9628.
- 84 J.-J. Xu, Z.-W. Chang, Y.-B. Yin and X.-B. Zhang, *ACS Cent. Sci.*, 2017, **3**, 598–604.
- 85 C. O. Laoire, S. Mukerjee, K. M. Abraham, E. J. Plichta and M. A. Hendrickson, *J. Phys. Chem. C*, 2009, **113**, 20127–20134.
- 86 C. O. Laoire, S. Mukerjee, K. M. Abraham, E. J. Plichta and M. A. Hendrickson, *J. Phys. Chem. C*, 2010, **114**, 9178–9186.
- 87 Z. Peng, S. A. Freunberger, L. J. Hardwick, Y. Chen, V. Giordani, F. Bardé, P. Novák, D. Graham, J.-M. Tarascon and P. G. Bruce, *Angew. Chem., Int. Ed.*, 2011, **50**, 6351–6355.
- 88 Y. Jing and Z. Zhou, *ACS Catal.*, 2015, **5**, 4309–4317.
- 89 C. Z. Shu, B. Li, B. S. Zhang and D. S. Su, *ChemSusChem*, 2015, **8**, 3973–3976.
- 90 J. Shui, F. Du, C. Xue, Q. Li and L. Dai, *ACS Nano*, 2014, **8**, 3015–3022.
- 91 Z. Z. Yang, L. Trahey, Y. Ren, M. K. Y. Chan, C. K. Lin, J. Okasinski and M. M. Thackeray, *J. Mater. Chem. A*, 2015, **3**, 7389–7398.
- 92 L. Trahey, N. K. Karan, M. K. Y. Chan, J. Lu, Y. Ren, J. Greeley, M. Balasubramanian, A. K. Burrell, L. A. Curtiss and M. M. Thackeray, *Adv. Energy Mater.*, 2013, **3**, 75–84.
- 93 P. Zhang, S. Zhang, M. He, J. Lang, A. Ren, S. Xu and X. Yan, *Adv. Sci.*, 2017, **4**, 1700172.
- 94 K. M. Abraham and Z. Jiang, *J. Electrochem. Soc.*, 1996, **143**, 1–5.
- 95 D. Sun, J. Yang and X. Yan, *Chem. Commun.*, 2015, **51**, 2134–2137.
- 96 Z. Peng, Y. Chen, P. G. Bruce and Y. Xu, *Angew. Chem., Int. Ed.*, 2015, **54**, 8165–8168.
- 97 Y.-C. Lu, H. A. Gasteiger, E. Crumlin, R. McGuire and Y. Shao-Horn, *J. Electrochem. Soc.*, 2010, **157**, A1016–A1025.
- 98 Y.-C. Lu, H. A. Gasteiger and Y. Shao-Horn, *J. Am. Chem. Soc.*, 2011, **133**, 19048–19051.
- 99 R. Gao, J. Zhu, X. Xiao, Z. Hu, J. Liu and X. Liu, *J. Phys. Chem. C*, 2015, **119**, 4516–4523.
- 100 R. Black, J. H. Lee, B. Adams, C. A. Mims and L. F. Nazar, *Angew. Chem., Int. Ed.*, 2013, **52**, 392–396.

- 101 R. Gao, L. Liu, Z. Hu, P. Zhang, X. Cao, B. Wang and X. Liu, *J. Mater. Chem. A*, 2015, **3**, 17598–17605.
- 102 Z. Lyu, L. Yang, Y. Luan, X. Renshaw Wang, L. Wang, Z. Hu, J. Lu, S. Xiao, F. Zhang, X. Wang, F. Huo, W. Huang, Z. Hu and W. Chen, *Nano Energy*, 2017, **36**, 68–75.
- 103 G. S. Hutchings, J. Rosen, D. Smiley, G. R. Goward, P. G. Bruce and F. Jiao, *J. Phys. Chem. C*, 2014, **118**, 12617–12624.
- 104 A. Debart, A. J. Paterson, J. Bao and P. G. Bruce, *Angew. Chem., Int. Ed.*, 2008, **47**, 4521–4524.
- 105 B. J. Bergner, A. Schuermann, K. Pepller, A. Garsuch and J. Janek, *J. Am. Chem. Soc.*, 2014, **136**, 15054–15064.
- 106 Y. Hase, J. Seki, T. Shiga, F. Mizuno, H. Nishikoori, H. Iba and K. Takechi, *Chem. Commun.*, 2016, **52**, 12151–12154.
- 107 J. Han, X. Guo, Y. Ito, P. Liu, D. Hojo, T. Aida, A. Hirata, T. Fujita, T. Adschiri, H. Zhou and M. Chen, *Adv. Energy Mater.*, 2016, **6**, 1501870.
- 108 C. Z. Shu, Y. M. Lin and D. S. Su, *J. Mater. Chem. A*, 2016, **4**, 2128–2136.
- 109 J. Herranz, A. Garsuch and H. A. Gasteiger, *J. Phys. Chem. C*, 2012, **116**, 19084–19094.
- 110 R. Cao, E. D. Walter, W. Xu, E. N. Nasybulin, P. Bhattacharya, M. E. Bowden, M. H. Engelhard and J.-G. Zhang, *ChemSusChem*, 2014, **7**, 2436–2440.
- 111 Q. Yu and S. Ye, *J. Phys. Chem. C*, 2015, **119**, 12236–12250.
- 112 D. Sharon, D. Hirsberg, M. Salama, M. Afri, A. A. Frimer, M. Noked, W. Kwak, Y. K. Sun and D. Aurbach, *ACS Appl. Mater. Interfaces*, 2016, **8**, 5300–5307.
- 113 F. S. Gittleson, R. E. Jones, D. K. Ward and M. E. Foster, *Energy Environ. Sci.*, 2017, **10**, 1167–1179.
- 114 L. Johnson, C. Li, Z. Liu, Y. Chen, S. A. Freunberger, P. C. Ashok, B. B. Praveen, K. Dholakia, J.-M. Tarascon and P. G. Bruce, *Nat. Chem.*, 2014, **6**, 1091.
- 115 X. W. Gao, Z. P. Jovanov, Y. H. Chen, L. R. Johnson and P. G. Bruce, *Angew. Chem., Int. Ed.*, 2017, **56**, 6539–6543.
- 116 S. Wu, Y. Qiao, S. Yang, M. Ishida, P. He and H. Zhou, *Nat. Commun.*, 2017, **8**, 15607.
- 117 K. U. Schwenke, M. Metzger, T. Restle, M. Piana and H. A. Gasteiger, *J. Electrochem. Soc.*, 2015, **162**, A573–A584.
- 118 D. G. Kwabi, T. P. Batcho, S. Feng, L. Giordano, C. V. Thompson and Y. Shao-Horn, *Phys. Chem. Chem. Phys.*, 2016, **18**, 24944–24953.
- 119 S. S. Zhang, D. Foster and J. Read, *Electrochim. Acta*, 2011, **56**, 1283–1287.
- 120 S. Matsuda, K. Uosaki and S. Nakanishi, *J. Power Sources*, 2017, **356**, 12–17.
- 121 C. Li, O. Fontaine, S. A. Freunberger, L. Johnson, S. Grugeon, S. Laruelle, P. G. Bruce and M. Armand, *J. Phys. Chem. C*, 2014, **118**, 3393–3401.
- 122 H.-D. Lim, B. Lee, Y. Zheng, J. Hong, J. Kim, H. Gwon, Y. Ko, M. Lee, K. Cho and K. Kang, *Nat. Energy*, 2016, **1**, 16066.
- 123 B. D. Adams, C. Radtke, R. Black, M. L. Trudeau, K. Zaghib and L. F. Nazar, *Energy Environ. Sci.*, 2013, **6**, 1772–1778.
- 124 B. Horstmann, B. Gallant, R. Mitchell, W. G. Bessler, Y. Shao-Horn and M. Z. Bazant, *J. Phys. Chem. Lett.*, 2013, **4**, 4217–4222.
- 125 Y. Zhang, X. Zhang, J. Wang, W. C. McKee, Y. Xu and Z. Peng, *J. Phys. Chem. C*, 2016, **120**, 3690–3698.
- 126 J. Bao, W. Xu, P. Bhattacharya, M. Stewart, J.-G. Zhang and W. Pan, *J. Phys. Chem. C*, 2015, **119**, 14851–14860.
- 127 V. Viswanathan, J. K. Norskov, A. Speidel, R. Scheffler, S. Gowda and A. C. Luntz, *J. Phys. Chem. Lett.*, 2013, **4**, 556–560.
- 128 B. D. McCloskey, D. S. Bethune, R. M. Shelby, T. Mori, R. Scheffler, A. Speidel, M. Sherwood and A. C. Luntz, *J. Phys. Chem. Lett.*, 2012, **3**, 3043–3047.
- 129 S. Kang, Y. Mo, S. P. Ong and G. Ceder, *Chem. Mater.*, 2013, **25**, 3328–3336.
- 130 B. M. Gallant, D. G. Kwabi, R. R. Mitchell, J. Zhou, C. V. Thompson and Y. Shao-Horn, *Energy Environ. Sci.*, 2013, **6**, 2518–2528.
- 131 J. Xie, Q. Dong, I. Madden, X. Yao, Q. Cheng, P. Dornath, W. Fan and D. Wang, *Nano Lett.*, 2015, **15**, 8371–8376.
- 132 G. A. Elia, J. Hassoun, W. J. Kwak, Y. K. Sun, B. Scrosati, F. Mueller, D. Bresser, S. Passerini, P. Oberhumer, N. Tsiouvaras and J. Reiter, *Nano Lett.*, 2014, **14**, 6572–6577.
- 133 C. A. Cao, X. Zhuang, Y. Su, Y. Zhang, F. Zhang, D. Wu and X. Feng, *Polym. Chem.*, 2014, **5**, 2057–2064.
- 134 Y. Cheng, S. Dou, M. Saunders, J. Zhang, J. Pan, S. Y. Wang and S. P. Jiang, *J. Mater. Chem. A*, 2016, **4**, 13881–13889.
- 135 Y. Wang, Z. Liang, Q. Zou, G. Gong and Y.-C. Lu, *J. Phys. Chem. C*, 2016, **120**, 6459–6466.
- 136 S. Ganapathy, B. D. Adams, G. Stenou, M. S. Anastasaki, K. Goubitz, X.-F. Miao, L. F. Nazar and M. Wagemaker, *J. Am. Chem. Soc.*, 2014, **136**, 16335–16344.
- 137 C. Liu, W. R. Brant, R. Younesi, Y. Dong, K. Edstrom, T. Gustafsson and J. Zhu, *ChemSusChem*, 2017, **10**, 1592–1599.
- 138 S. D. Song, W. Xu, J. M. Zheng, L. L. Luo, M. H. Engelhard, M. E. Bowden, B. Liu, C. M. Wang and J. G. Zhang, *Nano Lett.*, 2017, **17**, 1417–1424.
- 139 J. Hassoun, F. Croce, M. Armand and B. Scrosati, *Angew. Chem., Int. Ed.*, 2011, **50**, 2999–3002.
- 140 H. Zheng, D. Xiao, X. Li, Y. Liu, Y. Wu, J. Wang, K. Jiang, C. Chen, L. Gu, X. Wei, Y.-S. Hu, Q. Chen and H. Li, *Nano Lett.*, 2014, **14**, 4245–4249.
- 141 L. Zhong, R. R. Mitchell, Y. Liu, B. M. Gallant, C. V. Thompson, J. Y. Huang, S. X. Mao and Y. Shao-Horn, *Nano Lett.*, 2013, **13**, 2209–2214.
- 142 D. Gröbl, B. Bergner, D. Schröder, J. Janek and W. G. Bessler, *J. Phys. Chem. C*, 2016, **120**, 24623–24636.
- 143 W. Zhang, Y. Shen, D. Sun, Z. M. Huang, J. Zhou, H. Yan and Y. H. Huang, *Nano Energy*, 2016, **30**, 43–51.
- 144 S. H. Lee, W.-J. Kwak and Y.-K. Sun, *J. Mater. Chem. A*, 2017, **5**, 15512–15516.
- 145 D. G. Kwabi, V. S. Bryantsev, T. P. Batcho, D. M. Itkis, C. V. Thompson and Y. Shao-Horn, *Angew. Chem., Int. Ed.*, 2016, **55**, 3129–3134.
- 146 N. Mahne, B. Schafzahl, C. Leybold, M. Leybold, S. Grumm, A. Leitgeb, G. A. Strohmeier, M. Wilkening, O. Fontaine, D. Kramer, C. Slugovc, S. M. Borisov and S. A. Freunberger, *Nat. Energy*, 2017, **2**, 17036.

- 147 D. Zhai, H.-H. Wang, K. C. Lau, J. Gao, P. C. Redfern, F. Kang, B. Li, E. Indacochea, U. Das, H.-H. Sun, H.-J. Sun, K. Amine and L. A. Curtiss, *J. Phys. Chem. Lett.*, 2014, **5**, 2705–2710.
- 148 J. Yang, D. Zhai, H.-H. Wang, K. C. Lau, J. A. Schlueter, P. Du, D. J. Myers, Y.-K. Sun, L. A. Curtiss and K. Amine, *Phys. Chem. Chem. Phys.*, 2013, **15**, 3764–3771.
- 149 D. Xiao, S. Dong, J. Guan, L. Gu, S. Li, N. Zhao, C. Shang, Z. Yang, H. Zheng, C. Chen, R. Xiao, Y.-S. Hu, H. Li, G. Cui and L. Chen, *Adv. Energy Mater.*, 2015, **5**, 1400664.
- 150 J. Hojberg, B. D. McCloskey, J. Hjelm, T. Vegge, K. Johansen, P. Norby and A. C. Luntz, *ACS Appl. Mater. Interfaces*, 2015, **7**, 4039–4047.
- 151 M. D. Radin, C. W. Monroe and D. J. Siegel, *J. Phys. Chem. Lett.*, 2015, **6**, 3017–3022.
- 152 Y.-C. Lu and Y. Shao-Horn, *J. Phys. Chem. Lett.*, 2013, **4**, 93–99.
- 153 V. Viswanathan, K. S. Thygesen, J. S. Hummelshøj, J. K. Nørskov, G. Girishkumar, B. D. McCloskey and A. C. Luntz, *J. Chem. Phys.*, 2011, **135**, 214704.
- 154 S. Lau and L. A. Archer, *Nano Lett.*, 2015, **15**, 5995–6002.
- 155 R. R. Mitchell, B. M. Gallant, Y. Shao-Horn and C. V. Thompson, *J. Phys. Chem. Lett.*, 2013, **4**, 1060–1064.
- 156 O. Gerbig, R. Merkle and J. Maier, *Adv. Mater.*, 2013, **25**, 3129–3133.
- 157 M. D. Radin, C. W. Monroe and D. J. Siegel, *Chem. Mater.*, 2015, **27**, 839–847.
- 158 S. T. Kim, N.-S. Choi, S. Park and J. Cho, *Adv. Energy Mater.*, 2015, **5**, 1401030.
- 159 Q.-C. Liu, J.-J. Xu, D. Xu and X.-B. Zhang, *Nat. Commun.*, 2015, **6**, 7892.
- 160 J.-L. Shui, J. S. Okasinski, C. Chen, J. D. Almer and D.-J. Liu, *ChemSusChem*, 2014, **7**, 543–548.
- 161 K. R. Ryan, L. Trahey, J. S. Okasinski, A. K. Burrell and B. J. Ingram, *J. Mater. Chem. A*, 2013, **1**, 6915–6919.
- 162 M. Olivares-Marin, A. Sorrentino, R.-C. Lee, E. Pereiro, N.-L. Wu and D. Tonti, *Nano Lett.*, 2015, **15**, 6932–6938.
- 163 R. Wen, M. Hong and H. R. Byon, *J. Am. Chem. Soc.*, 2013, **135**, 10870–10876.
- 164 R. Wen and H. R. Byon, *Chem. Commun.*, 2014, **50**, 2628–2631.
- 165 Y. Qiao and S. Ye, *J. Phys. Chem. C*, 2016, **120**, 8033–8047.
- 166 B. D. McCloskey, R. Scheffler, A. Speidel, G. Girishkumar and A. C. Luntz, *J. Phys. Chem. C*, 2012, **116**, 23897–23905.
- 167 V. S. Bryantsev, V. Giordani, W. Walker, M. Blanco, S. Zecevic, K. Sasaki, J. Uddin, D. Addison and G. V. Chase, *J. Phys. Chem. A*, 2011, **115**, 12399–12409.
- 168 D. G. Kwabi, T. P. Batcho, C. V. Amanchukwu, N. Ortiz-Vitoriano, P. Hammond, C. V. Thompson and Y. Shao-Horn, *J. Phys. Chem. Lett.*, 2014, **5**, 2850–2856.
- 169 V. S. Bryantsev and F. Faglioni, *J. Phys. Chem. A*, 2012, **116**, 7128–7138.
- 170 J. Wandt, P. Jakes, J. Granwehr, H. A. Gasteiger and R.-A. Eichel, *Angew. Chem., Int. Ed.*, 2016, **55**, 6892–6895.
- 171 W.-J. Kwak, J.-B. Park, H.-G. Jung and Y.-K. Sun, *ACS Energy Lett.*, 2017, **2**, 2756–2760.
- 172 A. C. Luntz and B. D. McCloskey, *Nat. Energy*, 2017, **2**, 17056.
- 173 Y. Qiao, S. Wu, Y. Sun, S. Guo, J. Yi, P. He and H. Zhou, *ACS Energy Lett.*, 2017, **2**, 1869–1878.
- 174 M. Tulodziecki, G. M. Leverick, C. V. Amanchukwu, Y. Katayama, D. G. Kwabi, F. Barde, P. T. Hammond and Y. Shao-Horn, *Energy Environ. Sci.*, 2017, **10**, 1828–1842.
- 175 Y. Shen, W. Zhang, S. L. Chou and S. X. Dou, *Science*, 2016, 352.
- 176 C. Ling, R. Zhang, K. Takechi and F. Mizuno, *J. Phys. Chem. C*, 2014, **118**, 26591–26598.
- 177 G. Y. Zheng, S. W. Lee, Z. Liang, H. W. Lee, K. Yan, H. B. Yao, H. T. Wang, W. Y. Li, S. Chu and Y. Cui, *Nat. Nanotechnol.*, 2014, **9**, 618–623.
- 178 J. B. Goodenough and Y. Kim, *Chem. Mater.*, 2010, **22**, 587–603.
- 179 S. Choudhury, C. T.-C. Wan, W. I. Al Sadat, Z. Tu, S. Lau, M. J. Zachman, L. F. Kourkoutis and L. A. Archer, *Sci. Adv.*, 2017, **3**, 1602809.
- 180 E. Yoo and H. S. Zhou, *ACS Appl. Mater. Interfaces*, 2017, **9**, 21307–21313.
- 181 C. Wu, C. B. Liao, T. R. Li, Y. Q. Shi, J. S. Luo, L. Li and J. Yang, *J. Mater. Chem. A*, 2016, **4**, 15189–15196.
- 182 J. Steiger, D. Kramer and R. Mönig, *J. Power Sources*, 2014, **261**, 112–119.
- 183 G. A. Elia, J. B. Park, B. Scrosati, Y. K. Sun and J. Hassoun, *Electrochem. Commun.*, 2013, **34**, 250–253.
- 184 I. C. Jang, Y. Hidaka and T. Ishihara, *J. Power Sources*, 2013, **244**, 606–609.
- 185 U. R. Farooqui, A. L. Ahmad and N. A. Hamid, *Renewable Sustainable Energy Rev.*, 2017, **77**, 1114–1129.
- 186 D. J. Lee, H. Lee, Y. J. Kim, J. K. Park and H. T. Kim, *Adv. Mater.*, 2016, **28**, 857–863.
- 187 Q.-C. Liu, J.-J. Xu, S. Yuan, Z.-W. Chang, D. Xu, Y.-B. Yin, L. Li, H.-X. Zhong, Y.-S. Jiang, J.-M. Yan and X.-B. Zhang, *Adv. Mater.*, 2015, **27**, 5241–5247.
- 188 S.-K. Jeong, H.-Y. Seo, D.-H. Kim, H.-K. Han, J.-G. Kim, Y. B. Lee, Y. Iriyama, T. Abe and Z. Ogumi, *Electrochem. Commun.*, 2008, **10**, 635–638.
- 189 J. Qian, W. A. Henderson, W. Xu, P. Bhattacharya, M. Engelhard, O. Borodin and J.-G. Zhang, *Nat. Commun.*, 2015, **6**, 6362.
- 190 D. Aurbach, E. Pollak, R. Elazari, G. Salitra, C. S. Kelley and J. Affinito, *J. Electrochem. Soc.*, 2009, **156**, A694–A702.
- 191 X. Liang, Z. Y. Wen, Y. Liu, M. F. Wu, J. Jin, H. Zhang and X. W. Wu, *J. Power Sources*, 2011, **196**, 9839–9843.
- 192 G. Cheng, Y. Gao, T. Wang, Y. Sun, Z. Wei, L. Li, L. Ren, Y. Guo, X. Hu, Y. Lu, X. Wang, G. Liu, C. Zhang, J. Yu, Q. Pan-Hammarström, L. Hammarström, X. Wu, N. Li and Y. Zhao, *Nat. Commun.*, 2013, **4**, 1337.
- 193 B. Sun, X. D. Huang, S. Q. Chen, J. Q. Zhang and G. X. Wang, *RSC Adv.*, 2014, **4**, 11115–11120.
- 194 J. Uddin, V. S. Bryantsev, V. Giordani, W. Walker, G. V. Chase and D. Addison, *J. Phys. Chem. Lett.*, 2013, **4**, 3760–3765.

- 195 B. G. Kim, J. S. Kim, J. Min, Y. H. Lee, J. H. Choi, M. C. Jang, S. A. Freunberger and J. W. Choi, *Adv. Funct. Mater.*, 2016, **26**, 1747–1756.
- 196 S. J. Kang, T. Mori, J. Suk, D. W. Kim, Y. Kang, W. Wilcke and H.-C. Kim, *J. Mater. Chem. A*, 2014, **2**, 9970–9974.
- 197 H. Lee, Y. J. Kim, D. J. Lee, J. Song, Y. M. Lee, H. T. Kim and J. K. Park, *J. Mater. Chem. A*, 2014, **2**, 11891–11898.
- 198 Z. Guo, X. Dong, Y. Wang and Y. Xia, *Chem. Commun.*, 2015, **51**, 676–678.
- 199 G. A. Elia, D. Bresser, J. Reiter, P. Oberhumer, Y. K. Sun, B. Scrosati, S. Passerini and J. Hassoun, *ACS Appl. Mater. Interfaces*, 2015, **7**, 22638–22643.
- 200 W.-J. Kwak, H.-J. Shin, J. Reiter, N. Tsiouvaras, J. Hassoun, S. Passerini, B. Scrosati and Y.-K. Sun, *J. Mater. Chem. A*, 2016, **4**, 10467–10471.
- 201 S. C. Wu, K. Zhu, J. Tang, K. M. Liao, S. Y. Bai, J. Yi, Y. Yamauchi, M. Ishida and H. S. Zhou, *Energy Environ. Sci.*, 2016, **9**, 3262–3271.
- 202 J. Yin, J. M. Carlin, J. Kim, Z. Li, J. H. Park, B. Patel, S. Chakrapani, S. Lee and Y. L. Joo, *Adv. Energy Mater.*, 2015, **5**, 1401412.
- 203 K. R. Yoon, K. Shin, J. Park, S.-H. Cho, C. Kim, J.-W. Jung, J. Y. Cheong, H. R. Byon, H. M. Lee and I.-D. Kim, *ACS Nano*, 2018, **12**, 128–139.
- 204 S. M. Xu, Q. C. Zhu, J. Long, H. H. Wang, X. F. Xie, K. X. Wang and J. S. Chen, *Adv. Funct. Mater.*, 2016, **26**, 1365–1374.
- 205 Y. Lin, B. Moitoso, C. Martinez-Martinez, E. D. Walsh, S. D. Lacey, J. W. Kim, L. M. Dai, L. B. Hu and J. W. Connell, *Nano Lett.*, 2017, **17**, 3252–3260.
- 206 W. J. Kwak, K. C. Lau, C. D. Shin, K. Amine, L. A. Curtiss and Y. K. Sun, *ACS Nano*, 2015, **9**, 4129–4137.
- 207 D. F. Wu, Z. Y. Guo, X. B. Yin, Q. Q. Pang, B. B. Tu, L. J. Zhang, Y. G. Wang and Q. W. Li, *Adv. Mater.*, 2014, **26**, 3258–3262.
- 208 H. D. Lim, H. Song, H. Gwon, K. Y. Park, J. Kim, Y. Bae, H. Kim, S. K. Jung, T. Kim, Y. H. Kim, X. Lepro, R. Ovalle-Robles, R. H. Baughman and K. Kang, *Energy Environ. Sci.*, 2013, **6**, 3570–3575.
- 209 W. C. Yang, Z. Y. Qian, C. Y. Du, C. Hua, P. J. Zuo, X. Q. Cheng, Y. L. Ma and G. P. Yin, *Carbon*, 2017, **118**, 139–147.
- 210 J. Xiao, D. H. Wang, W. Xu, D. Y. Wang, R. E. Williford, J. Liu and J. G. Zhang, *J. Electrochem. Soc.*, 2010, **157**, A487–A492.
- 211 M. Mirzaeian and P. J. Hall, *Electrochim. Acta*, 2009, **54**, 7444–7451.
- 212 Y. N. Zhang, H. M. Zhang, J. Li, M. R. Wang, H. J. Nie and F. X. Zhang, *J. Power Sources*, 2013, **240**, 390–396.
- 213 B. Sun, S. Q. Chen, H. Liu and G. X. Wang, *Adv. Funct. Mater.*, 2015, **25**, 4436–4444.
- 214 Z. Guo, D. Zhou, X. Dong, Z. Qiu, Y. Wang and Y. Xia, *Adv. Mater.*, 2013, **25**, 5668–5672.
- 215 Y. L. Zhao, L. Xu, L. Q. Mai, C. H. Han, Q. Y. An, X. Xu, X. Liu and Q. J. Zhang, *Proc. Natl. Acad. Sci. U. S. A.*, 2012, **109**, 19569–19574.
- 216 J.-J. Xu, Z.-L. Wang, D. Xu, L.-L. Zhang and X.-B. Zhang, *Nat. Commun.*, 2013, **4**, 2438.
- 217 P. Zhang, M. He, S. Xu and X. B. Yan, *J. Mater. Chem. A*, 2015, **3**, 10811–10818.
- 218 B. M. Gallant, R. R. Mitchell, D. G. Kwabi, J. G. Zhou, L. Zuin, C. V. Thompson and Y. Shao-Horn, *J. Phys. Chem. C*, 2012, **116**, 20800–20805.
- 219 B. D. McCloskey, A. Speidel, R. Scheffler, D. C. Miller, V. Viswanathan, J. S. Hummelshoj, J. K. Nørskov and A. C. Luntz, *J. Phys. Chem. Lett.*, 2012, **3**, 997–1001.
- 220 J. Xiao, D. H. Mei, X. L. Li, W. Xu, D. Y. Wang, G. L. Graff, W. D. Bennett, Z. M. Nie, L. V. Saraf, I. A. Aksay, J. Liu and J. G. Zhang, *Nano Lett.*, 2011, **11**, 5071–5078.
- 221 W. Zhou, H. Z. Zhang, H. J. Nie, Y. W. Ma, Y. N. Zhang and H. M. Zhang, *ACS Appl. Mater. Interfaces*, 2015, **7**, 3389–3397.
- 222 R. A. Wong, A. Dutta, C. Z. Yang, K. Yamanaka, T. Ohta, A. Nakao, K. Waki and H. R. Byon, *Chem. Mater.*, 2016, **28**, 8006–8015.
- 223 M. M. Storm, M. Overgaard, R. Younesi, N. E. A. Reeler, T. Vosch, U. G. Nielsen, K. Edstrom and P. Norby, *Carbon*, 2015, **85**, 233–244.
- 224 J. K. Papp, J. D. Forster, C. M. Burke, H. W. Kim, A. C. Luntz, R. M. Shelby, J. J. Urban and B. D. McCloskey, *J. Phys. Chem. Lett.*, 2017, **8**, 1169–1174.
- 225 R. Black, S. H. Oh, J. H. Lee, T. Yim, B. Adams and L. F. Nazar, *J. Am. Chem. Soc.*, 2012, **134**, 2902–2905.
- 226 S. F. Tong, M. B. Zheng, Y. Lu, Z. X. Lin, X. P. Zhang, P. He and H. S. Zhou, *Chem. Commun.*, 2015, **51**, 7302–7304.
- 227 G. Y. Zhao, L. Zhang, J. X. Lv, C. L. Li and K. N. Sun, *J. Mater. Chem. A*, 2016, **4**, 1399–1407.
- 228 C. J. Liu, R. Younesi, C. W. Tai, M. Valvo, K. Edstrom, T. Gustafsson and J. F. Zhu, *J. Mater. Chem. A*, 2016, **4**, 9767–9773.
- 229 Z. L. Wang, D. Xu, J. J. Xu, L. L. Zhang and X. B. Zhang, *Adv. Funct. Mater.*, 2012, **22**, 3699–3705.
- 230 W. Y. Zhang, J. X. Zhu, H. X. Ang, Y. Zeng, N. Xiao, Y. B. Gao, W. L. Liu, H. H. Hng and Q. Y. Yan, *Nanoscale*, 2013, **5**, 9651–9658.
- 231 D. Y. Kim, M. Kim, D. W. Kim, J. Suk, O. O. Park and Y. Kang, *Carbon*, 2015, **93**, 625–635.
- 232 D. Y. Kim, M. Kim, D. W. Kim, J. Suk, J. J. Park, O. O. Park and Y. Kang, *Carbon*, 2016, **100**, 265–272.
- 233 M. I. Ionescu, *RSC Adv.*, 2017, **7**, 30365–30369.
- 234 Q. C. Zhu, F. H. Du, S. M. Xu, Z. K. Wang, K. X. Wang and J. S. Chen, *ACS Appl. Mater. Interfaces*, 2016, **8**, 3868–3873.
- 235 Y. Chen, F. J. Li, D. M. Tang, Z. L. Jian, C. Liu, D. Golberg, A. Yamada and H. S. Zhou, *J. Mater. Chem. A*, 2013, **1**, 13076–13081.
- 236 A. Abdelhafiz, A. Vitale, C. Joiner, E. Vogel and F. M. Alamgir, *ACS Appl. Mater. Interfaces*, 2015, **7**, 6180–6188.
- 237 Y. Zhao, R. Nakamura, K. Kamiya, S. Nakanishi and K. Hashimoto, *Nat. Commun.*, 2013, **4**, 2390.
- 238 W. B. Luo, S. L. Chou, J. Z. Wang and H. K. Liu, *J. Mater. Chem. A*, 2015, **3**, 18395–18399.

- 239 W. B. Luo, S. L. Chou, J. Z. Wang, Y. C. Zhai and H. K. Liu, *Small*, 2015, **11**, 2817–2824.
- 240 C. T. Zhao, C. Yu, S. H. Liu, J. Yang, X. M. Fan, H. W. Huang and J. S. Qiu, *Adv. Funct. Mater.*, 2015, **25**, 6913–6920.
- 241 Z. Zhang, J. Bao, C. He, Y. N. Chen, J. P. Wei and Z. Zhou, *Adv. Funct. Mater.*, 2014, **24**, 6826–6833.
- 242 J. H. Kim, A. G. Kannan, H. S. Woo, D. G. Jin, W. Kim, K. Ryu and D. W. Kim, *J. Mater. Chem. A*, 2015, **3**, 18456–18465.
- 243 H. R. Jiang, T. S. Zhao, L. Shi, P. Tan and L. An, *J. Phys. Chem. C*, 2016, **120**, 6612–6618.
- 244 F. Wu, Y. Xing, L. Li, J. Qian, W. J. Qu, J. G. Wen, D. Miller, Y. S. Ye, R. J. Chen, K. Amine and J. Lu, *ACS Appl. Mater. Interfaces*, 2016, **8**, 23635–23645.
- 245 Y. Y. Li, L. Wang, X. M. He, B. Tang, Y. X. Jin and J. L. Wang, *J. Energy Chem.*, 2016, **25**, 131–135.
- 246 Y. Yang, W. Liu, N. Wu, X. Wang, T. Zhang, L. Chen, R. Zeng, Y. Wang, J. Lu, L. Fu, L. Xiao and L. Zhuang, *ACS Appl. Mater. Interfaces*, 2017, **9**, 19800–19806.
- 247 C. J. Bondue, P. Reinsberg, A. A. Abd-El-Latif and H. Baltruschat, *Phys. Chem. Chem. Phys.*, 2015, **17**, 25593–25606.
- 248 X. Guo, B. Sun, J. Q. Zhang, H. Liu and G. X. Wang, *J. Mater. Chem. A*, 2016, **4**, 9774–9780.
- 249 Z. Q. Peng, S. A. Freunberger, Y. H. Chen and P. G. Bruce, *Science*, 2012, **337**, 563–566.
- 250 X. Guo, J. Han, P. Liu, L. Chen, Y. Ito, Z. Jian, T. Jin, A. Hirata, F. Li, T. Fujita, N. Asao, H. Zhou and M. Chen, *Sci. Rep.*, 2016, **6**, 33466.
- 251 D. Su, S. Dou and G. Wang, *NPG Asia Mater.*, 2015, **7**, e155.
- 252 F. F. Tu, J. P. Hu, J. Xie, G. S. Cao, S. C. Zhang, S. A. Yang, X. B. Zhao and H. Y. Yang, *Adv. Funct. Mater.*, 2016, **26**, 7725–7732.
- 253 G. Wang, F. Tu, J. Xie, G. Du, S. Zhang, G. Cao and X. Zhao, *Adv. Sci.*, 2016, **3**, 1500339.
- 254 G. Y. Zhao, L. Zhang, Y. N. Niu, K. N. Sun and D. Rooney, *J. Mater. Chem. A*, 2016, **4**, 4009–4014.
- 255 K. N. Jung, A. Riaz, S. B. Lee, T. H. Lim, S. J. Park, R. H. Song, S. Yoon, K. H. Shin and J. W. Lee, *J. Power Sources*, 2013, **244**, 328–335.
- 256 X. Y. Lu, Y. Yin, L. Zhang, L. X. Xi, S. Oswald, J. W. Deng and O. G. Schmidt, *Nano Energy*, 2016, **30**, 69–76.
- 257 X. Y. Lu, W. P. Si, X. L. Sun, B. Liu, L. Zhang, C. L. Yan and O. G. Schmidt, *Nano Energy*, 2016, **19**, 428–436.
- 258 H. Cao, X. H. Zhu, D. Wang, Z. K. Sun, Y. H. Deng, X. F. Hou and D. Y. Zhao, *ACS Catal.*, 2015, **5**, 27–33.
- 259 G. Y. Zhao, R. W. Mo, B. Y. Wang, L. Zhang and K. N. Sun, *Chem. Mater.*, 2014, **26**, 2551–2556.
- 260 S. C. Ma, Y. Wu, J. W. Wang, Y. L. Zhang, Y. T. Zhang, X. X. Yan, Y. Wei, P. Liu, J. P. Wang, K. L. Jiang, S. S. Fan, Y. Xu and Z. Q. Peng, *Nano Lett.*, 2015, **15**, 8084–8090.
- 261 C. T. Zhao, C. Yu, M. N. Banis, Q. Sun, M. D. Zhang, X. Li, Y. L. Liu, Y. Zhao, H. W. Huang, S. F. Li, X. T. Han, B. W. Xiao, Z. X. Song, R. Y. Li, J. S. Qiu and X. L. Sun, *Nano Energy*, 2017, **34**, 399–407.
- 262 H. G. Jung, Y. S. Jeong, J. B. Park, Y. K. Sun, B. Scrosati and Y. J. Lee, *ACS Nano*, 2013, **7**, 3532–3539.
- 263 E. Yilmaz, C. Yogi, K. Yamanaka, T. Ohta and H. R. Byon, *Nano Lett.*, 2013, **13**, 4679–4684.
- 264 Z. L. Jian, P. Liu, F. J. Li, P. He, X. W. Guo, M. W. Chen and H. S. Zhou, *Angew. Chem., Int. Ed.*, 2014, **53**, 442–446.
- 265 L. Shi, A. Xu and T. S. Zhao, *J. Phys. Chem. C*, 2016, **120**, 6356–6362.
- 266 Z. Q. Liu, N. N. Feng, Z. H. Shen, F. J. Li, P. He, H. G. Zhang and H. S. Zhou, *ChemSusChem*, 2017, **10**, 2714–2719.
- 267 X. D. Lin, Y. Cao, S. R. Cai, J. M. Fan, Y. J. Li, Q. H. Wu, M. S. Zheng and Q. F. Dong, *J. Mater. Chem. A*, 2016, **4**, 7788–7794.
- 268 J. Jiang, P. He, S. Tong, M. Zheng, Z. Lin, X. Zhang, Y. Shi and H. Zhou, *NPG Asia Mater.*, 2016, **8**, e239.
- 269 H. Cheng and K. Scott, *Electrochim. Acta*, 2014, **116**, 51–58.
- 270 D. Su, D. Han Seo, Y. Ju, Z. Han, K. Ostrikov, S. Dou, H.-J. Ahn, Z. Peng and G. Wang, *NPG Asia Mater.*, 2016, **8**, e286.
- 271 K. R. Yoon, G. Y. Lee, J. W. Jung, N. H. Kim, S. O. Kim and I. D. Kim, *Nano Lett.*, 2016, **16**, 2076–2083.
- 272 W. Cheng and R. G. Compton, *Angew. Chem., Int. Ed.*, 2015, **54**, 7082–7085.
- 273 P. Tan, Z. H. Wei, W. Shyy, T. S. Zhao and X. B. Zhu, *Energy Environ. Sci.*, 2016, **9**, 1783–1793.
- 274 J. B. Park, I. Belharouak, Y. J. Lee and Y. K. Sun, *J. Power Sources*, 2015, **295**, 299–304.
- 275 Y. Chang, S. Dong, Y. Ju, D. Xiao, X. Zhou, L. Zhang, X. Chen, C. Shang, L. Gu, Z. Peng and G. Cui, *Adv. Sci.*, 2015, **2**, 1500092.
- 276 L. Y. Chen, X. W. Guo, J. H. Han, P. Liu, X. D. Xu, A. Hirata and M. W. Chen, *J. Mater. Chem. A*, 2015, **3**, 3620–3626.
- 277 J. B. Park, X. Y. Luo, J. Lu, C. D. Shin, C. S. Yoon, K. Amine and Y. K. Sun, *J. Phys. Chem. C*, 2015, **119**, 15036–15040.
- 278 W. J. Kwak, H. G. Jung, S. H. Lee, J. B. Park, D. Aurbach and Y. K. Sun, *J. Power Sources*, 2016, **311**, 49–56.
- 279 K. Guo, Y. Li, T. Yuan, X. W. Dong, X. W. Li and H. Yang, *J. Solid State Electrochem.*, 2015, **19**, 821–829.
- 280 F. Wu, Y. Xing, X. Q. Zeng, Y. F. Yuan, X. Y. Zhang, R. Shahbazian-Yassar, J. G. Wen, D. J. Miller, L. Li, R. J. Chen, J. Lu and K. Amine, *Adv. Funct. Mater.*, 2016, **26**, 7626–7633.
- 281 W. Ai, Z. Luo, J. Jiang, J. Zhu, Z. Du, Z. Fan, L. Xie, H. Zhang, W. Huang and T. Yu, *Adv. Mater.*, 2014, **26**, 6186–6192.
- 282 Y. S. Jeong, J. B. Park, H. G. Jung, J. Kirn, X. Y. Luo, J. Lu, L. Curtiss, K. Amine, Y. K. Sun, B. Scrosati and Y. J. Lee, *Nano Lett.*, 2015, **15**, 4261–4268.
- 283 F. S. Gittleson, W. H. Ryu, M. Schwab, X. Tong and A. D. Taylor, *Chem. Commun.*, 2016, **52**, 6605–6608.
- 284 B. D. McCloskey, R. Scheffler, A. Speidel, D. S. Bethune, R. M. Shelby and A. C. Luntz, *J. Am. Chem. Soc.*, 2011, **133**, 18038–18041.

- 285 M. Aykol, S. Kim, V. I. Hegde, D. Snyder, Z. Lu, S. Hao, S. Kirklin, D. Morgan and C. Wolverton, *Nat. Commun.*, 2016, **7**, 13779.
- 286 M. H. Lu, D. Y. Chen, C. H. Xu, Y. Zhan and J. Y. Lee, *Nanoscale*, 2015, **7**, 12906–12912.
- 287 S. M. Cho, J. H. Yom, S. W. Hwang, I. W. Seong, J. Kim, S. H. Cho and W. Y. Yoon, *J. Power Sources*, 2017, **342**, 427–434.
- 288 W.-B. Luo, T. V. Pham, H.-P. Guo, H.-K. Liu and S.-X. Dou, *ACS Nano*, 2017, **11**, 1747–1754.
- 289 W. B. Luo, X. W. Gao, D. Q. Shi, S. L. Chou, J. Z. Wang and H. K. Liu, *Small*, 2016, **12**, 3031–3038.
- 290 M. Lee, Y. Hwang, K. H. Yun and Y. C. Chung, *J. Power Sources*, 2015, **288**, 296–301.
- 291 D. M. Jang, I. H. Kwak, E. L. Kwon, C. S. Jung, H. S. Im, K. Park and J. Park, *J. Phys. Chem. C*, 2015, **119**, 1921–1927.
- 292 H. J. Kim, S. C. Jung, Y. K. Han and S. H. Oh, *Nano Energy*, 2015, **13**, 679–686.
- 293 B. G. Kim, C. Jo, J. Shin, Y. Mun, J. Lee and J. W. Choi, *ACS Nano*, 2017, **11**, 1736–1746.
- 294 D. W. Choi, D. H. Wang, I. T. Bae, J. Xiao, Z. M. Nie, W. Wang, V. V. Viswanathan, Y. J. Lee, J. G. Zhang, G. L. Graff, Z. G. Yang and J. Liu, *Nano Lett.*, 2010, **10**, 2799–2805.
- 295 O. Oloniyo, S. Kumar and K. Scott, *J. Electron. Mater.*, 2012, **41**, 921–927.
- 296 J. Read, *J. Electrochem. Soc.*, 2002, **149**, A1190–A1195.
- 297 S. K. Ramchandra, C. Min-Seung, Y. Kwi-Sub, K. Tae-Sin and P. Chan-Jin, *Nanotechnology*, 2011, **22**, 395402.
- 298 M. Salehi and Z. Shariatnia, *Electrochim. Acta*, 2016, **188**, 428–440.
- 299 Y. Qin, J. Lu, P. Du, Z. Chen, Y. Ren, T. Wu, J. T. Miller, J. Wen, D. J. Miller, Z. Zhang and K. Amine, *Energy Environ. Sci.*, 2013, **6**, 519–531.
- 300 J. X. Li, N. Wang, Y. Zhao, Y. H. Ding and L. H. Guan, *Electrochem. Commun.*, 2011, **13**, 698–700.
- 301 Y. Cao, Z. K. Wei, J. He, J. Zang, Q. Zhang, M. S. Zheng and Q. F. Dong, *Energy Environ. Sci.*, 2012, **5**, 9765–9768.
- 302 G. Zhou, H. Liu, Z. Ma, H. Li and Y. Pei, *J. Phys. Chem. C*, 2017, **121**, 16193–16200.
- 303 S. Chen, J. Duan, P. Bian, Y. Tang, R. Zheng and S.-Z. Qiao, *Adv. Energy Mater.*, 2015, **5**, 1500936.
- 304 M. R. Gao, J. Jiang and S. H. Yu, *Small*, 2012, **8**, 13–27.
- 305 Y. P. Zheng, K. Song, J. Jung, C. Z. Li, Y. U. Heo, M. S. Park, M. Cho, Y. M. Kang and K. Cho, *Chem. Mater.*, 2015, **27**, 3243–3249.
- 306 P. C. Gao, A. H. Lu and W. C. Li, *J. Power Sources*, 2011, **196**, 4095–4101.
- 307 E. M. Benbow, S. P. Kelly, L. Zhao, J. W. Reutenauer and S. L. Suib, *J. Phys. Chem. C*, 2011, **115**, 22009–22017.
- 308 C. Cao, J. Xie, S. C. Zhang, B. Pan, G. S. Cao and X. B. Zhao, *J. Mater. Chem. A*, 2017, **5**, 6747–6755.
- 309 P. Zhang, D. F. Sun, M. He, J. W. Lang, S. Xu and X. B. Yan, *ChemSusChem*, 2015, **8**, 1972–1979.
- 310 P. W. Dunk, N. K. Kaiser, C. L. Hendrickson, J. P. Quinn, C. P. Ewels, Y. Nakanishi, Y. Sasaki, H. Shinohara, A. G. Marshall and H. W. Kroto, *Nat. Commun.*, 2012, **3**, 855.
- 311 P. Tan, L. Shi, W. Shyy and T. S. Zhao, *Energy Technol.*, 2016, **4**, 393–400.
- 312 Z. Liu, L. R. De Jesus, S. Banerjee and P. P. Mukherjee, *ACS Appl. Mater. Interfaces*, 2016, **8**, 23028–23036.
- 313 J. J. Chen, M. J. Vacchio, S. J. Wang, N. Chernova, P. Y. Zavalij and M. S. Whittingham, *Solid State Ionics*, 2008, **178**, 1676–1693.
- 314 X. C. Duan, J. Q. Yang, H. Y. Gao, J. M. Ma, L. F. Jiao and W. J. Zheng, *CrystEngComm*, 2012, **14**, 4196–4204.
- 315 J. Wang, L. L. Liu, C. M. Subramaniam, S. L. Chou, H. K. Liu and J. Z. Wang, *J. Appl. Electrochem.*, 2016, **46**, 869–878.
- 316 S. Liu, Y. Zhu, J. Xie, Y. Huo, H. Y. Yang, T. Zhu, G. Cao, X. Zhao and S. Zhang, *Adv. Energy Mater.*, 2014, **4**, 1301960.
- 317 X. P. Han, F. Y. Cheng, C. C. Chen, Y. X. Hu and J. Chen, *Nano Res.*, 2015, **8**, 156–164.
- 318 X. F. Hu, X. P. Han, Y. X. Hu, F. Y. Cheng and J. Chen, *Nanoscale*, 2014, **6**, 3522–3525.
- 319 X. F. Hu, F. Y. Cheng, X. P. Han, T. R. Zhang and J. Chen, *Small*, 2015, **11**, 809–813.
- 320 Z. H. Wei, T. S. Zhao, X. B. Zhu and P. Tan, *J. Power Sources*, 2016, **306**, 724–732.
- 321 W.-B. Luo, S.-L. Chou, W. Jia-Zhao, Y.-C. Zhai and H.-K. Liu, *Sci. Rep.*, 2015, **5**, 8012.
- 322 D. Wu, Z. Guo, X. Yin, Q. Pang, B. Tu, L. Zhang, Y.-G. Wang and Q. Li, *Adv. Mater.*, 2014, **26**, 3258–3262.
- 323 Y. X. Hu, T. R. Zhang, F. Y. Cheng, Q. Zhao, X. P. Han and J. Chen, *Angew. Chem., Int. Ed.*, 2015, **54**, 4338–4343.
- 324 Y. Q. Zhu, S. H. Liu, C. Jin, S. Y. Bie, R. Z. Yang and J. Wu, *J. Mater. Chem. A*, 2015, **3**, 13563–13567.
- 325 F. Jiao and H. Frei, *Angew. Chem., Int. Ed.*, 2009, **48**, 1841–1844.
- 326 S. Mao, Z. H. Wen, T. Z. Huang, Y. Hou and J. H. Chen, *Energy Environ. Sci.*, 2014, **7**, 609–616.
- 327 P. Abellan, B. L. Mehdi, L. R. Parent, M. Gu, C. Park, W. Xu, Y. H. Zhang, I. Arslan, J. G. Zhang, C. M. Wang, J. E. Evans and N. D. Browning, *Nano Lett.*, 2014, **14**, 1293–1299.
- 328 W. P. Ni, S. M. Liu, Y. Q. Fei, Y. D. He, X. Y. Ma, L. J. Lu and Y. Q. Deng, *J. Mater. Chem. A*, 2016, **4**, 7746–7753.
- 329 A. Debart, J. Bao, G. Armstrong and P. G. Bruce, *J. Power Sources*, 2007, **174**, 1177–1182.
- 330 P. E. Karthik, K. A. Raja, S. S. Kumar, K. L. N. Phani, Y. P. Liu, S. X. Guo, J. Zhang and A. M. Bond, *RSC Adv.*, 2015, **5**, 3196–3199.
- 331 P. Zhang, R. T. Wang, M. He, J. W. Lang, S. Xu and X. B. Yan, *Adv. Funct. Mater.*, 2016, **26**, 1354–1364.
- 332 J. Tang, S. C. Wu, T. Wang, H. Gong, H. B. Zhang, S. M. Alshehri, T. Ahamad, H. S. Zhou and Y. Yamauchi, *ACS Appl. Mater. Interfaces*, 2016, **8**, 2796–2804.
- 333 D. Su, S. Dou and G. Wang, *Sci. Rep.*, 2014, **4**, 5767.
- 334 R. Gao, Z. Y. Li, X. L. Zhang, J. C. Zhang, Z. B. Hu and X. F. Liu, *ACS Catal.*, 2016, **6**, 400–406.
- 335 W. H. Ryu, T. H. Yoon, S. H. Song, S. Jeon, Y. J. Park and I. D. Kim, *Nano Lett.*, 2013, **13**, 4190–4197.

- 336 C. Shang, S. Dong, P. Hu, J. Guan, D. Xiao, X. Chen, L. Zhang, L. Gu, G. Cui and L. Chen, *Sci. Rep.*, 2015, **5**, 8335.
- 337 K. Song, E. Cho and Y. M. Kang, *ACS Catal.*, 2015, **5**, 5116–5122.
- 338 J. Z. Zhu, X. D. Ren, J. J. Liu, W. Q. Zhang and Z. Y. Wen, *ACS Catal.*, 2015, **5**, 73–81.
- 339 J. Zhang, Z. Y. Lyu, F. Zhang, L. J. Wang, P. Xiao, K. D. Yuan, M. Lai and W. Chen, *J. Mater. Chem. A*, 2016, **4**, 6350–6356.
- 340 Q. C. Liu, J. J. Xu, Z. W. Chang and X. B. Zhang, *J. Mater. Chem. A*, 2014, **2**, 6081–6085.
- 341 M. He, P. Zhang, S. Xu and X. B. Yan, *ACS Appl. Mater. Interfaces*, 2016, **8**, 23713–23720.
- 342 Y. M. Cui, Z. Y. Wen and Y. Liu, *Energy Environ. Sci.*, 2011, **4**, 4727–4734.
- 343 G. Y. Zhao, Z. M. Xu and K. N. Sun, *J. Mater. Chem. A*, 2013, **1**, 12862–12867.
- 344 A. Riaz, K. N. Jung, W. Chang, S. B. Lee, T. H. Lim, S. J. Park, R. H. Song, S. Yoon, K. H. Shin and J. W. Lee, *Chem. Commun.*, 2013, **49**, 5984–5986.
- 345 C. Shen, Z. Y. Wen, F. Wang, T. Wu and X. W. Wu, *ACS Catal.*, 2016, **6**, 4149–4153.
- 346 S. F. Tong, M. B. Zheng, Y. Lu, Z. X. Lin, J. Li, X. P. Zhang, Y. Shi, P. He and H. S. Zhou, *J. Mater. Chem. A*, 2015, **3**, 16177–16182.
- 347 S. Ganapathy, Z. L. Li, M. S. Anastasaki, S. Basak, X. F. Miao, K. Goubitz, H. W. Zandbergen, F. M. Mulder and M. Wagemaker, *J. Phys. Chem. C*, 2016, **120**, 18421–18427.
- 348 X. F. Hu, Z. Q. Zhu, F. Y. Cheng, Z. L. Tao and J. Chen, *Nanoscale*, 2015, **7**, 11833–11840.
- 349 S. Lee, G.-H. Lee, H. J. Lee, M. A. Dar and D.-W. Kim, *Sci. Rep.*, 2017, **7**, 9495.
- 350 Z. Wang, Y. You, J. Yuan, Y.-X. Yin, Y. T. Li, S. Xin and D. Zhang, *ACS Appl. Mater. Inter.*, 2016, **8**, 6520–6528.
- 351 W. Y. Zhang, Y. Zeng, C. Xu, H. T. Tan, W. L. Liu, J. X. Zhu, N. Xiao, H. H. Hng, J. Ma, H. E. Hoster, R. Yazami and Q. Y. Yan, *RSC Adv.*, 2012, **2**, 8508–8514.
- 352 F. Wang, X. W. Wu, C. Shen and Z. Y. Wen, *J. Solid State Electrochem.*, 2016, **20**, 1831–1836.
- 353 J. Lu, Y. Qin, P. Du, X. Y. Luo, T. P. Wu, Y. Ren, J. G. Wen, D. J. Miller, J. T. Miller and K. Amine, *RSC Adv.*, 2013, **3**, 8276–8285.
- 354 W. T. Geng and T. Ohno, *J. Phys. Chem. C*, 2015, **119**, 1024–1031.
- 355 J. Yang, D. Ma, Y. Li, P. Zhang, H. Mi, L. Deng, L. Sun and X. Ren, *J. Power Sources*, 2017, **360**, 215–220.
- 356 D. Kundu, R. Black, E. J. Berg and L. F. Nazar, *Energy Environ. Sci.*, 2015, **8**, 1292–1298.
- 357 F. Wang, H. J. Li, Q. X. Wu, J. Fang, Y. Huang, C. L. Yin, Y. H. Xu and Z. K. Luo, *Electrochim. Acta*, 2016, **202**, 1–7.
- 358 C. Z. Yang, R. A. Wong, M. S. Hong, K. Yamanaka, T. Ohta and H. R. Byon, *Nano Lett.*, 2016, **16**, 2969–2974.
- 359 Y. Q. Gan, Y. Q. Lai, Z. Zhang, W. Chen, K. Du and J. Li, *J. Alloys Compd.*, 2016, **665**, 365–372.
- 360 X. Z. Zhang, D. Han, Y. B. He, D. Y. Zhai, D. Q. Liu, H. D. Du, B. H. Li and F. Y. Kang, *J. Mater. Chem. A*, 2016, **4**, 7727–7735.
- 361 G. Y. Zhao, L. Zhang, B. Y. Wang and K. N. Sun, *Electrochim. Acta*, 2015, **184**, 117–123.
- 362 J. L. He, B. B. Hu and Y. Zhao, *Adv. Funct. Mater.*, 2016, **26**, 5998–6004.
- 363 S. J. Amirfakhri, J. L. Meunier and D. Berk, *J. Power Sources*, 2014, **272**, 248–258.
- 364 D. Oh, J. F. Qi, B. H. Han, G. R. Zhang, T. J. Carney, J. Ohmura, Y. Zhang, Y. Shao-Horn and A. M. Belcher, *Nano Lett.*, 2014, **14**, 4837–4845.
- 365 H. Gong, H. R. Xue, T. Wang, H. Guo, X. L. Fan, L. Song, W. Xia and J. P. He, *ACS Appl. Mater. Interfaces*, 2016, **8**, 18060–18068.
- 366 H. R. Xue, X. W. Mu, J. Tang, X. L. Fan, H. Gong, T. Wang, J. P. He and Y. Yamauchi, *J. Mater. Chem. A*, 2016, **4**, 9106–9112.
- 367 H. R. Xue, S. C. Wu, J. Tang, H. Gong, P. He, J. P. He and H. S. Zhou, *ACS Appl. Mater. Interfaces*, 2016, **8**, 8427–8435.
- 368 B. Liu, P. F. Yan, W. Xu, J. M. Zheng, Y. He, L. L. Luo, M. E. Bowden, C. M. Wang and J. G. Zhang, *Nano Lett.*, 2016, **16**, 4932–4939.
- 369 W. M. Liu, T. T. Gao, Y. Yang, Q. Sun and Z. W. Fu, *Phys. Chem. Chem. Phys.*, 2013, **15**, 15806–15810.
- 370 A. Riaz, K. N. Jung, W. Chang, K. H. Shin and J. W. Lee, *ACS Appl. Mater. Interfaces*, 2014, **6**, 17815–17822.
- 371 F. F. Tu, J. Xie, S. C. Zhang, G. S. Cao, T. J. Zhu and X. B. Zhao, *J. Mater. Chem. A*, 2015, **3**, 5714–5721.
- 372 X. J. Lin, J. M. Su, L. Y. Li and A. S. Yu, *Electrochim. Acta*, 2015, **168**, 292–299.
- 373 C. Shen, Z. Y. Wen, F. Wang, K. Rui, Y. Lu and X. W. Wu, *J. Power Sources*, 2015, **294**, 593–601.
- 374 Y. Y. Liang, H. L. Wang, J. G. Zhou, Y. G. Li, J. Wang, T. Regier and H. J. Dai, *J. Am. Chem. Soc.*, 2012, **134**, 3517–3523.
- 375 S. C. Ma, L. Q. Sun, L. N. Cong, X. G. Gao, C. Yao, X. Guo, L. H. Tai, P. Mei, Y. P. Zeng, H. M. Xie and R. S. Wang, *J. Phys. Chem. C*, 2013, **117**, 25890–25897.
- 376 Y. Z. Chiang, C. Zhao, W. Melbourne, A. Wijayanti, K. Tran, J. Kim, N. Ishii, K. Legaspi, H. Koga, E. Schmidt, D. Zillikens, T. Hashimoto and D. Murrell, *Brit. J. Dermatol.*, 2015, **173**, 7–8.
- 377 X. C. Cao, J. Wu, C. Jin, J. H. Tian, P. Strasser and R. Z. Yang, *ACS Catal.*, 2015, **5**, 4890–4896.
- 378 J. J. Xu, Z. L. Wang, D. Xu, F. Z. Meng and X. B. Zhang, *Energy Environ. Sci.*, 2014, **7**, 2213–2219.
- 379 R. S. Kalubarme, H. S. Jadhav, D. T. Ngo, G.-E. Park, J. G. Fisher, Y.-I. Choi, W.-H. Ryu and C.-J. Park, *Sci. Rep.*, 2015, **5**, 13266.
- 380 H. Wu, W. Sun, Y. Wang, F. Wang, J. Liu, X. Yue, Z. Wang, J. Qiao, D. W. Rooney and K. Sun, *ACS Appl. Mater. Interfaces*, 2017, **9**, 12355–12365.
- 381 V. Neburchilov, H. J. Wang, J. J. Martin and W. Qu, *J. Power Sources*, 2010, **195**, 1271–1291.

- 382 S. H. Oh and L. F. Nazar, *Adv. Energy Mater.*, 2012, **2**, 903–910.
- 383 S. H. Oh, R. Black, E. Pomerantseva, J. H. Lee and L. F. Nazar, *Nat. Chem.*, 2012, **4**, 1004–1010.
- 384 W. Sun, Y. Wang, H. Wu, Z. Wang, D. Rooney and K. Sun, *Chem. Commun.*, 2017, **53**, 8711–8714.
- 385 S. L. Li, J. Xu, Z. Ma, S. M. Zhang, X. F. Wen, X. B. Yu, J. Yang, Z. F. Ma and X. X. Yuan, *Chem. Commun.*, 2017, **53**, 8164–8167.
- 386 B. Liu, W. Xu, P. F. Yan, P. Bhattacharya, R. G. Cao, M. E. Bowden, M. H. Engelhard, C. M. Wang and J. G. Zhang, *ChemSusChem*, 2015, **8**, 3697–3703.
- 387 J. Huang, B. Zhang, Z. Bai, R. Guo, Z.-L. Xu, Z. Sadighi, L. Qin, T.-Y. Zhang, G. Chen, B. Huang and J.-K. Kim, *Adv. Funct. Mater.*, 2016, **26**, 8290–8299.
- 388 J. X. Li, M. Z. Zou, W. W. Wen, Y. Zhao, Y. B. Lin, L. Z. Chen, H. Lai, L. H. Guan and Z. G. Huang, *J. Mater. Chem. A*, 2014, **2**, 10257–10262.
- 389 J. G. Kim, Y. Noh, Y. Kim, S. Lee and W. B. Kim, *Nanoscale*, 2017, **9**, 5119–5128.
- 390 J. Sunarso, S. S. Hashim, N. Zhu and W. Zhou, *Prog. Energy Combust. Sci.*, 2017, **61**, 57–77.
- 391 Y. L. Zhu, W. Zhou, Z. G. Chen, Y. B. Chen, C. Su, M. O. Tade and Z. P. Shao, *Angew. Chem., Int. Ed.*, 2015, **54**, 3897–3901.
- 392 P. Tan, M. Liu, Z. Shao and M. Ni, *Adv. Energy Mater.*, 2017, **7**, 1602674.
- 393 X. P. Han, Y. X. Hu, J. G. Yang, F. Y. Cheng and J. Chen, *Chem. Commun.*, 2014, **50**, 1497–1499.
- 394 Y. Wu, T. Wang, Y. Zhang, S. Xin, X. He, D. Zhang and J. Shui, *Sci. Rep.*, 2016, **6**, 24314.
- 395 E. Fabbri, R. Mohamed, P. Levecque, O. Conrad, R. Kotz and T. J. Schmidt, *ACS Catal.*, 2014, **4**, 1061–1070.
- 396 J. Suntivich, H. A. Gasteiger, N. Yabuuchi, H. Nakanishi, J. B. Goodenough and Y. Shao-Horn, *Nat. Chem.*, 2011, **3**, 647.
- 397 A. Grimaud, C. E. Carlton, M. Risch, W. T. Hong, K. J. May and Y. Shao-Horn, *J. Phys. Chem. C*, 2013, **117**, 25926–25932.
- 398 S. Malkhandi, P. Trinh, A. K. Manohar, A. Manivannan, M. Balasubramanian, G. K. S. Prakash and S. R. Narayanan, *J. Phys. Chem. C*, 2015, **119**, 8004–8013.
- 399 Y. L. Zhu, C. Su, X. M. Xu, W. Zhou, R. Ran and Z. P. Shao, *Chem. – Eur. J.*, 2014, **20**, 15533–15542.
- 400 G. X. Liu, H. B. Chen, L. Xia, S. Q. Wang, L. X. Ding, D. D. Li, K. Xiao, S. Dai and H. H. Wang, *ACS Appl. Mater. Interfaces*, 2015, **7**, 22478–22486.
- 401 Y. Zhao, Y. Hang, Y. Zhang, Z. Wang, Y. Yao, X. He, C. Zhang and D. Zhang, *Electrochim. Acta*, 2017, **232**, 296–302.
- 402 J. J. Xu, D. Xu, Z. L. Wang, H. G. Wang, L. L. Zhang and X. B. Zhang, *Angew. Chem., Int. Ed.*, 2013, **52**, 3887–3890.
- 403 P. Sennu, V. Aravindan, K. S. Nahm and Y.-S. Lee, *J. Mater. Chem. A*, 2017, **5**, 18029–18037.
- 404 Y. Liu, T. G. Kelly, J. G. G. Chen and W. E. Mustain, *ACS Catal.*, 2013, **3**, 1184–1194.
- 405 F. L. Qiu, P. He, J. Jiang, X. P. Zhang, S. F. Tong and H. S. Zhou, *Chem. Commun.*, 2016, **52**, 2713–2716.
- 406 B. D. Adams, R. Black, C. Radtke, Z. Williams, B. L. Mehdi, N. D. Browning and L. F. Nazar, *ACS Nano*, 2014, **8**, 12483–12493.
- 407 Z. Y. Wang, J. W. Sun, Y. H. Cheng and C. M. Niu, *J. Phys. Chem. Lett.*, 2014, **5**, 3919–3923.
- 408 Z. Y. Wang, X. Chen, Y. H. Cheng and C. M. Niu, *J. Phys. Chem. C*, 2015, **119**, 25684–25695.
- 409 Q.-C. Zhu, S.-M. Xu, M. M. Harris, C. Ma, Y.-S. Liu, X. Wei, H.-S. Xu, Y.-X. Zhou, Y.-C. Cao, K.-X. Wang and J.-S. Chen, *Adv. Funct. Mater.*, 2016, **26**, 8514–8520.
- 410 D. Kundu, R. Black, B. Adams, K. Harrison, K. Zavadil and L. F. Nazar, *J. Phys. Chem. Lett.*, 2015, **6**, 2252–2258.
- 411 Y. Lu, H. X. Ang, Q. Y. Yan and E. L. Fong, *Chem. Mater.*, 2016, **28**, 5743–5752.
- 412 Y. Q. Lai, W. Chen, Z. A. Zhang, Y. H. Qu, Y. Q. Gan and J. Li, *Electrochim. Acta*, 2016, **191**, 733–742.
- 413 Y. Zhao, K. Kamiya, K. Hashimoto and S. Nakanishi, *Angew. Chem., Int. Ed.*, 2013, **52**, 13638–13641.
- 414 Y. Zhao, K. Kamiya, K. Hashimoto and S. Nakanishi, *J. Am. Chem. Soc.*, 2015, **137**, 110–113.
- 415 M. J. Liu, Y. Z. Dong, Y. M. Wu, H. B. Feng and J. H. Li, *Chem. – Eur. J.*, 2013, **19**, 14781–14786.
- 416 F. J. Li, R. Ohnishi, Y. Yamada, J. Kubota, K. Domen, A. Yamada and H. S. Zhou, *Chem. Commun.*, 2013, **49**, 1175–1177.
- 417 S. M. Xu, Q. C. Zhu, M. Harris, T. H. Chen, C. Ma, X. Wei, H. S. Xu, Y. X. Zhou, Y. C. Cao, K. X. Wang and J. S. Chen, *Nano Lett.*, 2016, **16**, 5902–5908.
- 418 P. Ganesan, M. Prabu, J. Sanetuntikul and S. Shanmugam, *ACS Catal.*, 2015, **5**, 3625–3637.
- 419 A. T. Swesi, J. Masud and M. Nath, *Energy Environ. Sci.*, 2016, **9**, 1771–1782.
- 420 Y. Ji, H. Dong, M. Yang, T. Hou and Y. Li, *Phys. Chem. Chem. Phys.*, 2017, **19**, 20457–20462.
- 421 M. Asadi, B. Kumar, C. Liu, P. Phillips, P. Yasaei, A. Behranginia, P. Zapol, R. F. Klie, L. A. Curtiss and A. Salehi-Khojin, *ACS Nano*, 2016, **10**, 2167–2175.
- 422 S. P. Zhang, Z. N. Huang, Z. Y. Wen, L. L. Zhang, J. Jin, R. Shahbazian-Yassar and J. H. Yang, *Nano Lett.*, 2017, **17**, 3518–3526.
- 423 L. Y. Li, C. G. Chen, J. M. Su, P. Kuang, C. C. Zhang, Y. Yao, T. Huang and A. S. Yu, *J. Mater. Chem. A*, 2016, **4**, 10986–10991.
- 424 S. M. Dong, S. Wang, J. Guan, S. M. Li, Z. G. Lan, C. Chen, C. Q. Shang, L. X. Zhang, X. G. Wang, L. Gu, G. L. Cui and L. Q. Chen, *J. Phys. Chem. Lett.*, 2014, **5**, 615–621.
- 425 P. Sennu, M. Christy, V. Aravindan, Y. G. Lee, K. S. Nahm and Y. S. Lee, *Chem. Mater.*, 2015, **27**, 5726–5735.
- 426 Z. Ma, X. Yuan, Z. Zhang, D. Mei, L. Li, Z.-F. Ma, L. Zhang, J. Yang and J. Zhang, *Sci. Rep.*, 2015, **5**, 18199.
- 427 J. Read, *J. Electrochem. Soc.*, 2006, **153**, A96–A100.
- 428 J. Read, K. Mutolo, M. Ervin, W. Behl, J. Wolfenstine, A. Driedger and D. Foster, *J. Electrochem. Soc.*, 2003, **150**, A1351–A1356.

- 429 K. D. Cai, W. H. Pu, Y. Gao, J. B. Hou, C. S. Deng, C. Wang and Z. Q. Mao, *Int. J. Hydrogen Energy*, 2013, **38**, 11023–11027.
- 430 Y. C. Lu, B. M. Gallant, D. G. Kwabi, J. R. Harding, R. R. Mitchell, M. S. Whittingham and Y. Shao-Horn, *Energy Environ. Sci.*, 2013, **6**, 750–768.
- 431 D. Xu, Z. L. Wang, J. J. Xu, L. L. Zhang and X. B. Zhang, *Chem. Commun.*, 2012, **48**, 6948–6950.
- 432 W. B. Luo, S. L. Chou, J. Z. Wang, Y. M. Kang, Y. C. Zhai and H. K. Liu, *Chem. Commun.*, 2015, **51**, 8269–8272.
- 433 X. B. Zhu, T. S. Zhao, P. Tan, Z. H. Wei and M. C. Wu, *Nano Energy*, 2016, **26**, 565–576.
- 434 Y. F. Xu, Y. Zhao, J. Ren, Y. Zhang and H. S. Peng, *Angew. Chem., Int. Ed.*, 2016, **55**, 7979–7982.
- 435 J. Yi, S. H. Guo, P. He and H. S. Zhou, *Energy Environ. Sci.*, 2017, **10**, 860–884.
- 436 D. S. Hall, J. Self and J. R. Dahn, *J. Phys. Chem. C*, 2015, **119**, 22322–22330.
- 437 Q. Lu, Y. G. Gao, Q. Zhao, J. Li, X. H. Wang and F. S. Wang, *J. Power Sources*, 2013, **242**, 677–682.
- 438 H. Takezawa, S. Ito, H. Yoshizawa and T. Abe, *Electrochim. Acta*, 2017, **229**, 438–444.
- 439 Z. C. Zhang, J. Lu, R. S. Assary, P. Du, H. H. Wang, Y. K. Sun, Y. Qin, K. C. Lau, J. Greeley, P. C. Redfern, H. Iddir, L. A. Curtiss and K. Amine, *J. Phys. Chem. C*, 2011, **115**, 25535–25542.
- 440 S. Schaltin, G. Vanhoutte, M. X. Wu, F. Barde and J. Fransaer, *Phys. Chem. Chem. Phys.*, 2015, **17**, 12575–12586.
- 441 C. G. Chen, L. Y. Li, J. M. Su, C. C. Zhang, X. Chen, T. Huang and A. S. Yu, *Electrochim. Acta*, 2017, **243**, 357–363.
- 442 A. V. Sergeev, A. V. Chertovich, D. M. Itkis, A. Sen, A. Gross and A. R. Khokhlov, *J. Phys. Chem. C*, 2017, **121**, 14463–14469.
- 443 D. Xu, Z. L. Wang, J. J. Xu, L. L. Zhang, L. M. Wang and X. B. Zhang, *Chem. Commun.*, 2012, **48**, 11674–11676.
- 444 C. J. Bondue, M. Hegemann, C. Molls, E. Thome and H. Baltruschat, *J. Electrochem. Soc.*, 2016, **163**, A1765–A1775.
- 445 P. Schwager, S. Dongmo, D. Fenske and G. Wittstock, *Phys. Chem. Chem. Phys.*, 2016, **18**, 10774–10780.
- 446 N. Mozhzukhina, F. Marchini, W. R. Torres, A. Y. Tesio, L. P. M. De Leo, F. J. Williams and E. J. Calvo, *Electrochem. Commun.*, 2017, **80**, 16–19.
- 447 D. W. Kim, D. H. Lee, S. M. Ahn, D. Y. Kim, J. Suk, D. H. Choi and Y. K. Kang, *J. Power Sources*, 2017, **347**, 186–192.
- 448 M. Tokur, H. Algul, T. Cetinkaya, M. Uysal and H. Akbulut, *J. Electrochem. Soc.*, 2016, **163**, A1326–A1335.
- 449 S. S. Zhang, K. Xu and J. Read, *J. Power Sources*, 2011, **196**, 3906–3910.
- 450 M. Callsen, K. Sodeyama, Z. Futera, Y. Tateyama and I. Hamada, *J. Phys. Chem. B*, 2017, **121**, 180–188.
- 451 D. Sharon, D. Hirshberg, M. Afri, A. A. Frimer and D. Aurbach, *Chem. Commun.*, 2017, **53**, 3269–3272.
- 452 X. M. Ren, S. S. Zhang, D. T. Tran and J. Read, *J. Mater. Chem.*, 2011, **21**, 10118–10125.
- 453 D. Sharon, P. Sharon, D. Hirshberg, M. Salama, M. Afri, L. J. W. Shimon, W. J. Kwak, Y. K. Sun, A. A. Frimer and D. Aurbach, *J. Am. Chem. Soc.*, 2017, **139**, 11690–11693.
- 454 J. Sun, N. Zhao, Y. Li, X. Guo, X. Feng, X. Liu, Z. Liu, G. Cui, H. Zheng, L. Gu and H. Li, *Sci. Rep.*, 2017, **7**, 41217.
- 455 J. Yi and H. S. Zhou, *ChemSusChem*, 2016, **9**, 2391–2396.
- 456 S. Wu, J. Yi, K. Zhu, S. Bai, Y. Liu, Y. Qiao, M. Ishida and H. Zhou, *Adv. Energy Mater.*, 2017, **7**, 1601759.
- 457 M. Olivares-Marín, A. Sorrentino, E. Pereiro and D. Tonti, *J. Power Sources*, 2017, **359**, 234–241.
- 458 T. Kuboki, T. Okuyama, T. Ohsaki and N. Takami, *J. Power Sources*, 2005, **146**, 766–769.
- 459 M. L. Thomas, Y. Oda, R. Tatara, H.-M. Kwon, K. Ueno, K. Dokko and M. Watanabe, *Adv. Energy Mater.*, 2017, **7**, 1601753.
- 460 B. G. Kim, J. N. Lee, D. J. Lee, J. K. Park and J. W. Choi, *ChemSusChem*, 2013, **6**, 443–448.
- 461 L. Cecchetto, M. Salomon, B. Scrosati and F. Croce, *J. Power Sources*, 2012, **213**, 233–238.
- 462 J. H. Kim, H. S. Woo, S. J. Jin, J. S. Lee, W. Kim, K. Ryu and D. W. Kim, *RSC Adv.*, 2015, **5**, 80014–80021.
- 463 A. Chamaani, N. Chawla, M. Safa and B. El-Zahab, *Electrochim. Acta*, 2017, **235**, 56–63.
- 464 K. M. Abraham, Z. Jiang and B. Carroll, *Chem. Mater.*, 1997, **9**, 1978–1988.
- 465 S. N. Mohamed, N. A. Johari, A. M. M. Ali, M. K. Harun and M. Z. A. Yahya, *J. Power Sources*, 2008, **183**, 351–354.
- 466 J. Q. Zhang, B. Sun, X. Q. Xie, K. Kretschmer and G. X. Wang, *Electrochim. Acta*, 2015, **183**, 56–62.
- 467 K. N. Jung, J. I. Lee, J. H. Jung, K. H. Shin and J. W. Lee, *Chem. Commun.*, 2014, **50**, 5458–5461.
- 468 G. A. Elia, R. Bernhard and J. Hassoun, *RSC Adv.*, 2015, **5**, 21360–21365.
- 469 H. Kitaura and H. S. Zhou, *Adv. Energy Mater.*, 2012, **2**, 889–894.
- 470 J. Bai, H. Lu, Y. Cao, X. Li and J. Wang, *RSC Adv.*, 2017, **7**, 30603–30609.
- 471 J. R. Harding, C. V. Amanchukwu, P. T. Hammond and Y. Shao-Horn, *J. Phys. Chem. C*, 2015, **119**, 6947–6955.
- 472 J. Kumar, P. Kichambare, A. K. Rai, R. Bhattacharya, S. Rodrigues and G. Subramanyam, *J. Power Sources*, 2016, **301**, 194–198.
- 473 V. Giordani, D. Tozier, H. J. Tan, C. M. Burke, B. M. Gallant, J. Uddin, J. R. Greer, B. D. McCloskey, G. V. Chase and D. Addison, *J. Am. Chem. Soc.*, 2016, **138**, 2656–2663.
- 474 D. Chalasani and B. L. Lucht, *ECS Electrochem. Lett.*, 2012, **1**, A38–A42.
- 475 G. M. Veith, J. Nanda, L. H. Delmau and N. J. Dudney, *J. Phys. Chem. Lett.*, 2012, **3**, 1242–1247.
- 476 F. Marchini, S. Herrera, W. Torres, A. Y. Tesio, F. J. Williams and E. J. Calvo, *Langmuir*, 2015, **31**, 9236–9245.

- 477 E. Nasybulin, W. Xu, M. H. Engelhard, Z. M. Nie, S. D. Burton, L. Cosimbescu, M. E. Gross and J. G. Zhang, *J. Phys. Chem. C*, 2013, **117**, 2635–2645.
- 478 J. Lindberg, B. Wickman, M. Behm, A. Cornell and G. Lindbergh, *J. Electroanal. Chem.*, 2017, **797**, 1–7.
- 479 S. S. Zhang and J. Read, *J. Power Sources*, 2011, **196**, 2867–2870.
- 480 Y. Nishikami, T. Konishi, R. Omoda, Y. Aihara, K. Oyaizu and H. Nishide, *J. Mater. Chem. A*, 2015, **3**, 10845–10850.
- 481 H. Wan, Y. Mao, Z. X. Liu, Q. Y. Bai, Z. Peng, J. J. Bao, G. Wu, Y. Liu, D. Y. Wang and J. Y. Xie, *ChemSusChem*, 2017, **10**, 1385–1389.
- 482 F. J. Li, T. Zhang, Y. Yamada, A. Yamada and H. S. Zhou, *Adv. Energy Mater.*, 2013, **3**, 532–538.
- 483 B. Liu, W. Xu, P. F. Yan, X. L. Sun, M. E. Bowden, J. Read, J. F. Qian, D. H. Mei, C. M. Wang and J. G. Zhang, *Adv. Funct. Mater.*, 2016, **26**, 605–613.
- 484 Y. Liu, L. Suo, H. Lin, W. Yang, Y. Fang, X. Liu, D. Wang, Y. S. Hu, W. Han and L. Chen, *J. Mater. Chem. A*, 2014, **2**, 9020–9024.
- 485 J. M. Garcia, H. W. Horn and J. E. Rice, *J. Phys. Chem. Lett.*, 2015, **6**, 1795–1799.
- 486 C. V. Amanchukwu, H. H. Chang and P. T. Hammond, *J. Phys. Chem. C*, 2017, **121**, 17671–17681.
- 487 B. Zhou, L. Guo, Y. Zhang, J. Wang, L. Ma, W.-H. Zhang, Z. Fu and Z. Peng, *Adv. Mater.*, 2017, **29**, 1701568.
- 488 S. Meini, M. Piana, N. Tsiouvaras, A. Garsuch and H. A. Gasteiger, *Electrochem. Solid-State Lett.*, 2012, **15**, A45–A48.
- 489 S. Meini, S. Solchenbach, M. Piana and H. A. Gasteiger, *J. Electrochem. Soc.*, 2014, **161**, A1306–A1314.
- 490 Y. Qiao, S. Wu, J. Yi, Y. Sun, S. Guo, S. Yang, P. He and H. Zhou, *Angew. Chem., Int. Ed.*, 2017, **56**, 4960–4964.
- 491 S. Wu, Y. Qiao, S. Yang, J. Tang, P. He and H. Zhou, *ACS Catal.*, 2018, **8**, 1082–1089.
- 492 D. G. Kwabi, T. P. Batcho, C. V. Amanchukwu, N. Ortiz-Vitoriano, P. Hammond, C. V. Thompson and Y. Shao-Horn, *J. Phys. Chem. Lett.*, 2014, **5**, 2850–2856.
- 493 D. Sharon, M. Afri, M. Noked, A. Garsuch, A. A. Frimer and D. Aurbach, *J. Phys. Chem. Lett.*, 2013, **4**, 3115–3119.
- 494 M. J. Trahan, S. Mukerjee, E. J. Plichta, M. A. Hendrickson and K. M. Abraham, *J. Electrochem. Soc.*, 2013, **160**, A259–A267.
- 495 K. U. Schwenke, M. Metzger, T. Restle, M. Piana and H. A. Gasteiger, *J. Electrochem. Soc.*, 2015, **162**, A573–A584.
- 496 N. Mahne, O. Fontaine, M. O. Thotiyil, M. Wilkening and S. A. Freunberger, *Chem. Sci.*, 2017, **8**, 6716–6729.
- 497 J. B. Park, J. Hassoun, H. G. Jung, H. S. Kim, C. S. Yoon, I. H. Oh, B. Scrosati and Y. K. Sun, *Nano Lett.*, 2013, **13**, 2971–2975.
- 498 L. Yang, J. T. Frith, N. Garcia-Araez and J. R. Owen, *Chem. Commun.*, 2015, **51**, 1705–1708.
- 499 M. J. Lacey, J. T. Frith and J. R. Owen, *Electrochem. Commun.*, 2013, **26**, 74–76.
- 500 V. Pande and V. Viswanathan, *ACS Energy Lett.*, 2017, **2**, 60–63.
- 501 S. Matsuda, K. Hashimoto and S. Nakanishi, *J. Phys. Chem. C*, 2014, **118**, 18397–18400.
- 502 A. Y. Tesio, D. Blasi, M. Olivares-Marin, I. Ratera, D. Tonti and J. Veciana, *Chem. Commun.*, 2015, **51**, 17623–17626.
- 503 Y. H. Chen, S. A. Freunberger, Z. Q. Peng, O. Fontaine and P. G. Bruce, *Nat. Chem.*, 2013, **5**, 489–494.
- 504 M. K. Bates, Q. Y. Jia, H. Doan, W. T. Liang and S. Mukerjee, *ACS Catal.*, 2016, **6**, 155–161.
- 505 J. Zhang, B. Sun, Y. Zhao, K. Kretschmer and G. Wang, *Angew. Chem., Int. Ed.*, 2017, **56**, 8505–8509.
- 506 J. Han, G. Huang, Y. Ito, X. Guo, T. Fujita, P. Liu, A. Hirata and M. Chen, *Adv. Energy Mater.*, 2017, **7**, 1601933.
- 507 D. Sun, Y. Shen, W. Zhang, L. Yu, Z. Yi, W. Yin, D. Wang, Y. Huang, J. Wang, D. Wang and J. B. Goodenough, *J. Am. Chem. Soc.*, 2014, **136**, 8941–8946.
- 508 H. Yang, Q. Wang, R. Zhang, B. D. Trimm and M. S. Whittingham, *Chem. Commun.*, 2016, **52**, 7580–7583.
- 509 B. J. Bergner, M. R. Busche, R. Pinedo, B. B. Berkes, D. Schröder and J. Janek, *ACS Appl. Mater. Interfaces*, 2016, **8**, 7756–7765.
- 510 S. Y. Bie, Y. Q. Zhu, J. M. Su, C. Jin, S. H. Liu, R. Z. Yang and J. Wu, *J. Mater. Chem. A*, 2015, **3**, 22448–22453.
- 511 N. Feng, X. Mu, X. Zhang, P. He and H. Zhou, *ACS Appl. Mater. Interfaces*, 2017, **9**, 3733–3739.
- 512 S. Ha, Y. Kim, D. Koo, K.-H. Ha, Y. Park, D.-M. Kim, S. Son, T. Yim and K. T. Lee, *J. Mater. Chem. A*, 2017, **5**, 10609–10621.
- 513 J. C. Henderson, Y. Kiya, G. R. Hutchison and H. D. Abruna, *J. Phys. Chem. C*, 2008, **112**, 3989–3997.
- 514 X. Hu, J. Wang, Z. Li, J. Wang, D. H. Gregory and J. Chen, *Nano Lett.*, 2017, **17**, 2073–2078.
- 515 K. P. C. Yao, J. T. Frith, S. Y. Sayed, F. Bardé, J. R. Owen, Y. Shao-Horn and N. Garcia-Araez, *J. Phys. Chem. C*, 2016, **120**, 16290–16297.
- 516 Z. Liu, Y. Zhang, C. Jia, H. Wan, Z. Peng, Y. Bi, Y. Liu, Z. Peng, Q. Wang, H. Li, D. Wang and J.-G. Zhang, *Nano Energy*, 2017, **36**, 390–397.
- 517 S. Matsuda, S. Mori, Y. Kubo, K. Uosaki, K. Hashimoto and S. Nakanishi, *Chem. Phys. Lett.*, 2015, **620**, 78–81.
- 518 W.-H. Ryu, F. S. Gittleson, J. M. Thomsen, J. Li, M. J. Schwab, G. W. Brudvig and A. D. Taylor, *Nat. Commun.*, 2016, **7**, 12925.
- 519 D. Sun, Y. Shen, W. Zhang, L. Yu, Z. Q. Yi, W. Yin, D. Wang, Y. H. Huang, J. Wang, D. L. Wang and J. B. Goodenough, *J. Am. Chem. Soc.*, 2014, **136**, 8941–8946.
- 520 Z. Y. Guo, C. Li, J. Y. Liu, Y. G. Wang and Y. Y. Xia, *Angew. Chem., Int. Ed.*, 2017, **56**, 7505–7509.
- 521 X. Zeng, L. Leng, F. Liu, G. Wang, Y. Dong, L. Du, L. Liu and S. Liao, *Electrochim. Acta*, 2016, **200**, 231–238.
- 522 T. H. Yoon and Y. J. Park, *RSC Adv.*, 2014, **4**, 17434–17442.
- 523 S. H. Yoon and Y. J. Park, *Sci. Rep.*, 2017, **7**, 42617.
- 524 W.-J. Kwak, D. Hirshberg, D. Sharon, H.-J. Shin, M. Afri, J.-B. Park, A. Garsuch, F. F. Chesneau, A. A. Frimer, D. Aurbach and Y.-K. Sun, *J. Mater. Chem. A*, 2015, **3**, 8855–8864.

- 525 T. Liu, M. Leskes, W. J. Yu, A. J. Moore, L. N. Zhou, P. M. Bayley, G. Kim and C. P. Grey, *Science*, 2015, **350**, 530–533.
- 526 Z. Liang and Y.-C. Lu, *J. Am. Chem. Soc.*, 2016, **138**, 7574–7583.
- 527 S. Matsuda, S. Mori, K. Hashimoto and S. Nakanishi, *J. Phys. Chem. C*, 2014, **118**, 28435–28439.
- 528 W. J. Kwak, D. Hirshberg, D. Sharon, M. Afri, A. A. Frimer, H. G. Jung, D. Aurbach and Y. K. Sun, *Energy Environ. Sci.*, 2016, **9**, 2334–2345.
- 529 Y. G. Zhu, X. Wang, C. Jia, J. Yang and Q. Wang, *ACS Catal.*, 2016, **6**, 6191–6197.
- 530 X. Gao, Y. Chen, L. R. Johnson, Z. P. Jovanov and P. G. Bruce, *Nat. Energy*, 2017, **2**, 17118.
- 531 S. H. Lee, J.-B. Park, H.-S. Lim and Y.-K. Sun, *Adv. Energy Mater.*, 2017, **7**, 1602417.
- 532 M. Balaish and Y. Ein-Eli, *J. Mater. Chem. A*, 2017, **5**, 14152–14164.